

**Novel Use of P- and S-wave Seismic Attenuation for Deep Natural
Gas Exploration and Development
DE-FC26-04NT42243**

**Final Report
October 1, 2004 to September 30, 2006**

Issued: October 2006

Contributors

Dr. Joel Walls*

Dr. M. T. Taner*

Richard Uden*

Scott Singleton*

Naum Derzhi*

Dr. Gary Mavko**

Dr. Jack Dvorkin**

*Principal Contractor:

Rock Solid Images

2600 S. Gessner Suite 650

Houston, TX, 77036

**Subcontractor:

Petrophysical Consulting Inc.

730 Glenmere Way

Emerald Hills, CA, 94062

DISCLAIMER

This report was prepared as an account of work sponsored by the United States Government. Neither the United States Government nor any agency thereof, nor any of their employees, makes any warranty, expressed or implied, or assumes any legal liability or responsibility for the accuracy, completeness, or usefulness of any information, apparatus, product, or process disclosed, or represents that its use would not infringe privately owned rights. Reference herein to any specific commercial product, process, or service by trade name, trademark, manufacturer, or otherwise does not necessarily constitute or imply its endorsement, recommendation, or favoring by the United States Government or any agency thereof. The views and opinions of authors expressed herein do not necessarily state or reflect those of the United States Government or any agency thereof.

ABSTRACT

Deeply buried gas reservoirs along the Gulf of Mexico shelf are an important future energy resource for the U.S. One of the greatest problems encountered by operators in this area is identifying commercially viable targets for drilling. Because of the great depth of the reservoirs (over 15,000 ft), the most common 3D seismic methods for direct hydrocarbon indication, such as AVO (amplitude versus offset), are not reliable. Many wells have been drilled on deep AVO anomalies, only to find that they contain noncommercial quantities of gas (the so called “fizz-water” problem). Other problems in detecting deep gas formations are caused by inadequate offset in the seismic data acquisition and by high fluid pressures, which tend to make gas look more like water in a seismic sense.

In 2004, Rock Solid Images undertook a project to demonstrate novel and robust techniques for reducing hydrocarbon indicator risk in deep gas sands by exploiting an additional set of completely independent indicators – the rock inelastic properties. These inelastic properties of P-wave and S-wave energy from multicomponent seismic provide a crucial added dimension of discrimination for pore fluids and lithology.

The objective of this project was to develop and test a new methodology for computing P-wave and S-wave attenuation from standard well log data, using the log-derived attenuation for generating P-wave synthetic seismic traces with and without attenuation effects, and extracting seismic attenuation attributes from multicomponent P-wave and S-wave seismic data and relating these to the presence of high GOR oil or natural gas.

The objective was achieved, resulting in a new algorithm to compute both Q_p and Q_s from conventional well log data, an algorithm to create full offset, full waveform synthetics incorporating the effects of attenuation, and two algorithms to compute attenuation from seismic data. We found that attenuation in seismic data can be related to gas-bearing reservoirs, and can be used as a reconnaissance tool in exploration; that attenuation can have a substantial impact on seismic response, both post-stack and pre-stack, and cause significant changes in seismic amplitude with offset, especially at the bottom of a gas zone; and we concluded that attenuation should be used in conjunction with other seismic attributes such as elastic attributes and geologic context in order to reduce risk in the search for DHIs. However, attenuation alone can be a valuable tool in deep targets because AVO may fail in these environments

TABLE OF CONTENTS

DISCLAIMER	2
ABSTRACT	3
TABLE OF CONTENTS	4
EXECUTIVE SUMMARY	7
PART 1: ROCK PHYSICS RELATIONS FOR QP AND QS	8
P-WAVE ATTENUATION IN RESERVOIR AND NON-RESERVOIR ROCK	8
DEFINITIONS AND BASICS	9
MODULUS DISPERSION AND ATTENUATION AT PARTIAL SATURATION	13
MODULUS DISPERSION AND ATTENUATION IN WET ROCK	22
EXAMPLES OF ATTENUATION CALCULATION	25
COMPARISON TO DATA	28
A THEORETICAL ESTIMATE OF S-WAVE ATTENUATION IN SEDIMENT	33
S-WAVE ATTENUATION DATA	34
S-WAVE ATTENUATION THEORY	38
COMPARING Q_p/Q_s WITH Q_p/Q_{ps}	42
A SIMPLE DERIVATION	43
LABORATORY EXAMPLE	46
PART 1 SUMMARY	47
PART 2: SYNTHETIC SEISMOGRAM MODELING WITH Q	49
MODELING ATTENUATION EFFECTS IN A GAS RESERVOIR	49
SYNTHETIC SEISMIC TRACES AT NORMAL INCIDENCE	50
SYNTHETIC SEISMIC GATHERS	52
AVO CURVES FROM GATHERS	53
TUNING AND ATTENUATION	55
HALF-SPACE MODELING OF PP REFLECTIONS WITH ATTENUATION	60
THE EARTH MODEL	60
CALCULATING THE AVO RESPONSE	62
ACCOUNTING FOR ATTENUATION IN AVO	62
APPROXIMATIONS	63
ATTENUATION EFFECT ON AVO – ANALYTICAL APPROXIMATION	64
IMPLEMENTATION	65
TESTING	66
HALF-SPACE MODELING OF PS REFLECTIONS WITH OFFSET	68

MATLAB APPLET FOR MODELING THE EARTH BEYOND THE WELL 73

PART 2 SUMMARY 75

PART 3: PROPERTIES OF PORE FLUIDS AT HIGH PRESSURE AND TEMPERATURE.. 77

 COMPARISON TO THE BATZLE-WANG (1992) EQUATIONS..... 77

 EFFECT ON ELASTIC PROPERTIES OF SAND 79

 EFFECT ON AVO RESPONSE..... 80

 FLUID PROPERTIES 81

 PART 3 SUMMARY 81

PART 4: ATTENUATION AND DISPERSION FROM SEISMIC AND LINK TO WELL

DATA 83

 GENERAL DEFINITIONS 83

 “CLOSING THE LOOP” FOR Q..... 84

 SPECTRAL RATIO METHODS 85

 SPECTRAL RATIO FOR STRATIGRAPHIC ATTENUATION..... 86

 SPECTRAL RATIO FOR INTRINSIC Q, PLUS STRATIGRAPHIC ATTENUATION
 86

 SPECTRAL RATIO FOR SPATIALLY VARIABLE INTRINSIC Q 88

 SPECTRAL RATIO ANALYSIS IN THE TIME DOMAIN 90

 GABOR-MORLET TRANSFORM & Q ESTIMATION 91

 JTFA LOG SPECTRAL RATIO METHOD 92

 JTFA FREQUENCY SHIFT METHOD 94

 PART 4 SUMMARY 98

PART 5: TESTING WITH FIELD DATA..... 100

 EUGENE ISLAND MULTI COMPONENT FIELD DATA 100

 WELL SELECTION..... 101

 VELOCITY SURVEYS 102

 P-WAVE VELOCITY AT DEPTH..... 104

 STACKED SEISMIC DATA INSPECTION 105

 WELL LOG DATA AND ROCK PHYSICS MODELING..... 109

 ROCK PHYSICS MODEL..... 110

 P-TO-S TRANSFORM..... 114

 ATTENUATION MODELING..... 115

 SYNTHETIC SEISMIC MODELING WITH ATTENUATION 118

 PRE-STACK PP SEISMIC GATHER REVIEW 120

 TEMPORAL REGISTRATION OF PS TO PP SEISMIC DATA..... 121

 PS TO PP REGISTRATION RESULTS 123

SEISMIC INELASTIC ATTRIBUTES RESPONSE..... 126
 RESPONSE ON PP DATA VOLUME 126
 RESPONSE ON PS DATA VOLUME 130
PART 5 SUMMARY 135
PROJECT ACCOMPLISHMENTS AND CONCLUSIONS..... 139
REFERENCES 145
LIST OF ACRONYMS 148
APPENDIX 1: PAPERS PRESENTED 152
APPENDIX 2: DEEP GAS EXPLORATION USING P- AND S-WAVE SEISMIC
ATTENUATION (ARTICLE SUBMITTED TO *GAS TIPS*) 181
APPENDIX 3: FINAL PRESENTATION 189

EXECUTIVE SUMMARY

This project focused on developing new technology to facilitate the analysis of attenuation effects in surface seismic data. The particular environment for which this technology was being developed was deep gas. The project focused on three major goals:

1. To develop methods of computing P-wave and S-wave attenuation from standard well log data such as porosity, V_{clay} , and S_w .
2. To develop methods of using the log-derived attenuation for generating P-wave synthetic seismic traces, with and without attenuation effects.
3. To develop new methods of computing attenuation-related attributes from reflection seismic data – both P-wave and mode-converted PS-wave.

These goals were accomplished, and we have shown through testing with different field examples, that attenuation-related seismic attributes can be useful in identifying producing deep gas formations.

The main conclusions and key findings from this project are:

- 1 Rock physics methods can be used to compute both Q_p and Q_s from conventional well log data.
- 2 Q_p and Q_s can be computed from PP and PS seismic data, respectively.
- 3 Attenuation can have a substantial impact on seismic response, both post-stack and pre-stack, and cause significant changes in seismic amplitude with offset, especially at the bottom of a gas zone.
- 4 Attenuation in seismic data can be related to gas bearing reservoirs, and can be used as a reconnaissance tool in exploration.
- 5 Attenuation should be used in conjunction with other seismic attributes, such as elastic attributes and geologic context. However, attenuation can be a valuable tool in deep targets because AVO may fail in these environments.

PART 1: ROCK PHYSICS RELATIONS FOR QP AND QS

One critical objective of this project was to introduce a theoretical model for calculating S-wave attenuation in the subsurface from such inputs as porosity, mineralogy, hydrocarbon type and saturation, and pore pressure. This extended the theoretical model we previously developed for calculating P-wave attenuation from the same volumetric inputs. One use of these models is to produce attenuation pseudo-logs in a well where other, standard, well log curves are available. In addition, the model-driven log curves will be used for pre-stack or offset synthetic seismic modeling at the well and tie with real seismic. The seismic synthetic models can be PP (P down and P up), or SS (S down and S up), or PS (P down and S up), the latter being the case for OBC (Ocean Bottom Cable). Another use is to calculate attenuation in a pseudo-well where the original rock properties in an existing well are perturbed to reflect possible variability existing in the subsurface.

Below, we review the attenuation model for Qp and introduce the Qs model by subsequently analyzing attenuation in a partially saturated rock and a fully saturated rock. The attenuation in the fully saturated (or wet) rock serves as the attenuation background to which additional attenuation is added due to the partial saturation.

By comparing our model results to some of the available laboratory and field data, we conclude that the models are satisfactory for estimating attenuation in sediment realistically.

P-WAVE ATTENUATION IN RESERVOIR AND NON-RESERVOIR ROCK

Wave-induced variations of pore pressure in partially saturated rock or in fully saturated, elastically heterogeneous rock result in oscillatory liquid flow. The viscous losses during this flow are responsible for wave attenuation. The same viscous effects determine the changes in the dynamic elastic moduli of the system versus frequency. These changes are necessarily linked to P-wave attenuation via the causality condition. The low-frequency compressional modulus of partially saturated rock is estimated by means of theoretical fluid substitution, using the rock's dry-frame modulus and the harmonic average of the moduli of individual fluid components as the effective bulk modulus of the pore-fluid mix. The high-frequency compressional modulus of partially saturated rock is estimated by assuming that fluid distribution is patchy; i.e., some

large-scale patches are fully water saturated while others contain gas. The difference between the low-frequency and high-frequency moduli is translated into the inverse quality factor by adopting a viscoelastic model (e.g., the standard linear body). The same causality link between the modulus-frequency dispersion and attenuation is used to estimate the latter in fully saturated rock. The necessary condition for attenuation is elastic heterogeneity in rock. The low-frequency compressional modulus is calculated by substituting theoretically the pore fluid into the spatially averaged rock's dry-frame modulus while the high-frequency modulus is the spatial average of the heterogeneous saturated-rock modulus. The difference between these two estimates may give rise to noticeable P-wave attenuation if elastic heterogeneity in rock is substantial.

DEFINITIONS AND BASICS

Attenuation and the Inverse Quality Factor

The attenuation coefficient α is defined as the exponential decay coefficient of a harmonic wave:

$$A(x, t) = A_0 \exp[-\alpha(\omega)x] \exp[i(\omega t - kx)], \quad (1.1)$$

where A is the amplitude of the signal at time t ; A_0 is the amplitude of the input signal; t is time; x is the spatial coordinate; $\omega = 2\pi f$ is the angular frequency; f is frequency; and k is the wave number. The attenuation coefficient is related to the inverse quality factor Q^{-1} as

$$\alpha = Q^{-1} \pi f / V = \pi / (QTV) = \pi / (Q\lambda), \quad (1.2)$$

where V is the phase velocity; T is the period; and λ is the wavelength. By substituting Equation (1.2) into Equation (1.1) we obtain:

$$\frac{A(x, t)}{A_0} = \exp\left[-\frac{\pi x}{Q\lambda}\right] \exp[i(\omega t - kx)]. \quad (1.3)$$

To understand better the practical meaning of the quality factor Q , let us determine over how many wavelengths the amplitude decreases by a factor of 10^n . We find from Equation (1.3):

$$\exp\left[-\frac{\pi x}{Q\lambda}\right] = 10^{-n} \Rightarrow \frac{x}{\lambda} = n \frac{2.3}{\pi} Q = 0.733nQ, \quad (1.4)$$

which means that the required number of wavelengths is $0.733nQ$.

Similarly, the number of wavelengths past which the amplitude decreases by a factor of 2^n is $0.221nQ$. If $Q = 5$ ($Q^{-1} = 0.2$), the amplitude decreases by a factor of 2 as the wave travels 1.1

wavelengths and by a factor of 10 as the wave travels 3.7 wavelengths. If $Q = 10$ ($Q^{-1} = 0.1$), the amplitude decreases by a factor of 2 as the wave travels 2.2 wavelengths and by a factor of 10 as it travels 7.3 wavelengths.

Sometimes α is measured in dB per unit length. The conversion coefficient is 8.686:

$$\alpha_{[\text{dB/Length}]} = 8.686Q^{-1}\pi f / V. \quad (1.5)$$

Adding Attenuation from Separate Mechanisms

In an attempt to relate wave attenuation to reservoir properties and conditions, we often have to consider separate attenuation mechanisms described by different mathematical models. For example, elastic waves may attenuate in a dry sandstone frame due to viscoelastic clay present in the frame. If this sandstone is partially saturated, additional attenuation may be due to wave-induced viscous fluid flow. The question is how to add attenuation separately calculated for these two mechanisms to assess the resulting total attenuation.

Let us assume that the first attenuation mechanism acts to reduce the input-signal amplitude by a factor of n , from A_0 to $A_1 = A_0 \exp(-\alpha_1 x)$, over distance x while the second mechanism independently acts to reduce the initial amplitude by a factor of m , from A_0 to $A_2 = \exp(-\alpha_2 x)$, over the same distance. Let us also assume that when acting together, the two mechanisms reduce the initial amplitude over distance x by a factor nm . The resulting amplitude is

$$A_{Sum} = nmA_0 = \frac{A_1}{A_0} \frac{A_2}{A_0} A_0 = A_0 e^{-\alpha_1 x} e^{-\alpha_2 x} = A_0 e^{-(\alpha_1 + \alpha_2)x}, \quad (1.6)$$

which means that the attenuation coefficients calculated for separate attenuation mechanisms can be simply added. If we further assume that the phase velocity and dominant frequency are the same for separate mechanisms we obtain from Equation (1.2) that the inverse quality factor from separate mechanism adds arithmetically, while the quality factor adds harmonically.

Upscaling Attenuation

If the amplitude A_0 of the input signal reduces to $A_1 = A_0 \exp(-\alpha_1 x_1)$ after the wave travels distance x_1 with attenuation coefficient α_1 , it further reduces to $A_2 = A_1 \exp(-\alpha_2 x_2)$ after it travels additional distance x_2 with attenuation coefficient α_2 . As a result,

$$A_2 = A_0 e^{-(\alpha_1 x_1 + \alpha_2 x_2)} \equiv A_0 e^{-\alpha(x_1 + x_2)}, \quad (1.7)$$

where α is the average (upscaled) attenuation coefficient over distance $x_1 + x_2$. As a result,

$$\alpha = \alpha_1 \frac{x_1}{x_1 + x_2} + \alpha_2 \frac{x_2}{x_1 + x_2}, \quad (1.8)$$

which means that the attenuation coefficient has to be upscaled arithmetically (as $\langle \alpha \rangle$).

Strictly speaking, the inverse quality factor cannot be upscaled arithmetically because $Q^{-1} = \alpha V / \pi f$ and both V and f may change from interval to interval. A correct expression for averaging (upscaling) the inverse quality factor over a long interval is

$$\overline{Q^{-1} \frac{\pi f}{V}} = \left\langle Q^{-1} \frac{\pi f}{V} \right\rangle. \quad (1.9)$$

The average (upscaled) inverse quality factor $\overline{Q^{-1}}$ can be defined through the average velocity \overline{V} and average attenuation coefficient $\overline{\alpha}$ as

$$\overline{Q^{-1}} = \overline{\alpha} \overline{V} / \pi f, \quad (1.10)$$

where $\overline{\alpha}$ is the arithmetic average of the attenuation coefficient and \overline{V} is the upscaled velocity, which should be calculated from the Backus (harmonic) average of the elastic modulus $M = \rho V^2$, where ρ is the bulk density:

$$\overline{V} = \sqrt{\overline{M} / \overline{\rho}}, \quad \overline{M} = \langle M^{-1} \rangle^{-1}, \quad \overline{\rho} = \langle \rho \rangle. \quad (1.11)$$

Modulus (Velocity) Changes and Attenuation

If the deformational response of a physical material to a load depends not only on the magnitude of the load but also on the rate of change of the load, the material is called *viscoelastic*. While in an elastic material the stress σ is related to the strain ε by the linear Hooke's law

$$\sigma_{ij} = \lambda \delta_{ij} \varepsilon_{kk} + 2\mu \varepsilon_{ij}, \quad (1.12)$$

where λ and μ are Lamé's coefficients, such relations in a viscoelastic material are more complicated. Some examples of constitutive equations that express these relations are

$$2\dot{\chi}_{ij} = \dot{\chi}_{ij} / \mu + \sigma_{ij} / \eta \quad (1.13)$$

for Maxwell's solid;

$$\sigma_{ij} = 2\eta \dot{\chi}_{ij} + 2\mu \varepsilon_{ij} \quad (1.14)$$

for Voigt's solid; and

$$\eta \dot{\alpha}_{ij} + (E_1 + E_2)\sigma_{ij} = E_2(\eta \dot{\alpha}_{ij} + E_1 \varepsilon_{ij}) \quad (1.15)$$

for the standard linear solid (SLS), where E_1 and E_2 are additional elastic moduli and η is a material constant resembling viscosity.

If Hooke's law is used to calculate the elastic moduli of a viscoelastic medium, these moduli become complex simply because of a phase shift between the strain and stress. Of course, the presence of an imaginary part in an expression for these moduli is merely for mathematical convenience.

Physically this simply means that the deformational response of a viscoelastic material to stress is not instantaneous but rather shifted in time. Consider an SLS physical representation by a combination of springs and a dashpot (Figure 1.1). Due to the presence of a viscous dashpot element, the system will react stiffer to fast excitation and softer to slow excitation.

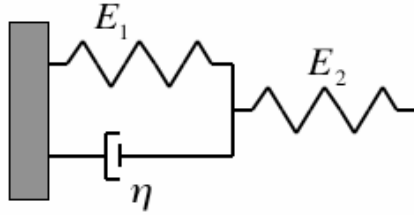


Figure 1.1. A spring/dashpot system with a response described by the SLS constitutive law, as in Equation (1.15).

In other words, the apparent effective modulus of the system will be larger for high-frequency excitation than for low-frequency excitation. This effect will translate into speed of a high-frequency wave being greater than that of a low-frequency wave. It is often called velocity-frequency or modulus-frequency dispersion.

In a viscoelastic medium, the modulus-frequency dispersion and inverse quality factor are linked by the causality Kramers-Kronig relations (Mavko et al., 1998)

$$Q^{-1}(\omega) = \frac{|\omega|}{\pi M_R(\omega)} \int_{-\infty}^{\infty} \frac{M_R(\alpha) - M_R(0)}{\alpha} \frac{d\alpha}{\alpha - \omega}, \quad (1.16)$$

$$M_R(\omega) - M_R(0) = \frac{-\omega}{\pi} \int_{-\infty}^{\infty} \frac{Q(\alpha) M_R(\alpha)}{|\alpha|} \frac{d\alpha}{\alpha - \omega},$$

where ω is the angular frequency and $M_R(\omega)$ is the real part of the complex modulus $M(\omega)$.

Two simple viscoelastic models give examples of linking attenuation to modulus-frequency dispersion (Mavko et al., 1998). According to SLS, the elastic modulus M is related to linear

frequency f as

$$M(f) = \frac{M_0 M_\infty [1 + (f/f_{CR})^2]}{M_\infty + M_0 (f/f_{CR})^2}, \quad (1.17)$$

where M_0 is the low-frequency limit; M_∞ is the high-frequency limit; and f_{CR} is the critical frequency at which the transition occurs from the low-frequency to the high-frequency limit.

The corresponding inverse quality factor is

$$Q^{-1}(f) = \frac{(M_\infty - M_0)(f/f_{CR})}{\sqrt{M_0 M_\infty [1 + (f/f_{CR})^2]}}. \quad (1.18)$$

The maximum inverse quality factor is at $f = f_{CR}$:

$$Q_{\max}^{-1} = \frac{M_\infty - M_0}{2\sqrt{M_0 M_\infty}}. \quad (1.19)$$

The constant (or nearly constant) Q (CQ) model assumes that the quality factor is constant within a frequency range. Then the inverse quality factor is

$$Q^{-1}(f) = \frac{\pi}{\log(f_1/f_0)} \frac{M_1 - M_0}{2M_0}, \quad (1.20)$$

where M_0 is the modulus at frequency f_0 and M_1 is the modulus at frequency f_1 where both frequency values (f_0 and f_1) are within the constant Q range. It follows from Equation (1.20) that the modulus changes proportionally to the logarithm of frequency, i.e.,

$$M = M_0 \left(\frac{2}{\pi Q} \log \frac{f}{f_0} + 1 \right). \quad (1.21)$$

MODULUS DISPERSION AND ATTENUATION AT PARTIAL SATURATION

Relaxed and Unrelaxed Patches

The frequency range of seismic waves used in practical application spans four orders of magnitude, from 10^1 (seismic) to 10^4 (sonic logging) Hz. The pore-scale Biot's and squirt flow attenuation mechanisms are not likely to be engaged at these frequencies. In partially saturated rock, viscoelastic effects and attenuation may arise from the oscillatory liquid cross-flow between fully liquid-saturated patches and the surrounding rock with partial gas saturation. The length scale of these patches is at least an order of magnitude larger than the pore scale.

To recognize physical reasons for the existence of patchy saturation, consider a relatively

large volume of rock that includes several smaller sand volumes whose clay content and/or grain size vary. Such variations usually dramatically affect permeability (e.g., Yin, 1993) and, simultaneously, capillary pressure curves and irreducible water saturation.

In a state of capillary equilibrium, capillary pressure is the same for adjacent patches whose irreducible water saturation is different. As a result, at partial saturation, some patches (with large irreducible water saturation) may be fully water saturated, while other patches (with smaller irreducible water saturation) may contain gas (Knight et al., 1998). The whole volume will have patchy liquid distribution.

Visual proof that patches may form in oil-water and air-water systems in the laboratory was presented by Chatenever and Calhoun (1952) and Cadoret (1993). Indirect evidence that patches exist in situ was presented by Brie et al. (1995) and Dvorkin et al. (1999).

The reaction of rock with patchy saturation to loading due to elastic wave propagation depends on the frequency of the wave. If the frequency is low, i.e., the loading is slow, the oscillations of the pore pressure in a fully liquid-saturated patch and partially saturated domains next to it equilibrate. The patch is “relaxed.” Conversely, if the frequency is high, i.e., the loading of the rock is fast, the resulting oscillatory variations of pore pressure cannot equilibrate between the fully saturated patch and the domain outside. The patch is “unrelaxed.” The response of the unrelaxed patch is not influenced by the presence of gas next to it.

The critical size L below which the patch is relaxed can be estimated as

$$L = \sqrt{\frac{1}{f} \frac{kK_w}{\phi\mu}}, \quad (1.22)$$

where k is the permeability, K_w is the bulk modulus of the liquid, ϕ is the porosity, and μ is the dynamic viscosity of the liquid in the patch. Example calculations of the critical size are displayed in Figure 1.2. At 100 Hz and permeability 1 D, this size is about 0.3 m, which means that larger patches will be unrelaxed while smaller patches will be relaxed. For permeability 1 mD, the critical size is about 0.01 m, which means that any patch of a larger size will be unrelaxed at 100 Hz.

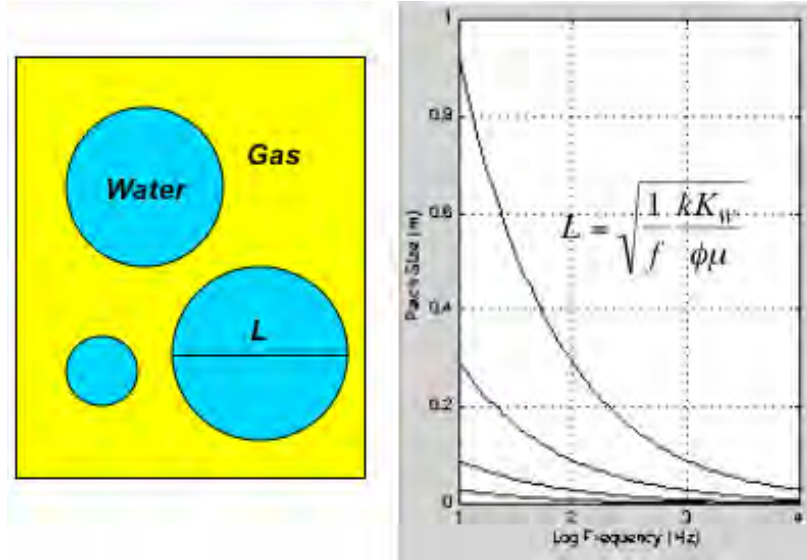


Figure 1.2. Left – Schematic of macroscopic fully saturated patches in a partially saturated reservoir. Right – Critical length versus frequency for a patch saturated with water with the bulk modulus of 2.5 GPa and viscosity 1 cPs, as given by Equation (1.22). The porosity of the patch is 0.3. The permeability is 1 mD for the lower curve and 1D for the upper curve, with an order of magnitude increment in between.

Relaxed Patches: Low-Frequency Elastic Modulus

If the patches in partially saturated rock are relaxed, which may occur at very low frequency, it is valid to use the concept of the effective pore fluid that is a mixture of liquid and gas. The effective bulk modulus of this mixture (K_F) is the harmonic (or isostress) average of the moduli of water (K_W) and gas (K_G):

$$\frac{1}{K_F} = \frac{S_W}{K_W} + \frac{1-S_W}{K_G}, \quad (1.23)$$

where S_W is water saturation. This type of pore fluid averaging implies “uniform” fluid saturation.

Then the bulk modulus of the partially saturated region K_{Sat0} is determined by Gassmann's equation

$$K_{Sat0} = K_S \frac{\phi K_{Dry} - (1 + \phi) K_F K_{Dry} / K_S + K_F}{(1 - \phi) K_F + \phi K_S - K_F K_{Dry} / K_S}, \quad (1.24)$$

where K_{Dry} is the bulk modulus of the dry frame of the rock, K_S is the bulk modulus of the mineral phase, and ϕ is the total porosity. The shear modulus of the partially saturated region

G_{Sat} is the same as that of the dry-rock frame G_{Dry} . The compressional modulus at low frequency (M_{Sat0}) is

$$M_{Sat0} = K_{Sat0} + \frac{4}{3}G_{Dry}. \quad (1.25)$$

Mavko et al. (1995) give an approximate V_p -only fluid-substitution equation that can be used to calculate the compressional modulus of saturated rock directly from that of the dry frame (M_{Dry}):

$$M_{Sat0} = M_S \frac{\phi M_{Dry} - (1 + \phi)K_F M_{Dry} / M_S + K_F}{(1 - \phi)K_F + \phi M_S - K_F M_{Dry} / M_S}, \quad (1.26)$$

where M_S is the compressional modulus of the mineral phase.

Unrelaxed Patches: High-Frequency Elastic Modulus

If the patches in partially saturated rock are unrelaxed, which may occur at high frequency, the concept of the effective pore fluid is not applicable. The bulk modulus of a fully saturated patch (K_p) will be that of the fully liquid saturated rock:

$$K_p = K_S \frac{\phi K_{Dry} - (1 + \phi)K_W K_{Dry} / K_S + K_W}{(1 - \phi)K_W + \phi K_S - K_W K_{Dry} / K_S}. \quad (1.27)$$

If we assume that all liquid in partially saturated rock is concentrated in fully saturated patches and the rest of the rock is filled with gas, the volumetric concentration of the fully saturated patches in the system is S_w . If we assume in addition that the shear modulus is the same for the liquid-saturated and gas-saturated patches, the effective compressional modulus of the partially saturated rock ($M_{Sat\infty}$) is the harmonic average of the compressional moduli of the fully saturated (M_p) and dry ($M_{S_w=0}$) patches (Mavko et al., 1998):

$$\frac{1}{M_{Sat\infty}} = \frac{S_w}{M_p} + \frac{1 - S_w}{M_{S_w=0}}, \quad (1.28)$$

or, in terms of the bulk and shear moduli,

$$\frac{1}{K_{Sat\infty} + (4/3)G_{Dry}} = \frac{S_w}{K_p + (4/3)G_{Dry}} + \frac{1 - S_w}{K_{S_w=0} + (4/3)G_{Dry}}, \quad (1.29)$$

where $K_{Sat\infty}$ and $K_{S_w=0}$ are the bulk moduli of the fully saturated and dry patches, respectively.

These moduli can be calculated from Gassmann's equation as

$$K_P = K_S \frac{\phi K_{Dry} - (1 + \phi) K_W K_{Dry} / K_S + K_W}{(1 - \phi) K_W + \phi K_S - K_W K_{Dry} / K_S} \quad (1.30)$$

and

$$K_{S_{w=0}} = K_S \frac{\phi K_{Dry} - (1 + \phi) K_G K_{Dry} / K_S + K_G}{(1 - \phi) K_G + \phi K_S - K_G K_{Dry} / K_S}. \quad (1.31)$$

Expressions for M_P and $M_{S_{w=0}}$ using the Mavko et al. (1995) approximate V_p -only fluid-substitution equation are

$$M_P = M_S \frac{\phi M_{Dry} - (1 + \phi) K_W M_{Dry} / M_S + K_W}{(1 - \phi) K_W + \phi M_S - K_W M_{Dry} / M_S} \quad (1.32)$$

and

$$M_{S_{w=0}} = M_S \frac{\phi M_{Dry} - (1 + \phi) K_G M_{Dry} / M_S + K_G}{(1 - \phi) K_G + \phi M_S - K_G M_{Dry} / M_S}, \quad (1.33)$$

respectively.

Consider soft sand with porosity 0.3; clay content 0.05; and the dry-frame bulk and shear moduli 2.6 and 3.2 GPa, respectively. The bulk moduli of water and gas are 2.64 and 0.04 GPa, respectively. Figure 1.3, below, displays the low-frequency and high-frequency compressional modulus of this sand versus water saturation as calculated using the above equations.

The calculated difference between the low-frequency and high-frequency compressional modulus is zero in dry rock and fully water-saturated rock. The maximum is at about 0.9 water saturation. The difference between the Gassmann fluid substitution results and approximate V_p -only fluid substitution results is very small.

Attenuation from Modulus Dispersion

The calculated difference between the compressional modulus for uniform and patchy fluid saturation is essentially the modulus-frequency dispersion for partially saturated rock. In order to calculate attenuation, we have to assume that the rock is viscoelastic and select a model to describe its behavior.

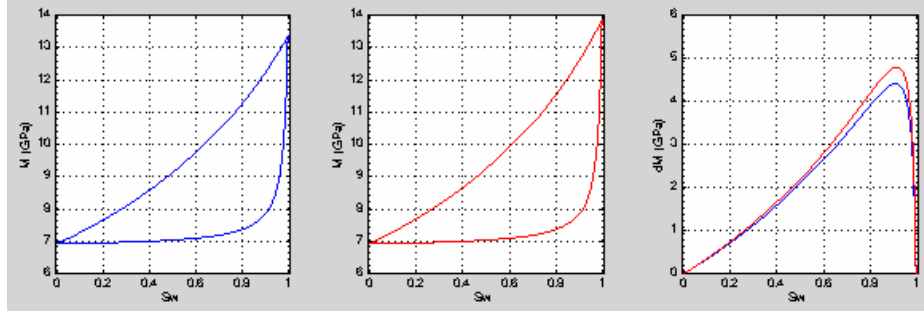


Figure 1.3. Compressional modulus versus water saturation for low-frequency and high-frequency equations. Left – Gassmann’s fluid substitution. Middle – v_p -only fluid substitution. Right – difference between high-frequency and low-frequency compressional modulus using Gassmann’s fluid substitution (blue) and v_p -only fluid substitution (red).

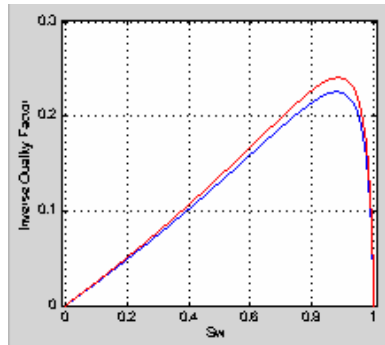


Figure 1.4. The maximum inverse quality factor according to Equation (1.20) using Gassmann’s fluid substitution (blue) and v_p -only fluid substitution (red).

A simple approach (but not necessarily a correct one) is to use Equation (1.20) to calculate the maximum inverse quality factor for given modulus dispersion. Figure 1.4 displays Q_{\max}^{-1} versus water saturation for the example used in Figure 1.3. As expected, the inverse quality factor is largest at about 0.9 water saturation where the modulus-frequency dispersion is largest.

Role of Irreducible Water Saturation

Real gas reservoirs always have irreducible water saturation S_{WIr} . Let us assume that whenever $S_w < S_{WIr}$, the pore fluid is distributed within the rock uniformly and, as a result, the bulk modulus of the pore-fluid mix is given by Equation (1.24) and the bulk modulus of the saturated rock is given by Equation (1.25). Let us add water to partially saturated rock to arrive at water saturation $S_w > S_{WIr}$. Let us also assume that all additional water (above the irreducible

water) is concentrated in fully saturated patches that start to appear as soon as S_W exceeds S_{Wlrr} .

The volumetric concentration f_p of these patches in the partially saturated rock is

$$f_p = \frac{S_W - S_{Wlrr}}{1 - S_{Wlrr}}. \quad (1.34)$$

The bulk modulus of the fully saturated patch is given by Equation (1.31). The bulk modulus $K_{S_W=S_{Wlrr}}$ of the surrounding rock at $S_W = S_{Wlrr}$ is given by Gassmann's equation

$$K_{S_W=S_{Wlrr}} = K_S \frac{\phi K_{Dry} - (1 + \phi) K_{Flrr} K_{Dry} / K_S + K_{Flrr}}{(1 - \phi) K_{Flrr} + \phi K_S - K_{Flrr} K_{Dry} / K_S}, \quad (1.35)$$

where

$$\frac{1}{K_{Flrr}} = \frac{S_{Wlrr}}{K_W} + \frac{1 - S_{Wlrr}}{K_G}. \quad (1.36)$$

The bulk modulus of rock with patchy saturation at $S_W > S_{Wlrr}$ is given by the constant-shear-modulus equation, the same as Equation (1.29):

$$\begin{aligned} \frac{1}{K_{Satlrr\infty} + (4/3)G_{Dry}} &= \frac{f_p}{K_P + (4/3)G_{Dry}} + \frac{1 - f_p}{K_{S_W=S_{Wlrr}} + (4/3)G_{Dry}} \\ &= \frac{(S_W - S_{Wlrr})/(1 - S_{Wlrr})}{K_P + (4/3)G_{Dry}} + \frac{(1 - S_W)/(1 - S_{Wlrr})}{K_{S_W=S_{Wlrr}} + (4/3)G_{Dry}}, \end{aligned} \quad (1.37)$$

while the bulk modulus of the system at $S_W \leq S_{Wlrr}$ is given by Equations (1.23) and (1.24).

The same logic can be used to estimate the compressional modulus of rock with residual water saturation from the approximate V_p -only fluid substitution equations. For $S_W \leq S_{Wlrr}$, it is calculated from Equations (1.23) and (1.26) while for $S_W > S_{Wlrr}$

$$\frac{1}{M_{Satlrr\infty}} = \frac{(S_W - S_{Wlrr})/(1 - S_{Wlrr})}{M_P} + \frac{(1 - S_W)/(1 - S_{Wlrr})}{M_{S_W=S_{Wlrr}}}, \quad (1.38)$$

where M_P is given by Equation (1.32) and

$$M_{S_W=S_{Wlrr}} = M_S \frac{\phi M_{Dry} - (1 + \phi) K_{Flrr} M_{Dry} / M_S + K_{Flrr}}{(1 - \phi) K_{Flrr} + \phi M_S - K_{Flrr} M_{Dry} / M_S}, \quad (1.39)$$

with K_{Flrr} coming from Equation (1.36).

The compressional modulus is plotted versus water saturation in Figure 1.5, assuming that the irreducible water saturation is 0.3. The difference between the high-frequency and low-frequency compressional modulus is smaller than shown in Figure 1.3. This difference will reduce even further if we increase S_{Wlrr} . As in the example shown in Figure 1.3, the difference

between the results of Gassmann’s fluid substitution and V_p -only fluid substitution is negligible.

As shown in the Figure 1.4 example, Q_{\max}^{-1} can be calculated from Equation (1.20). It is plotted versus water saturation in Figure 1.6. As expected from the modulus difference in Figure 1.5, the larger the irreducible water saturation the smaller the attenuation.

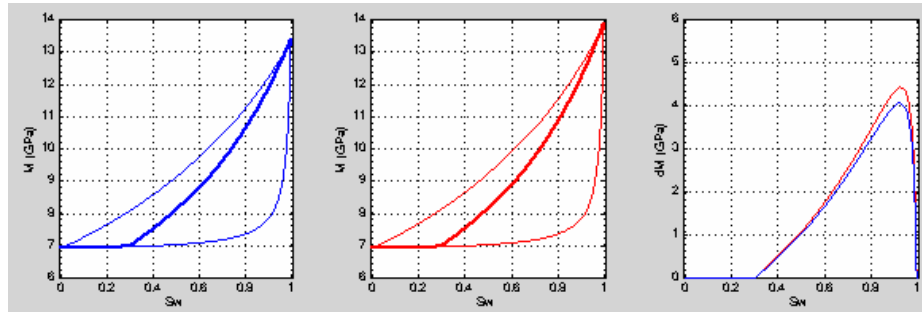


Figure 1.5. Compressional modulus versus water saturation with irreducible water saturation 0.3 (bold curves). Left – Gassmann’s fluid substitution. Middle – v_p -only fluid substitution. Right – difference between high-frequency and low-frequency compressional modulus using Gassmann’s fluid substitution (blue) and v_p -only fluid substitution (red).

An important conclusion about the effect of irreducible water saturation on attenuation is that as the former increases the latter decreases. We may expect very small attenuation in sand with large water saturation if the irreducible water saturation is large as well. This means that large attenuation does not necessarily manifest high water saturation (residual gas) as could be implied from the calculations shown in Figure 1.4. Quantitative interpretation of seismic attenuation has always to take into account the character of the rock.

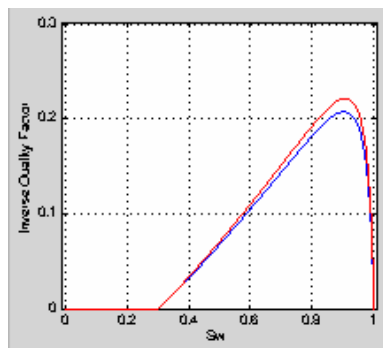


Figure 1.6. The maximum inverse quality factor according to Equation (1.20) using Gassmann’s fluid substitution (blue) and v_p -only fluid substitution (red) for irreducible water saturation 0.3.

“Effective Pore Fluid” for Patchy Fluid Substitution

It is still possible to employ the effective pore fluid concept to estimate the bulk and compressional moduli of partially saturated rock for patchy saturation if the bulk modulus of this effective pore fluid (K_{FP}) is calculated as the arithmetic average of those of gas and water:

$$K_{FP} = S_w K_w + (1 - S_w) K_G. \quad (1.40)$$

Then K_{FP} can be used instead of the harmonically averaged effective-fluid modulus in Gassmann’s or V_p -only fluid substitution equations as

$$K_{Sat\infty} = K_S \frac{\phi K_{Dry} - (1 + \phi) K_{FP} K_{Dry} / K_S + K_{FP}}{(1 - \phi) K_{FP} + \phi K_S - K_{FP} K_{Dry} / K_S}. \quad (1.41)$$

Equation (1.41) can be modified to account for irreducible water saturation. In this case, the bulk modulus of the effective pore fluid (K_{FPirr}) is calculated from Equation (1.24) for $S_w < S_{wIrr}$ and as

$$K_{FPirr} = \frac{S_w - S_{wIrr}}{1 - S_{wIrr}} K_w + \frac{1 - S_w}{1 - S_{wIrr}} K_{FIrr} \quad (1.42)$$

for $S_w > S_{wIrr}$, where K_{FIrr} is the bulk modulus of the uniform gas/water mix at $S_w = S_{wIrr}$, as given by Equation (1.23).

The results of calculating the compressional modulus of partially saturated rock using Equation (1.40), Equation (1.42), and Gassmann’s fluid substitution are compared to the rigorously calculated “patchy” modulus (as described in the above sections) in Figure 1.7 for the example used above.

These results are close enough to the rigorous “patchy” curves and are acceptable given the uncertainty of the assumptions used. Nevertheless, it is important to emphasize that Equations (1.41) and (1.42) provide convenient but physically deceptive approximations. Unlike the harmonic (isostress) average of the bulk moduli of the pore-fluid components, the arithmetic average does not have a clear physical foundation.

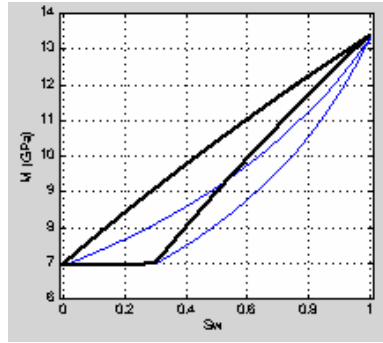


Figure 1.7. The compressional modulus versus water saturation using arithmetically averaged bulk modulus of the pore fluid, as given by Equations (1.40) and (1.42), in bold black, compared to rigorously calculated “patchy” modulus (thin blue curves). The calculations are done for zero and 0.3 irreducible water saturation.

MODULUS DISPERSION AND ATTENUATION IN WET ROCK

Elastic Heterogeneity and Squirt Flow

Seismic energy in porous rock with fluid dissipates due to wave-induced oscillatory cross-flow. The viscous-flow friction irreversibly transfers part of the energy into heat. This flow can be especially strong in partially saturated rock where the viscous fluid phase (water) moves in and out of the gas-saturated pore space. Such viscous-friction losses may also occur in wet rock where elastic heterogeneity is present. Deformation due to a stress wave is relatively strong in the softer portion of the rock and weak in the stiffer portion. The spatial heterogeneity in the deformation of the solid frame forces the fluid to flow between the softer and stiffer portions. Such cross-flow may occur at all spatial scales.

Microscopic “squirt-flow” is developed at the sub-millimeter pore scale because a single pore may include compliant crack-like and stiff equi-dimensional parts (Mavko and Jizba, 1991). Macroscopic “squirt-flow” which is more relevant to the seismic prospecting scale may occur due to elastic heterogeneity in the rock frame elastic moduli. This mechanism has recently received a rigorous mathematical treatment by Pride et al. (2003) in a “double-porosity” model. However, there is a simple way of quantifying the effect of macroscopic “squirt-flow” on seismic wave attenuation.

Example

Seismic energy in porous rock with fluid dissipates due to wave-induced oscillatory cross-flow. The viscous-flow friction irreversibly transfers part of the energy into heat. This flow can be especially strong in partially saturated rock where the viscous fluid phase (water) moves in and out of the gas-saturated pore space. Such viscous-friction losses may also occur in wet rock where elastic heterogeneity is present. Deformation due to a stress wave is relatively strong in the softer portion of the rock and weak in the stiffer portion. The spatial heterogeneity in the deformation of the solid frame forces the fluid to flow between the softer and stiffer portions. Such cross-flow may occur at all spatial scales.

Consider a model rock that is fully water-saturated (wet) and has two parts. One part (80% of the rock volume) is shale with porosity 0.4, clay content 0.8 (the rest is quartz), and the P-wave velocity 1.9 km/s. The other part (the remaining 20%) is clean, high-porosity, slightly cemented sand, with porosity 0.3 and the P-wave velocity 3.4 km/s. The compressional modulus is 7 GPa in the shale and 25 GPa in the sand. Because of the difference between the compliance of the sand and shale parts, their deformation due to a passing wave is different, which leads to macroscopic “squirt-flow.”

At high frequency, there is essentially no cross-flow between sand and shale simply because the flow cannot fully develop during the short cycle of oscillation. The effective elastic modulus of the system is the harmonic (Backus) average of the moduli of the two parts: $M_{\infty} = 16$ GPa.

At low frequency, the cross-flow can easily develop. In this case, the fluid reacts to the combined deformation of the dry frame of the sand and shale. The dry-frame compressional modulus in the shale is 2 GPa, while that in the sand is 20 GPa. The dry-frame modulus of the combined dry frame can perhaps be estimated as the harmonic average of the two: 7 GPa. The arithmetically averaged porosity of the model rock is 0.32. To estimate the effective compressional modulus of the combined dry frame with water, we theoretically substitute water into this combined frame. The result is $M_0 = 13$ GPa. The maximum inverse quality factor Q_{\max}^{-1} according to Equation (1.19) is about 0.1 ($Q = 10$), which translates into a noticeable attenuation coefficient 0.05 dB/m at 50 Hz.

Application to a Vertical Interval

The above-described averaging technique for attenuation estimate in wet rock can be applied to well log curves by means of a moving averaging window. Specifically, in a heterogeneous interval, we estimate the average porosity ϕ_{Eff} as the arithmetic average of individual porosities:

$$\phi_{Eff} = \langle \phi \rangle; \quad (1.43)$$

and the effective dry-frame compressional modulus M_{DryEff} as the Backus (harmonic) average of individual moduli:

$$M_{DryEff} = \langle M_{Dry}^{-1} \rangle^{-1}. \quad (1.44)$$

The effective saturated-rock compressional modulus at very low frequency can be calculated by applying the V_p -only fluid substitution equation (Mavko et al., 1995) to the domain where the averaging was conducted:

$$M_0 = M_S \frac{\phi_{Eff} M_{DryEff} - (1 + \phi_{Eff}) K_W M_{DryEff} / M_S + K_W}{(1 - \phi_{Eff}) K_W + \phi_{Eff} M_S - K_W M_{DryEff} / M_S}, \quad (1.45)$$

where M_S is the mineral-phase compressional modulus, assumed the same for all individual parts of the rock. M_S can be estimated by averaging the mineral-component moduli in the entire volume of the rock by, e.g., Hill's (1952) average.

At high frequency, the individual parts of the domain appear undrained, i.e., the oscillatory flow simply cannot develop because the period of the oscillation is small and the pore-fluid is viscous. Then, the saturated-rock compressional moduli of each individual part can be calculated by applying the V_p -only fluid substitution equation individually to each part. The effective saturated-rock compressional modulus of the whole domain is the Backus (1962) average of the individual saturated-rock compressional moduli:

$$M_\infty = \left\langle \left(M_S \frac{\phi M_{Dry} - (1 + \phi) K_F M_{Dry} / M_S + K_F}{(1 - \phi) K_F + \phi M_S - K_F M_{Dry} / M_S} \right)^{-1} \right\rangle^{-1}. \quad (1.46)$$

Finally, Q_{max}^{-1} is calculated from Equation (1.19).

EXAMPLES OF ATTENUATION CALCULATION

Gulf Coast Gas Well

Consider a Gulf Coast well (Well A) that penetrates an over-pressured shale interval with gas sand at the bottom (Figure 1.8). Overpressure in the shale is manifested by the abnormal increase in the bulk density and impedance (under compaction) with increasing depth. The impedance in the gas sand is smaller than that in the shale above it. The calculated inverse quality factor is (as expected) large in the gas sand, with Q becoming as low as 8, and negligibly small in the shale, except for the upper part where elastic heterogeneity in the shale is present and, as a result, Q is about 80.

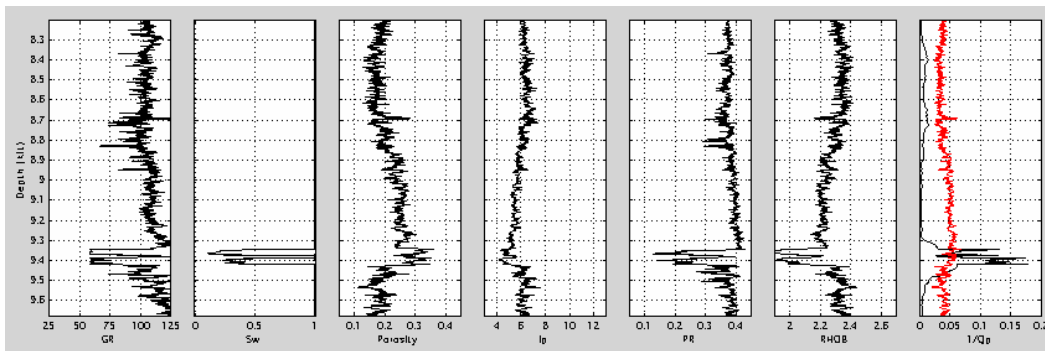


Figure 1.8. Well log curves in an over-pressured Gulf Coast gas Well A. From left to right: gamma-ray, water saturation, total porosity, P-wave impedance, Poisson's ratio, bulk density, and the inverse quality factor. The red curve in the inverse quality factor frame is calculated according to the Koeseomadinata and McMechan (2001) equations.

Let us next calculate the elastic properties in the interval under examination for wet conditions by theoretically replacing the gas in the sand by the formation water using Gassmann's fluid substitution. The resulting impedance in the sand is larger than that in the shale above it (Figure 1.9). This impedance difference constitutes discernable elastic heterogeneity in the interval. The result of this elastic heterogeneity is attenuation that stands out of the background, with Q reaching as low as 20.

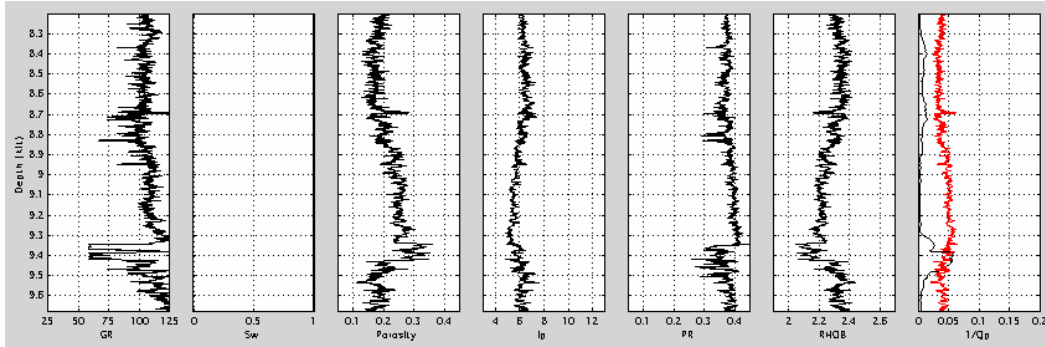


Figure 1.9. Same as Figure 1.8 but for the wet interval, where the elastic properties are calculated from the original well log data via fluid substitution.

Gas Wells with Consolidated Sand and Shale

Consider three gas wells with fairly consolidated sand and shale intervals. The porosity in the upper sand in Well B is about 0.3, while that in the lower sand is about 0.25 and is much stiffer than the upper sand (Figure 1.10). The calculated quality factor appears to depend strongly on the stiffness of the gas reservoir. It is about 7 in the upper, relatively soft sand, and about 20 in the lower, relatively stiff sand.

The results of attenuation calculation in Well C (Figure 1.11) show that the quality factor is about 10 in high-porosity but stiff (possibly contact-cemented) gas sand intervals. An interesting feature in this well is large attenuation, with Q as low as 7 in a strongly elastically heterogeneous sequence of shale and wet sand between 17 and 18 kft.

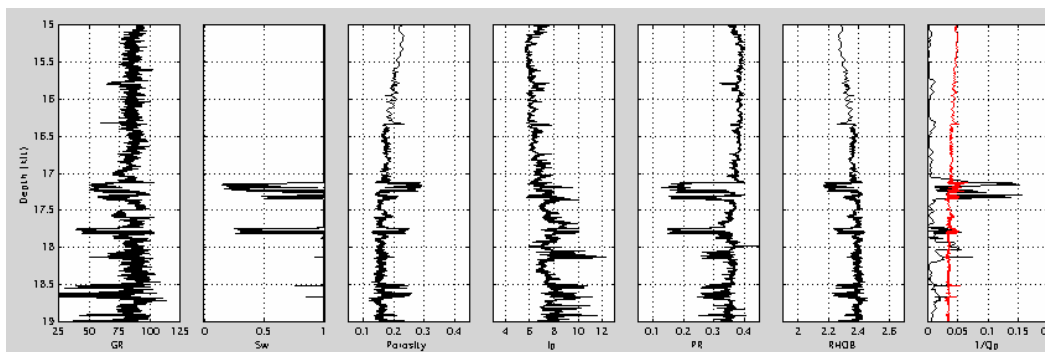


Figure 1.10. Same as Figure 1.8, but for Well B.

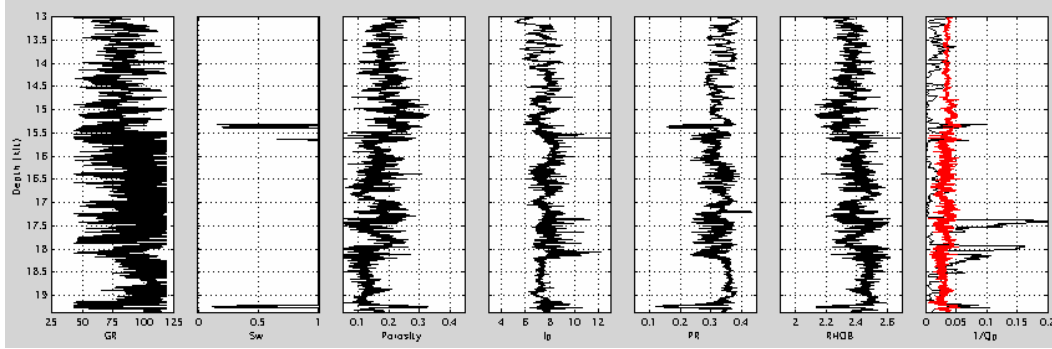


Figure 1.11. Same as Figure 1.8, but for Well C.

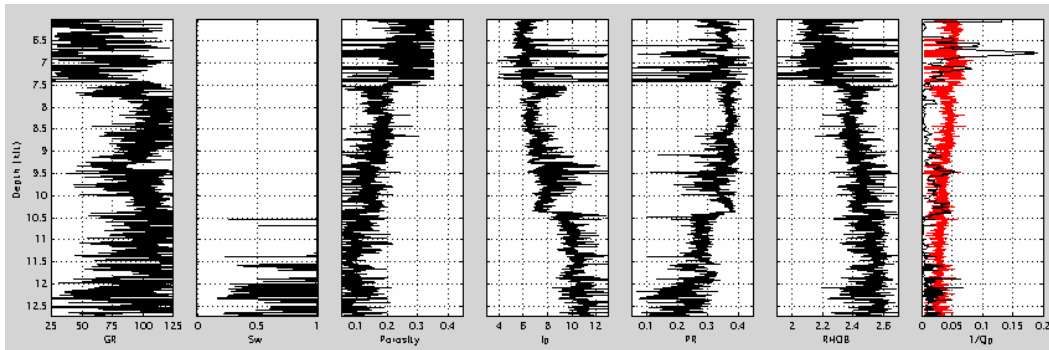


Figure 1.12. Same as Figure 1.8, but for Well D.

Gas sand in Well D (Figure 1.12) has small-to-medium porosity and large impedance. Accordingly, the attenuation in this gas-sand interval is small, with Q as high as 30. Attenuation due to strong elastic heterogeneity in the upper part of Well D is much higher; Q is as low as 7.

Gas Well with Very Soft Sand

The example in Figure 1.13, Well E, shows fairly large attenuation, with Q as low as 6 in very soft unconsolidated shallow gas sand.

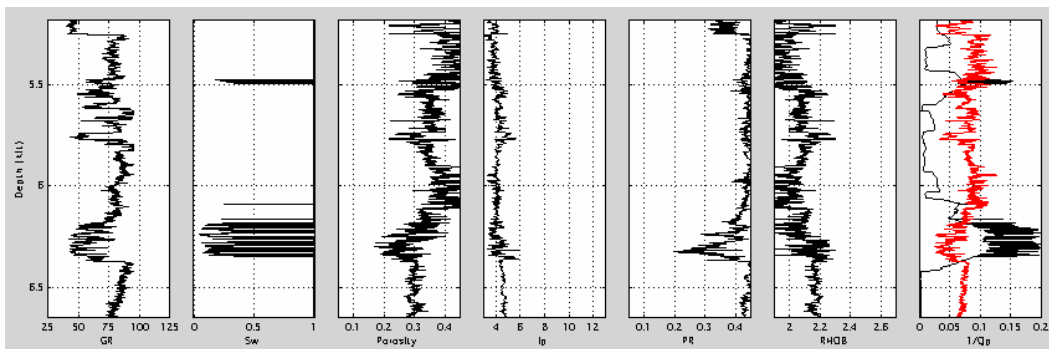


Figure 1.13. Same as Figure 1.8, but for Well E.

The background attenuation in the shale and wet sand is negligibly small except where

elastic heterogeneity is present, such as at the very top of the interval, where Q in a wet sand/shale sequence drops down to 20.

Oil Well

The example in Figure 1.14, Well F, shows that attenuation strongly depends on the type of hydrocarbon. While Q could be as low as 6 in gas sand, it does not fall below 20 in oil sand except for the lowest oil-saturated interval in this well. There, attenuation due to the presence of oil adds to attenuation due to elastic heterogeneity, with the resulting Q reaching as low as 10.

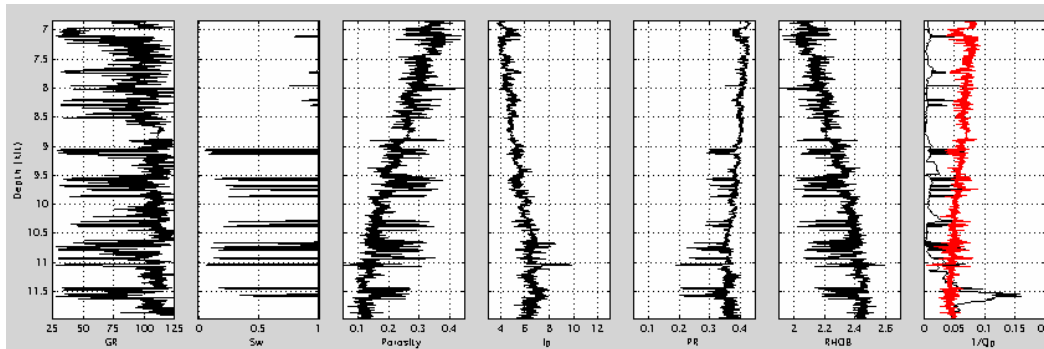


Figure 1.14. Same as Figure 1.8, but for Well F.

COMPARISON TO DATA

Field Data

Consistent and accurate field measurements of Q are very scarce due to practical difficulties related to the extraction of attenuation from field reflection seismic data, and from cross-well, VSP, and full waveform borehole data. Toksoz and Johnston (1981) estimate that Q is 32 in Pierre shale in Colorado, following the data of McDonal et al. (1958). Hamilton (1972) reports that the in-situ-measured Q in marine sediments is about 30 in wet sand and may be as high as 100, and even 400, in silt and clay. Leary et al. (1988) use VSP data to find Q exceeding 300 in basement rock at depths below 1.8 km.

Juhlin (1990a) determined Q for rocks in the Siljan (Sweden) impact structure using VSP data recorded down to 5.7 km (Juhlin, 1988, 1990b). The dominant crystalline rocks are granites. Attenuation changes substantially as a function of depth. In the upper 1.0–1.5 km, Q is about 30; it is between 150 and 200 below this depth interval. The dominant frequency is between about 50 and 100 Hz. The difference in Q values correlates with the intensity of

fracturing, which is heavy in the upper interval.

Q values estimated from seismic events are usually very high. Kvamme and Havskov (1988) estimate Q of about 950 at 10 Hz. Lilwall (1988) uses Q between 100 and 200 in the upper 3 km of the crust.

In contrast, Pujol et al. (1998) report surprisingly low Q , between 14 and 32, in crystalline rock between 3.6 and 4.5 km depth in the KTB well in Germany. These estimates come from VSP data in the 8 to 50 Hz frequency range. The authors cannot adequately explain this unusually high attenuation and suggest that it may be due to wave scattering.

Hackert and Para (2004) report Q of 33 as calculated from high-resolution 2D seismic data over a Florida carbonate high-porosity aquifer system, where the P-wave velocity is between 2 and 3 km/s and density is about 2 g/cc.

Quan and Harris (1997) use cross-well tomography to estimate attenuation at the Devine test site in the 200 to 2000 Hz frequency range. Q is between 30 and 50 in a soft sand/shale sequence (P-wave velocity varies from 2.6 to 3.0 km/s) and reaches 100 in chalk and limestone.

Several studies explore attenuation in methane-hydrate-bearing sediment. The value of these data for an attenuation investigation in conventional reservoirs and non-reservoir rock is that ranges of Q values in sediment without methane hydrate are reported as well. Wood et al. (2000) report Q between 90 and 600 for wet shale and shale with small quantities of methane hydrate at the Blake Ridge in the Atlantic. All values of Q less than 90 were associated with gassy sediments where, at some locations, the quality factor was registered as low as 6. Pratt et al. (2003) use cross-well tomography data at the Mallik site to estimate Q as high as 50 in wet shale and sand that do not contain methane hydrate. These estimates agree with those of Guerin and Goldberg (2002), who use sonic waveforms collected at the same site and report Q of about 50 in the wet sediment (sand/shale) without methane hydrate.

In both of the above investigations at the Mallik methane hydrate site, Q could be as low as 5 in sand where methane hydrate (but no free gas) is present. The velocity in the sediment with methane hydrate is much larger than in wet sediment without the hydrate. This effect is somewhat unexpected, because one intuitively assumes that the stiffer the sediment the smaller the attenuation. Dvorkin and Uden (2004) apply the above-described theory of attenuation in wet rock. They explain this effect quantitatively as a result of elastic heterogeneity in the sediment, due to its preferential stiffening by methane hydrate present in the pore space.

A study by Klimentos (1995) is perhaps one of the most relevant to applying attenuation to

hydrocarbon exploration. It reports, based on sonic waveform analysis, that Q falls between 5 and 10 in gas sandstone of about 12% porosity (Q^{-1} between 0.1 and 0.2) and may easily exceed 100 (Q^{-1} equals 0.01) in oil- and water-saturated intervals. These estimates match our theoretically calculated attenuation values for the wells in the examples presented above.

Laboratory Data

Most laboratory attenuation measurements have been conducted on one-inch-size samples in the ultrasonic frequency range between 10^5 and 10^6 Hz. As such, these results may not necessarily be relevant to the field-scale phenomena that occur at 10 to 100 ft scale and in the frequency range between 10^1 and 10^4 Hz.

As an example of ultrasonic laboratory attenuation data in wet rock, consider measurements of Klimentos and McCann (1990) conducted on a large number of sandstone samples in the 0% to 40% porosity range and 0% to 30% clay content at 40 MPa differential pressure (Figure 1.15).

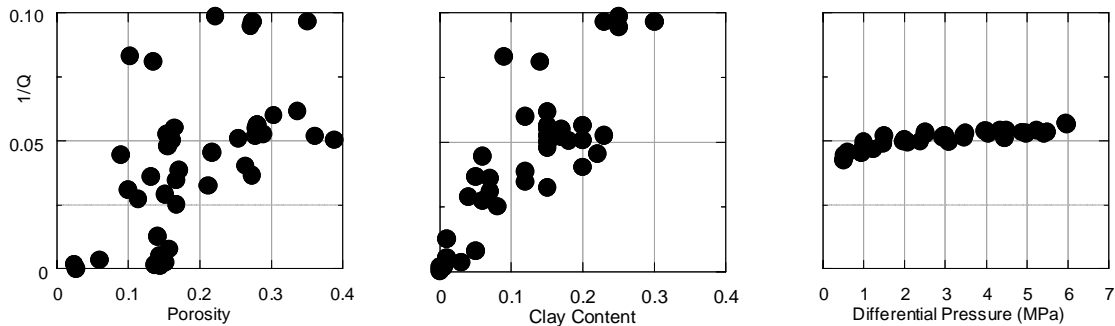


Figure 1.15. Ultrasonic laboratory data for wet sandstone. Left – The inverse quality factor from Klimentos and McCann (1990) plotted versus porosity. Middle – The same data plotted versus clay content. Right – The inverse quality factor in unconsolidated sand data from Prasad (2002) plotted versus differential pressure (the difference between the hydrostatic confining and pore pressure). The vertical scale is the same in all frames.

The quality factor in this dataset appears to exceed 100. Another example is by Prasad (2002), where Q , in unconsolidated high-porosity sand at very low differential pressure, is about 20 (Figure 1.15).

A number of laboratory measurements are due to the resonant bar technique, where relatively large samples are excited at a frequency of about 1 kHz, which is relevant to some field applications. A classical example of such data in partially saturated sandstone, due to Murphy (1982), is shown in Figure 1.16. Typically, two types of elastic waves are excited in resonant

bars, the shear S-waves and extensional E-waves, and corresponding quality factors (Q_S and Q_E , respectively) are obtained. Winkler and Nur (1979) show that the P-wave quality factor Q_P (or simply Q as denoted in this paper) can be expressed through Q_S and Q_E as

$$\frac{(1-\nu)(1-2\nu)}{Q_P} = \frac{1+\nu}{Q_E} - \frac{2\nu(2-\nu)}{Q_S}, \quad (1.47)$$

where ν is Poisson's ratio. For $\nu = 0.25$ we have, from Equation (1.47),

$$3Q_P^{-1} = 10Q_E^{-1} - 7Q_S^{-1}. \quad (1.48)$$

Q_P^{-1} , calculated from Q_E^{-1} and Q_S^{-1} under the assumption that $\nu = 0.25$, is also plotted versus water saturation in Figure 1.16. The resulting Q is about 13 in the zero to 0.7 water saturation range, and becomes as low as 7 at very high water saturation. At full water saturation, Q is large—about 40.

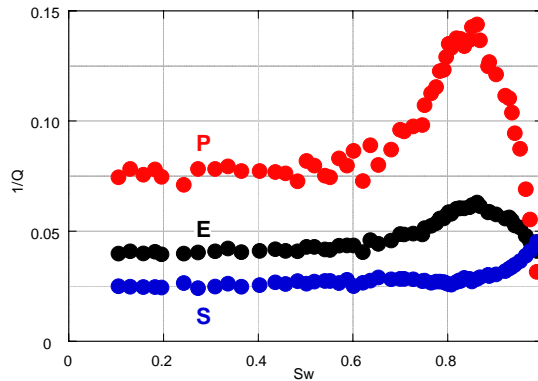


Figure 1.16. Resonance bar attenuation data in Massillon sandstone of 23% porosity (Murphy, 1982). The inverse quality factor is plotted versus water saturation. Frequency is between 300 and 600 Hz. The E- and S-wave data (black and blue, respectively) are measured, while P-wave data (red) are calculated according to Equation (1.49).

An important result is derived from Koesoemadinata and McMechan (2001), who statistically summarize many laboratory attenuation data, and provide an algorithm for calculating Q as a function of porosity, clay content, water saturation, differential pressure, permeability, and frequency. The main problem is that most of the data used are from the ultrasonic frequency range, and extension of statistical correlations into the field frequency and scale range may not be valid. Nevertheless, we use this algorithm and calculate Q for the above-examined well data. The resulting inverse quality factor is plotted together with that calculated according to our theory in Figures 1.8 to 1.14.

Two important observations result from these calculations: (1) the inverse quality factor due

to Koesoemadinata and McMechan (2001) is consistently unrealistically small in gas reservoirs, and (2) the inverse quality factor in the non-reservoir rock is fairly large and often exceeds 0.05, which means that Q is smaller than 20.

Attenuation in the Reservoir

The theoretical model for attenuation in reservoir and non-reservoir rock put forth in this paper predicts a quality factor as small as 5 or 10 in gas-saturated sandstone.

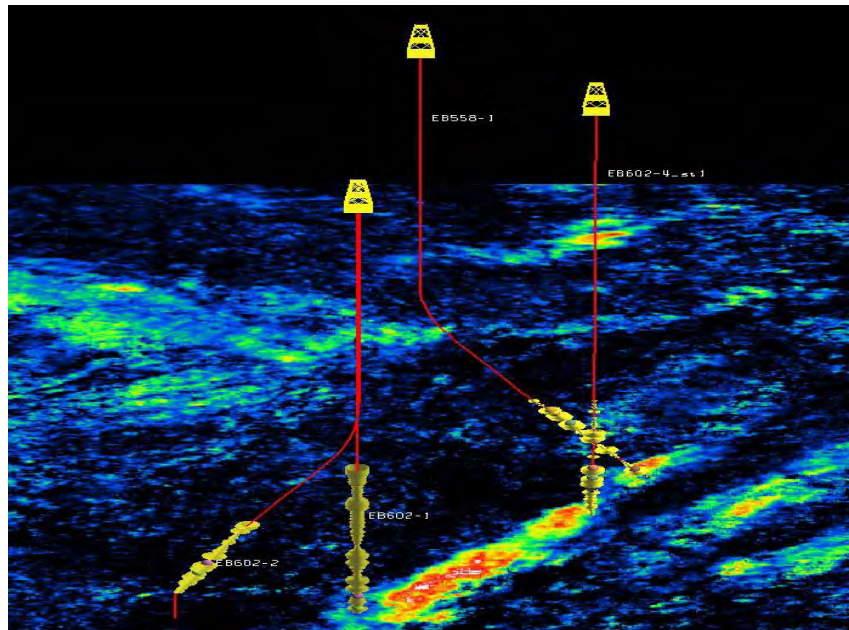


Figure 1.17. Attenuation calculated from seismic in a gas field. Red color indicates high attenuation.

This high attenuation stands out of the background attenuation in non-reservoir rock as it is supposed to do according to several field analyses of seismic data (Taner, 2002, Figure 1.17; Burnett et al., 2003; Castagna et al., 2003; Ebrum, 2004). Conversely, the Koesoemadinata and McMechan (2001) relations do not forecast the anticipated large attenuation contrast between reservoir and non-reservoir rock. (The latter offer, in fact, the only alternative way of calculating attenuation from measurable rock properties, barring several mathematical theories that require highly arbitrary input.)

As a result, we suggest that the theory of attenuation in hydrocarbon reservoirs offered here be used for realistic estimates of Q from rock properties and conditions routinely measured in the well bore.

Background Attenuation

In all the above examples, the background attenuation in the shale and wet sand, according to our theory, is practically nonexistent, with Q as high as 100 except where discernable elastic heterogeneity is present. The Koesoemadinata and McMechan (2001) relations predict much larger background attenuation with, in most cases, amounts for Q as low as 20 and even as low as 10 in especially soft rock (Figure 1.13). Is this low- Q background realistic?

Let us remind ourselves that, according to the definition of the quality factor and Equation (1.4), the amplitude of an elastic wave decreases by a factor of 10^n after the wave travels distance $0.733nQ\lambda$, where λ is the wavelength. If the P-wave velocity is 3000 m/s and frequency is 50 Hz, the wavelength is 60 m. For $Q = 20$, the amplitude will decrease by a factor of 10 after the wave travels about 900 m (or 3000 ft) and by a factor of 100 along the distance of 6000 ft. Similarly, for $Q = 30$ this distance is 12000 ft.

These estimates mean that if the background Q is as low as predicted by the Koesoemadinata and McMechan (2001) relations, seismic reflections may be impossible to record. Simply said, an elastic wave will not propagate over a realistically long distance. This also means that the background Q of 100 and larger, as predicted by our theory (except where considerable elastic heterogeneity is present), is perhaps a realistic estimate. Moreover, this large background Q is more consistent with the background values measured in the crust (see an overview of field measurements above).

A THEORETICAL ESTIMATE OF S-WAVE ATTENUATION IN SEDIMENT

Some laboratory and field data (albeit very sparse) indicate that the S-wave attenuation in a sediment sample (a) weakly depends on water saturation, and (b) approximately equals the P-wave attenuation at 100% water saturation. Our theoretical model matches these observations. In this model we assume (a) the S-wave inverse quality factor is related to the shear-modulus-versus-frequency dispersion by the same viscoelastic relation as the P-wave inverse quality factor (e.g., the standard linear solid), and (b) the shear-modulus-versus-frequency dispersion is linked to the compressional-modulus-versus-frequency dispersion. To model the latter link, we

assume that the reduction in the compressional modulus between the high-frequency and low-frequency limits is due to the introduction of a hypothetical set of aligned defects or flaws (e.g., cracks). Next we assume that the *same set of defects* is responsible for the reduction in the shear modulus between the high-frequency and low-frequency limits. Finally, by using Hudson’s theory for cracked media, we link the shear-modulus-versus-frequency dispersion to the compressional-modulus-versus-frequency dispersion and show that the proportionality coefficient between the two is a function of the P-to-S-wave velocity ratio (or Poisson’s ratio). This coefficient falls between 0.5 and 3.0 for Poisson’s ratio between 0.25 to 0.35, which are typical values for saturated earth materials.

S-WAVE ATTENUATION DATA

Laboratory Data

Laboratory measurements conducted at ultrasonic frequency on small rock plugs, as well as in a lower frequency range using the resonant-bar technique on larger samples, indicate that the S-wave inverse quality factor (Q_s^{-1}) is weakly dependent on water saturation and is approximately the same as the inverse P-wave quality factor at full saturation ($Q_s^{-1} \approx Q_p^{-1}$).

Examples include resonant-bar data from Murphy (1982) for Massillon sandstone (Figure 1.18) and ultrasonic data for Vycor glass (Figure 1.19).

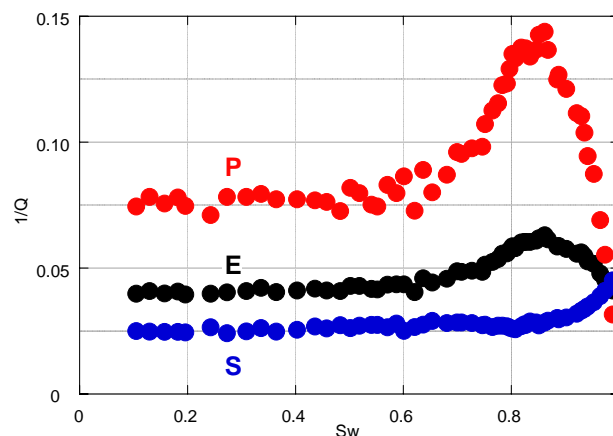


Figure 1.18. Resonance bar attenuation data in Massillon sandstone of 23% porosity (Murphy, 1982). The inverse quality factor is plotted versus water saturation. Frequency is between 300 and 600 Hz. The E- and S-

wave data (black and blue, respectively) are measured while the P-wave inverse quality factor (red) is calculated from these data according to Winkler (1980).

The Vycor glass data displayed in Figure 1.19 are very close to those presented by Winkler (1980). Prasad (2002) demonstrates the proximity of the P- to S-wave attenuation on an unconsolidated high-porosity sand sample at ultrasonic frequencies (Figure 1.20).

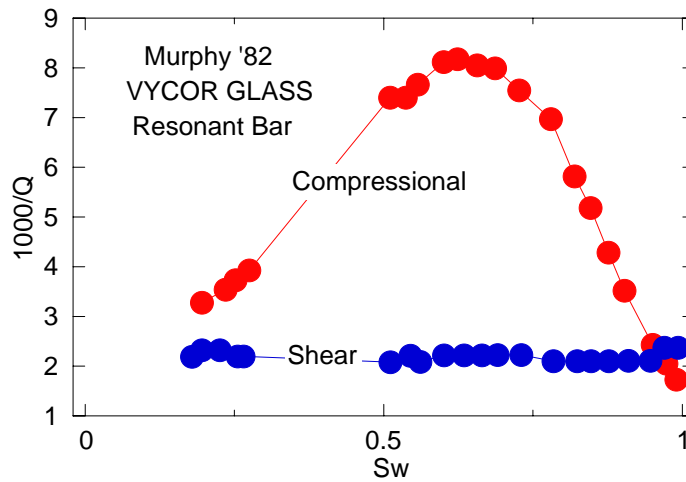


Figure 1.19. Ultrasonic attenuation data in Vycor glass (Murphy, 1982). The inverse quality factor is plotted versus water saturation.

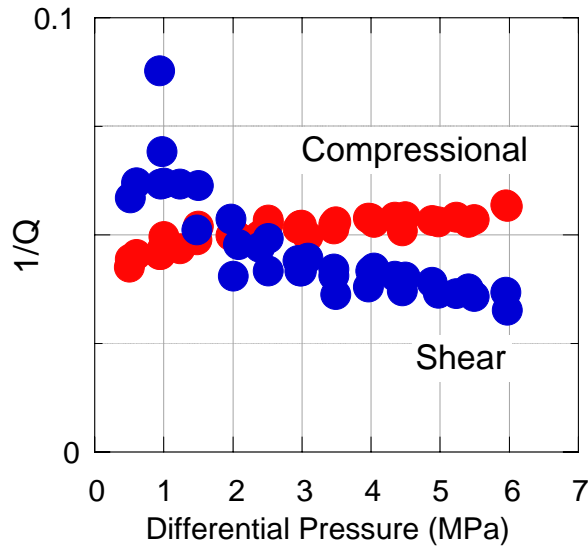


Figure 1.20. Ultrasonic attenuation data in water-saturated unconsolidated sand (Prasad, 2002). The inverse quality factor is plotted versus differential pressure.

Lucet (1989) shows that the P-wave attenuation is close to S-wave attenuation in a limestone sample at ultrasonic frequency (Figure 1.21). However, Q_p^{-1} is larger than Q_s^{-1} at low (resonant-bar) frequency.

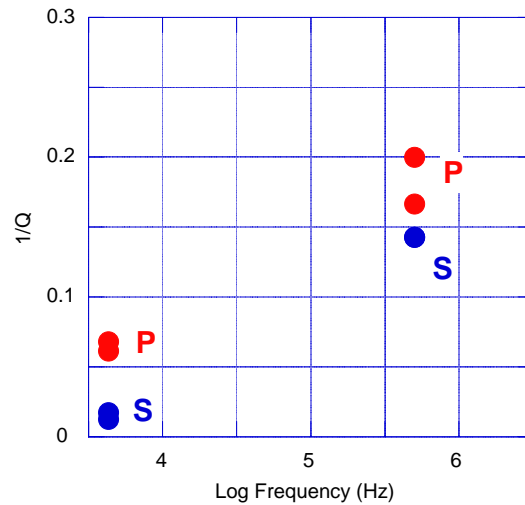


Figure 1.21. Attenuation in a water-saturated limestone sample (Lucet, 1989).

Field Data

Reliable field data for Q_p^{-1} and Q_s^{-1} is even more sparse than lab data. Useful results are due to Klimentos (1995) who shows from well log data that the S-wave attenuation is approximately the same as the P-wave attenuation in liquid-saturated sandstone while in gas-saturated intervals the P-wave attenuation is much larger than the S-wave attenuation (Figure 1.22).

Sun et al. (2000) compute the P- and S-wave attenuation from monopole sonic data. The reported Q_p^{-1} and Q_s^{-1} are essentially the same in the low-shale-content interval but may be different in the shale.

Guerin and Goldberg (2002) calculate Q_p^{-1} and Q_s^{-1} from monopole and dipole data in a methane hydrate well. They empirically relate the inverse quality factor to the methane hydrate saturation of the pore space (S_{MH}) by a linear fit as $Q_p^{-1} = 0.029 + 0.0012S_{MH}$ and $Q_s^{-1} = 0.065 + 0.0017S_{MH}$, where S_{MH} is less than 1. Generally, Q_s^{-1} exceeds Q_p^{-1} but the factor is not large and varies between 1.5 and 2.0.

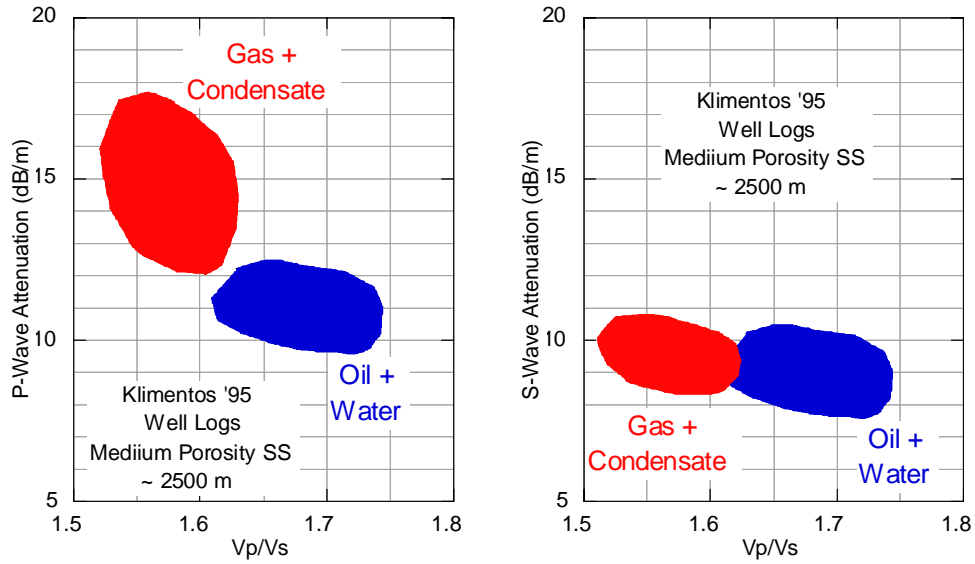


Figure 1.22. P and S-wave attenuation calculated from full-waveform sonic and dipole log data in medium-porosity sandstone with oil, water, gas, and gas condensate. After Klimentos (1995).

S-WAVE ATTENUATION THEORY

Attenuation and Modulus Dispersion

Our first assumption is that the inverse quality factor relates to the modulus-frequency dispersion by a viscoelastic causality relation, such as, e.g., for the Standard Linear Solid (Mavko et al., 1998):

$$2Q_p^{-1} = \frac{M_\infty - M_0}{\sqrt{M_0 M_\infty}}, \quad 2Q_s^{-1} = \frac{G_\infty - G_0}{\sqrt{G_0 G_\infty}}, \quad (1.49)$$

where M and G are the compressional and shear moduli, respectively, and the subscripts “ ∞ ” and “0” refer to the high- and low-frequency limits, respectively.

We will also assume that the S-wave attenuation is pore-fluid-independent and proceed with our analysis for fully-water-saturated porous sediment.

Compressional Modulus Dispersion

We will use the Dvorkin and Mavko compressional modulus dispersion theory for wet sediment (Dvorkin and Mavko, 2005; Dvorkin and Uden, 2004). This theory states that the necessary condition for attenuation is elastic heterogeneity in rock. The low-frequency compressional modulus is calculated by theoretically substituting the pore fluid into the spatially averaged rock’s dry-frame modulus, while the high-frequency modulus is the spatial average of the heterogeneous saturated-rock modulus. The difference between these two estimates may give rise to noticeable P-wave attenuation if elastic heterogeneity in rock is substantial.

Link between Compressional and Shear Modulus Dispersion

The physical basis for linking the compressional to shear modulus dispersion is the fact that there is a compressional element in shear deformation (pure shear, Figure 1.23). Therefore, if a material includes viscoelastic elements that are responsible for the frequency stiffening in the deformation-deformation mode, they will contribute to the stiffening in the pure-shear-deformation mode. Mavko and Jizba (1991) use this principle to estimate the contribution of soft crack-like pores containing liquid to the shear-modulus dispersion at ultrasonic frequency at

the pore-scale (the microscopic squirt-flow). They show that the dispersion of the inverse shear modulus is about 4/15 of that in the inverse bulk modulus.

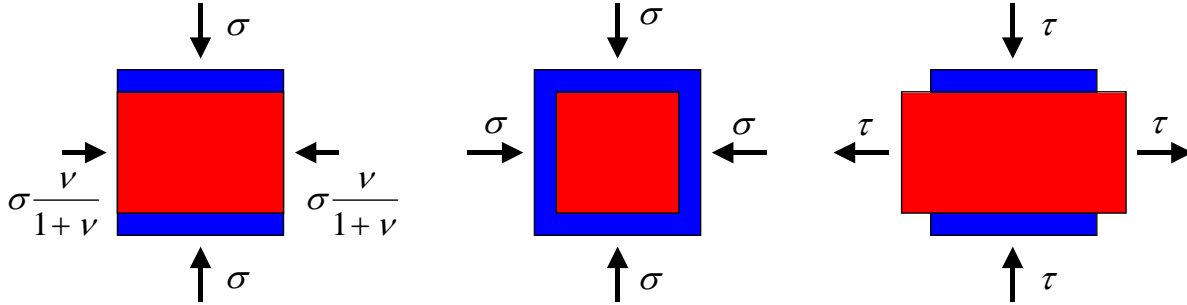


Figure 1.23. From left to right – compressional, bulk, and pure shear deformation. Blue is the undeformed body, while red is the deformed body. The arrows indicate the tractions acting on the body.

We will use the same principle. Specifically, we will assume that the reduction in the compressional modulus of *wet* rock between the high-frequency limit and low-frequency limit is due to the introduction of a hypothetical system of aligned defects (cracks) into the material. Next, we will adopt Hudson's theory for cracked media (e.g., Mavko et al., 1998) to quantify these defects. Specifically, the reduction in the compressional modulus in the direction of normal to the set of cracks is

$$M_{\infty} - M_0 = \Delta c_{11}^{\text{Hudson}} \approx \varepsilon \frac{\lambda^2}{\mu} \frac{4(\lambda + 2\mu)}{3(\lambda + \mu)} \equiv \varepsilon \frac{4}{3} \frac{(M - 2G)^2}{G} \frac{M}{M - G}, \quad (1.50)$$

where $\Delta c_{11}^{\text{Hudson}}$ is the change in the anisotropic stiffness component; λ and μ are Lamé's constants of the background medium ($\mu \equiv G$); and ε is the crack density -- $\varepsilon = 3\phi/(4\pi\alpha)$ -- where ϕ is the porosity and α the aspect ratio. Assuming that $M = \sqrt{M_0 M_{\infty}}$ we find from Equations (1.49) and (1.50) that

$$2Q_p^{-1} = \frac{M_{\infty} - M_0}{\sqrt{M_0 M_{\infty}}} = \varepsilon \frac{4}{3} \frac{(M - 2G)^2}{G(M - G)} = \varepsilon \frac{4}{3} \frac{(M/G - 2)^2}{(M/G - 1)}. \quad (1.51)$$

The corresponding change in the shear modulus for the same set of aligned defects is given by the stiffness component c_{44} . The change in this component ($\Delta c_{44}^{\text{Hudson}}$) due to the presence of

cracks is

$$G_{\infty} - G_0 = \Delta c_{44}^{\text{Hudson}} \approx \varepsilon \mu \frac{16(\lambda + 2\mu)}{3(3\lambda + 4\mu)} \equiv \varepsilon G \frac{16}{3} \frac{M}{3M - 2G}. \quad (1.52)$$

Assume next that $G = \sqrt{G_0 G_{\infty}}$. Then Equations (1.50) and (1.53) yield

$$2Q_s^{-1} = \frac{G_{\infty} - G_0}{\sqrt{G_0 G_{\infty}}} = \varepsilon \frac{16}{3} \frac{M}{3M - 2G} = \varepsilon \frac{16}{3} \frac{M/G}{3M/G - 2}. \quad (1.53)$$

By combining Equations (1.51) and (1.53), we find

$$\frac{Q_p^{-1}}{Q_s^{-1}} = \frac{1}{4} \frac{(M/G - 2)^2 (3M/G - 2)}{(M/G - 1)(M/G)}, \quad (1.54)$$

where

$$\frac{M}{G} = \frac{2 - 2\nu}{1 - 2\nu} = \frac{V_p^2}{V_s^2}, \quad (1.55)$$

and ν is Poisson's ratio.

In another variant of the same approach, we may assume that the same set of defects is now randomly oriented in the material and thus does not introduce anisotropy. In this case the reduction in the isotropic shear modulus $\Delta\mu^{\text{Hudson}}$ is

$$G_{\infty} - G_0 = \Delta\mu^{\text{Hudson}} \approx \varepsilon \frac{2}{15} \mu \left[\frac{16(\lambda + 2\mu)}{3(3\lambda + 4\mu)} + \frac{8(\lambda + 2\mu)}{3(\lambda + \mu)} \right]. \quad (1.56)$$

In this case we find

$$2Q_s^{-1} = \frac{G_{\infty} - G_0}{\sqrt{G_0 G_{\infty}}} = \varepsilon \frac{16}{15} \left[\frac{2M/G}{3M/G - 2} + \frac{M/G}{3(M/G - 1)} \right] \quad (1.57)$$

and, as a result,

$$\frac{Q_p^{-1}}{Q_s^{-1}} = \frac{5}{4} \frac{(M/G - 2)^2}{(M/G - 1)} \left/ \left[\frac{2M/G}{3M/G - 2} + \frac{M/G}{3(M/G - 1)} \right] \right. \quad (1.58)$$

Equations (1.54) and (1.58) present two versions for calculating Q_s^{-1} from Q_p^{-1} . It is important to remember that *in these calculations the wet-rock Q_p^{-1} has to be used*, i.e., in a hydrocarbon-saturated interval the original fluid has to be substituted for water and Q_p^{-1} calculated afterwards.

Finally, in the third variant of this approach, we assume that the reduction in the compressional modulus is due to a set of randomly oriented isotropic defects, and the same set of

defects is responsible for the reduction in the shear modulus.

$$\begin{aligned} \frac{Q_p^{-1}}{Q_s^{-1}} &= \frac{4}{3} \frac{1}{\lambda/\mu+2} + \frac{5}{12} \frac{(3\lambda/\mu+4)(3\lambda/\mu+2)^2}{(\lambda/\mu+2)(9\lambda/\mu+10)} \\ &= \frac{1}{M/G} \left[\frac{4}{3} + \frac{5}{4} \frac{(M/G-2/3)(M/G-4/3)^2}{M/G-8/9} \right]. \end{aligned} \quad (1.59)$$

The Q_p^{-1}/Q_s^{-1} as given by Equations (1.54), (1.58), and (1.59) is plotted versus ν in Figure 1.24. The three curves, due to the three equations used, differ from each other. However, most importantly, they all predict Q_p^{-1}/Q_s^{-1} between 1 and 3 in the Poisson's ratio range between 0.30 and 0.35, which is typical for wet sediment. This predicted range of Q_p^{-1}/Q_s^{-1} matches the experimental observations.

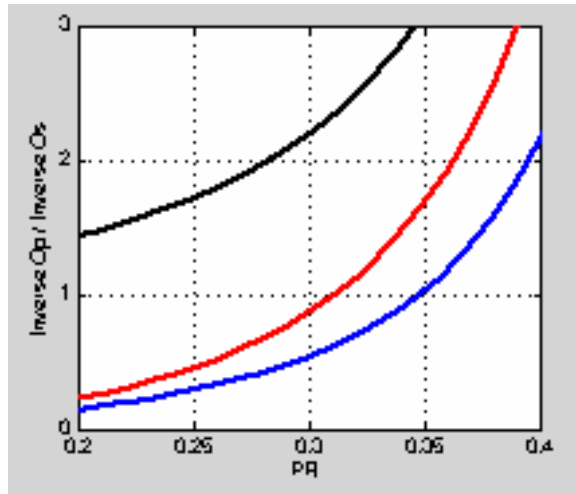


Figure 1.24. P-to-S inverse quality factor ratio versus Poisson's ratio. Blue curve (bottom) is from Equation (1.55), red curve (middle) is from Equation (1.59), and black curve (top) is from Equation (1.60).

Caveats

The theory essentially assumes that the waves propagate normal to the bedding or, more precisely, normal to the hypothetical defects responsible for the modulus dispersion. In more rigorous treatment of the problem, the direction of wave propagation needs to be taken into account, or at least its effects on the errors evaluated.

COMPARING Q_p/Q_s WITH Q_p/Q_{ps}

We have developed algorithms to estimate attenuation from seismic. Most efforts have focused on estimating P-wave attenuation (Q_p) from P-wave stacks. In this project, the same algorithms have been applied to P-to-S-wave converted mode stacks, yielding an *apparent* attenuation, which we shall label Q_{ps} . Physically, the observed attenuation Q_{ps} incorporates the combined effects of losses during P-wave downward propagation and S-wave upward propagation.

The vast majority of laboratory and theoretical rock physics work has focused on attenuation of the pure modes, Q_p and Q_s . An exception is the work with resonant bars, such as that of Cadoret (1993) and Lucet (1989), in which they more naturally measure Q_s and Q_E —the latter being the attenuation associated with an extensional wave in an unconfined bar. From measurements of Q_s and Q_E one can solve for Q_p using the following relation (Mavko, et al., 1998):

$$\frac{(1-\nu)(1-2\nu)}{Q_p} = \frac{(1+\nu)}{Q_E} - \frac{2\nu(2-\nu)}{Q_s}, \quad (1.60)$$

where ν is the Poisson's ratio. However, Lucet has pointed out that attempting to extract Q_p from Equation (1.60) is very sensitive to measurements errors in Q_s and Q_E , leading to unreliable results for Q_p . She found, instead, that when comparing resonant bar results with theory or other direct measurements of Q_p , such as from ultrasonics, it is better to convert those Q_p values to Q_E .

In this section, we will consider a similar question: Is it better to convert our field estimates of (Q_p, Q_{ps}) to (Q_p, Q_s) , or to convert rock physics data and theories from (Q_p, Q_s) to (Q_p, Q_{ps}) ?

Earlier in this chapter, we developed models for Q_p and Q_s that incorporate three important observations:

- Q_p is very sensitive to partial saturation, especially partial saturation with gas
- Q_s is generally independent of saturation
- Q_p is approximately equal to Q_s at full water saturation

As a result, we can infer general rules of thumb:

- $Q_p/Q_s \sim 1$ for wet sand or shale
- $Q_p/Q_s \ll 1$ for gas sand

In this section, we develop the connections between Q_p/Q_s ratio, which has been extensively studied, and the ratio Q_p/Q_{PS} , which may be more directly observable in the field. We find similar rules of thumb:

- $Q_p/Q_{PS} \sim 1$ for wet sand or shale
- $Q_p/Q_{PS} \ll 1$ for gas sand

A SIMPLE DERIVATION

Consider a homogenous attenuation layer of thickness z , as shown in Figure 1.25. The attenuation for two-way propagation of P-waves scales as the quantity

$$\frac{T_p}{Q_p} \tag{1.61}$$

where T_p is the two-way vertical P-wave travel time through the layer. Similarly, the attenuation for downward P plus converted upward S scales as

$$\frac{T_p}{Q_p} + \frac{T_s}{Q_s} \equiv \frac{2T_{PS}}{Q_{PS}} \tag{1.62}$$

where T_s is the two-way vertical S-wave travel time, and T_{PS} is the mode-converted two-way travel time of P-down and S-up.

It is important to point out that, strictly speaking, there is no mode conversion from P to S for normal incidence waves. However, the converted wave stack has an effective NMO applied, which registers events to the time axis as though both the downward vertical P-wave and upward vertical S-wave exist. In fact, a more advanced analysis would involve reformulating the scaling in Equations (1.61) and (1.62) to reflect all pre-stack rays and then estimating the combined apparent Q as seen on the stacks. This pre-stack analysis would be appropriate for both P-wave and mode-converted stacks.

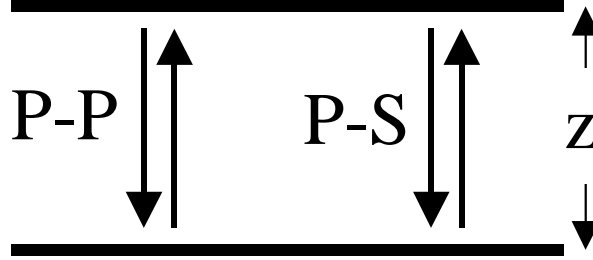


Figure 1.25. Diagram of PP and PS propagation.

A second set of equations involves travel times.

$$T_P = \frac{2z}{V_P}; \quad T_S = \frac{2z}{V_S}; \quad T_{PS} = \frac{z}{V_P} + \frac{z}{V_S}. \quad (1.63)$$

These combine to yield the relation

$$T_{PS} = T_P \left(1 + \frac{V_P}{V_S} \right) / 2. \quad (1.64)$$

If we divide Equation (1.63) by expression (1.62) we get

$$1 + \frac{T_S}{T_P} \frac{Q_P}{Q_S} = \frac{2T_{PS}}{T_P} \frac{Q_P}{Q_{PS}}. \quad (1.65)$$

Now, inserting Equation (1.64) into Equation (1.65) yields

$$\frac{Q_P}{Q_S} = \left(1 + \frac{V_P}{V_S} \right) \frac{Q_P}{Q_{PS}} - \frac{V_P}{V_S} \quad (1.66)$$

or

$$\frac{Q_P}{Q_{PS}} = \frac{\left(\frac{Q_P}{Q_S} + \frac{V_S}{V_P} \right)}{\left(1 + \frac{V_S}{V_P} \right)}. \quad (1.67)$$

Figure 1.26 plots Equation (1.67), showing the relationship between Q_P/Q_{PS} and Q_P/Q_S .

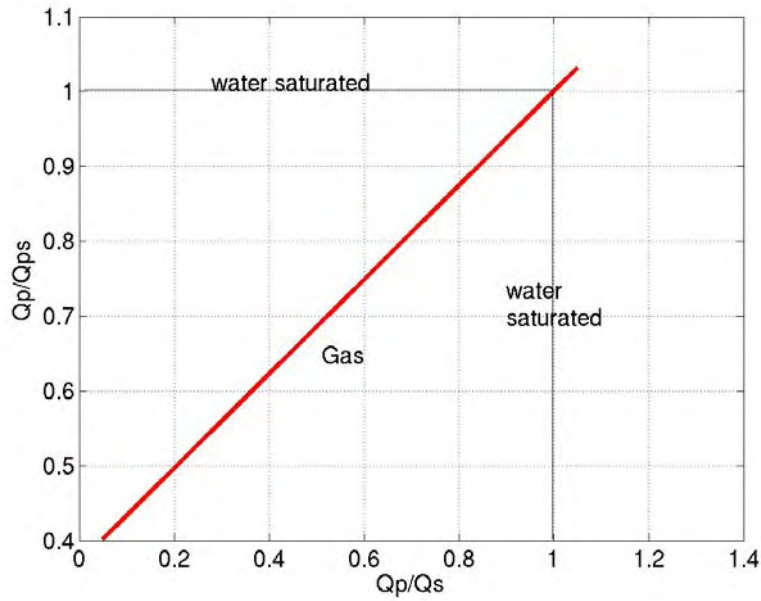


Figure 1.26. Plot of Q_p/Q_{PS} and Q_p/Q_S .

In Figure 1.26, we label the "water-saturated" lines, which laboratory work generally suggests should be $Q_p \approx Q_S$. From Equation (1.68), we see that when $Q_p \approx Q_S$, then also $Q_p \approx Q_{PS}$. For gas, we expect that $Q_p < Q_S$, which also implies that $Q_p < Q_{PS}$. Figure 1.26 shows that Q_p/Q_{PS} and Q_p/Q_S vary linearly. The slope is such that a small change in Q_p/Q_{PS} relates to a much larger change in Q_p/Q_S . This might suggest that we should convert our field measurements of (Q_p, Q_S) to expand the sensitivity, but of course there is little advantage in doing this, since expanding the range of the signal also expands the range of the noise. In fact, it appears that we are better off converting theories to the (Q_p, Q_{PS}) than vice versa.

To estimate Q_p and Q_S separately (rather than their ratio), we go back to Equation (1.66):

$$\frac{Q_p}{Q_S} = \left(1 + \frac{V_P}{V_S}\right) \frac{Q_p}{Q_{PS}} - \frac{V_P}{V_S}. \quad (1.68)$$

Dividing through by Q_p yields

$$\frac{1}{Q_S} = \left(1 + \frac{V_P}{V_S}\right) \frac{1}{Q_{PS}} - \frac{V_P}{V_S} \frac{1}{Q_p}, \quad (1.69)$$

which allows us to estimate Q_S by subtracting (with weights) Q_p from Q_{PS} . The inverse of Equation (1.69) is

$$Q_{PS} = Q_P \frac{\left(1 + \frac{V_S}{V_P}\right)}{\left(\frac{Q_P}{Q_S} + \frac{V_S}{V_P}\right)}. \quad (1.70)$$

LABORATORY EXAMPLE

Figure 1.27, below, shows these concepts applied to a laboratory example. Cadoret (1993) measured Q_E and Q_S vs. water saturation using a resonant bar technique. His curves are shown in red and blue. For comparison, we show the Q_P curve (green), computed using Equation (1.61). A curve of Q_{PS} , computed using Equation (1.69), is shown in magenta. We see the often-observed result that Q_S is independent of saturation, while all P-dependent quantities, Q_E , Q_P , and Q_{PS} , show the dependence on saturation.

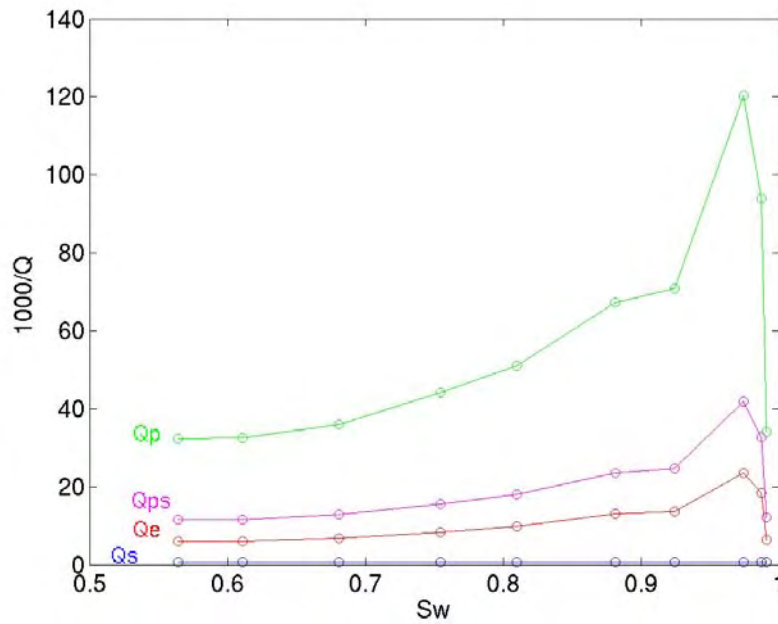


Figure 1.27. Attenuation vs. saturation. Cadoret measured the curves for Q_e and Q_s .

PART 1 SUMMARY

P-Wave Attenuation Theory: The P-wave attenuation theory offered here involves a number of assumptions, the strongest of which is perhaps the supposition that a wave-induced oscillatory cross-flow of the pore fluid can develop between earth layers that may have very low permeability, such as in shale. Another limitation of this theory is that it does not allow for predicting attenuation as a function of frequency. Instead, it calculates the maximum possible inverse quality factor.

The strong points of this theory are (1) it is based on first principles; (2) it allows for calculating Q from basic inputs that are readily available from borehole measurements; and (3) it produces Q values that are consistent with field measurements.

An alternative to this simple approach is to use mathematically involved theories such as by Dvorkin and Nur (1993), Dvorkin et al. (1995), or, most recently, Pride et al. (2003). The problem of practical implementation of these theories is, of course, not the complexity of mathematical expressions involved, but rather the fact that they require inputs that are not readily available (such as permeability) or, most importantly, are arbitrary (such as the squirt-flow length and the spatial scales of porosity type).

Therefore, we feel that the theory of P-wave attenuation put forth in this project is theoretically and practically viable, and can and should be used for realistic attenuation calculations in reservoir and non-reservoir rock.

S-Wave Attenuation Theory: A simple theoretical model offered here relates the P-to-S inverse quality factor ratio to the Poisson's ratio of the background sediment. It relies on a large number of assumptions that are not necessarily honored in real rock. Yet, the attenuation ratio provided by the model is realistic and matches experimental observations. The main result is that in wet rock the P- and S-wave quality factors are approximately the same.

Q_p/Q_{ps} Relationships: In this project we developed the connections between the Q_p/Q_s ratio, which has been extensively studied with laboratory and theoretical work, and the ratio

Q_p/Q_{pS} , which may be more directly observable in the field using converted mode data. We find the attenuation-related rules of thumb for saturation:

- $Q_p/Q_{pS} \sim 1$ for wet sand or shale
- $Q_p/Q_{pS} \ll 1$ for gas sand

The theoretical formulation suggests that it is probably advantageous to interpret attenuation data in the (Q_p, Q_{pS}) instead of converting field data to the (Q_p, Q_s) domain. Application of the theory indicates that classical laboratory data showing Q_p/Q_s can be an indicator of gas should also apply to observed Q_p/Q_{pS}

PART 2: SYNTHETIC SEISMOGRAM MODELING WITH Q

MODELING ATTENUATION EFFECTS IN A GAS RESERVOIR

In this report we compute and compare synthetic traces in an earth model containing a gas reservoir. We specifically search for the impact of including realistic attenuation versus ignoring it with a perfectly elastic model. The traces are computed using a ray-tracing algorithm, which was previously reported. In all cases, our simulations assume a Ricker wavelet, though we explore the effects of different center frequencies.

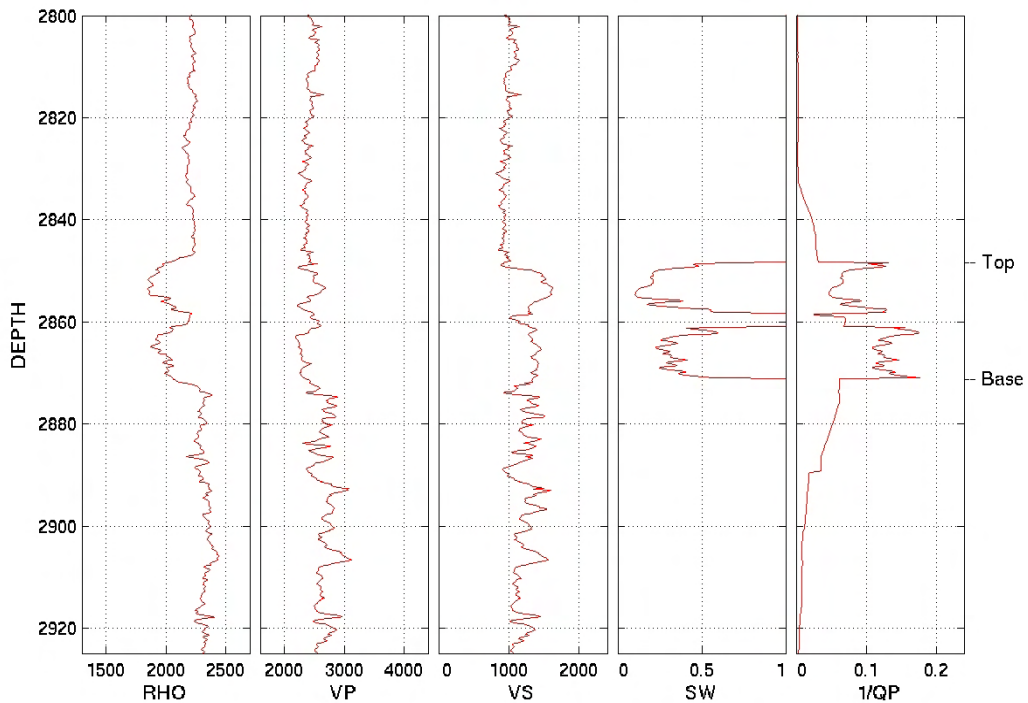


Figure 2.1. Well logs used as inputs to the modeling. The gas-sand interval, between “top” and “base” has noticeable attenuation, with the inverse quality factor reaching 0.15 in the lower portion of the reservoir.

The well shown here in Figure 2.1 is located in the Gulf Coast. It contains an over-pressured shale sequence and a gas reservoir underneath.

The reservoir is comprised of two parts, separated by a shale break. The inverse quality factor shown in Figure 2.1 is computed from measured well log data, using the attenuation model

for reservoir and non-reservoir rock reported earlier. Attenuation appears to be essentially nonexistent in the shale and noticeable in the gas sand.

SYNTHETIC SEISMIC TRACES AT NORMAL INCIDENCE

Figures 2.2 and 2.3, below, compare various normal incidence traces. On the left side of Figure 2.2, we display 50-Hz traces in elastic versus attenuating earth models. Overall, as expected from the attenuation model used in the synthetic seismic algorithm, certain velocity dispersion is evident, with the finite-attenuation trace (red) slightly delayed relative to the purely elastic earth trace (blue). The reflection from the top of the gas reservoir is slightly smaller in the attenuating model than in the elastic model, due to the small losses in the overburden.

The base-gas reflection shows much larger differences, resulting from the low inverse quality factor in the gas zone (between “top” and “base”). Note that the low inverse quality factor in the gas reservoir causes larger velocity dispersion, so that the top-to-base thickness in the attenuating model is about 4 ms larger than in the elastic model. The base-gas reflector and all subsequent reflections are much smaller in the attenuating model than in the elastic model.

On the right side of Figure 2.2, we display 30-Hz traces in elastic versus attenuating earth models. Again, some overall velocity dispersion is evident, small in the overburden and larger in the reservoir, with the finite-attenuation trace slightly delayed relative to the elastic trace. In both traces, the top of the gas reservoir corresponds to an inflection in the seismic trace, rather than the trace being trough-center, due mostly to the lack of resolution at the lower frequency.

The trace from the attenuating model shows decreasing amplitude below the top of the gas reservoir, compared to the elastic trace. The apparent reservoir thickness is also about 5 ms larger in the attenuating model than in the elastic model.

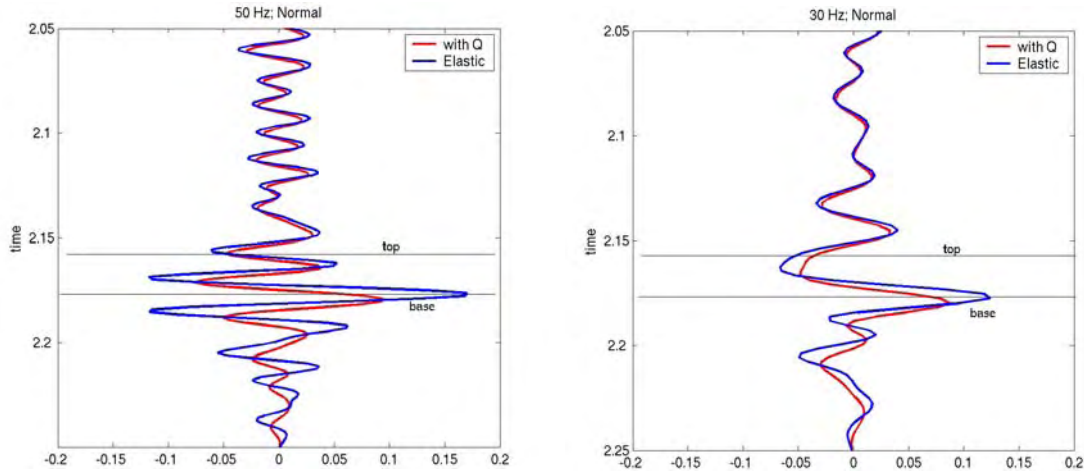


Figure 2.2. Comparison of normal incidence traces with finite attenuation (red) and purely elastic earth (blue) for a 50 Hz Ricker wavelet (left panel) and a 30 Hz Ricker wavelet (right panel).

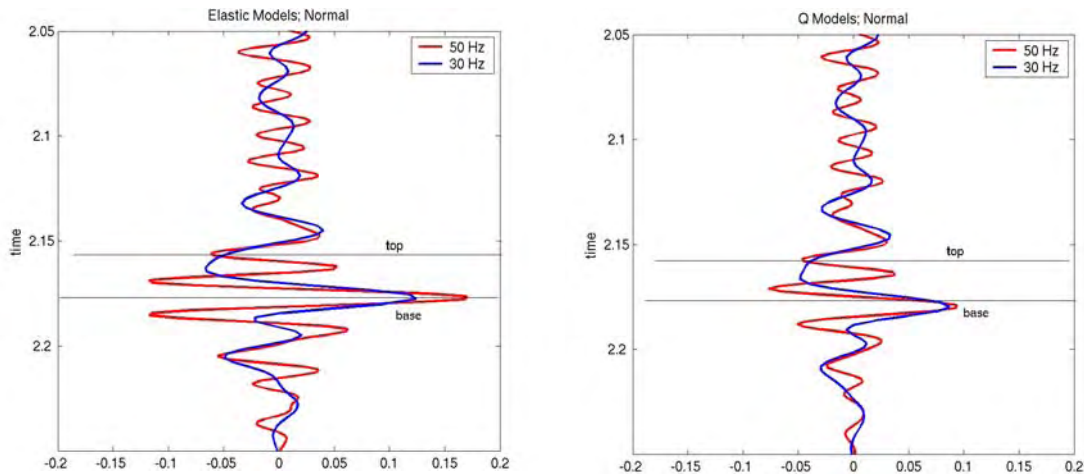


Figure 2.3. Comparison of normal incidence traces with a 30 Hz (blue) and a 50 Hz (red) Ricker wavelet for the purely elastic earth model (left panel) and the attenuating earth model (right panel).

On the left side of Figure 2.3, we compare 50-Hz versus 30-Hz simulations in the elastic earth model. At 30 Hz, the location of the top of the gas reservoir becomes ambiguous, and the amplitude of the reflection at the base of the gas reservoir differs from that at 50 Hz. Since there is no attenuation used in generating either of the two traces, these differences in the amplitude are entirely due to the decrease in resolution at the lower frequency.

On the right side of Figure 2.3, we compare the 50-Hz versus 30-Hz simulations in the attenuating earth model. In this case, the top and base amplitudes are similar, although their locations differ.

Also, the resolvability of features within the reservoir is quite different between the 50 Hz trace and 30 Hz trace. The velocity dispersion is essentially the same for both traces, since they are generated for the earth models with the same attenuation assigned to the layers.

SYNTHETIC SEISMIC GATHERS

Figures 2.4 and 2.5 show ray-tracer-generated CMP gathers for the earth model with finite attenuation, using Ricker wavelets of 50 Hz, 40 Hz, 30 Hz, and 20 Hz, respectively. The near-offset traces for 50 Hz and 30 Hz correspond to those shown in Figure 2.2.

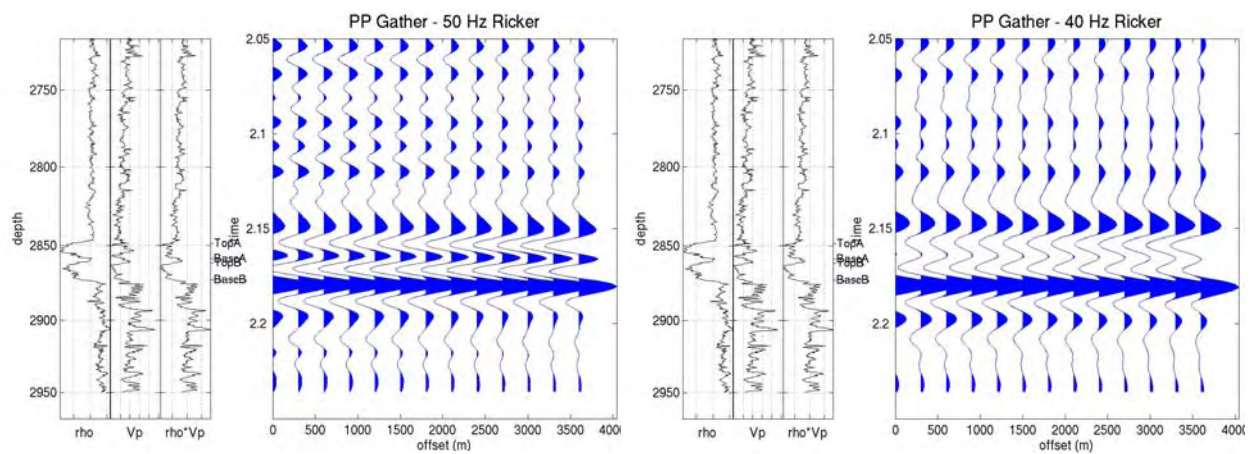


Figure 2.4. AVO gather for the attenuating earth model with a 50 Hz Ricker wavelet (left panel) and a 30 Hz Ricker wavelet (right panel).

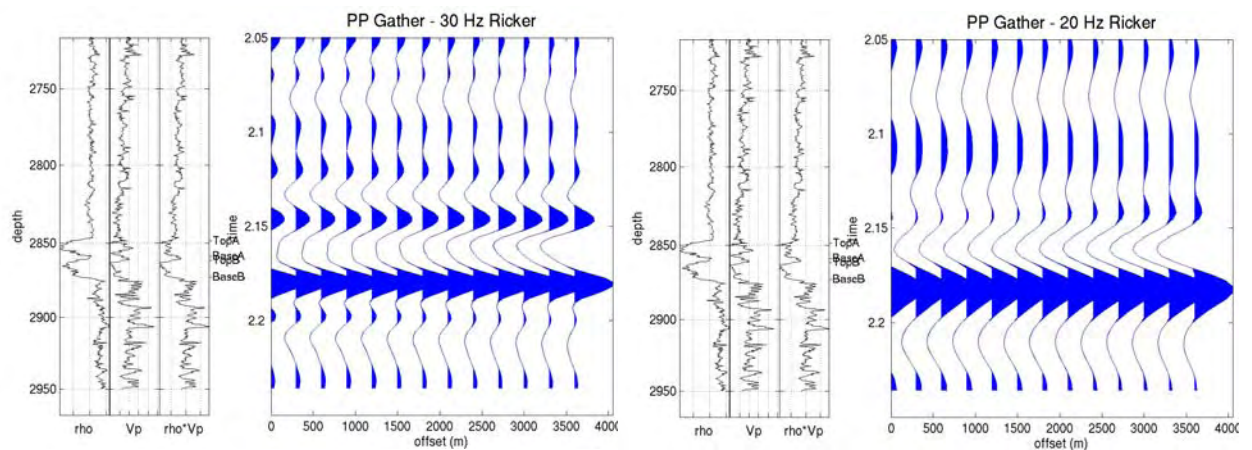


Figure 2.5. AVO gather for the attenuating earth model with a 30 Hz Ricker wavelet (left panel) and a 20 Hz Ricker wavelet (right panel).

For frequencies of 40 Hz and 50 Hz, we can resolve the top of the gas reservoir as a negative reflection (trough) and the base gas as a positive reflection (peak). Furthermore, the shaley interval separating the upper gassy layer from the lower gassy layer correlates with a peak on the seismic. Between 40 Hz and 30 Hz, the resolution drastically changes. The top of the gas reservoir falls within a very broad trough, and, as a result, it is hardly possible to distinguish the location of the top gas. Furthermore, the two separate layers within the gas reservoir are no longer evident on the seismic, though the base-associated positive reflector is still evident.

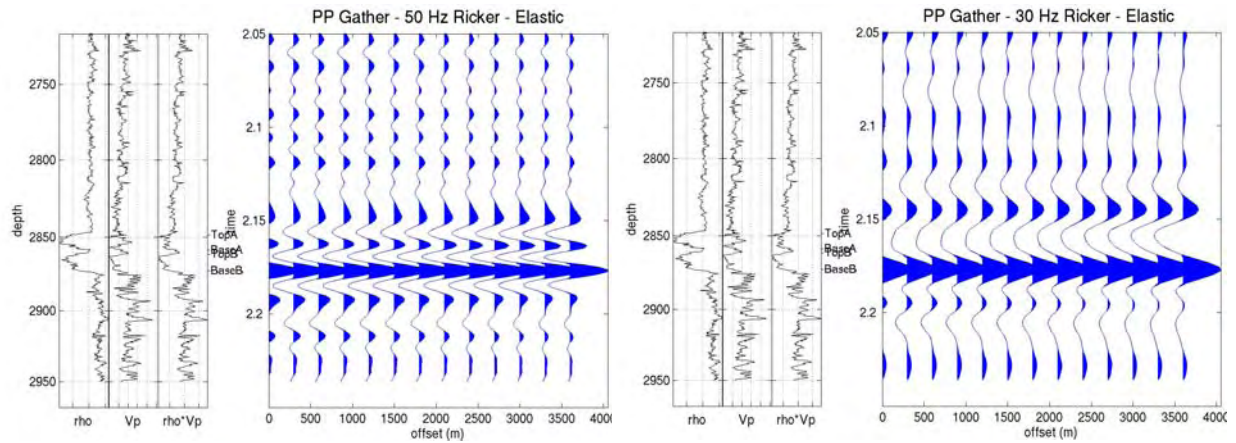


Figure 2.6. AVO gather for the purely elastic earth model with a 50 Hz Ricker wavelet (left panel), and with a 30 Hz Ricker wavelet (right panel).

Figure 2.6 compares the pure elastic earth calculations at 50 Hz and 30 Hz, respectively. These are the elastic equivalents of the left sides of Figures 2.4 and 2.5. The use of the elastic models results in the same qualitative change versus frequency as the finite-attenuation models. At the higher frequency, the top, base, and middle of the reservoir are resolvable. At lower frequency, the top of the reservoir falls somewhere within the broad trough.

AVO CURVES FROM GATHERS

Figure 2.7 shows AVO picked along the top gas and base gas for the attenuating model at 50 Hz (the gather is shown in Figure 2.4, left side) and for the purely elastic model at 50 Hz (the gather is shown in Figure 2.6, left side). Specifically, for the AVO curve at the top, we picked the trough located near the top of the gas reservoir, and for the base we picked the peak located at the base of the reservoir.

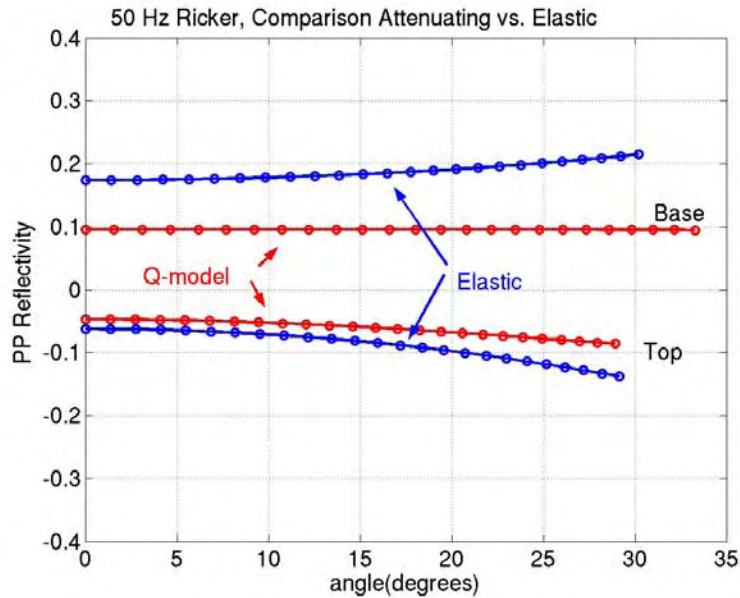


Figure 2.7. AVO curves picked at the top and bottom of the gas reservoir for the purely elastic earth model (blue) and attenuating model (red) from the gathers generated with a 50 Hz Ricker wavelet.

Because the base-gas peak and trough are slightly delayed (as compared to the purely-elastic earth) due to velocity dispersion inherent in the attenuating earth model, we, in fact, pick the events occurring at slightly different arrival times. As we saw earlier, particularly in Figure 2.2, attenuation in the reservoir has a small impact on the top-gas amplitude, although the modestly attenuating overburden does reduce the top-gas reflection. One effect that is evident from the top reflections is that the AVO gradient is reduced by the attenuating overburden. This is because the far-offset signals travel a longer path than the near-offset signals, and, therefore, suffer greater losses. The base gas reflections in the attenuating model have amplitudes only about half of what we see in the elastic model. This is partly due to the overburden, but mostly due to large attenuation occurring in the gas reservoir itself. Once again, we see that the attenuation reduces the AVO gradient. There is also the possibility that the slight stretching of the wavelet due to dispersion results in a slightly different interference of the various reflections, impacting the observed amplitudes.

TUNING AND ATTENUATION

The question “How does attenuation affect AVO?” has been asked many times and answered several times. One argument that may help answer the question is that attenuation is related mathematically to velocity-frequency dispersion, which means once we assume attenuation, reflectivity becomes frequency dependent. The problem with this argument is that it not only makes reflectivity frequency-dependent but also makes it model-dependent, where by “model” we mean the model selected to link attenuation to velocity dispersion. A choice for this model is somewhat arbitrary and even more so is the choice of parameters to be used within the model selected. Therefore, it may be difficult to predict, within the framework of pure visco-elasticity, how real seismic reflectivity is affected by attenuation.

Here we pose the question “How does attenuation affect AVO?” in a different way. We do not take into account the velocity dispersion linked to attenuation, and we essentially neglect this mathematical effect. Instead, we consider an attenuating layer placed inside a perfectly elastic medium and explore whether the reflection from the bottom of this layer, which is affected and altered by attenuation, is altered enough to change the reflection and/or waveform at the attenuating layer.

Consider a wavelet $w(t)$ descending upon a three-layer “boxcar” sequence (Figure 2.8) where a low-impedance layer (e.g., gas sand) is sandwiched between two identical higher-impedance semi-infinite layers (e.g., shale). The reflectivity series that corresponds to this impedance structure is assumed, for simplicity, to be a unit impulse of -1 and +1.

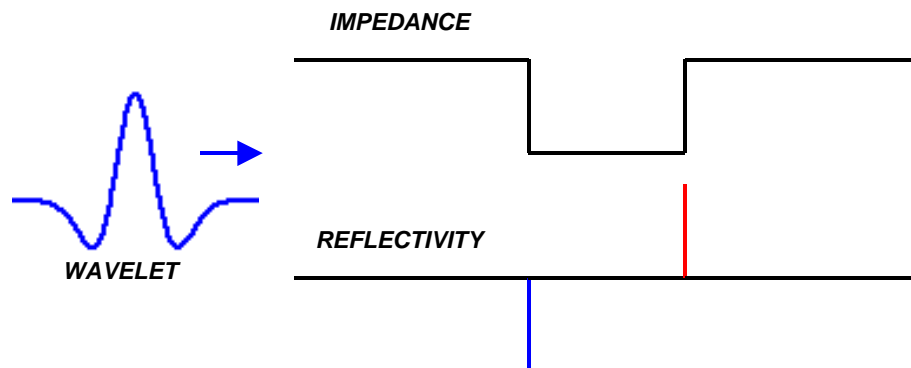


Figure 2.8. Impedance “boxcar” structure and corresponding reflectivity series.

The seismic trace $R(t)$ is the convolution of the wavelet $w(t)$ with this reflectivity series, which simply is

$$R(t) = -w(t - \tau) + w(t - \tau - \Delta t), \quad (2.1)$$

where τ is the two-way travel time to the top of the gas reservoir and Δt is the two-way travel time through the reservoir:

$$\Delta t = \frac{2h}{V}, \quad (2.2)$$

where h is the thickness of the layer and V is the speed of sound.

Let us next assume that there is no attenuation outside the low-impedance layer, while the quality factor Q inside the layer is finite. The reduction factor of the wavelet amplitude due to this attenuation is

$$\exp\left[-\frac{\pi}{Q} \frac{2h}{\lambda}\right] = \exp\left[-\frac{\pi}{Q} \frac{2h}{VT}\right] = \exp\left[-\frac{\pi}{Q} \frac{\Delta t}{T}\right] = \exp\left[-\frac{\pi}{Q} f\Delta t\right], \quad (2.3)$$

where λ is the wavelength, T is the period, and f is the frequency.

Therefore, with attenuation present inside the low-impedance layer, the trace $R(t)$ will be

$$R(t) = -w(t) + e^{-\frac{\pi}{Q} f\Delta t} w(t - \Delta t), \quad (2.4)$$

where we set $\tau = 0$.

For the Ricker wavelet,

$$w(t) = e^{-\frac{a^2 t^2}{2}} (1 - a^2 t^2), \quad (2.5)$$

where

$$a = 2\pi f \sqrt{\frac{\pi}{8}}, \quad (2.6)$$

where f is the mean frequency.

Using Equations (2.5) and (2.6) we find

$$w(t) = e^{-\frac{\pi^3 f^2}{4} t^2} \left(1 - \frac{\pi^3 f^2}{2} t^2\right). \quad (2.7)$$

Finally, by substituting Equation (2.7) into Equation (2.4) we have

$$R(t) = -e^{-\frac{\pi^3 f^2}{4} t^2} \left(1 - \frac{\pi^3 f^2}{2} t^2\right) + e^{-\frac{\pi}{Q} f \Delta t} e^{-\frac{\pi^3 f^2}{4} (t - \Delta t)^2} \left[1 - \frac{\pi^3 f^2}{2} (t - \Delta t)^2\right]. \quad (2.8)$$

Computations according to Equation (2.8) have been conducted for the inverse quality factor 0.2, frequency 25 Hz and the travel time through the attenuating layer Δt gradually increasing in geometric progression with a factor of 2, starting with 0.001 s and ending with 0.064 s. The results are shown in Figures 2.9 to 2.15.

Finally, in Figures 2.16 and 2.17 we show the tuning behavior for very (unrealistically) large attenuation with the inverse quality factor 0.5 (the quality factor 2). The results are qualitatively similar to those obtained for the inverse quality factor 0.2.

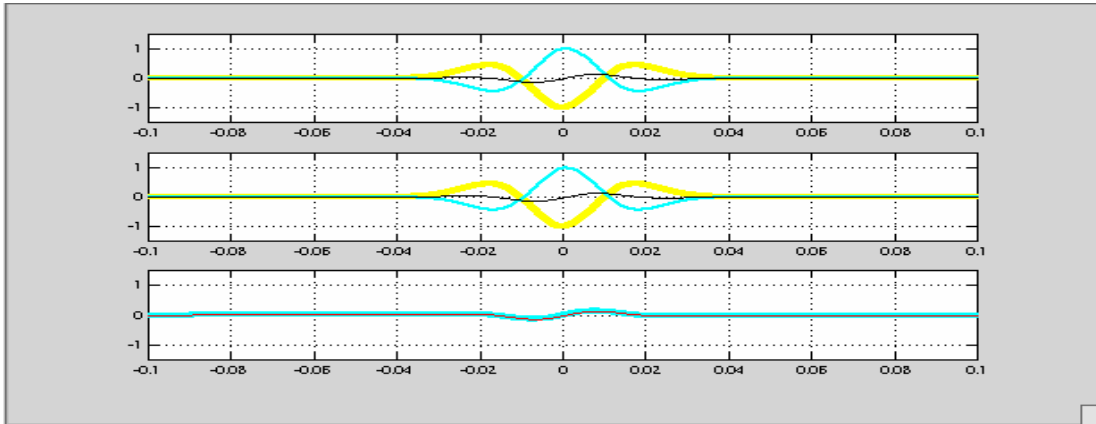


Figure 2.9. Waveform for a boxcar reservoir. Top — Perfectly elastic earth. The reflection from the top displays in yellow; the reflection from the bottom displays in cyan; and black is the superposition of the two. Middle — Same for attenuating earth. Bottom — The summary trace for purely elastic earth (cyan) and attenuating earth (red, which displays as the dark line under the cyan). The travel time in the reservoir is 0.001 s.

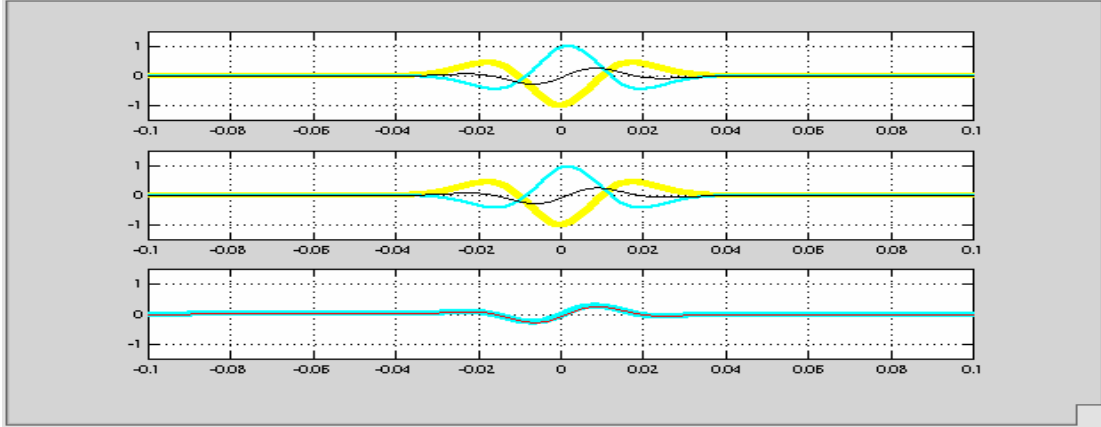


Figure 2.10. Same as Figure 2.9, but for the travel time in the reservoir 0.002 s.

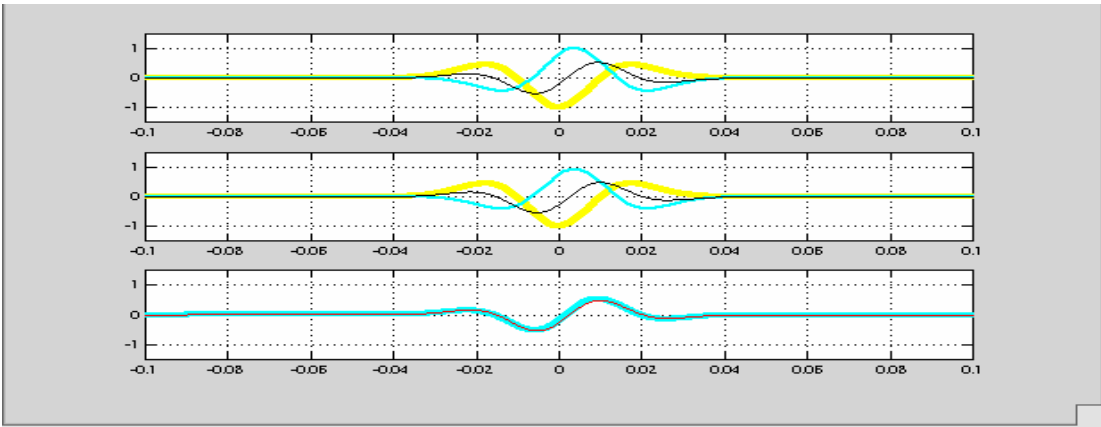


Figure 2.11. Same as Figure 2.9, but for the travel time in the reservoir 0.004 s.

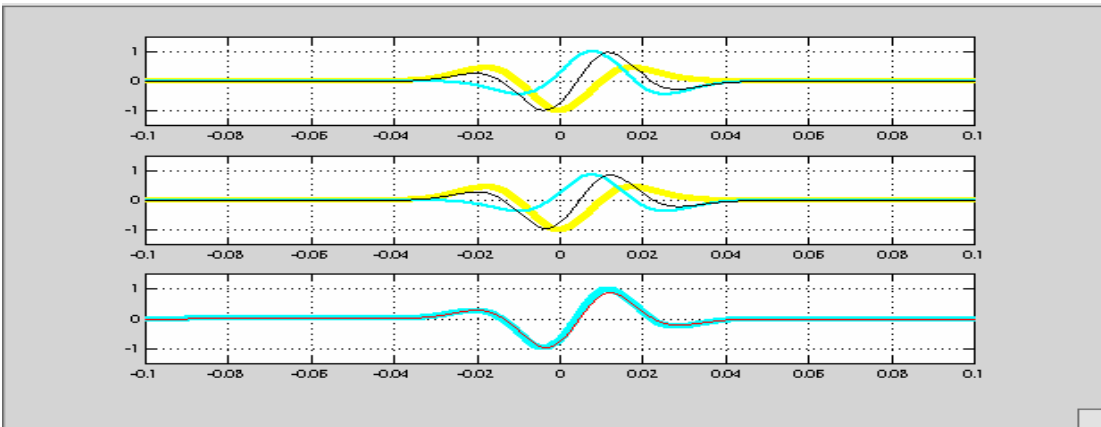


Figure 2.12. Same as Figure 2.9, but for the travel time in the reservoir 0.008 s.

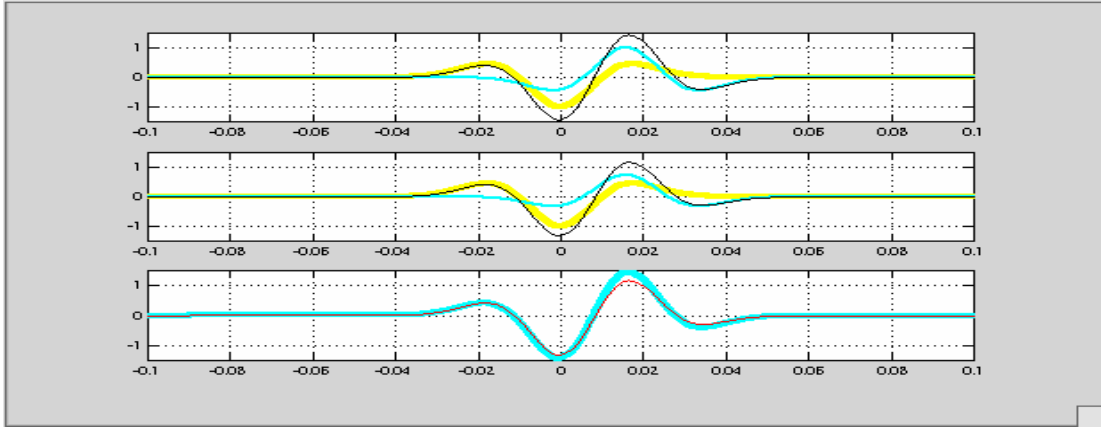


Figure 2.13. Same as Figure 2.9, but for the travel time in the reservoir 0.016 s.

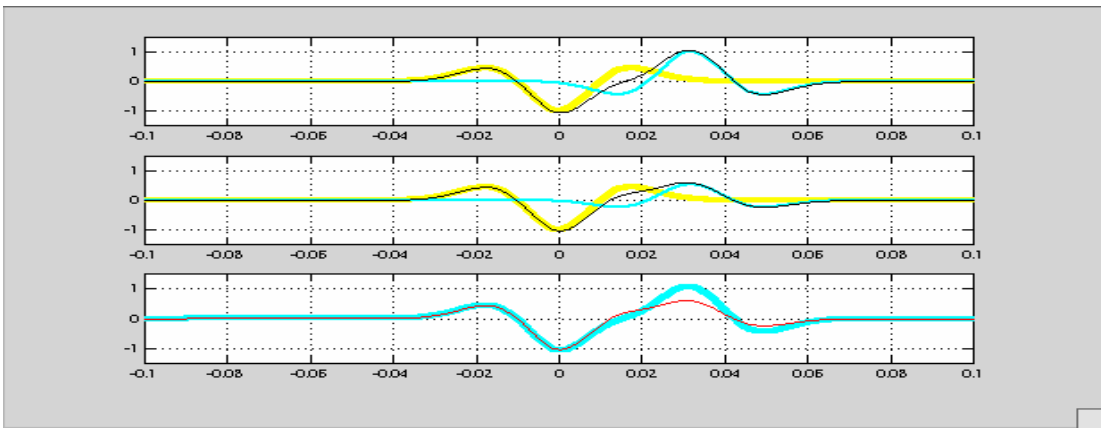


Figure 2.14. Same as Figure 2.9, but for the travel time in the reservoir 0.032 s.

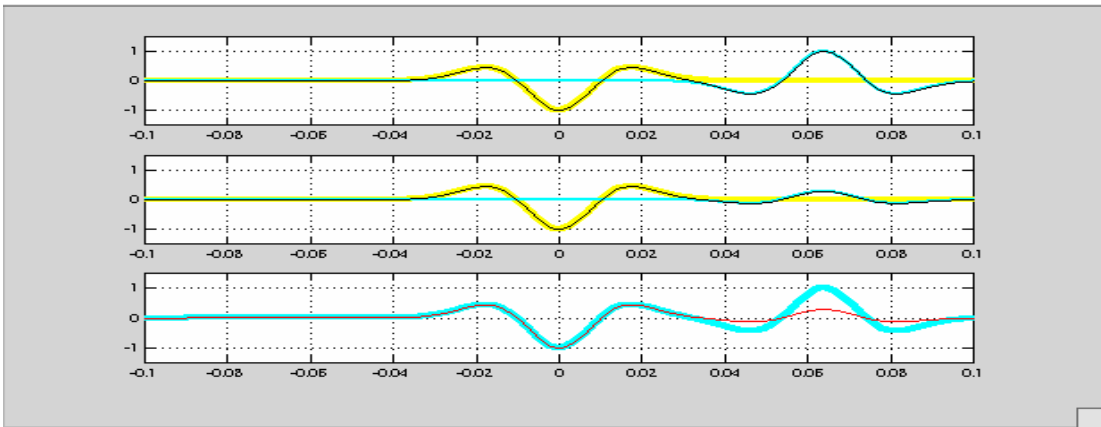


Figure 2.15. Same as Figure 2.9, but for the travel time in the reservoir 0.064 s.

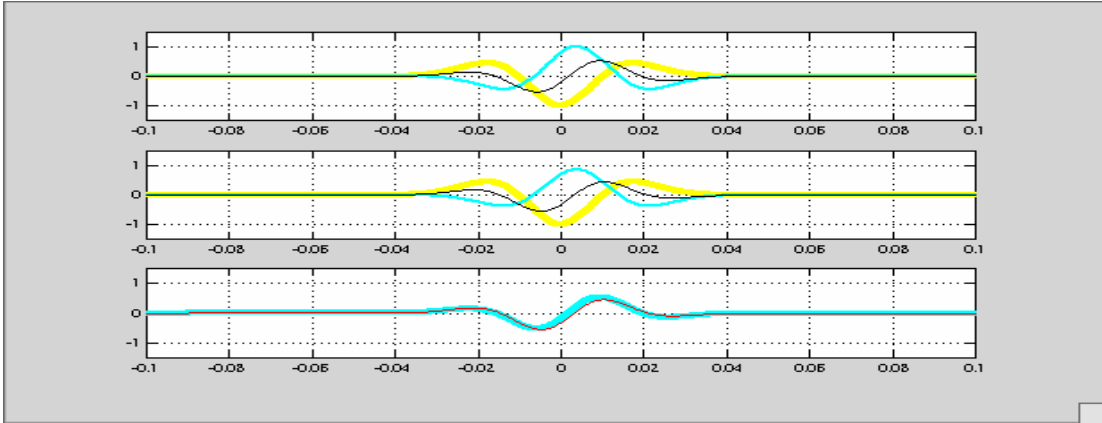


Figure 2.16. Same as Figure 2.9, but for inverse quality factor 0.5, and travel time in the reservoir 0.004 s.

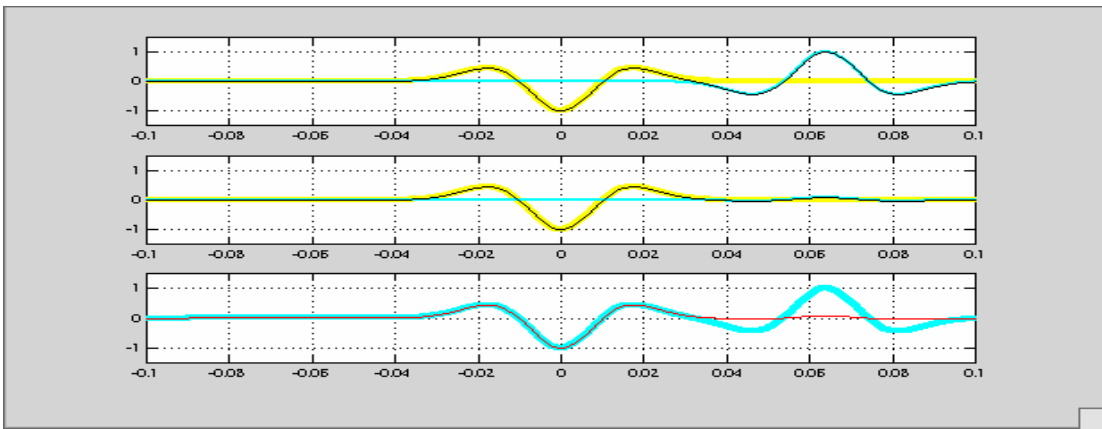


Figure 2.17. Same as Figure 2.9, but for inverse quality factor 0.5, and travel time in the reservoir 0.064 s.

HALF-SPACE MODELING OF PP REFLECTIONS WITH ATTENUATION

The following MATLAB Applet was used to model a representative shale/gas sand half-space for both the elastic and inelastic case.

THE EARTH MODEL

The earth model used in this applet is a three-layer set, with sand in the middle surrounded by two shale layers (Figure 2.18). The properties of the bottom shale layer are identical to those of the shale layer located above the sand. The upper shale layer is treated as a half-space. The reflection is modeled at the upper interface, between the upper shale layer and sand.

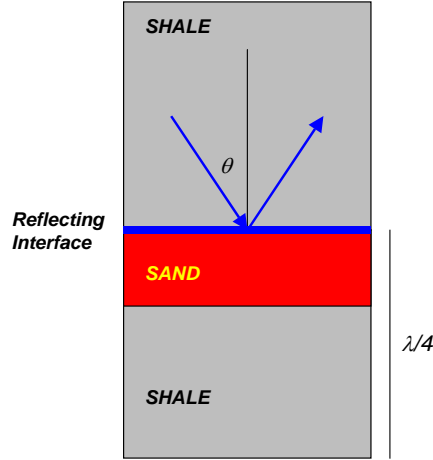


Figure 2.18. Earth model used in rock-AVO-Q.

A finite thickness is assigned to the sand layer. This thickness is measured as a fraction of the quarter-wavelength ($\lambda/4$). It is assumed that if the sand layer's thickness is a fraction s of $\lambda/4$ then the effective elastic moduli of the half-space below the reflecting interface are the Backus average of those of the sand and shale, where the fraction of the sand is s while the fraction of the shale is $1-s$. Specifically,

$$M_L = \left(\frac{s}{M_{SS}} + \frac{1-s}{M_{SH}} \right)^{-1}, \quad G_L = \left(\frac{s}{G_{SS}} + \frac{1-s}{G_{SH}} \right)^{-1}, \quad (2.9)$$

where M_L and G_L are the effective compressional and shear moduli of the half-space below the reflecting interface, respectively; M_{SS} and G_{SS} are the compressional and shear moduli of the sand layer, respectively; and M_{SH} and G_{SH} are those of the shale.

The effective bulk density of the lower half-space (ρ_L) is the arithmetic average of those of the sand (ρ_{SS}) and shale (ρ_{SH}) with volumetric proportions s and $1-s$, respectively:

$$\rho_L = s\rho_{SS} + (1-s)\rho_{SH}. \quad (2.10)$$

The effective velocity and impedance of the lower half-space are calculated from the effective elastic moduli and density via the standard theory-of-elasticity equation.

The effective quality factor of the lower half-space (Q_L^{-1}) is calculated from those of the sand (Q_{SS}^{-1}) and shale (Q_{SH}^{-1}). The attenuation coefficient averages arithmetically, which means that the ratio of the inverse quality factor and velocity averages arithmetically:

$$\frac{Q_L^{-1}}{V_L} = s \frac{Q_{SS}^{-1}}{V_{SS}} + (1-s) \frac{Q_{SH}^{-1}}{V_{SH}}, \quad (2.11)$$

where V_L is the effective velocity in the lower half-space while V_{SS} and V_{SH} are the velocities in the sand and shale, respectively. The effective P- and S-wave velocity in the lower half-space is calculated from the effective elastic moduli and density as

$$V_{LP} = \sqrt{M_L / \rho_L}, \quad V_{LS} = \sqrt{G_L / \rho_L}. \quad (2.12)$$

Therefore,

$$Q_L^{-1} = V_L \left[s \frac{Q_{SS}^{-1}}{V_{SS}} + (1-s) \frac{Q_{SH}^{-1}}{V_{SH}} \right]. \quad (2.13)$$

Equation (2.13) is applicable to both P- and S-waves.

CALCULATING THE AVO RESPONSE

The P-to-P reflectivity R_{pp} versus angle θ is calculated using the Wiggins approximation, which provides results that are very close to the exact Zoeppritz equations:

$$\begin{aligned} R_{pp}(\theta) &= R_{pp}(0) + B \sin^2 \theta, \quad B = R_{pp}(0) - 2R_{ss}(0), \\ R_{pp}(0) &= (I_{p2} - I_{p1}) / (I_{p2} + I_{p1}), \quad R_{ss}(0) = (I_{s2} - I_{s1}) / (I_{s2} + I_{s1}), \end{aligned} \quad (2.14)$$

where I_p and I_s stand for the impedance (P and S, respectively), and the subscripts “1” and “2” indicate the upper and lower half-space, respectively.

Here the lower half-space is the mix of the sand and shale with the elastic and inelastic properties calculated according to Equations (2.9), (2.10), and (2.14).

ACCOUNTING FOR ATTENUATION IN AVO

Attenuation will be accounted for merely via the corresponding velocity-frequency dispersion. In other words, the reflectivity *without* attenuation will be calculated according to Equation (2.14), with the impedances assigned to the shale and sand according to the rock physics model selected. The reflectivity *with* attenuation will be calculated according to Equation (2.14) but with the impedances *reduced* from their original values due to the velocity-frequency dispersion.

The reduction in the impedance is the maximum possible reduction occurring between the infinitely high frequency and zero frequency. The reduction in the impedance is calculated through the reduction in the corresponding elastic modulus. The latter is linked to the maximum inverse quality factor (Q_{\max}^{-1}) via the Standard Linear Solid relation

$$Q_{\max}^{-1} = \frac{M_{\infty} - M_0}{2\sqrt{M_0 M_{\infty}}}, \quad (2.15)$$

where M_{∞} is the high-frequency modulus (either compressional or shear), which is, in fact, the modulus assigned to a half-space according to the rock physics model selected, and M_0 is the modulus reduced due to attenuation. Q_{\max}^{-1} is, in fact, the inverse quality factor assigned to the earth according to our rock physics model.

We find from Equation (2.15) that if $Q_{\max}^{-1} \ll 1$

$$M_0 = M_{\infty}(1 - 2Q_{\max}^{-1}). \quad (2.16)$$

The same equation is valid for the shear modulus.

Finally, in calculating AVO, we will use Equation (2.14) with the originally assigned elastic properties for modeling reflectivity *without attenuation* and the same set of equations, but with the elastic properties corrected (reduced) according to Equation (2.16) for modeling reflectivity *with attenuation*. We will also assume that in the shale and wet sand Q is large and equals 100. In other words, no correction for Q is needed in these media.

APPROXIMATIONS

In the computer implementation of the above-described modeling, we replace the exact Backus average by an approximate impedance average. Specifically, the modulus is the ratio of the impedance squared and density: $M = I_p^2 / \rho$. By assuming that the variations of the bulk density between the sand and shale are not very large, we can replace the exact Equations (2.9) by approximate equations

$$I_{pL} = \sqrt{\left(\frac{s}{I_{pSS}^2} + \frac{1-s}{I_{pSH}^2} \right)^{-1}}, \quad I_{sL} = \sqrt{\left(\frac{s}{I_{sSS}^2} + \frac{1-s}{I_{sSH}^2} \right)^{-1}}, \quad (2.17)$$

where I_{pL} and I_{sL} are the effective P- and S-wave impedances of the lower half-space,

respectively; I_{pSS} and I_{sSS} are the P- and S-wave impedances of the sand, respectively; and I_{pSH} and I_{sSH} are those of the shale. Also, instead of exact Equation (2.14) we will use

$$Q_L^{-1} = sQ_{SS}^{-1} + (1-s)Q_{SH}^{-1}. \quad (2.18)$$

Finally, instead of Equation (2.16) we will use

$$I_{p0} = I_{p\infty} \sqrt{1 - 2Q_{\max}^{-1}} \approx I_{p\infty} (1 - Q_{\max}^{-1}). \quad (2.19)$$

We have shown (see theoretical papers attached) that the inverse S-wave quality factor is about the same as the inverse P-wave quality factor in *wet* sediment. Here we assume that Q_p in wet sediment (shale and wet sand) is very large. As a result, Q_s is large as well, and no correction for the S-wave attenuation is needed.

ATTENUATION EFFECT ON AVO – ANALYTICAL APPROXIMATION

It follows from Equations (2.14) that

$$\begin{aligned} R_{PP}(\theta) &= (1 + \sin^2 \theta)R_{PP}(0) - 2\sin^2 \theta R_{SS}(0), \\ R_{PP}^Q(\theta) &= (1 + \sin^2 \theta)R_{PP}^Q(0) - 2\sin^2 \theta R_{SS}^Q(0), \end{aligned} \quad (2.20)$$

where the superscript Q indicates that the reflectivity with attenuation is taken into account, while the reflectivity without a superscript is purely elastic reflectivity.

By subtracting the second of the above equations from the first one and taking into account that because the S-wave attenuation is small $R_{SS}(0) \approx R_{SS}^Q(0)$, we find that

$$R_{PP}(\theta) - R_{PP}^Q(\theta) \approx (1 + \sin^2 \theta) [R_{PP}(0) - R_{PP}^Q(0)] \quad (2.21)$$

The P-wave reflectivity at zero angle is, according to Equations (2.14) and (2.19),

$$\begin{aligned} R_{PP}(0) &= \frac{I_{P2} - I_{P1}}{I_{P2} + I_{P1}}, \\ R_{PP}^Q(0) &= \frac{I_{P2}^Q - I_{P1}^Q}{I_{P2}^Q + I_{P1}^Q} \approx \frac{I_{P2}(1 - Q_P^{-1}) - I_{P1}^Q}{I_{P2}^Q(1 - Q_P^{-1}) + I_{P1}^Q}. \end{aligned} \quad (2.22)$$

Therefore, by taking into account that the attenuation in the shale is small, i.e., $I_{P1}^Q \approx I_{P1}$, we find that

$$R_{PP}(\theta) - R_{PP}^Q(\theta) \approx (1 + \sin^2 \theta) \frac{I_{P2} - I_{P2}(1 - Q_P^{-1})}{I_{P2} + I_{P1}} = (1 + \sin^2 \theta) \frac{I_{P2} Q_P^{-1}}{I_{P2} + I_{P1}} \approx (1 + \sin^2 \theta) \frac{Q_P^{-1}}{2}. \tag{2.23}$$

In other words, the effect of attenuation on AVO is

$$R_{PP}(\theta) - R_{PP}^Q(\theta) = \frac{Q_P^{-1}}{2} + \sin^2 \theta \frac{Q_P^{-1}}{2} \tag{2.24}$$

which means that both the intercept and gradient are reduced due to attenuation by the same decrement $0.5Q_P^{-1}$.

IMPLEMENTATION

The applet is implemented with the standard interface and input dialogue. The latter requests various basic parameters (Figure 2.19).

The image shows a graphical user interface window titled "Specify input parameters". It contains several input fields, each with a label and a text box containing a numerical value:

- Water Salinity (ppm): 45000
- Gas Gravity (Specific): 0.65
- Oil API: 35
- GOR (1/1): 200
- Pore Pressure (psi): 5500
- Temperature (F): 200
- Gas Saturation: 0.75
- Oil Saturation: 0.65
- Irreducible Water Saturation: .05

At the bottom of the window, there are two buttons: "Cancel" on the left and "OK" on the right.

Figure 2.19. Input dialogue used rock-AVO-Q.

Once the input is specified, the main frame is displayed with the gas sand, oil sand, wet sand, and shale domains shown and color-coded by the total porosity (Figure 2.20). The modeled average Q in each lithology is printed in the frame.

The AVO curves as well as the gradient-intercept plots and synthetic gathers are calculated and displayed after two points in the lithology domains are selected, and the thickness of the sand layer is selected afterwards (three clicks per one run). The AVO curves and gradient-intercept points are accumulated in their respective frames, while the synthetic gathers are replotted each time (Figure 2.20).

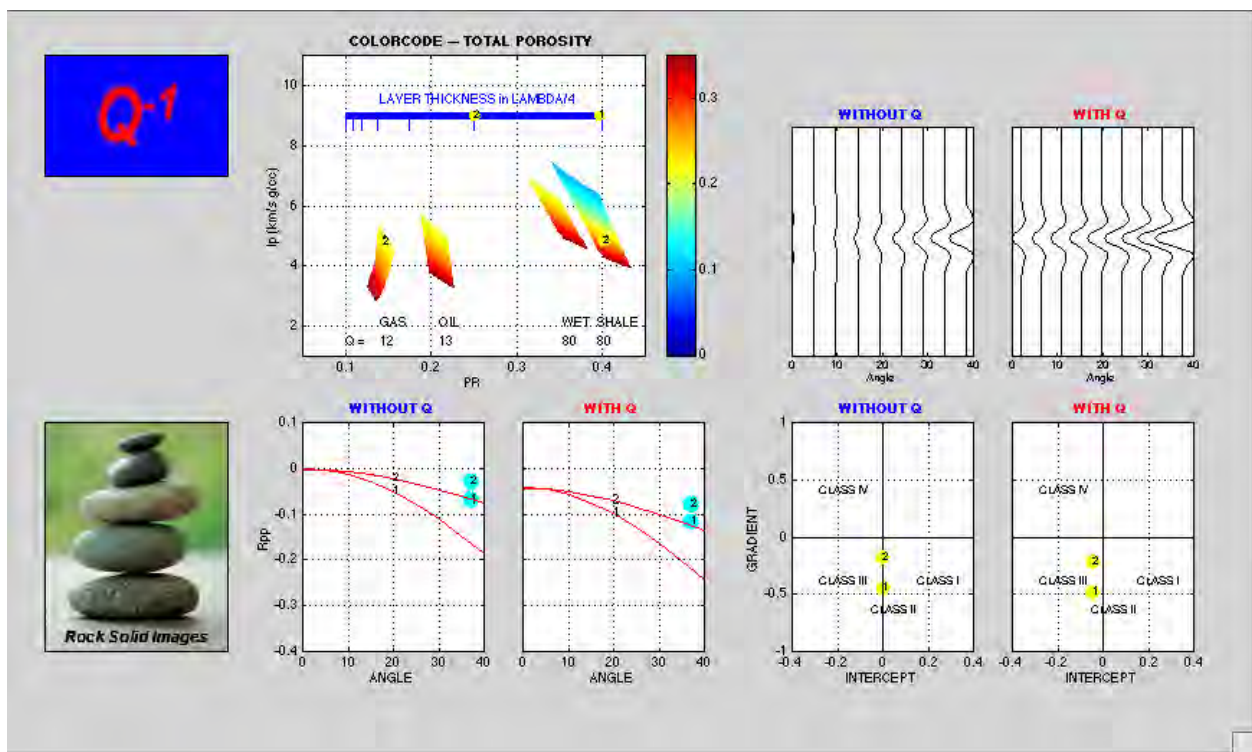


Figure 2.20. Rock-AVO-Q showing the difference attenuation may cause in low-contrast sand reflection.

TESTING

It is interesting to assess the effect of attenuation on AVO under extreme circumstances, where the attenuation in gas sand is large, e.g., due to high water saturation. To mimic these circumstances, we select the inputs as shown in Figure 2.21.

The inverse quality factor in the gas sand is calculated to be as small as 0.33 (Figure 2.22). This large attenuation strongly affects the AVO response by significantly reducing both the

intercept and gradient.

Specify input parameters

Water Salinity (ppm)

Gas Gravity (Specific)

Oil API

GOR (l/l)

Pore Pressure (psi)

Temperature (F)

Gas Saturation

Oil Saturation

Irreducible Water Saturation

Figure 2.21. Input dialogue used rock-AVO-Q.

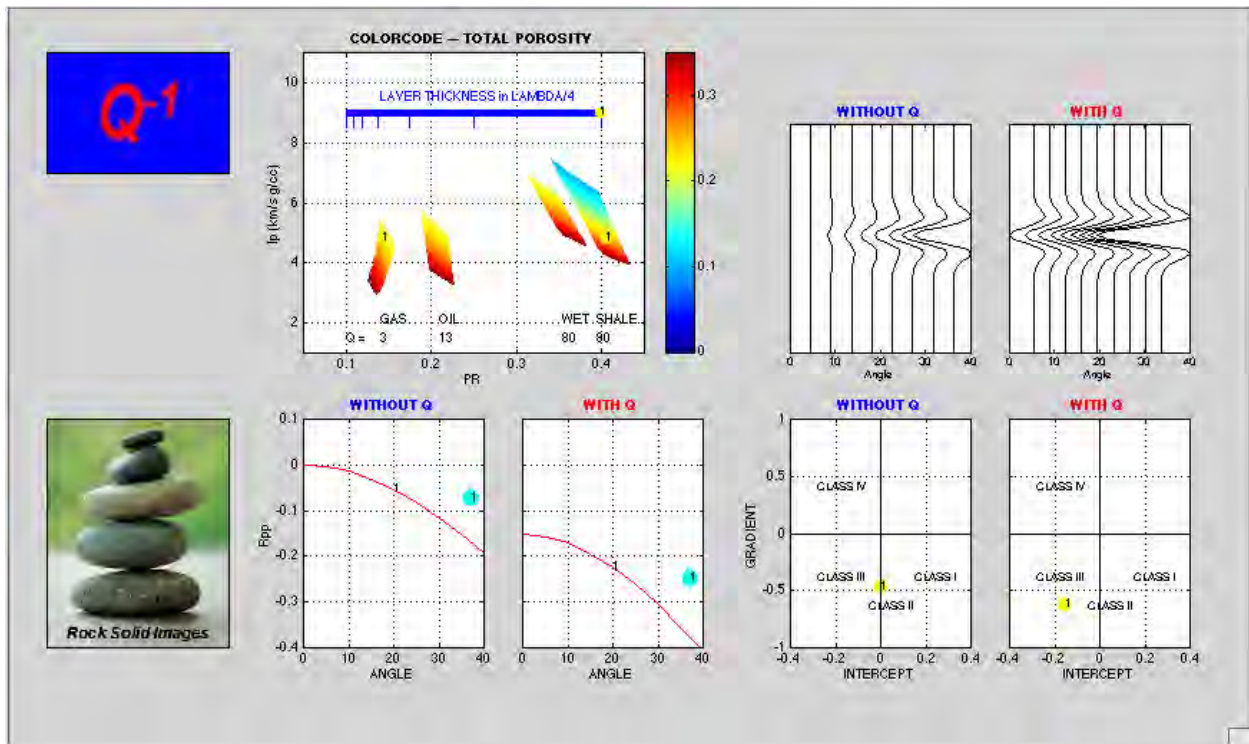


Figure 2.22. Rock-AVO-Q panel corresponding to the input shown in Figure 2.21.

HALF-SPACE MODELING OF PS REFLECTIONS WITH OFFSET

A new MATLAB Applet has been designed to forward model P-to-S reflections. This applet will help the user to assess quickly the amplitude response based on the rock properties of the reservoir and overburden.

The applet uses exact Zoeppritz equations and the constant-cement rock physics model relevant to a deep well to be used in this project. The look of this applet is different from the PP applet because we need the velocity and density for exact Zoeppritz equations. As a result, we start with porosity, clay content, and water saturation, instead of setting points in the impedance-Poisson's ratio plane as before. The shale is assumed to be always wet, while the sand may contain gas. The fluid property panel looks the same as usual.

The applet operates in the following fashion:

Step 1 – Set up the fluid properties, temperature, and pressure by overwriting the default values in the dialogue panel, as shown below. Once the parameters are entered, click OK.

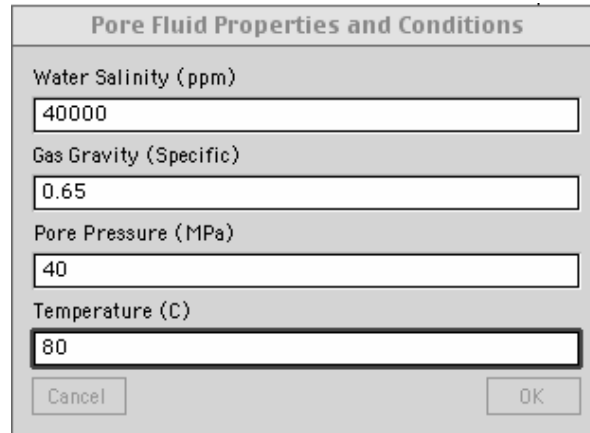
Step 2 – The main panel appears with the clay content–porosity–saturation window. By clicking once inside this window, first select the clay content and porosity for the overburden shale. The projection of the point selected by the cursor on the horizontal axis is porosity; its projection on the vertical axis is clay content. (Porosity is the horizontal axis; clay content is the vertical axis).

Step 3 – In the same way, by a single click, select the clay content and porosity in the reservoir sand.

Step 4 – Click once on the light-blue vertical bar at the right-hand margin of this window to select the water saturation in the sand. Immediately following this click, the application calculates the elastic properties of the shale and sand, and plots them in the impedance–Poisson's ratio window next to the porosity–clay–saturation setup window (yellow for the sand and black for the shale). In the two windows below, the P-to-P reflectivity and P-to-S reflectivity are plotted versus the angle of incidence, according to Zoeppritz equations.

This three-click process can be repeated several times on the same applet popup. The number of the trial is displayed in the windows and next to the calculated reflectivity curves.

See examples below in Figures 2.24 – 2.26, starting with the fluid setup window (Figure 2.23). Depending on the preference of the user, the windows may appear colored (as in most examples below) or plain (the last pane displayed).



Pore Fluid Properties and Conditions	
Water Salinity (ppm)	40000
Gas Gravity (Specific)	0.65
Pore Pressure (MPa)	40
Temperature (C)	80
Cancel	OK

Figure 2.23. Input Dialogue for PS applet

In the examples, the shale and sand values of mineralogy, porosity, and saturation shown by the numbers 1 and 2 in the top left frame compare two model scenarios. The porosity axis is horizontal, the clay axis is vertical (left-hand side), and the saturation axis is vertical (right-hand side). These volumetric fractions are then mapped through the constant-cement rock physics model to produce the elastic values of P-wave Impedance and Poisson’s Ratio shown in the top right frame.

The elastic values for the half-space are mapped through the Zoeppritz equations to produce the PP and PS reflectivity versus offset shown in the bottom left and right frames, respectively.

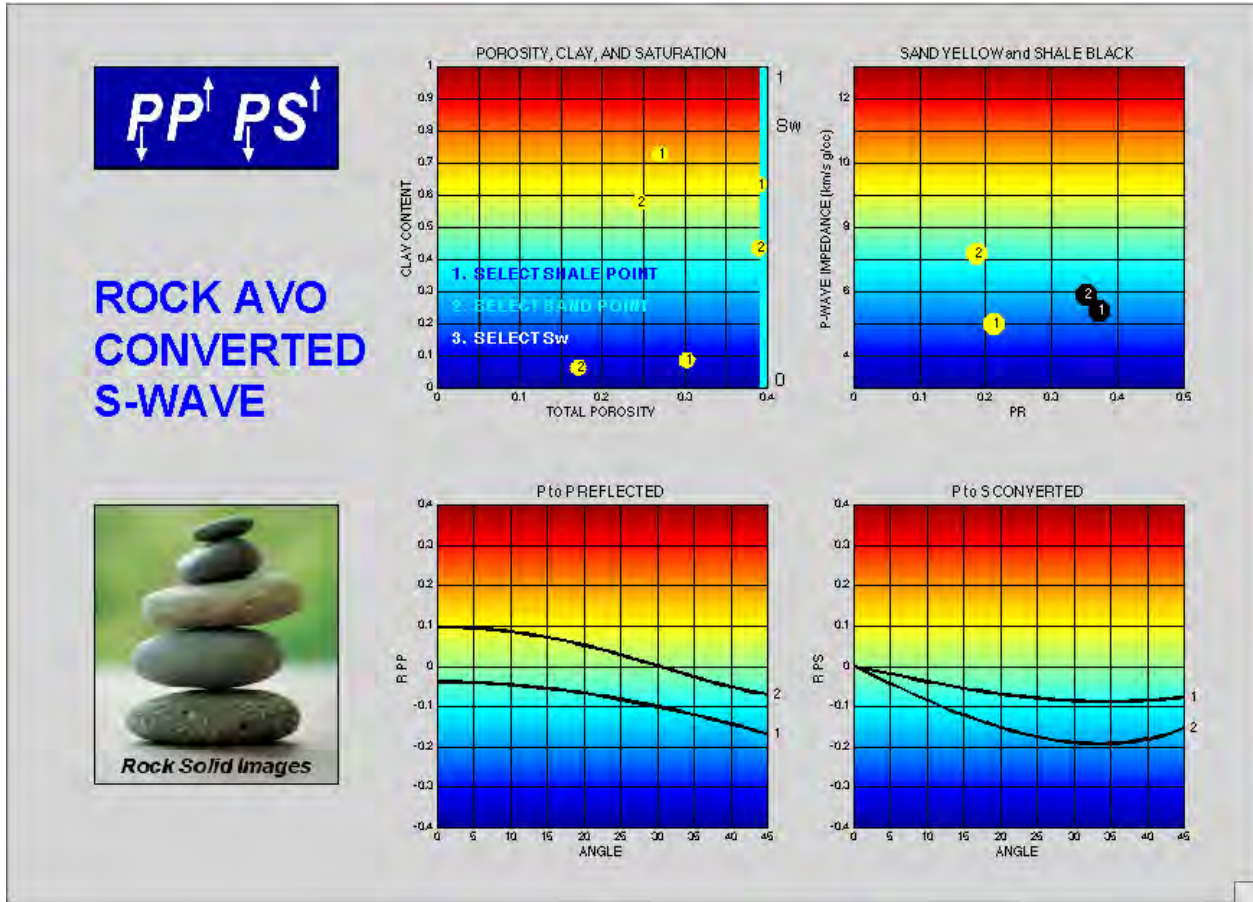


Figure 2.24. Example A for the two model scenarios shown by the numbers 1 and 2.

In example A, the shale-clay, sand-clay, porosity, and saturation values are similar between the two models, while the sand porosity for model 1 is greater than for model 2. This results in a positive PP reflectivity for the hard gas sand model (2) and a Class III AVO response for the soft gas sand model (1). The PS reflectivity is negative for both models, with model 2 exhibiting the stronger response (more porosity contrast).

This comparison illustrates the difficulty of interpreting PP and PS data amplitudes, since the PP and PS reflectivity for model 2 is likely to have opposite polarity for a tight (hard) gas sand. Conversely, PP and PS reflections for soft gas sand have the same polarity.

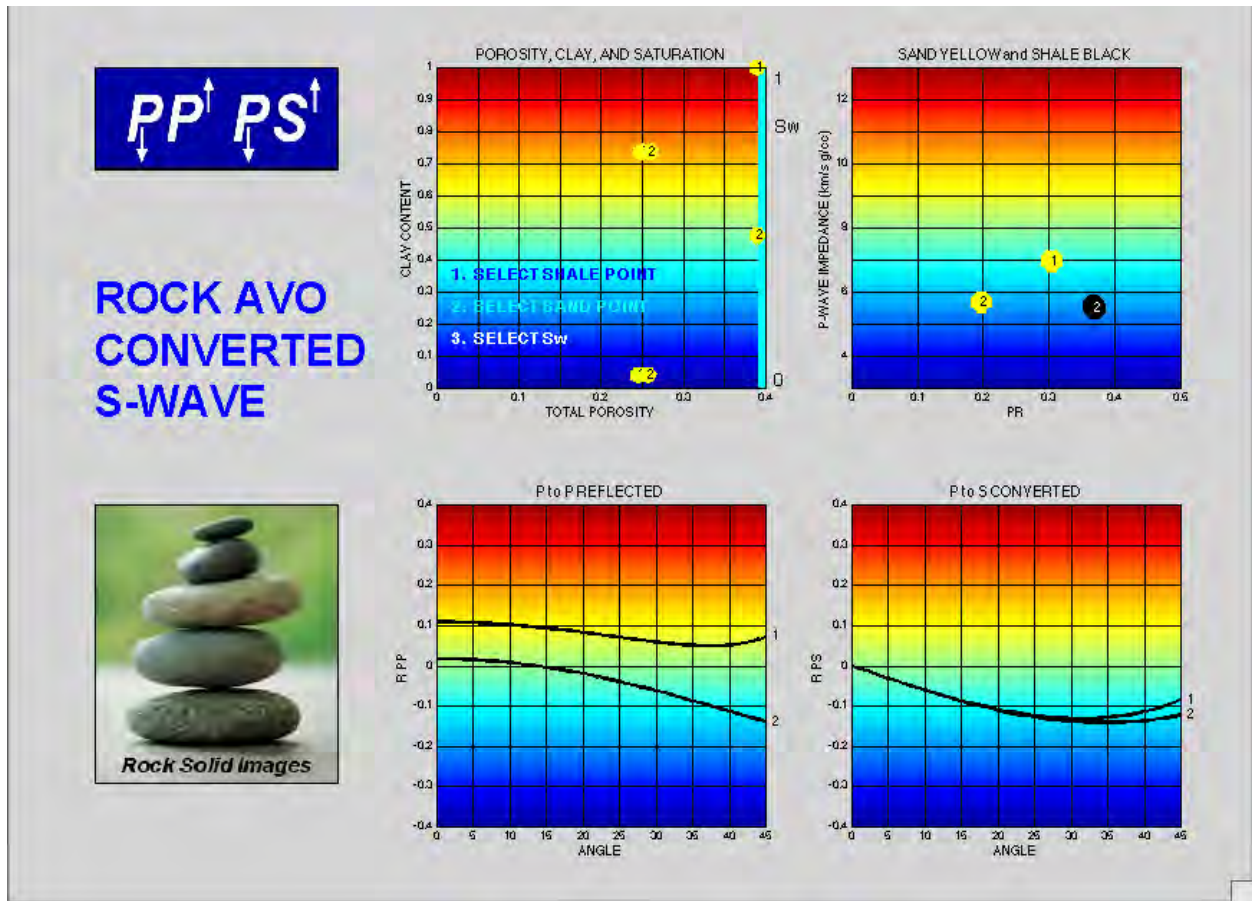


Figure 2.25. Example B for the two model scenarios shown by the numbers 1 and 2.

In example B, the shale-clay, sand-clay, porosity, and saturation values are very similar between the two models, while the sand saturation is wet for model 1 and 50% for model 2. This results in a positive PP reflectivity for the wet gas sand model (1) and a Class II AVO response for the gas sand model (2). The PS reflectivity is negative for both models, with little to no sensitivity to fluid saturation.

Coupling this comparison with that from example A illustrates that the PS amplitude data with offset can detect variation in porosity but not fluid saturation by using the PS AVO gradient.

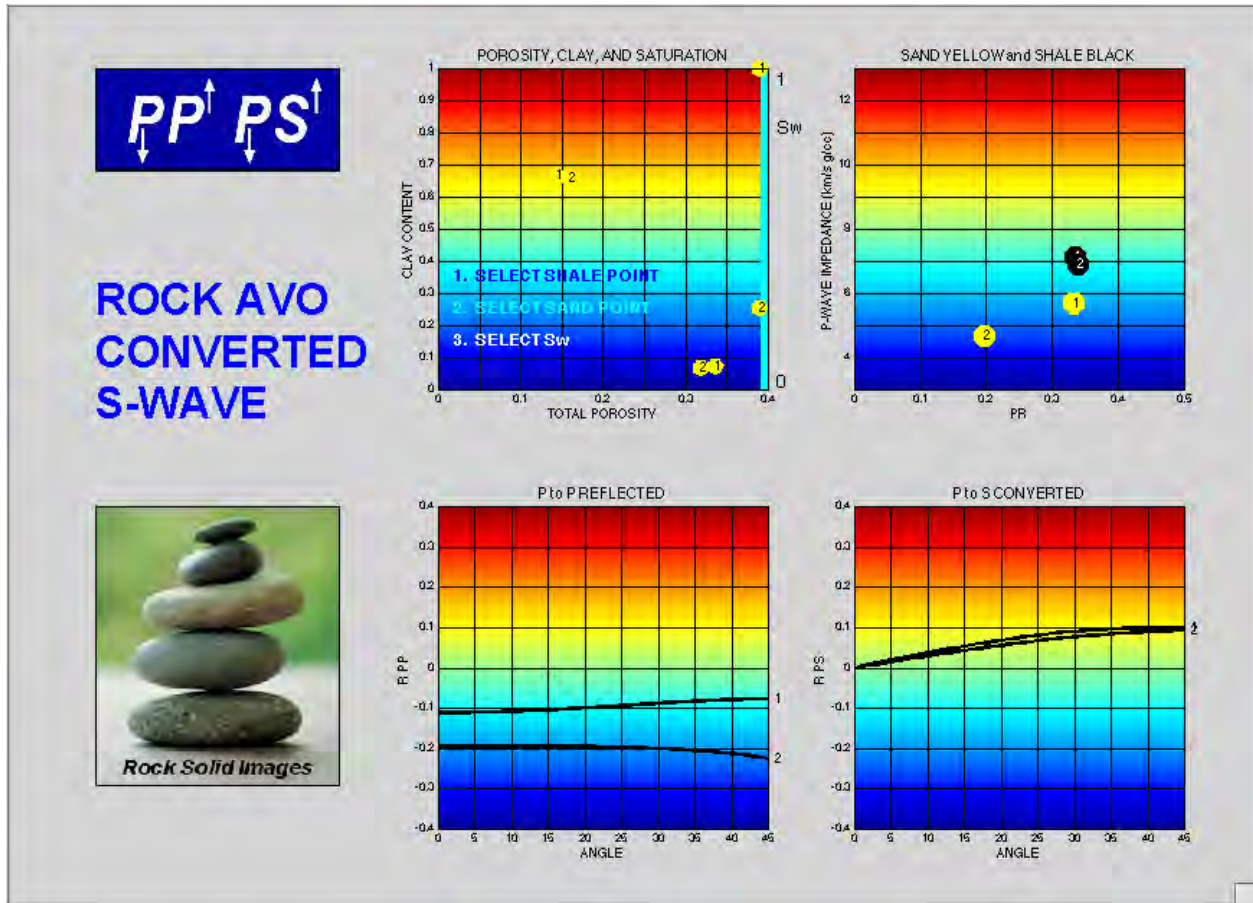


Figure 2.26. Example C for the two model scenarios shown by the numbers 1 and 2.

In example C, the shale-clay, sand-clay, porosity, and saturation values are very similar between the two models, except the shale is hard and the sand is soft (higher porosity), while the sand saturation is wet for model 1 and 25% for model 2. This results in a strong negative Class IV AVO PP reflectivity for the wet gas sand model (1) and a weak Class III AVO response for the gas sand model (2). The PS reflectivity is positive for both models, with little to no sensitivity to fluid saturation.

This example further confirms the insensitivity of PS AVO reflectivity to fluid saturation. It also shows another example of polarity reversal between PP and PS offset reflectivity for a soft sand overlain by a hard shale.

MATLAB APPLET FOR MODELING THE EARTH BEYOND THE WELL

Arguably, the central question of petroleum-oriented earth sciences is “What rock properties may stand behind the observed seismic amplitude?” It can be addressed from different perspectives and at different levels of complexity. The geologist may identify the spatial arrangement of reflectors with a turbidite channel, sheet sand, or a levee. The rock physicist strives to use this information and go farther by quantifying the properties and conditions within a geo-body. A powerful tool of approaching this goal is called *perturbational* forward modeling.

The principle of this methodology is to vary systematically the properties and conditions in the subsurface within geologically plausible ranges, to calculate the resulting elastic properties and attenuation, and to generate synthetic seismic traces. These traces are then matched to real seismic data. The main assumption is that if the seismic response is similar, the underlying earth properties are similar as well.

To explore this approach, we have built software that allows the user to create a 1.5-dimensional earth model in a clastic environment by placing a number of sand layers inside a shale background. The user specifies the clay content, total porosity, and water saturation in sand layers by clicking inside the panels provided in this software. A rock physics model is then used to relate the properties and conditions of the sediment to its elastic properties. Finally, a synthetic-seismic gather is generated and displayed.

The current implementation of this package does not account for attenuation. In the future, attenuation will be included in this modeling, and, in addition, synthetic P-to-S traces will be generated.

The starting point of the modeling is a panel where the fluid properties, frequency, and geometry are specified (Figure 2.27).

Presented here is an example of synthetic seismic gathers for two sand layers embedded in shale and saturated with gas (Figure 2.28). The rock physics model used here shall be calibrated to existing wells in the vicinity of the seismic survey under examination.

Parameter	Value
Water Salinity (ppm)	36000
Gas Gravity (Specific)	0.65
Oil Gravity (API)	30
GOR (l/l)	100
Pore Pressure (MPa)	70.
Temperature (C)	120.
Frequency (Hz)	25
Number of Sand Layers	2

Figure 2.27. The start-up dialogue to specify fluid properties, frequency, and number of sand layers.

The example shown in Figure 2.28 illustrates two sand layers embedded in shale. The left-hand panel is used to locate the sand layer's tops and bases. The next three panels are used to define the clay, porosity, and saturation for: shale – sand 1 – shale – sand 2 – shale (five entries in all).

The selected rock physics model uses these volumetric fractions to compute the elastic properties shown in panels 5 (V_p , V_s , RHO_b) and 6 (I_p , PR). Finally, on the right, the volumetric fractions are consolidated and the offset reflectivity convolved with an appropriate wavelet (25 Hz Ricker wavelet in this case), together with the stack (red curve).

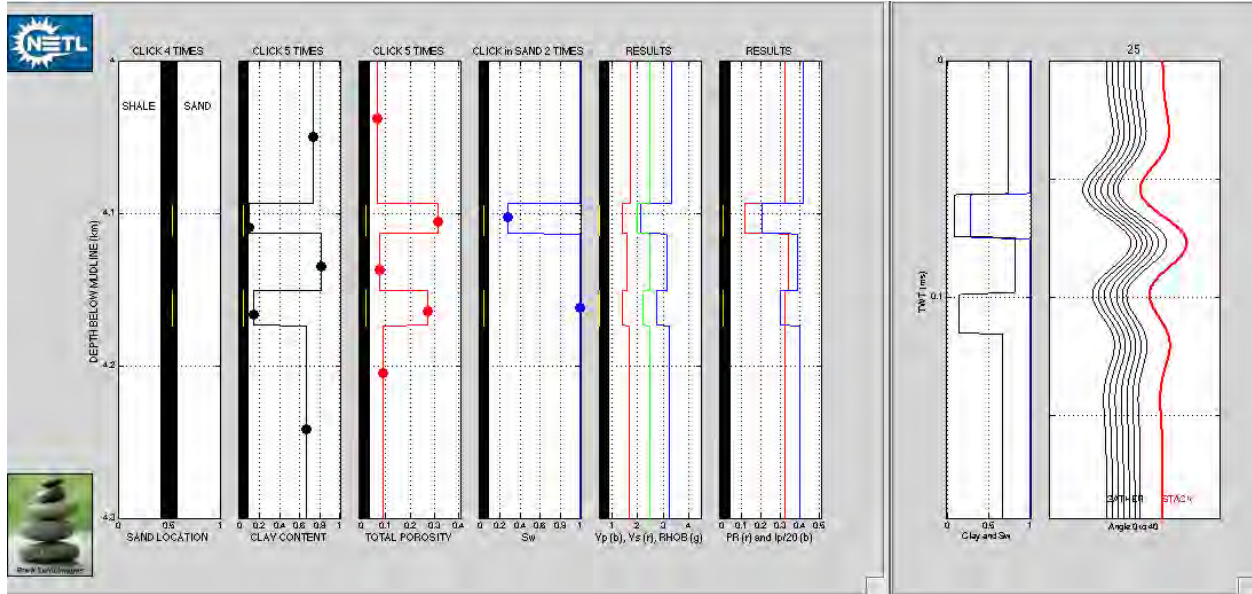


Figure 2.28. Synthetic seismic gather for two sand layers embedded in shale and saturated with gas.

PART 2 SUMMARY

Synthetic Seismic Modeling with Attenuation: We have shown synthetic traces, both at normal incidence and with offset, in an earth model containing a gas reservoir. We compared traces including effects of realistic attenuation with models assuming a perfectly elastic earth, using Ricker wavelets of 20, 30, 40, and 50 Hz. We find that:

- Lower frequencies lead to lower resolution. In the modeling shown here, striking changes in the reservoir signature occur between 40 Hz and 30 Hz.
- Attenuation leads to velocity dispersion, both in the overburden and in the reservoir. This dispersion tends to delay arrivals in the attenuation model. The very low Q and large dispersion in the gas reservoir also leads to an apparently thicker reservoir (in time) relative to an elastic earth.
- Attenuation in the overburden has a small effect on normal incidence amplitudes at the reservoir top. This attenuation reduces the far offset amplitudes relative to the near offset amplitudes, because the far offset traces travel a longer path.
- The large attenuation in the reservoir leads to greatly reduced base gas amplitudes and greatly reduced gradient.

- The reduction in AVO gradient from attenuation could cause gas to be mistaken for oil, and oil to be mistaken for water.
- Signatures of gas in this exercise are the increased-time thickness of the reservoir interval, lower impedances in the reservoir interval, and large contrasts in base amplitude relative to top amplitude due to attenuation in the reservoir.
- Seismic bandwidth appears to be crucial in identifying the tops as well as the extent of the reservoir, as well as in estimating the uncertainty when matching synthetic and real seismic data.

Tuning and Attenuation:

- Attenuation does not affect the tuning behavior as far as reflections at the top of the attenuating layer are concerned.
- As expected, attenuation does affect the reflection at the bottom of the attenuating layer.
- The latter effect could be fairly strong and affect the summary waveform associated with the attenuating layer.
- The same behavior as shown for the normal-incidence reflections will persist for the P-to-P reflection at an angle and, as a result, it will not affect the AVO curves at the top of the reservoir but will affect those picked at the bottom and, in general, will affect the waveforms associated with angle-stacked reflectivity.
- All the above conclusions hold if there is no attenuation above the main attenuating layer. The situation will change for a stack of attenuating reservoirs.

Matlab Applets: Three Matlab Applets were designed for use in modeling seismic gathers with and without attenuation. The first models PP reflections; the second models PS reflections; and the third has the ability to modify a stratigraphic sequence to model variations beyond the well bore. These help the geophysicist understand the seismic responses associated with the reservoir.

PART 3: PROPERTIES OF PORE FLUIDS AT HIGH PRESSURE AND TEMPERATURE

Commonly used fluid substitution equations by Gassmann (1951) indicate that the elastic properties of rocks, especially relatively soft sediments, can be strongly affected by the compressibility of the pore fluid. This difference in seismic properties is due to the strong difference between the bulk modulus of gas, oil, and water.

Because of the strong influence of the pore fluid properties on the seismic response, the industry needs to have reliable ways of estimating the bulk modulus and density of pore fluid, especially natural gas, versus pore pressure and temperature. Batzle and Wang (1992), in their classical Geophysics publication, provided equations that relate the bulk modulus and density of gas, oil, and water to gas gravity, oil gravity, gas-to-oil ratio, brine salinity, and, most important, pressure and temperature. These equations (BW) are widely used in the industry. Experiments on measuring the needed fluid properties continue (e.g., Han and Batzle, 2000). However, the pressure range of applicability of the BW equations as well as recent experiments does not extend beyond 50 MPa.

The normal pore pressure in the subsurface (in MPa) is approximately ten times the vertical depth in km. This means that 50 MPa occurs at approximately 5 km TVD. In over-pressured formations, the pressure may be higher even at shallower depths. Also, tremendous amounts of domestic natural gas (55 Tcf offshore, according to MMS, and 135 Tcf onshore, according to USGS) may be available at depths below 15,000 ft (about 5 km TVD) and as deep as 25,000 ft (about 7.5 km). This promising domestic gas potential calls for improvements in the interpretation of very deep seismic events and, as part of this technical task, valid estimates for the bulk modulus and density of the pore fluid, especially gas, in deep reservoirs at very high pressure.

COMPARISON TO THE BATZLE-WANG (1992) EQUATIONS

NIST provides two software packages, REFPROP7 for calculating the needed properties of natural gases, and NACL for calculating the properties of brine. Both packages provide

adiabatic as well as isothermal properties, the former relevant to geophysics and the latter to petroleum engineering. The packages are based on equations of state calibrated by an extensive experimental database (e.g., Setzmann and Wagner, 1991).

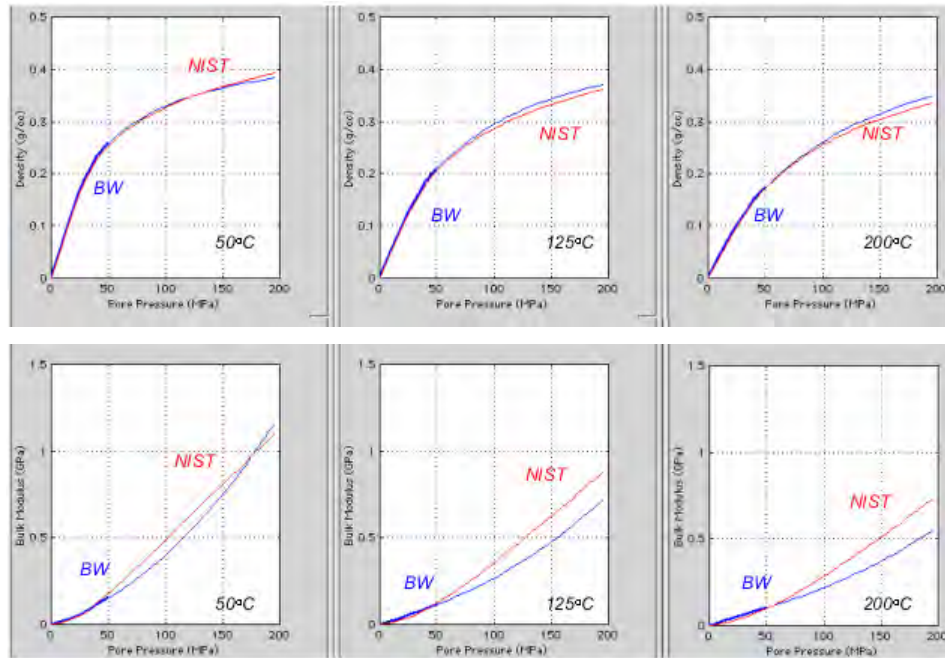


Figure 3.1. The density (top) and bulk modulus (bottom) of methane versus pressure and at varying temperature. The red curves are according to NIST while the blue curves are according to BW. The bold parts of the BW curves are for pressure below 50 MPa in which range the BW equations have been validated.

Examples of calculations of the density and adiabatic bulk modulus for pure methane versus pressure at temperature 50, 125, and 200°C are shown in Figure 3.1. In the same figure we present curves calculated for the same conditions according to the Batzle and Wang (BW) equations. Although the BW equations have not been validated above 50 MPa, we use them in the entire range of pressure under examination.

The NIST and BW density curves for pure methane are essentially the same below 50 MPa and only slightly deviate from each other in the range between 50 and 200 MPa. The bulk modulus from NIST and BW are similar below 50 MPa and get progressively farther apart as pressure increases to 200 MPa. The maximum difference at the extreme conditions of 200°C and 200 MPa is about 25%. This means that the BW equations for the density of methane can be used with confidence at very high pressures, but the bulk modulus values at 100 MPa and above will be substantially underestimated.

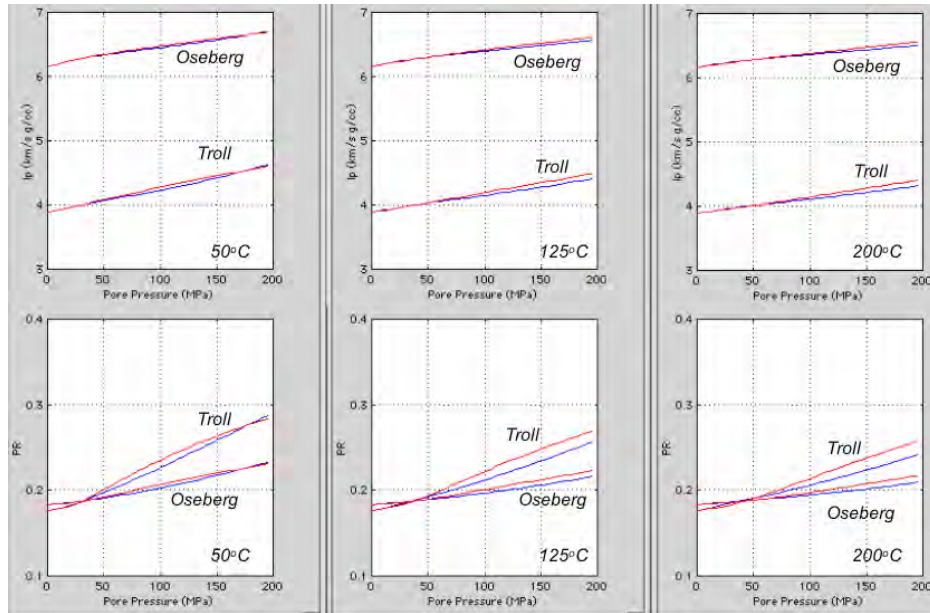


Figure 3.2. The impedance (top) and Poisson's ratio (bottom) for the Troll and Oseberg samples versus pressure and at varying temperature. In these calculations the only variables were the density and bulk modulus of methane as displayed in Figure 3.2. The red curves are according to NIST; the blue curves are according to BW.

EFFECT ON ELASTIC PROPERTIES OF SAND

In order to understand how the properties of methane at high pressure and temperature affect the elastic properties of sand, we select two high-porosity sand samples from the North Sea. One sample comes from the Troll field. It is friable and has 34% porosity and the room-dry P- and S-wave velocity 2.224 and 1.394 km/s, respectively. The other sample comes from the Oseberg field. It is slightly cemented fast sand of 30% porosity and the dry-room velocity 3.330 km/s for P- and 2.073 km/s for S-waves.

Gassmann's fluid substitution was used to calculate the impedance and Poisson's ratio (PR) of these two samples as the air in the pores was replaced by methane in the range of temperature and pressure considered in the previous section. During this exercise, the only variables were the density and bulk modulus of methane versus temperature and pressure.

The results shown in Figure 3.2 indicate that the impedance in both samples will be affected, although not strongly, by the changes in methane's properties due to temperature and pressure. The effect on PR is more pronounced, especially, in the softer Troll sample. In this sample, the increase in PR is from about 0.2 to about 0.3 as the pore pressure varies between zero and 200 MPa. This change may eventually translate into the AVO type of deep soft sand. The difference

in the impedance curves between BW-92 and NIST results is small, as shown in Figure 3.2. However, Poisson’s ratio is more sensitive to the differences, especially at certain combinations of pressure and temperature.

EFFECT ON AVO RESPONSE

We use full-offset synthetic seismic modeling to evaluate how gas property change with pressure may affect the AVO signatures of gas sand. For this purpose we select a well with gas sand at the bottom (Figure 3.3). First we calculate synthetic seismic traces for the conditions existing in the well. Next we theoretically substitute the original gas in the pay at not-very-high pressure by gas at ultrahigh pressure, according to gas property calculations shown in Figure 3.1. This fluid substitution affects both the impedance and PR of the gas sand in the well. These elastic property changes affect the AVO response of the sand extracted from the synthetic gather. While for the real in-situ conditions the AVO response at the top of the sand is of Class III, the response for the sand with gas at ultrahigh pressure is much weaker and merges towards weak Class II.

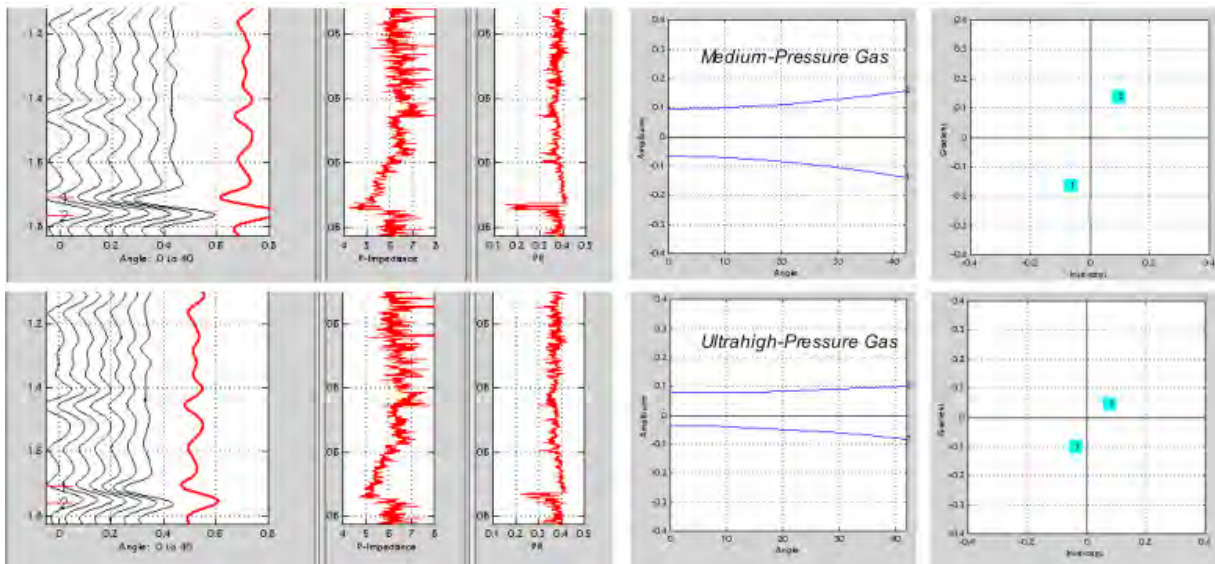


Figure 3.3. Synthetic seismic for a well with gas sand for the in-situ (top) and ultrahigh pressure (bottom) conditions. From left to right: gather (black) and stack (red); impedance and PR in the well; half-space diagram containing AVO curves extracted from the gather at the top of the sand (lower) and bottom of the sand (upper); gradient versus intercept cross-plot for these AVO curves. In the cross-plot, the numbers in the cyan squares correspond to those in the half-space diagram and in the gather.

FLUID PROPERTIES

We have computed the properties of NaCl brine versus temperature (from 25 to 250°C) and pressure (fixed at 100 MPa). The difference between the NIST model and BW-92 is minimal both for the density and bulk modulus.

To explore the effects of high pressure and temperature on gases other than methane, we also computed bulk modulus and density for pure ethane, propane, and butane. As shown in Figure 3.4, these computations show that for methane (specific gravity 0.56), BW-92 modulus is about 26% lower than NIST at 125 MPa and 200 C. For propane (specific gravity 1.52), BW-92 modulus is about 56% higher than NIST at 125 MPa and 200C. For butane (specific gravity 2.01) the differences are even larger.

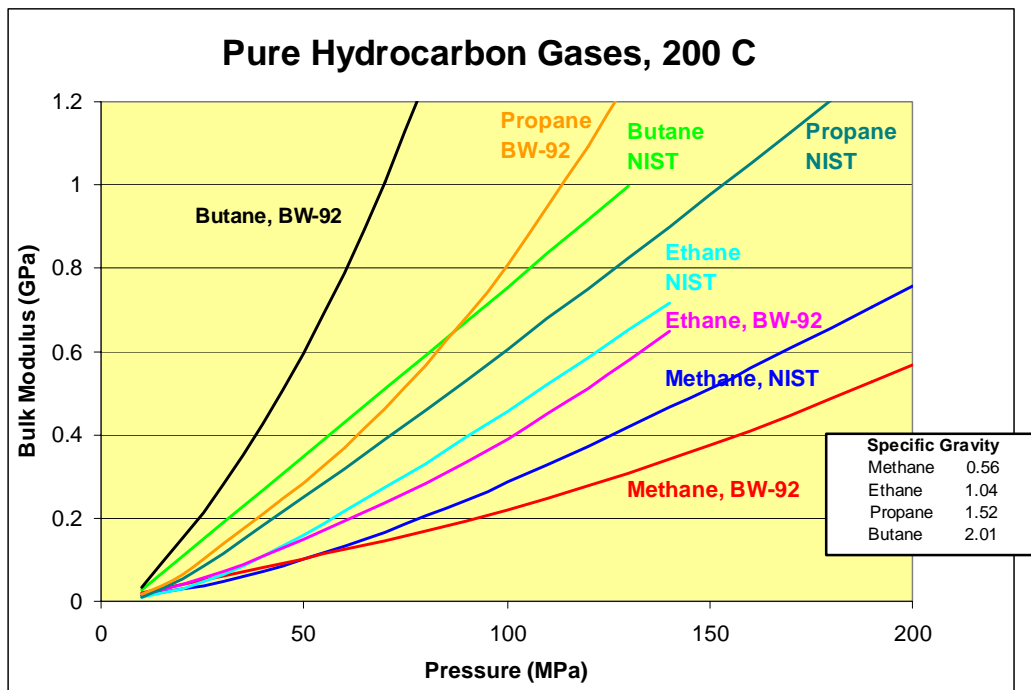


Figure 3.4: Effect of pressure on adiabatic bulk modulus of methane, ethane, propane and butane as computed by Batzle-Wang, 1992, and NIST model (200 C).

PART 3 SUMMARY

We used software from the National Institute of Standards and Testing (NIST) to assess the adiabatic bulk modulus and density of natural gas and brine at pressures up to 200 MPa and temperatures up to 200°C. The calculations are based on equations of state which are calibrated

and verified by many experimental measurements. The results indicate that as pressure increases from the normal range of 20 to 50 MPa to the very high range of 150 to 200 MPa, the bulk modulus of methane may increase tenfold, from about 0.1 to about 1.0 GPa. The latter values are comparable to those for oil. For heavier hydrocarbon gases (ethane, propane, butane, and their mixtures) the modulus will be even higher.

This strong increase in the bulk modulus of natural gas may affect the seismic response of deep gas sands and, therefore, needs to be accounted for during the interpretation of deep-gas seismic events as well as in forward modeling. We show, using real well log data as input into synthetic seismic modeling, that although the character of the AVO response may be not affected by the pressure-related changes in gas properties, the magnitude of this response will be definitely affected. Ultrahigh pressure may affect the properties of natural gas to a degree that translates into seismic signature type in very deep gas targets.

The Batzle and Wang equations and NIST model for NaCl brine give similar results for density and compressibility over a wide range of pressure and temperature. For gas density, BW-92 and NIST models gives similar results over a wide range of pressure and temperature. However for adiabatic bulk modulus, there are substantial differences between BW-92 and NIST at high pressure and temperature, and the differences depend on the gas specific gravity.

PART 4: ATTENUATION AND DISPERSION FROM SEISMIC AND LINK TO WELL DATA

GENERAL DEFINITIONS

Two key parameters govern measurement of the attenuation of seismic waves propagating through the layered earth: the attenuation coefficient $a(f)$, where f =frequency, and the Quality factor Q . The quantity $1/Q$ is called the internal friction or dissipation factor. Furthermore, we must distinguish between an apparent Q (measured directly from seismic data), an intrinsic Q (energy lost irreversibly to internal friction and converted into heat) and an extrinsic Q (an *apparent* energy loss or gain caused by the redistribution of seismic energy resulting from multiple internal scattering).

We can distinguish between two kinds of attenuation: the first occurs at layer interfaces. The energy in an incident P or S-wave is split into P and S- wave transmission and reflection branches. In this case there is no *net loss* of energy---it is merely redistributed among the separate transmission and reflection branches. So, strictly speaking, this is not attenuation.

The second kind of attenuation results from heat losses caused by solid friction as the wave propagates through the earth. This energy is lost irreversibly. On the other hand, the energy redistribution process taking place at each interface can be used to estimate extrinsic attenuation. O'Doherty and Anstey (1971) originated the classical statement that "more up is less down". We next examine what this statement implies for the estimation of the extrinsic portion of measured seismic attenuation.

Intrinsic attenuation is, like seismic velocity, a characteristic of a homogeneous layer. Therefore a measurement of attenuation implies measurement of an average quantity over some time or depth interval. We may eventually even have to define the average, interval and RMS values of attenuation and its associated seismic dispersion. A propagating seismic wave undergoes dispersion when its different frequency components travel at different velocities. A number of mechanisms can give rise to seismic dispersion: the one concerning us here is related to the causality principle, which implies that seismic absorption and seismic dispersion *cannot be independently specified*.

In particular, the so-called Kramers-Krönig (K-K) conditions (Futterman, 1962) establish the consequences of the basic fact that seismic attenuation must be causal and hence physically realizable. Yet, more than one attenuation law can be constructed that satisfies causality. Now a causal, physically realizable system must be either minimum-phase or non minimum-phase. Treitel and Taner (2002) came to the conclusion that the attenuation operator is best implemented as a minimum-phase operator. While it is theoretically possible to design *causal non-minimum phase* attenuation operators, the resulting added computational complexities do not seem warranted, given current data quality. Minimum phase operators do satisfy the K-K conditions and are physically realizable. For intrinsic Q , the phase changes relates to Q , frequency varying propagation velocity and the propagation distance. Thus our model relates intrinsic Q via the K-K conditions to *frequency dependent* propagation velocities. This, in turn means that a seismic pulse undergoes continuous changes in shape as it propagates in such an attenuating medium. In particular, such a pulse generally *broadens* with *increasing* travel time.

Q is related to the attenuation coefficient $\alpha(f)$ by

$$\frac{1}{Q} = \frac{\alpha(f)v_p}{\pi f}, \quad (4.1)$$

where v_p is the P wave velocity, f =frequency and $\alpha(f)$ represents a frequency dependent absorption coefficient. The absorption can be modeled simply as

$$A(f, x) = A(f, 0) \exp\{-\alpha(f)x\}, \quad (4.2)$$

where x is the travel distance. Combining Equations (4.1) and (4.2), we obtain a useful expression in terms of the travel time, t :

$$A_t(f) = A_0(f) \exp(-\pi ft / Q), \quad (4.3)$$

which is our basic Q model.

“CLOSING THE LOOP” FOR Q

This section discusses results from our efforts to “close the loop” for Q , a term that describes our effort to estimate Q from data generated with known Q . The workflow generates 1-D earth models with known Q assigned to various layers; then generates normal incidence synthetics, simulating recorded reflection seismic traces in the attenuating earth; and applies Q -estimation

algorithms to the traces to extract an apparent profile of Q ; and finally compares the estimated Q with the initial model Q , as a means to objectively evaluate the performance of our tools.

Of the various technologies discussed in this report, the methods for estimating Q from seismic are the least mature. In contrast, our rock physics models for predicting Q_p and Q_s from rock and fluid properties agree well with lab and field data, and they are based on first principles of rock inelasticity. Although the uncertainty for rock physics modeled Q can be as large as 10-20%, this is much better than our ability to invert real field seismic for Q . Furthermore, our ability to model *relative* changes in Q is much better – for example, predicting the change of Q with saturation in a given rock. Algorithms for simulating wave propagation in an attenuating earth appear to be reliable and robust. We will use the well-known Kennett invariant imbedding algorithm for the full-waveform modeling.

The challenge is to develop robust and efficient algorithms for estimating Q from field seismic records. Q indicators can include low amplitude, low frequency, a change in spectral shape, and a change in wavelet shape (phase). Practical difficulties in the field arise from distinguishing these indicators from imperfections in acquisition and processing, though the synthetics will correspond to “perfect” data.

We will show that algorithms for estimating Q suffer from a common limitation – the trade-off between accuracy and resolution. We can get excellent average Q -values from whole-trace analysis, but resolving spatial variations in Q , for example the low- Q in layers as thin as a few wavelengths, is still problematic.

Another serious problem is separating Q effects from reflection effects. Attenuation causes changes in amplitude, spectra and phase, which accumulate during propagation. However, anomalous impedance contrasts and thin-bed sequences also impact amplitude spectra and phase.

We use the Spectral ratio method to illustrate the concept of “closing the loop”.

SPECTRAL RATIO METHODS

Recorded traces will *always* show signs of attenuation. Most noticeable in field data are the systematic decreases of amplitudes and frequencies deeper in the section. We can understand these losses by considering a plane wave with initial amplitude A_0 . At distance x and time t , the amplitude at a particular wave front can be written as:

$$A(x,t) = A_0 \exp\left(\frac{-\pi ft}{Q}\right) \quad (4.4)$$

where f is the frequency and t is the propagation time. Taking the log of both sides of Equation (4.4) gives

$$\ln\left(\frac{A(x,t)}{A_0}\right) = \ln(A(x,t)) - \ln(A_0) = \frac{-\pi ft}{Q}. \quad (4.5)$$

From Equation (4.5) we see that the log of the ratio of measured to initial spectra decreases linearly with frequency, with a slope of t/Q . *This simple observation is the basis for a variety of spectral methods for Q -estimation.*

SPECTRAL RATIO FOR STRATIGRAPHIC ATTENUATION

Field traces will *always* show signs of attenuation, because of *scattering* or “*stratigraphic filtering*,” even if the earth model is elastic. In this case, energy is lost from the wave arrivals, not because it is dissipated into heat, but because it is delayed or sent elsewhere by multiple scattering. Scattering attenuation is also sometimes call *extrinsic attenuation*. We use scattering attenuation as the first illustration of the spectral ratio method for estimating Q from seismic.

The logs on the left of Figure 4.1 were used to generate normal incidence full-waveform synthetics in an elastic earth. Synthetics were generated using the normal incidence Kennett algorithm (modeling all multiples), with a 50 Hz Ricker wavelet. Because the earth layering is changing rapidly, the wave encounters a lot of scattering attenuation. Spectra were estimated in a 120 ms window shallow in the trace and another 120 ms window deep in the trace via the maximum entropy method, using the Berg-technique for autocorrelation estimation, which is particularly well-suited for short data windows. We observe that the relative loss of spectral power decreases linearly with frequency. Using Equation (4.5), we use the relative changes in slope to estimate an extrinsic or scattering $Q_{scatter} \approx 360 \pm 30$.

SPECTRAL RATIO FOR INTRINSIC Q , PLUS STRATIGRAPHIC ATTENUATION

The same logs as in Figure 4.1 were used to generate normal incidence full-waveform synthetics, but now in an attenuating earth model with an intrinsic $Q \approx 50$ everywhere, see Figure 4.2. Spectra were again estimated in a shallow window and a deep window, and again we

observe the loss of spectral power linearly increasing with frequency. The relative changes in slope allow us to estimate a total $Q \approx 44 \pm 5$.

Figures 4.1 and 4.2 illustrate another important challenge for the practical use of Q as an indicator of rock properties. The measured Q will always be the sum of scattering attenuation, which is the result of heterogeneity, and intrinsic attenuation, which is a rock property. To a good approximation, we consider that the losses from scattering and intrinsic loss are additive, which allows us to write

$$\frac{1}{Q_{observed}} \approx \frac{1}{Q_{scatter}} + \frac{1}{Q_{intrinsic}} \quad (4.6)$$

The scattering attenuation in Figure 4.1 was estimated to be $Q_{scatter} \approx 360$, and the observed total attenuation was found in Figure 4.2 to be $Q_{scatter} \approx 44$. Then using Equation (4.6), we can solve for the intrinsic attenuation

$$\frac{1}{Q_{intrinsic}} \approx \frac{1}{Q_{obs}} - \frac{1}{Q_{scatter}} \Rightarrow \frac{1}{50} \approx \frac{1}{44} - \frac{1}{360} \quad (4.7)$$

where $Q_{intrinsic} \approx 50$ was the intrinsic attenuation specified in the earth model. Spectrally derived estimates of Q from Figures 4.1 and 4.2 have uncertainties of about 15-20%.

The examples in Figures 4.1 and 4.2 illustrate two points:

- Spectral ratios can give stable estimates of apparent Q , especially if the data windows are long and the separation between shallow and deep windows is large. The long windows give better statistical accuracy of the spectral estimate, and the large window separation ensures that the spectral change is large relative to estimation uncertainty.
- Q estimated from seismic traces is always the sum of intrinsic and extrinsic losses. Even if the apparent Q can be measured stably and accurately, the intrinsic Q can only be extracted if we have an independent estimate of the extrinsic Q .

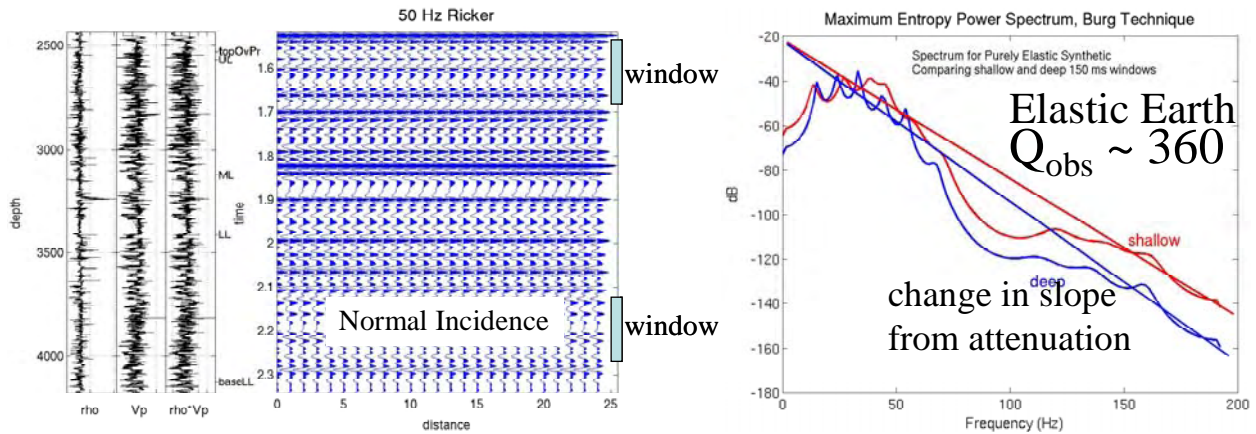


Figure 4.1. Synthetic example of stratigraphic attenuation in an elastic earth model. Left —Thinly layered earth revealed by well logs leads to synthetics with a lot of scattering. Right —Spectral estimates in a shallow (red) window and a deep (blue) window of the trace, showing a linearly increasing loss with frequency.

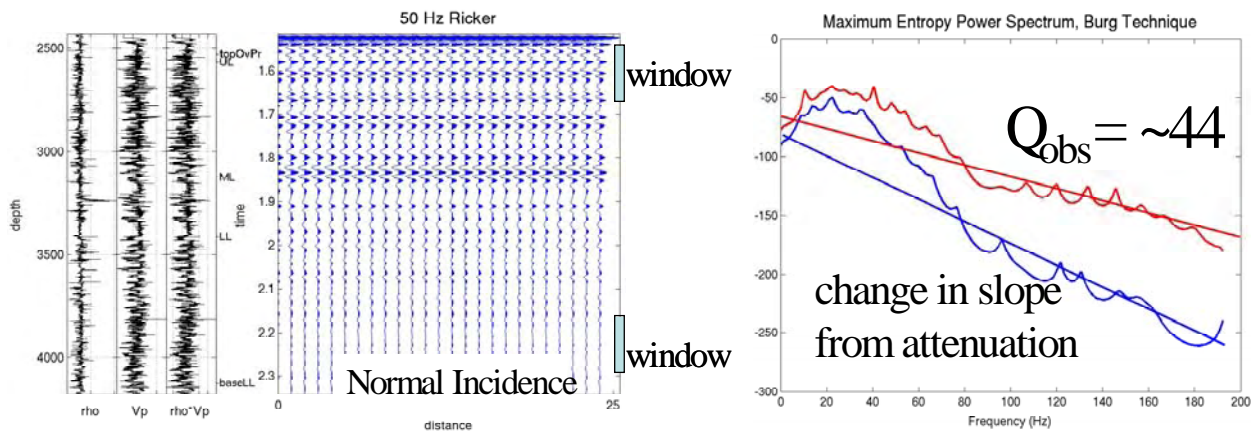


Figure 4.2. Synthetic example of attenuation in an earth model having intrinsic $Q=50$, everywhere. Left —Thinly layered earth revealed by well logs leads to synthetics with a lot of loss from both scattering and intrinsic attenuation. Right —Spectral estimates in a shallow (red) window and a deep (blue) window of the trace, showing a linearly increasing loss with frequency.

SPECTRAL RATIO FOR SPATIALLY VARIABLE INTRINSIC Q

Figure 4.3 shows an example having a background intrinsic $Q \approx 300$, and a localized reservoir, 140 ms thick, having $Q \approx 30$. Spectra were again estimated in a shallow window and a deep window, and again we observe the loss of spectral power linearly increasing with

frequency. The relative changes in slope allow us to estimate a total $Q \approx 62 \pm 7$. The intrinsic and extrinsic attenuations can be added as:

$$\frac{t}{Q_{obs}} \approx \frac{t}{Q_{scatter}} + \frac{t-t_r}{300} + \frac{t_r}{30}; \quad t \approx .65; t_r \approx .14; \quad (4.8)$$

where t is the time difference between the shallow and deep reservoirs and t_r is the propagation time through the reservoir. In Equation (4.8), $(t-t_r)/300$ refers to the background intrinsic loss, $t/360$ is the background scattering loss, and $t_r/30$ is the loss in the reservoir. We see that the total $Q_{observed} \approx 62 \pm 7$ is consistent with the intrinsic $Q \approx 30$ in the reservoir.

From this example, we see that the presence of the reservoir can be detected by comparing the spectral content of the seismic shallow and deep in the section. However, the Q-signature of the reservoir varies as t_r/Q , so that a thinner reservoir or a larger Q reservoir might be undetectable.

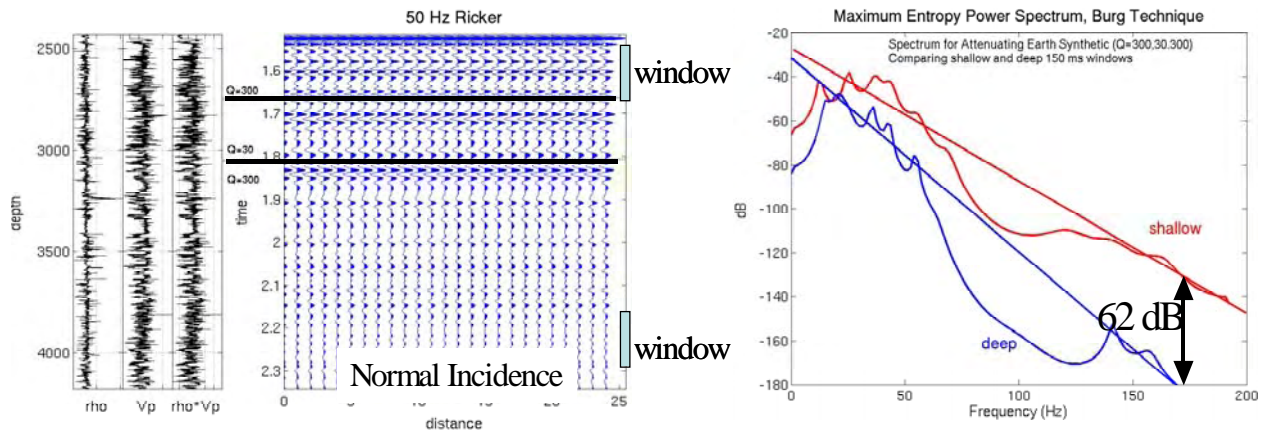


Figure 4.3. Synthetic example of attenuation in an earth model having intrinsic $Q=300$ everywhere, except in a shallow window having $Q=30$. Left —Thinly layered earth revealed by well logs leads to synthetics with a log of loss from both scattering and intrinsic attenuation. Right —Spectral estimates in a shallow (red) window and a deep (blue) window of the trace, showing a linearly increasing loss with frequency.

Note also that this exercise says nothing about resolving the spatial location or extent of the reservoir. One approach to implementing the method illustrated in Figure 4.3 is for supporting a prospect. A candidate reservoir might be indicated by impedance inversion, attribute analysis, or amplitude analysis. Subsequent evaluation of whether or not it is hydrocarbon-bearing might be tested by comparing shallow and deep spectra, as we have done here.

SPECTRAL RATIO ANALYSIS IN THE TIME DOMAIN

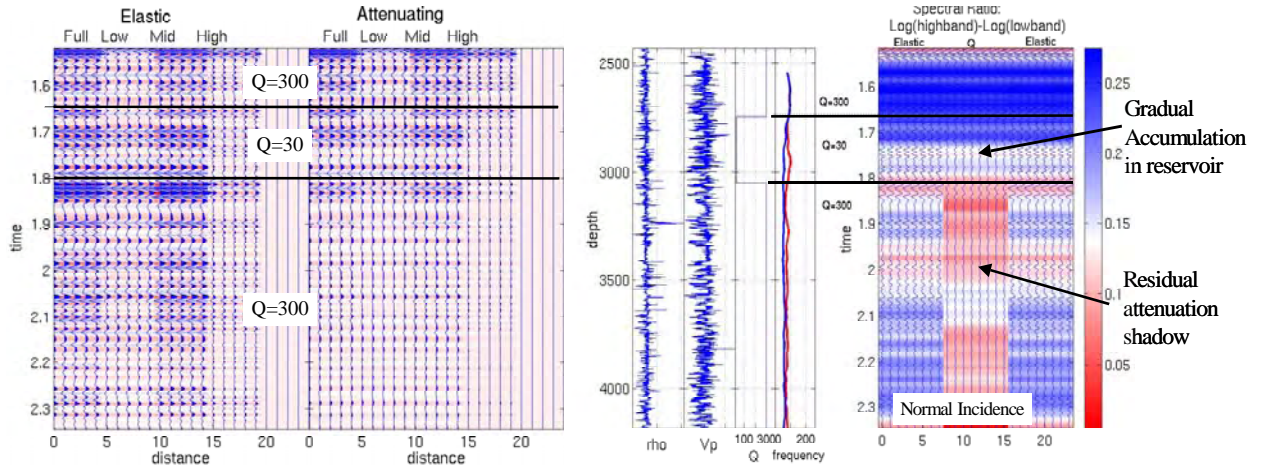


Figure 4.4. Synthetic example of attenuation in an earth model having intrinsic $Q=300$ everywhere, except in a shallow window having $Q=30$. Left — Seismograms showing full band and decomposition into low, mid, and high bands. Right — Seismic traces for elastic and attenuating earth, with difference of the log amplitudes in high and low bands (spectral ratio) shown in color.

Figure 4.4 shows synthetic seismograms similar to Figures 4.1 and 4.3. On the left we compare the fully elastic model with the attenuating model containing a low- Q reservoir, as in Figure 4.3. In both cases the full-band seismic traces are decomposed into low, mid, and high frequency bands (equally divided into the three lowest quarter bandwidths).

At the right, the traces in the elastic and attenuating earth models are superimposed on the color-coded spectral slope, estimated as

$$slope = \log\left(\frac{high - band\ envelope}{low - band\ envelope}\right), \quad (4.9)$$

where *envelope* refers to the envelope of the analytic signal of the trace.

In principle, the attenuation can be estimated from the change of spectral slope with depth, using Equation (4.5). Here we simply point out that qualitatively the attenuating layer is characterized by a fairly abrupt change in spectral slope.

GABOR-MORLET TRANSFORM & Q ESTIMATION

Joint Time-Frequency Analysis (JTFA) is today one of the principal tools used to analyze non-stationary data, for example seismic recordings. One of the earliest methods of this kind is the Gabor-Morlet transform. It logically relates to the Fourier transform, and was first described by Gabor (1946). It was later reintroduced and modified by Morlet et al (1982). The technique allows us to study spectral changes over time.

After evaluating different methods for Q estimation, the following two methods were found to be the most dependable. The first method is called the *JTFA Log Spectral Ratio Method*, and it relies on the basic spectral ratio equation to determine Q , but instead uses the JTFA method and spectral balancing to achieve an estimate of attenuation. The second method is called the *JTFA Frequency Shift Method*. It uses JTFA (Figure 4.5) to determine a zone of anomalous absorption lying in a larger background region exhibiting average absorption properties. It also uses spectral balancing as a means to estimate the amount of absorption.

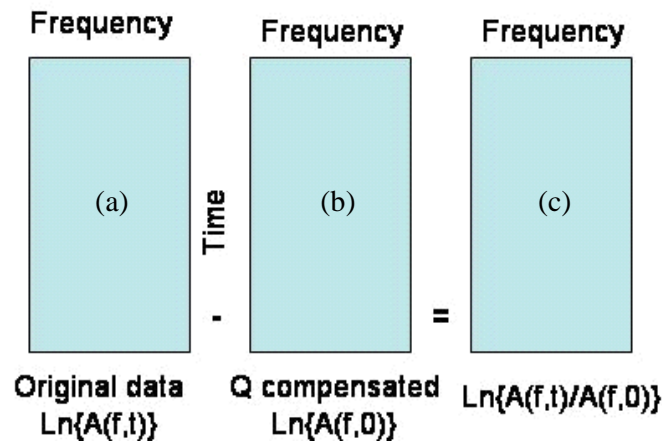


Figure 4.5. A diagrammatic representation of Joint Time-Frequency Analysis. The blue boxes represent Joint Time-Frequency plots with a y-axis of time and an x-axis consisting of N different spectra, one for each spectral band chosen in the Gabor-Morlet JTFA input parameters, as in Figure 4.6. The observed attenuated data (a) is spectrally balanced and thus Q -compensated (b). The difference between (a) and (b) then allows us to estimate $1/Q$ (c).

JTFA LOG SPECTRAL RATIO METHOD

Consider the expression

$$A(f,t) = A(f,0) \exp(-\pi ft / Q) \tag{4.10}$$

where f is the circular frequency in Hz, $A(f,t)$ is the Joint Time Frequency (JTF) spectrum of the observed attenuated trace, $A(f,0)$ is the JTF spectrum of the *spectrally balanced* trace, and $\exp(-\pi ft / Q)$ is the (non-dispersive) attenuation operator.

Taking natural logs of both sides of Equation (4.10) and rearranging terms,

$$\text{Ln}\{A(f,t)\} - \text{Ln}\{A(f,0)\} = -\pi ft / Q, \tag{4.11}$$

from which we obtain the desired value of $1/Q$ in the form (Figure 4.5)

$$1/Q = [\text{Ln}\{A(f,0)\} - \text{Ln}\{A(f,t)\}] / \pi ft, \tag{4.12}$$

Examples of the two methods are shown using the input data shown in Figure 4.7. The magenta ellipse highlights the hydrocarbon bearing sands in the section.

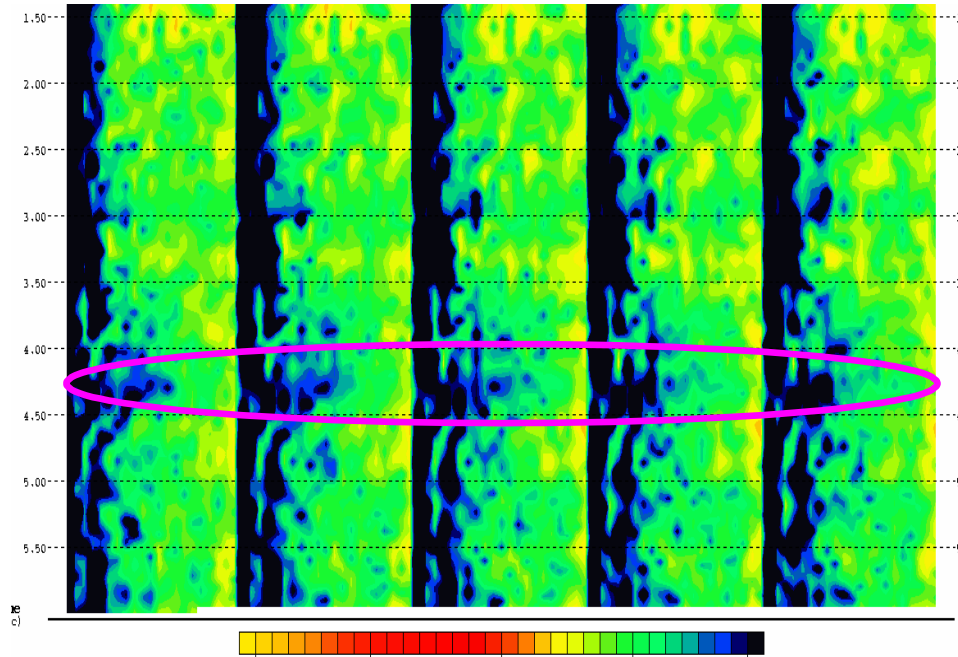


Figure 4.6. Five Joint Time-Frequency plots (representing 5 CMPs) showing natural log differences between the original and spectrally balanced data. Vertical axis is time; horizontal axis is frequency, with low to high from left to right. Darker colors represent zones of relatively large log differences per cycle. Note the large frequency differences about 4.0–4.5 sec, corresponding to the attenuation anomaly in Figure 4.8.

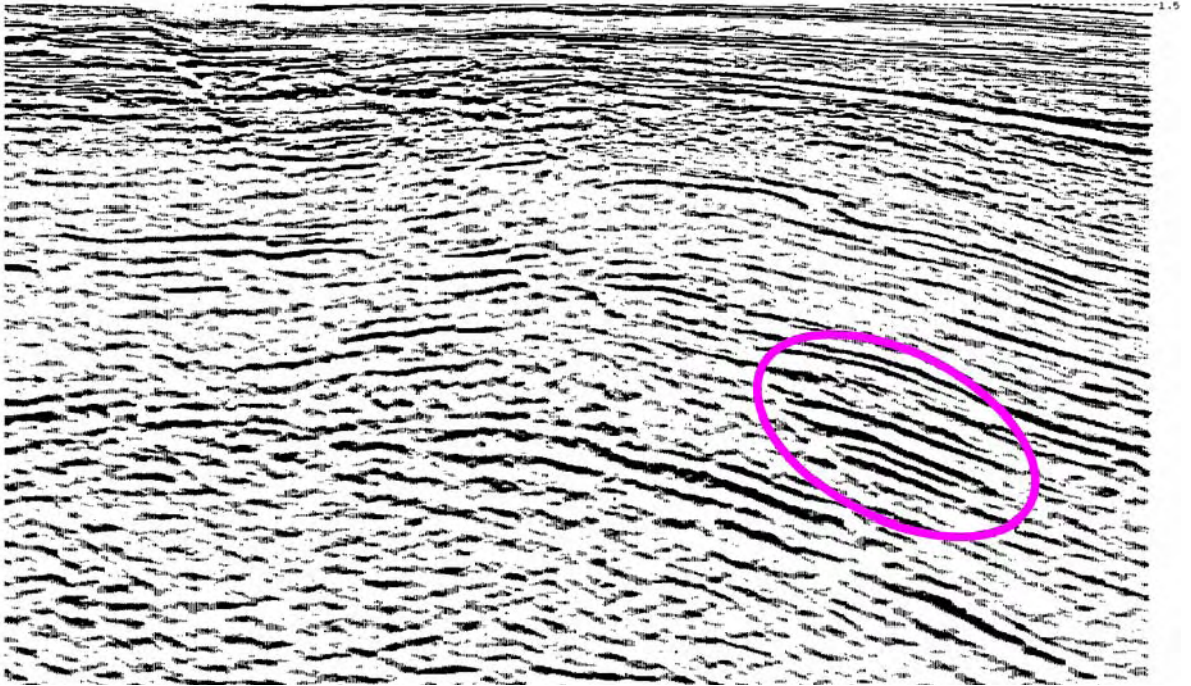


Figure 4.7. Input data taken from the Gulf of Mexico, used to illustrate the seismic Q methods.

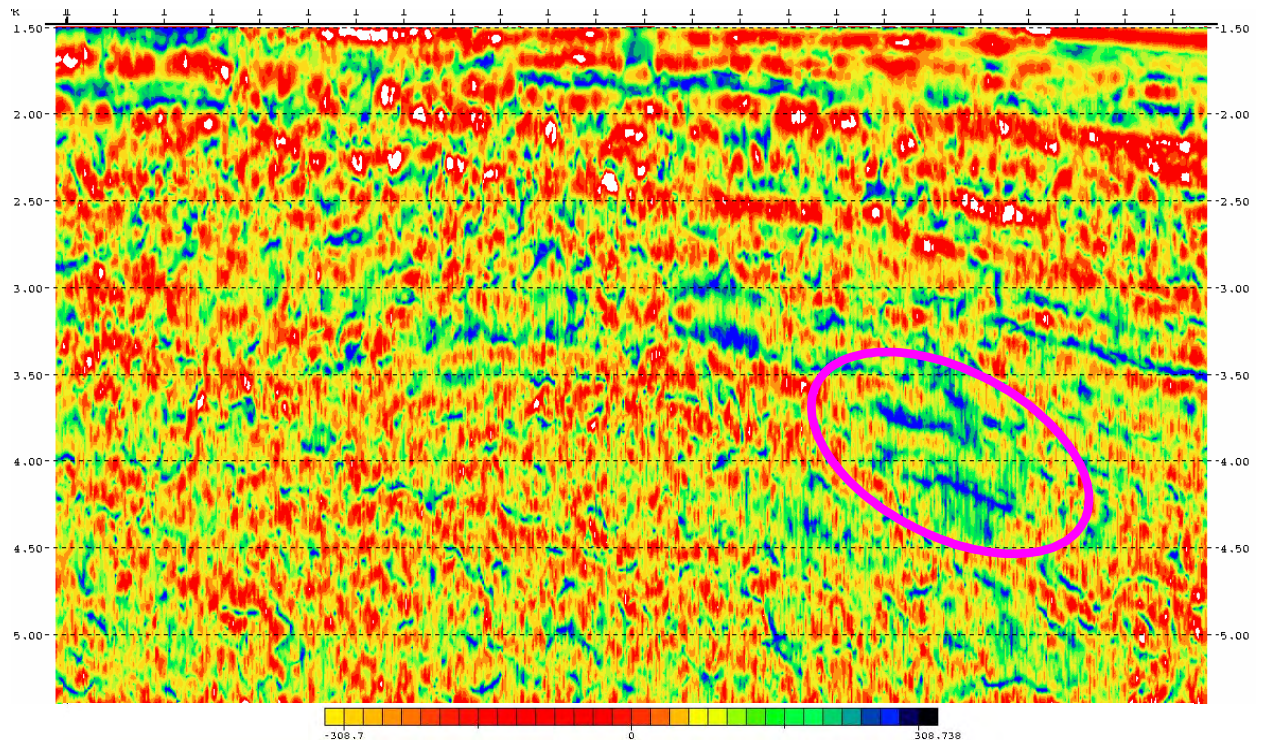


Figure 4.8. Gulf Coast example of the Log Spectral Ratio Method. The dark blue areas represent high attenuation zones, while the reds and yellows represent zones of lower attenuation.

JTFA FREQUENCY SHIFT METHOD

Attenuation is like a low pass filter, hence it suppresses higher frequencies proportionally more than the lower frequencies. Therefore, if we can measure frequency shifts in the data, we can estimate relative and/or approximate Q. In this method, we essentially estimate the anomalous absorptive zones in the data. The program runs Gabor-Morlet decomposition to generate JTFA spectra, which in turn reveals the time-varying nature of the data and demonstrates the non-stationarity inherent in seismic data.

Spectral Balancing

The basic principle of this and other Gabor-Morlet techniques is that joint time-frequency is run before and after spectral balancing. Since spectral balancing changes only the amplitude spectra of the sub-bands, it is not a complete Q compensation. However, since we are measuring only the mean or RMS frequencies, not the phase, spectral balancing will be acceptable for Q compensation. The difference in the mean or RMS frequencies at each time interval before and after spectral balancing is then measured and scaled to indicate relative attenuation.

Gabor-Morlet

The Gabor-Morlet JFTA method (Morlet et al, 1982) allows us to decompose a given seismic trace $f(t)$ into its so-called sub-bands, $G(t, f)$, which are functions of both time and frequency. This decomposition is accomplished by convolving $f(t)$ with a so-called Gabor-Morlet wavelet,

$$g(\tau, f) = e^{-i2\pi f\tau} e^{-\alpha\tau^2}, \quad (4.13)$$

where α is a constant controlling the width of the modulating Gaussian. The sub-bands are

$$G(t, f) = \sum_{\tau} f(t - \tau)g(\tau, f). \quad (4.14)$$

Since the sub-bands are complex functions, we identify the sub-band magnitudes with the so-called joint frequency-time amplitude spectrum $a(t, f)$ of the seismic trace

$$a(f, t) = |G(f, t)|. \quad (4.15)$$

Typically, analysis of Gabor-Morlet sub-bands involves computing the first and the second moments of the joint frequency time spectra at each data sample. The first moment is the average (or mean) of each $a(f, t)$,

$$F_{ave}(t) = \frac{\sum_f f a(f,t)}{\sum_f a(f,t)}, \quad (4.16)$$

while the second moment is the square of the root mean squared (RMS) value of each $a(f,t)$,

$$F_{RMS}^2(t) = \frac{\sum_f f^2 a(f,t)}{\sum_f a(f,t)}. \quad (4.17)$$

The difference between Equation (4.17) and the square of Equation (4.16) is the frequency variance, or bandwidth,

$$\sigma^2(t) = F_{RMS}^2(t) - F_{ave}^2(t). \quad (4.18)$$

However, we should note that for this method we are not using bandwidth (Equation 4.18) or second moment (RMS, Equation 4.17) in any of our calculations. Other methods, such as VSP Q estimation (Taner, 2006) do use bandwidth calculations.

Trend

The central analytical component to this method is an attempt to eliminate extrinsic attenuation (scattering) by the means of trend removal. In general, seismic data will experience an increasing amount of attenuation with depth as a result of the growing number of attenuating layers and interfaces it must pass through. However, our objective is to measure only intrinsic attenuation (absorption). Therefore, we seek to remove the progressively increasing attenuation profile caused by scattering while at the same time preserving anomalously attenuating zones caused by absorption. This is achieved by trend removal.

We estimate a general trend line by means of a low pass filter applied to the mean frequency curves given by Equation (4.12). Local variation in the trend profile is computed in the same way, but with a filter amplifying the shorter wave-lengths. Let $CL(t)$ and $CS(t)$ be the outputs from such long and short wavelength filters, respectively. Then the difference between the trend and the local variation is

$$AZ(t) = CS(t) - CL(t), \quad (4.19)$$

where negative $AZ(t)$ values indicate areas of anomalous lower frequency and narrower bandwidth; that is, they indicate zones of anomalously high absorption. Figure 4.5 illustrates how the Gabor-Morlet JTFA algorithm we have just described works on a given seismic trace.

Procedure

- Spectrally balance seismic traces.
- Compute JTFA of seismic traces before and after spectral balancing.
- Subtract the JTFA of the original data from the spectrally balanced data.
- Compute the mean frequency of each time on the JTFA difference data.
- Low pass filter difference data mean frequency and compute its average over a large number of traces to obtain an areal trend of frequency decay with time.
- Subtract the areal trend from the short-wavelength difference data mean frequency. Negative-valued zones represent higher than normal absorption, positive-valued zones represent the lower than normal absorption (Figure 4.9).

The resultant anomalous absorption data values are multiplied by a scalar. The scalar is chosen, after the elimination of outliers, to make the difference between low and high absorption layers clearly differentiable (values range from 1 to 301). Absorption is the property that is measured, meaning that high numbers indicate anomalous absorption.

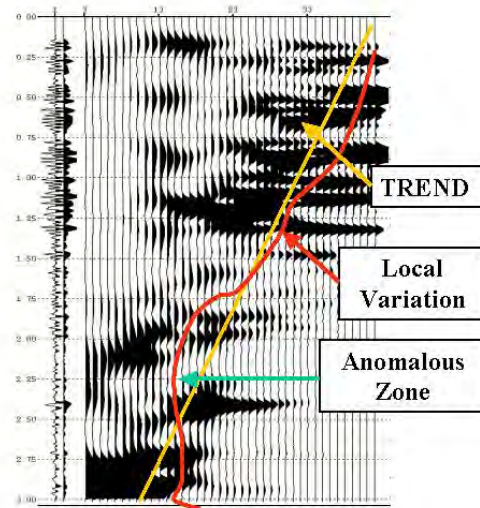


Figure 4.9. The Gabor-Morlet decomposition of a seismic trace. On the left side are the seismic traces, and on the right are the instantaneous amplitudes of the Gabor-Morlet sub-bands, as defined above, with sub-band frequency on the horizontal axis. The differences between the estimated trend and the local variation then are assumed to represent zones of anomalous absorption.

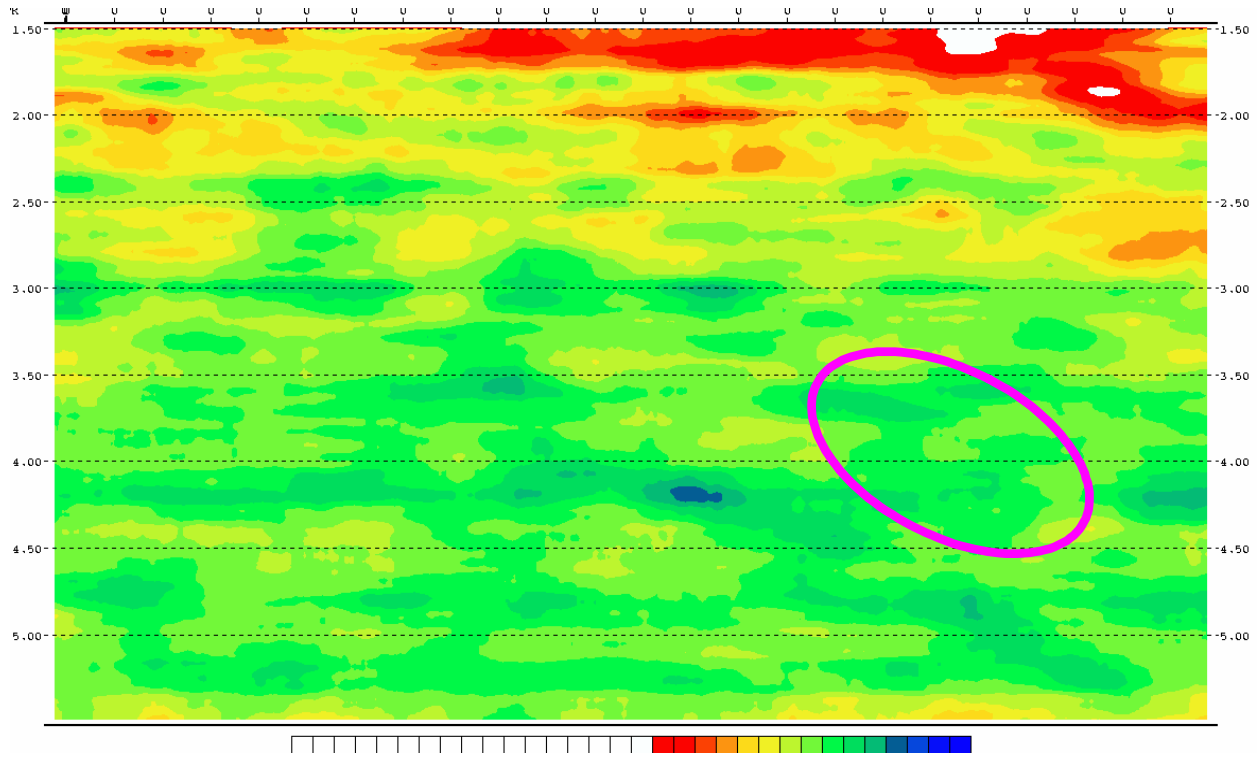


Figure 4.10. Long wavelength (time and space) filtered output of the frequency-shift profile. We assume that this section represents an estimate of extrinsic attenuation. Blue = higher attenuation. Red = lower attenuation.

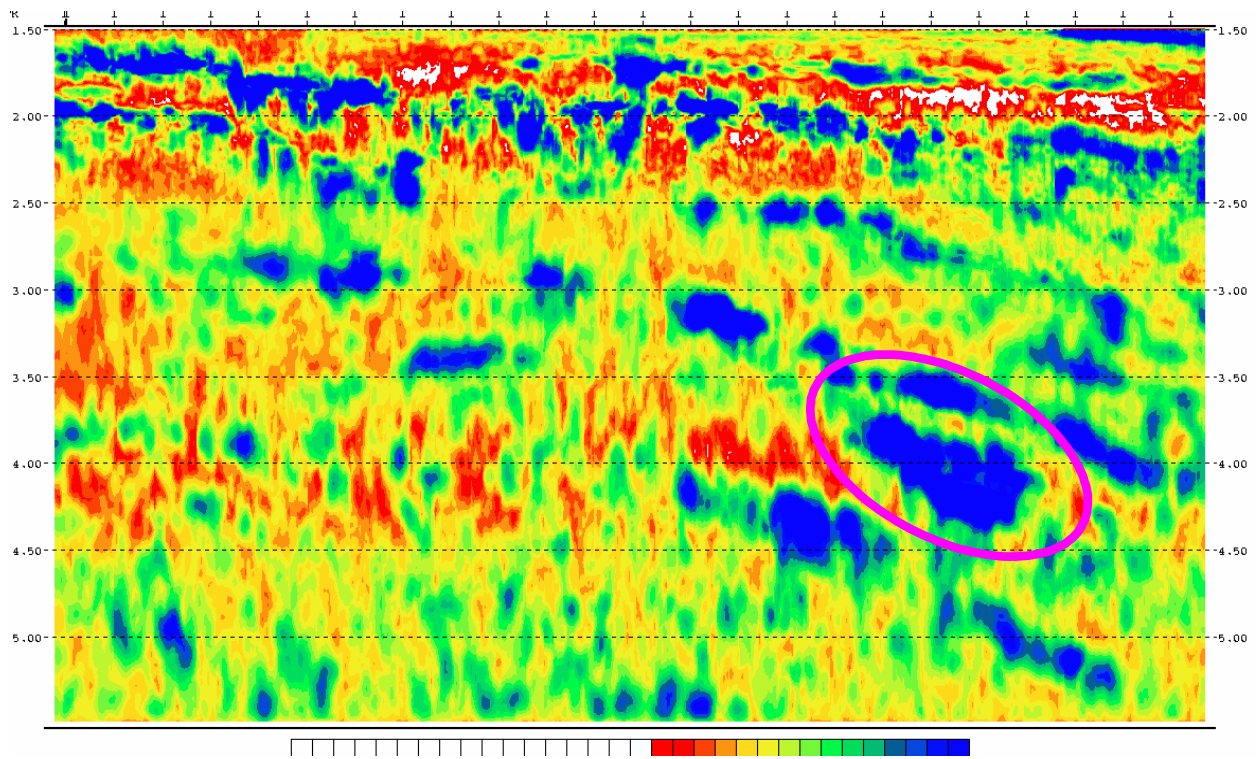


Figure 4.11. The frequency shift method of estimating highly absorptive zones. Blue = high local absorption. Red = low local absorption. The original data is shown in Figure 4.7.

This method estimates zones of absorption above the general areal average. After spectrally balancing the data and subtracting the original from the spectrally balanced data, we compute mean frequencies from the JTFA difference data and determine a long wavelength trend line of these differences (Figure 4.10). This is subtracted from locally computed (short wavelength) values of the mean frequency profile to isolate anomalous zones (Figure 4.11).

PART 4 SUMMARY

Spectral Ratio Analysis Techniques for Q Estimation:

- The effects of finite Q are to decrease amplitude, attenuate higher frequencies faster than lower frequencies, stretch wavelets, and rotate wavelet phase.
- It is difficult to resolve thin Q-layers, but it is easier to detect their presence from their “shadow” – the difference between spectra shallow and deep in the section
- Q-effects can be measured from spectral ratios.
- Accuracy of Q from spectral ratios increases with longer data windows and longer separation between shallow and deep windows, obviously at the expense of resolution
- Spectral ratios can be performed in the time domain from amplitudes and band-pass ratios.
- It is easier to detect relative changes than absolutes.
- An additional practical problem in the field might result from the phenomenon of “wave-front healing.” Because of wave diffraction plus undershooting from multiple offsets, the loss of high frequencies near a low-Q reservoir might recover with depth. Depending on how windows for spectral ratios are chosen, healing might diminish or mask the Q.

Gabor-Morlet Seismic Q Estimation Algorithms: Two different methods for Q estimation of seismic data have been presented. These two methods, while differing in their measurement technique for Q and in their response to attenuation, are nevertheless based on the same principle. The technique is Gabor-Morlet Joint Time-Frequency Analysis, and it is used to separate the frequency spectra into discrete, well-behaved bands.

The new Q-measurement technique presented here is the comparison of frequency bands within the *same time interval* by spectrally balancing the frequency bands to approximate the

seismic section as it would appear before having undergone attenuation (if dispersion is ignored). The spectrally balanced section can then be compared with the original section to derive an estimate for attenuation

PART 5: TESTING WITH FIELD DATA

EUGENE ISLAND MULTI COMPONENT FIELD DATA

Ocean Bottom Cable (OBC) seismic data were obtained from Seitel Data Inc (Seitel) located in the Eugene Island area of the Gulf of Mexico. The OBC system deployed 4 receiver components, 3 orthogonal geophones plus 1 hydrophone. This data was processed to PP and PS stack volume reflection amplitudes by Seitel over the total area shown in Figure 5.1 (left).

Data for this project was acquired over the southern area (approximately 20 x 10 km) shown in Figure 5.1 (right) covering partly or fully blocks EI306 - 310, EI313 - 317 and EI328 - 332. The UTM coordinate ranges are approximately described by UTM Easting 618000 – 638000 and UTM northing of 3121000 – 3131000 (UTM zone 15).

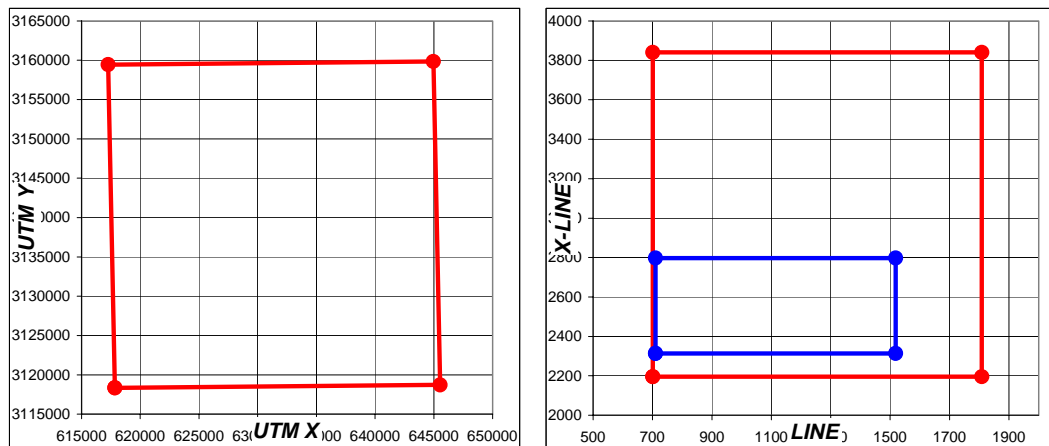


Figure 5.1. The total survey area - left panel in UTM coordinate space; the total survey area (red) and project area (blue) in seismic IN-LINE and X-LINE coordinate space.

The UTM coordinates were transformed to the seismic IN-LINE and X-LINE coordinates using the reference points shown in Table 5.1. This was done for ease of use in the seismic data visualization system and for attribute generation. The blue area (Figure 5.1) defining the seismic area is depicted by the points in Table 5.2.

These data were the principal data used for field testing although other data from other areas has been shown in prior chapters.

POINT	X	Y	IN-LINE	X-LINE
P1	617837.00	3118347.00	701	2196
P2	617259.01	3159443.00	701	3840
P3	644956.52	3159832.55	1809	3840
P4	645534.51	3118736.55	1809	2196

Table 5.1. The UTM X, Y coordinates and seismic IN-LINE, X-LINE coordinate reference points.

SEISMIC	IN-LINE	X-LINE
1	710	2314
2	1519	2314
3	1519	2797
4	710	2797

Table 5.2. The seismic coordinate reference points defining the blue rectangle in Figure 5.1.

WELL SELECTION

The blue area in Figure 5.1 was used to select well locations within the project area. We found 40 wells having a total depth (TD) greater than 10000 ft within this area, 13 of which were younger than 25 years (1980 or later) as shown in Figure 5.2. 10000 ft was chosen as the start of “deep” data zone.

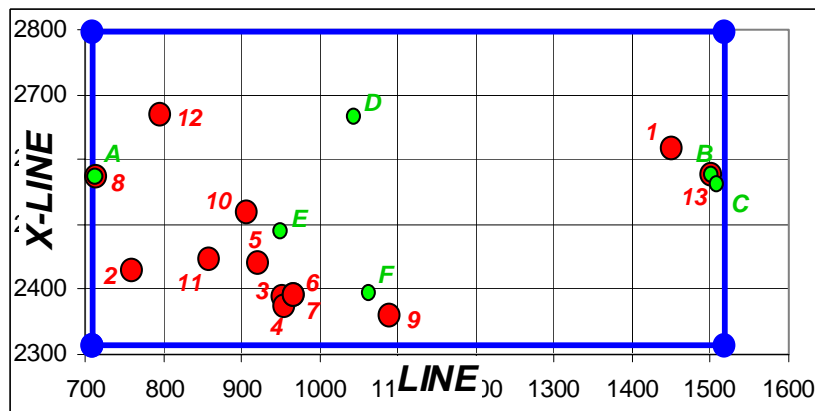


Figure 5.2. Bottom hole locations of the 13 youngest wells greater than 10000 ft TD within the seismic data area shown in red. Green wells are the velocity survey wells.

The well coordinates were given in latitude and longitude and these were converted to UTM X & Y (zone 15) using the CORPSCON software available from the Internet – see Corps of Engineers Coordinate System (Table 5.3).

We recommended using younger wells as the most likely to have more reliable log suites to use for attenuation model building.

API	DATE	TVDSS	UTMX	UTMY	IN-LINE	X-LINE	WELL
177104156100	7/19/2003	16573	636442	3129178	1451	2619	1
177104153401	1/4/2002	12614	619225	3124193	760	2429	2
177104139801	8/2/2000	11274	624059	3123277	953	2390	3
177104139800	1/24/1995	12535	624149	3122939	956	2376	4
177104139600	12/10/1994	11710	623251	3124548	921	2441	5
177104139301	10/22/1994	12163	624395	3123333	966	2392	6
177104139300	10/17/1994	12074	624429	3123356	967	2393	7
177104132700	12/3/1990	10253	618042	3127845	715	2576	8
177104131800	8/5/1990	11909	627480	3122607	1089	2361	9
177104108300	10/30/1984	10122	622885	3126511	907	2520	10
177104072300	4/5/1982	13043	621673	3124721	858	2449	11
177104097000	2/8/1982	10130	620052	3130196	796	2669	12
177104082000	1/27/1980	12921	637720	3128181	1502	2578	13

Table 5.3. Selected well names, bottom hole coordinates, and TD date.

These wells are the key wells used for the project.

VELOCITY SURVEYS

Velocity surveys were found for six wells in the seismic area (Table 5.4, Figure 5.2 wells A – F). Two of the velocity surveys match two of the wells selected by TD and date: well 8, velocity well A, and well 13, velocity well B.

The PP velocities from the velocity surveys were compared for general quality and consistency to establish a single velocity function over the seismic area to convert the well depths to seismic two-way PP time.

API	DATE	TVDSS	UTM X	UTM Y	IN-LINE	X-LINE	WELL
177104132700	12/3/1990	10253	618042	3127845	715	2576	A
177104082000	1/27/1980	12921	637720	3128181	1502	2578	B
177104047800	8/28/1975	10145	637872	3127806	1508	2563	C
177104045600	7/21/1975	9900	626222	3130207	1043	2666	D
177104021700	8/2/1973	11897	623992	3125833	951	2492	E
177104001800	3/18/1971	11005	626825	3123475	1063	2396	F

Table 5.4. Six velocity survey wells, bottom hole coordinates in seismic survey area.

Figure 5.3 shows an overall similar pattern in PP interval velocity V_p , but some wild data was seen in several wells. After a qualitative assessment of the velocity data it was concluded that wells A and D were quite noisy, wells C and E were marginal, while wells B and F were consistent and acceptable. Wells B and F were selected to compute the single velocity function.

The mid time between knees was used to plot the velocity data as the mid point of the interval pertaining to the interval velocity computed from the velocity survey.

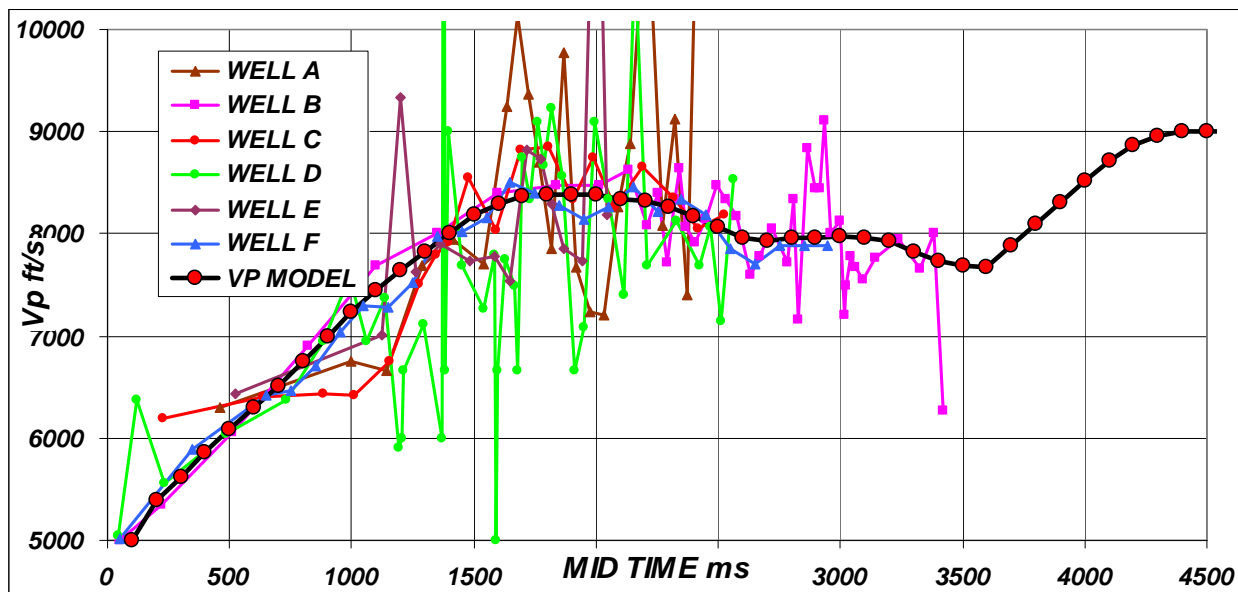


Figure 5.3. Velocity surveys – computed interval PP velocity versus mid time between survey depth locations. The velocity model computed from Velocity surveys B, F averaged, smoothed, and resampled to 100 ms.

In spite of the noisy velocity data it was seen that the overall similar interval velocities would produce a time to depth curve that would not vary greatly over the seismic survey area. Therefore a single function is proposed for the project area.

The interval velocities from wells B and F were re-sampled to 2 ms sample rate, smoothed over a 400 ms running window, then resampled to 100 ms to define the model for PP and PS travel times (see red points in Figure 5.3).

Note that after approximately 1500 ms two-way time, the interval velocity measures approximately 8000 ft/s. The cause is interpreted to be over-pressured rocks, and should this over-pressure condition continue past 15000 ft, then the shale would likely be “soft” compared to the gas sand matrix.

P-WAVE VELOCITY AT DEPTH

The deepest well TD is about 3500 ms PP time, but the target times are greater than 4000 ms and we would like to understand if the shale rock encasing the gas sands is over-pressured.

Consider a layer thickness d and velocities defines by v , total one-way travel time from surface is T and within the layer given by t and subscript p and s representing pressure and shear modes, respectively. We consider two sections, the first with two-way travel times using P velocity, and the second section one-way down going using P wave velocity and one-way up going using S wave velocity. We can express these as -

$$T_{pN} = \sum_{n=1}^N \frac{d_n}{v_{pn}}, \text{ and} \tag{5.1a}$$

$$T_{sN} = \sum_{n=1}^N \frac{d_n}{v_{sn}}. \tag{5.1b}$$

Then define the PP and PS time to the next layer top as

$$T_{pp(N+1)} = T_{ppN} + 2.dn/V_{pn} \tag{5.2a}$$

$$T_{ps(N+1)} = T_{psN} + dn/V_{pn} + dn/V_{sn}, \tag{5.2b}$$

from which

$$V_{pn} = 2.dn/(T_{pp(N+1)} - T_{ppN}) \tag{5.3a}$$

$$V_{sn} = dn/\{(T_{ps(N+1)} - T_{psN}) - (T_{pp(N+1)} - T_{ppN})/2\}, \tag{5.3b}$$

and the velocity ratio is

$$V_{pn}/V_{sn} = 2(T_{ps(N+1)} - T_{psN})/(T_{pp(N+1)} - T_{ppN}) - 1. \tag{5.4}$$

If the upper time is taken as zero then Equation (5.4) reverts to Equation (5.5)

$$V_p/V_s = 2.T_{ps}/T_{pp} - 1. \tag{5.5}$$

A number of observation points were obtained for PP and PS seismic times by interpreting the same event in both volumes in the data area. The observation events were chosen as carefully as possible through out the volumes by selecting more discrete events to improve the accuracy of the times.

These times were used to compute the local V_p/V_s ratio according to Equation (5.4) and are shown in Figure 5.4. At depth, the local V_p/V_s ratio was approximately 2.3, and using the right panel of Figure 5.4, predicts a p-wave velocity of about 9000 ft/s.

The Castagna mud rock line (MRL) was used to predict the shear velocity from the V_p interval velocity model, assuming this shear velocity predictor is valid in over-pressured rock.

$$V_s = aV_p + b, \tag{5.6}$$

where $a = 0.862$, $b = -3846$ ft/s, shown as the red curve in Figure 5.4.

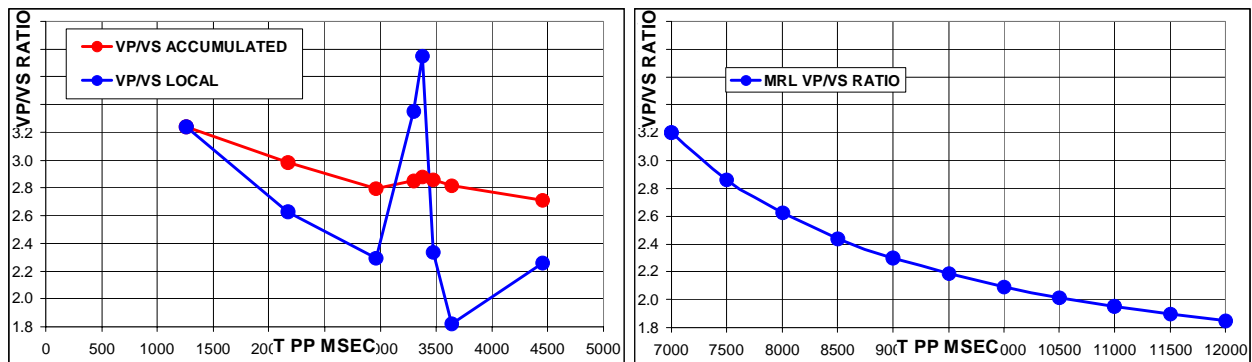


Figure 5.4. Left panel — V_p/V_s ratio from observations points (blue). Right panel — V_p/V_s ratio from Castagna’s mud rock line.

This method is quite sensitive to the ratio computation but gives an indication that the deeper rock is still over-pressured although not as much as shown in Figure 5.3. The model was extended to depth as shown by the model velocity of 9000 ft/s at 4500 ms PP time. More observation points would provide greater statistics to the process, but the principle remains the same.

STACKED SEISMIC DATA INSPECTION

To review the seismic data, two traverses were made through the volumes. Their locations are shown in Figure 5.5, and were focused on the central wells in the area.

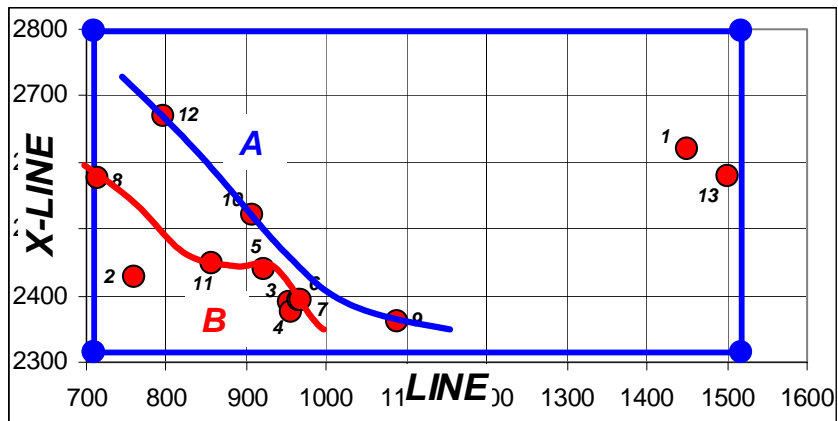


Figure 5.5. Approximate locations of Traverses A and B.

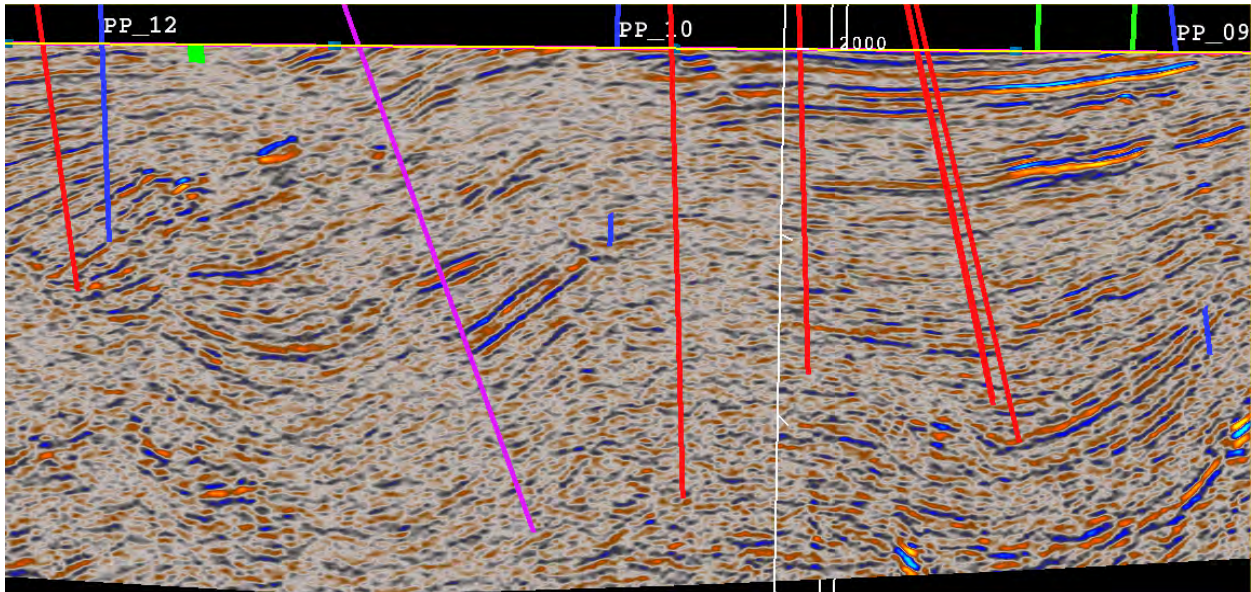


Figure 5.6a. Traverse A – PP seismic amplitude data looking NE, blue wells define traverse; red and magenta wells are in foreground, green in background.

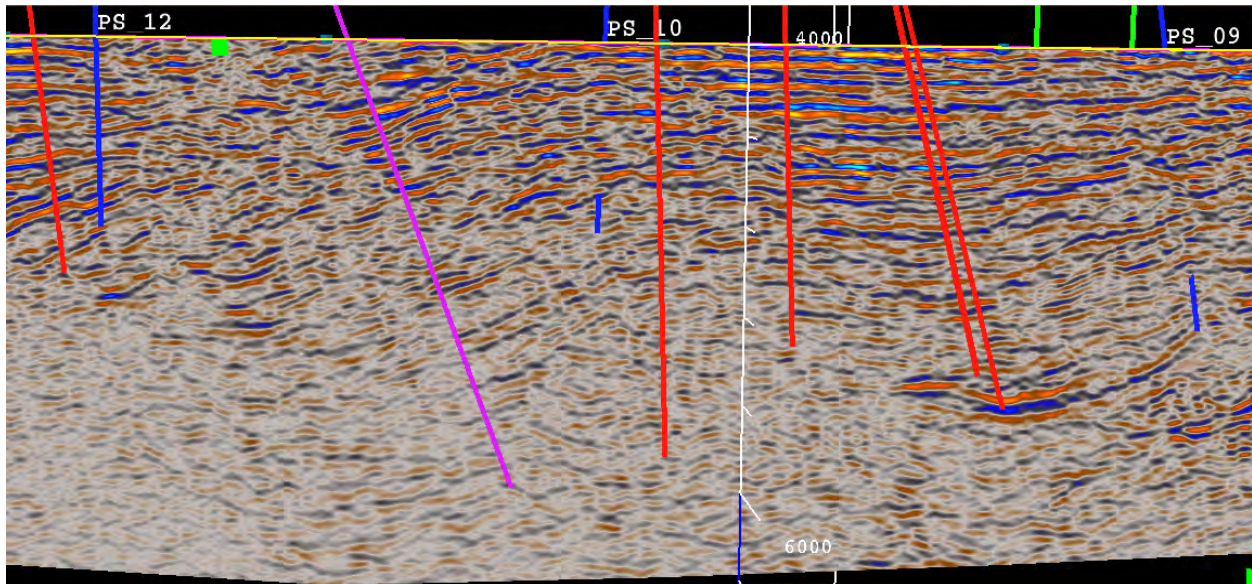


Figure 5.6b. Traverse A – PS seismic amplitude data looking NE, blue wells define traverse; red and magenta wells are in foreground, green in background.

Figure 5.6a covered 2.0 – 4.0 sec two-way seismic time at 1.0 vertical scale and Figure 5.6b covered 4.0 – 8.0 sec two-way time at 0.5 vertical scale. Figure 5.7a covered 2.0 – 4.0 sec two-way seismic time at 0.5 vertical scale and Figure 5.7b covered 4.0 – 8.0 sec two-way time at 0.5 vertical scale.

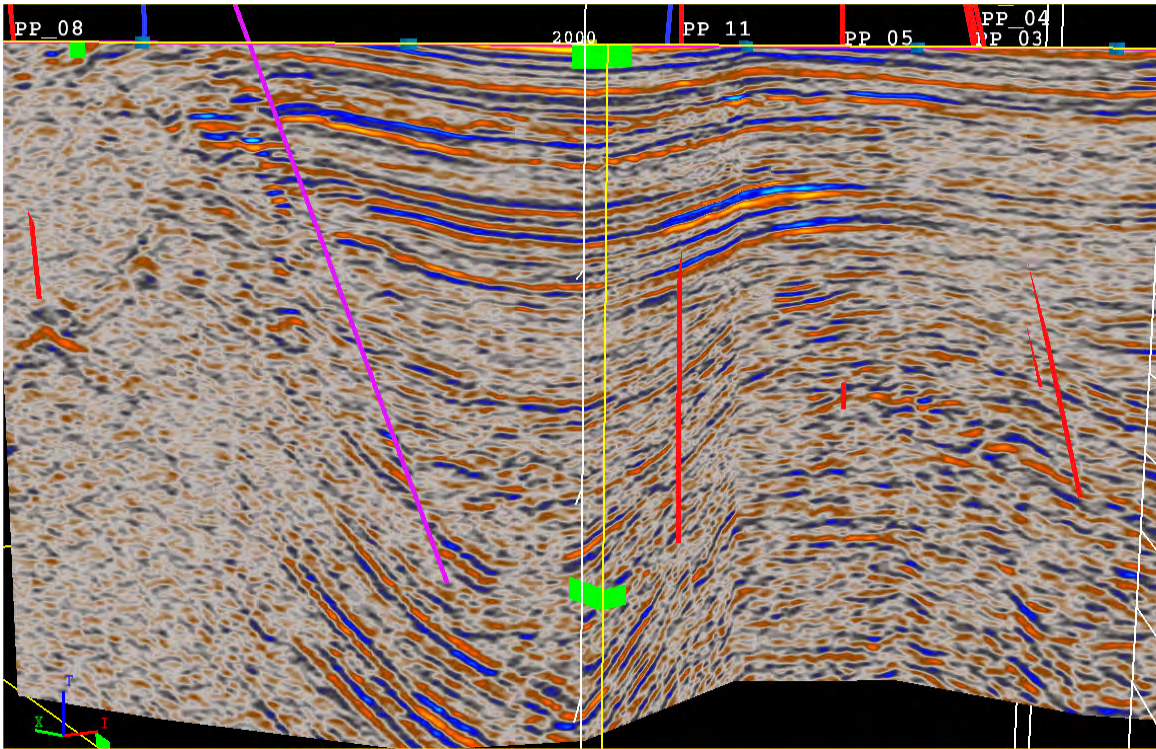


Figure 5.7a. Traverse B – PP seismic amplitude data looking NE, blue wells define traverse; red and magenta wells are in foreground, green in background.

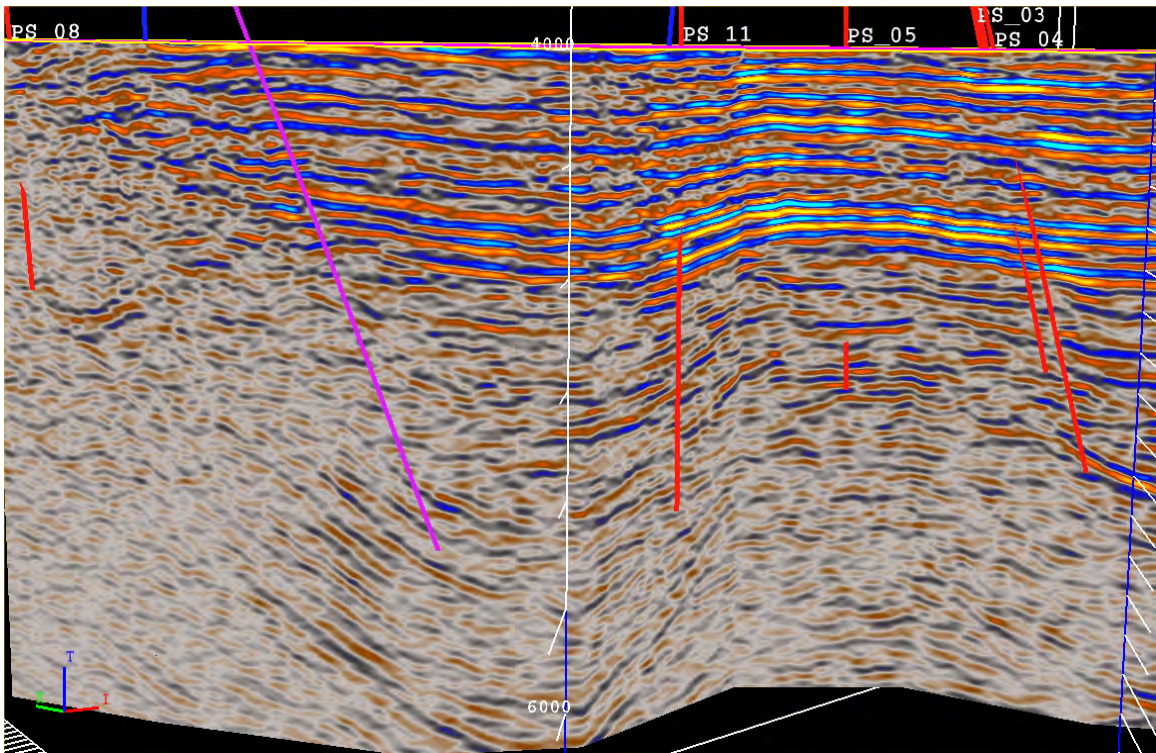


Figure 5.7b. Traverse B – PS seismic amplitude data looking NE, blue wells define traverse; red and magenta wells are in foreground, green in background.

The seismic traverses indicate a high degree of lateral variation in the deep event signal, and continuity. Also the deeper structures partially exhibit high structural dip – this means that the seismic imaging process is important if the PS events are to align with the PP events.

Reasonably spatially continuous seismic data is evident down to about 4 sec PP two-way time but not always present down to approximately 8 sec PS two-way time. The best deep data is located in the South Western quadrant of the survey area, along with four commercial status wells. “Best data” is defined by the presence of deep (after 4 sec PP time) reflections on both PP and PS sections.

An estimate of the deep P-wave velocity data indicated that the rocks within the zone 4.0 – 4.5 sec PP time exhibit some over-pressure, but not as great as between 2.5-3.5 sec PP time.

WELL LOG DATA AND ROCK PHYSICS MODELING

Studying the log data from Table 3 indicated 4 wells with commercial status in our study area. The four wells are located in the Western half of the survey area and the seismic data in this area shows the most promising deep events. Logs for these wells were obtained from MMS, however the log suites are not complete as shown by the key log curves in Table 5.5.

API OUT	WELL	BULK	P-WAVE	S-WAVE	NEUTRON
	NUM	DENSITY	VELOCITY	VELOCITY	POROSITY
177104153401	2	NO	YES	YES	NO
177104132700	8	YES	YES	NO	YES
177104131800	9	NO	YES	NO	NO
177104108300	10	YES	NO	NO	NO

Table 5.5. Wells with commercial status and acceptable log suites.

The key well log curves are displayed in Figure 5.8. The data from depth below 15,000 ft are available only in well #2. We observe that the character of P- and S-wave velocity does not change with depth, likely due to the lack of compaction caused by over-pressure. This fact means that the relations established at a shallow depth are possibly applicable at the target depths below 15,000 ft, although sand cementation cannot be ruled out.

ROCK PHYSICS MODEL

Following this assumption, we established a rock physics model and the corresponding transforms that are likely to be applicable to the seismic data under examination. To accomplish this we used the data from well #8 to establish a velocity-porosity-lithology transform and then the P- and S-wave data from well #2 to establish a P-to-S-wave velocity transform.

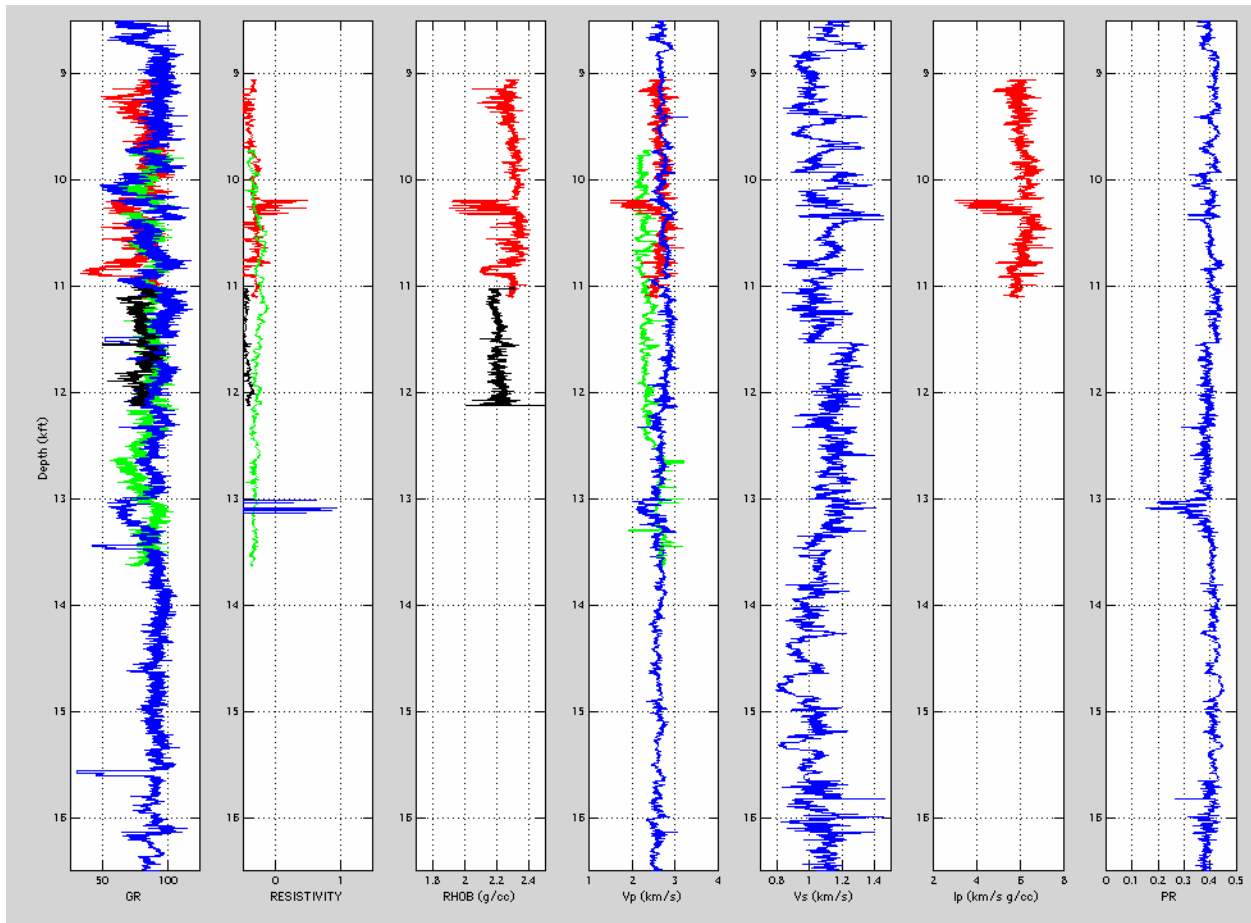


Figure 5.8. Log data display for the four wells under examination. From left to right: GR; resistivity (decimal logarithm); bulk density; P-wave velocity; S-wave velocity; P-wave impedance; and Poisson's ratio. The color-code is: blue for well # 2; red for well # 8; green for well # 9; and black for well # 10.

The gas saturation in well # 8 was calculated from the resistivity curve while the clay content was estimated by linearly scaling the gamma-ray curve between its minimum and maximum values. It was assumed that the formation water has the bulk modulus 2.85 GPa and density 1.01 g/cc while the gas has bulk modulus 0.14 GPa and density 0.26 g/cc. The total porosity was

calculated from the bulk density by assuming that the density tool samples the virgin formation with gas saturation as calculated from resistivity.

The measured impedance and P-wave velocity are compared to the curves due to the uncemented (soft-sand) model. The proximity of the data and model (yellow curves in Figure 5.9) indicates that this model is appropriate for the well under examination. This model was then used to predict the S-wave velocity (absent in the measured data) from the P-wave velocity.

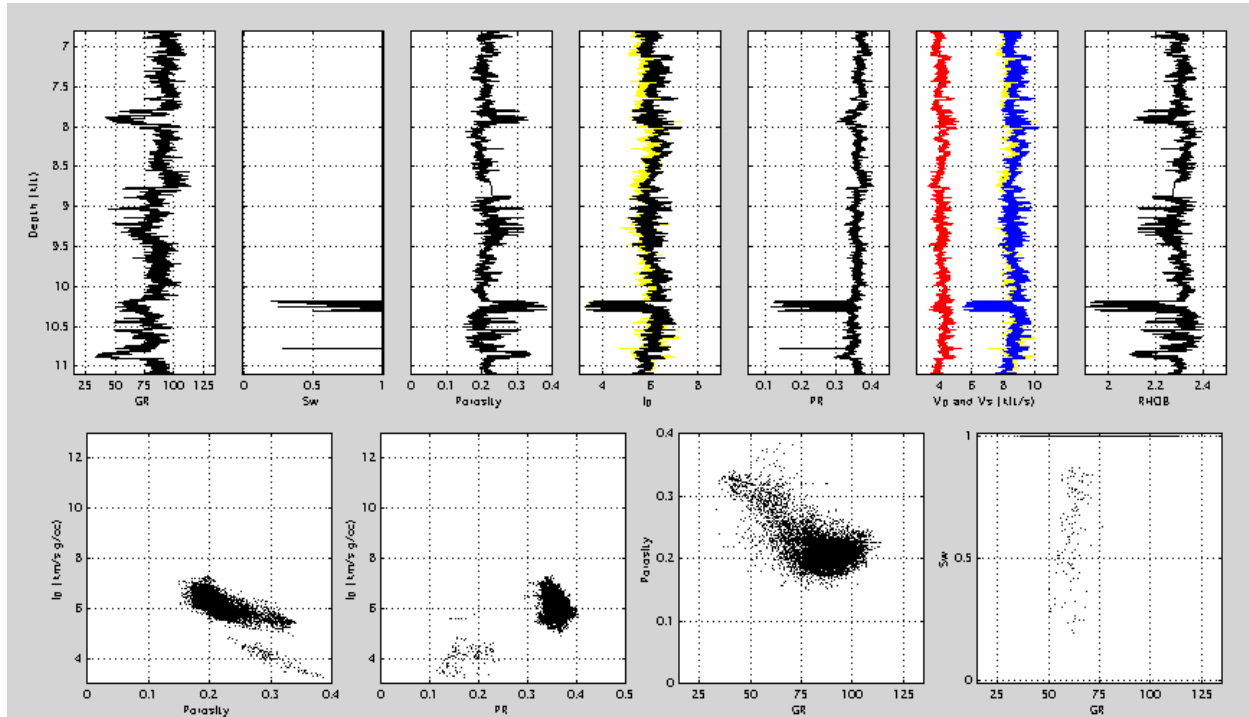


Figure 5.9. Log data display for well # 8. Top, from left to right — gamma-ray; water saturation; total porosity; P-wave impedance; Poisson’s ratio (predicted); P- and S-wave (predicted) velocity; and bulk density. Bottom, from left to right — impedance versus porosity; impedance versus Poisson’s ratio; porosity versus gamma-ray; and water saturation versus gamma-ray. The yellow curves superimposed upon the data in the impedance and velocity frames in the top row are calculated from the soft-sand model using the porosity and clay as well as the pore-fluid properties as inputs.

The in-situ impedance is plotted versus the total porosity and Poisson’s ratio (PR) in Figure 5.10 where the data are color-coded by gamma-ray and by water saturation. Similar cross-plots are shown in Figure 5.11, but for wet conditions where the elastic properties and density were calculated using the P-wave-only fluid substitution. The soft-sand model curves for water-

saturated rock are superimposed upon the wet-condition data to further emphasize the relevance of this model. The curves are produced for varying porosity and each for a fixed clay content. The latter variable changes from one to zero with step 0.2.

These model curves fully encompass the well log data and the data supports the soft sand rock physics model.

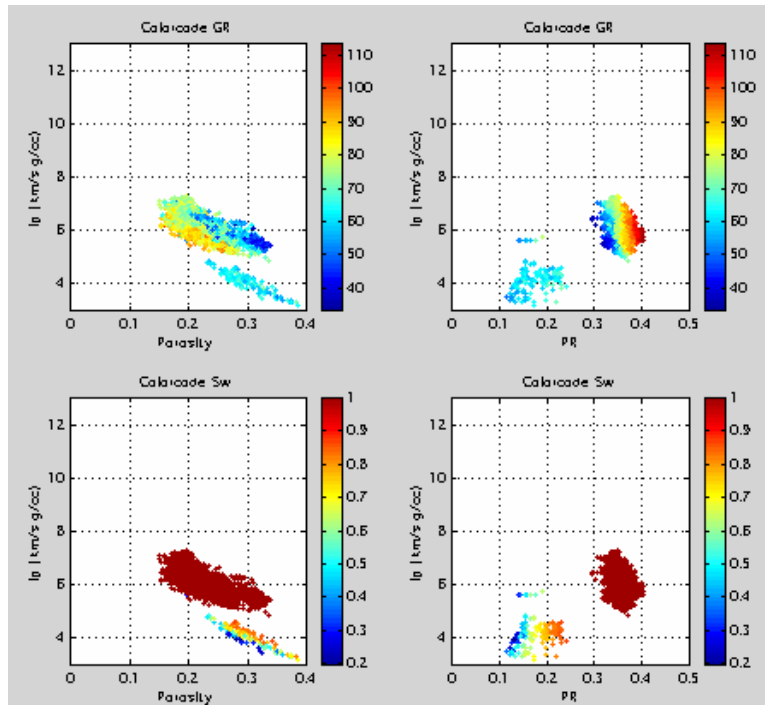


Figure 5.10. Well # 8. Impedance versus porosity (left) and versus Poisson's ratio (right). The data in the top row are color-coded by GR while that in the bottom row are color-coded by water saturation. In situ data.

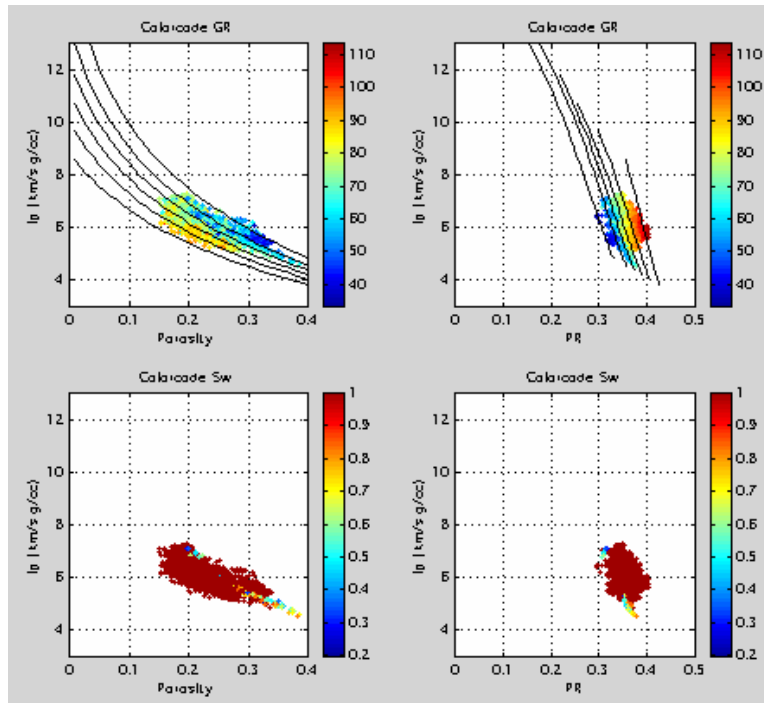


Figure 5.11. Well # 8. Same as Figure 3 but for wet conditions. The model curves in the top row are from the soft-sand model for clay content varying from one (top curve in the impedance-porosity display and left-most curve in the impedance-PR display) to zero with step 0.2.

The summary of the impedance-porosity transforms and P-to-S transforms is shown in Figure 5.12. We observe that the impedance-porosity transform for gas sand spans a fairly narrow band for the clay content between zero and 20%. This sand will be identified by its low Poisson’s ratio which is distinctively smaller than that in the shale and/or wet sand.

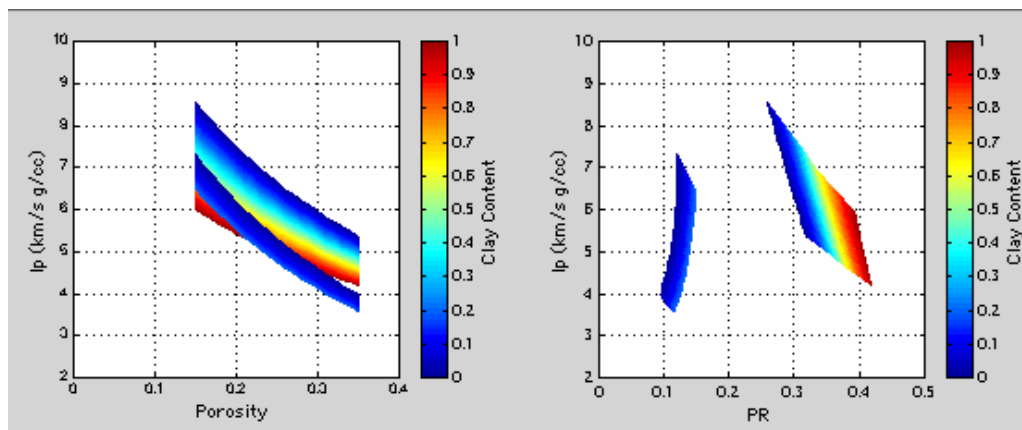


Figure 5.12: Impedance-porosity (left) and impedance-Poisson’s ratio (right) transforms from the soft-sand rock physics model. The multi-color stripes are for wet rock with clay content between zero and 100%. The dark-blue stripes are for gas sand with clay content between zero and 20%.

P-TO-S TRANSFORM

The P- and S-wave velocity as well as the velocity ratio and Poisson’s ratio for well #2 are shown in Figure 5.13. The green curves in this figure are from the Mud-rock transform.

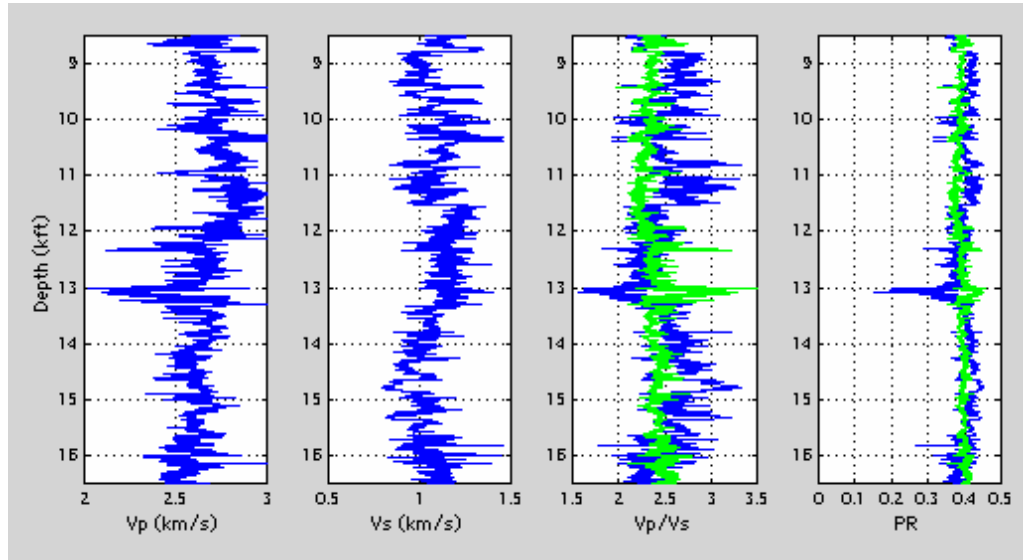


Figure 5.13: Well #2. Velocity, velocity ratio, and Poisson’s ratio versus depth. Green curves are from the Mud rock transform.

Typically, this transform provides the upper bound for Poisson’s ratio in clastic sediment. We observe, however, that the measured Poisson’s ratio exceeds that predicted by the Mud-rock transform.

Figure 5.14 displays the V_p/V_s ratio versus V_p for well #2. Superimposed upon this cross-plot are the model lines from the rock physics model established earlier as well as the Mud-rock curve for wet sediment and the Greenberg-Castagna transform for sand with gas. We observe reasonable proximity of our model curves to the Mud-rock and Greenberg-Castagna transforms. Some of the data fall above the Mud-rock line. Our conclusion is that it is likely that the measured Poisson’s ratio is unrealistically large and our rock physics model can still be applicable for the purpose of seismic interpretation.

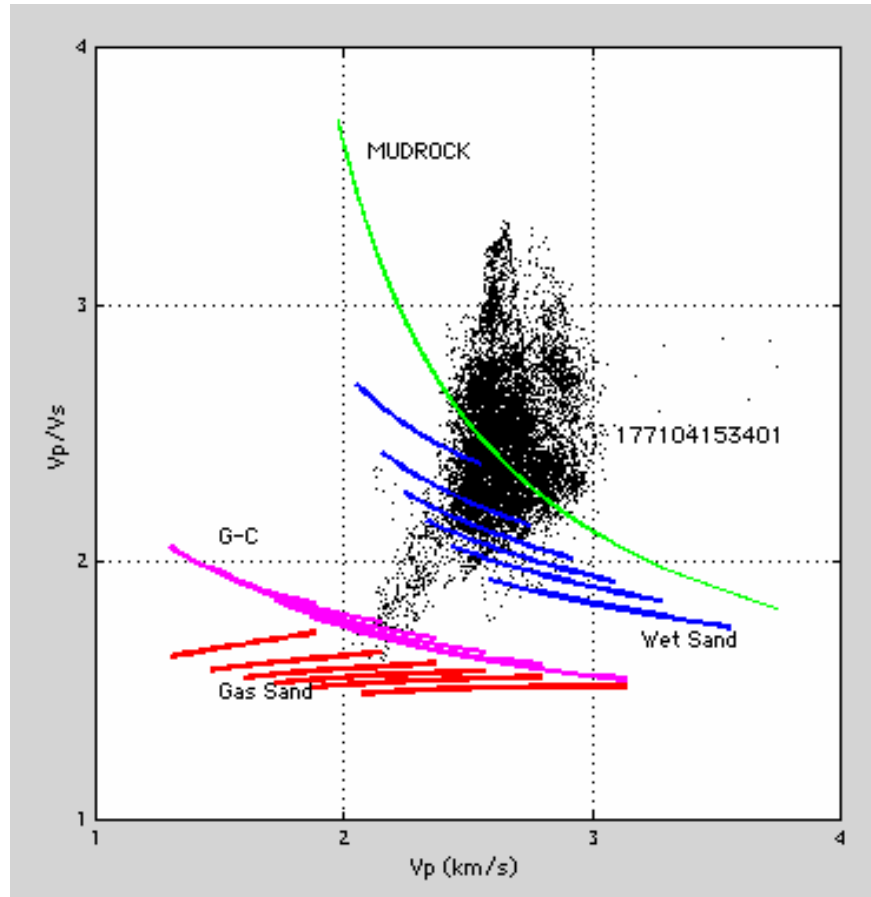


Figure 5.14. Well # 2. V_p/V_s ratio versus V_p (black symbols). Wet sediment (blue) and gas sediment (red) transforms according to the soft-sand model. The Mud-rock transform (green) for wet sediment and Greenberg-Castagna transform for gas sediment (magenta).

ATTENUATION MODELING

The results of P- and S-wave attenuation modeling indicate that the P-wave inverse quality factor (Q_p^{-1}) is only significant in the gas reservoir and small elsewhere (Figures 5.15, 5.16). The inverse S-wave quality factor (Q_s^{-1}) is small everywhere in the interval and close to Q_p^{-1} as calculated in wet rock.

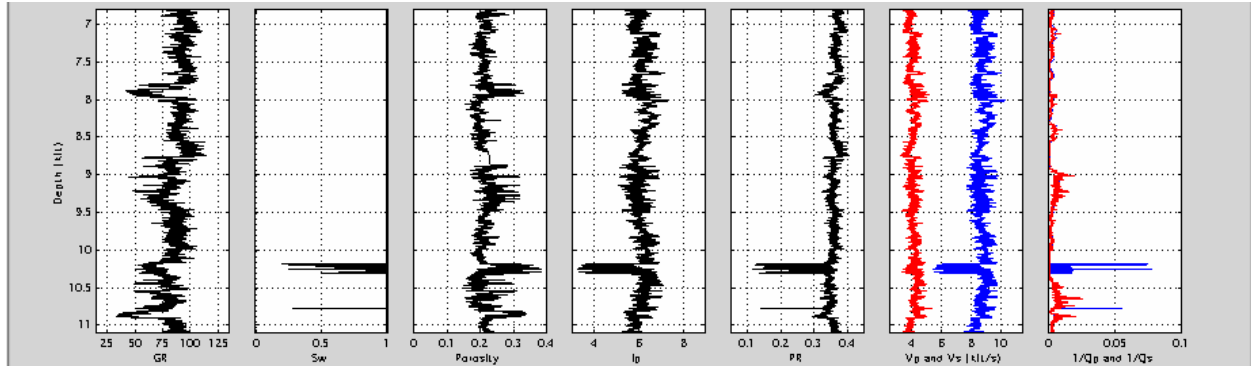


Figure 5.15. Well # 8 log display with the inverse quality factor shown in the last frame (P in blue and S in red).

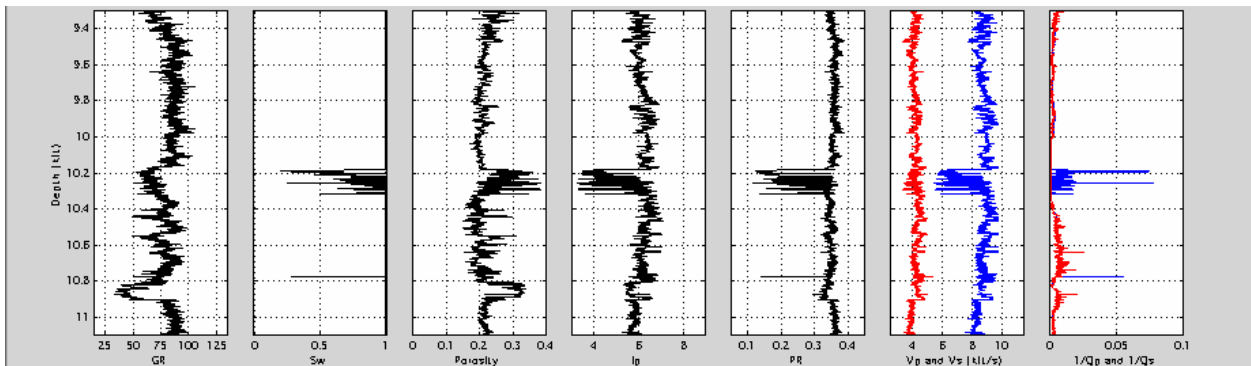


Figure 5.16. Same as Figure 5.15, zoomed on the bottom part of the well.

Figure 5.17 displays the ratio of the P-to-S inverse quality factors (Q_p^{-1}/Q_s^{-1}) plotted versus the P-to-S-wave velocity ratio (V_p/V_s) and color-coded by water saturation (S_w). This cross-plot is for the in-situ conditions.

The low V_p/V_s is typical of gas sand where Q_p^{-1}/Q_s^{-1} is coincidentally large. Therefore, these attributes as well as their hybrids, when extracted from seismic data, may serve as hydrocarbon indicators.

Notice that for the wet low-gamma-ray sand in the bottom part of the well Q_p^{-1}/Q_s^{-1} is small although the V_p/V_s (and PR) contrast between this sand and surrounding shale is negative (but not as strong as in the gas sand). This negative contrast may still produce an AVO anomaly that can be mistakenly attributed to a gas reservoir (Figure 5.18). Under such circumstances, the attenuation ratio (Q_p^{-1}/Q_s^{-1}) may serve as a unique hydrocarbon indicator.

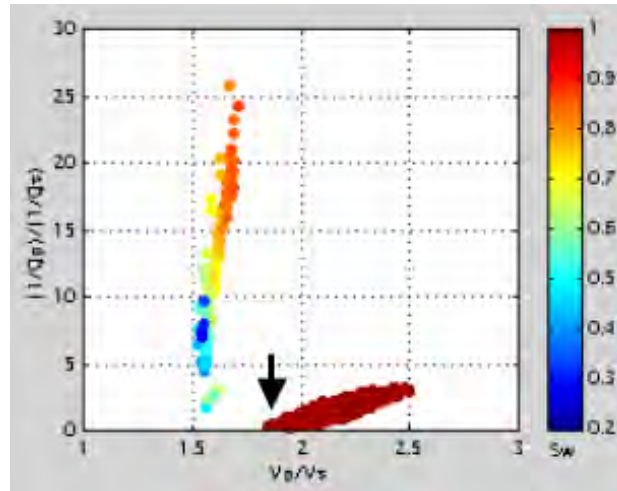


Figure 5.17. Inverse quality factor ratio versus velocity ratio from Figure 5.15 color-coded by water saturation. The arrow points to the data for the two wet sand intervals located just above 8 and 11 kft (see GR track in Figure 5.15).

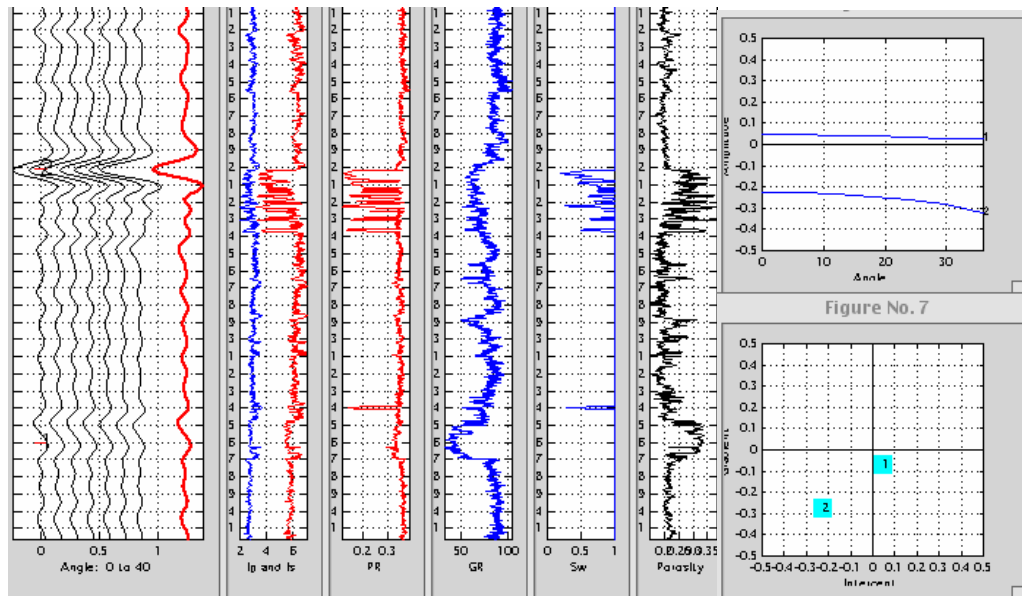


Figure 5.18. Synthetic seismic traces (40 Hz) in the bottom part of the well showing that the wet sand (pick “1” on the gather) may exhibit a negative gradient, although not as strong as gas sand (pick “2” on the gather). From left to right – gather (black) and stack (red); P- and S-wave impedance; Poisson’s ratio; GR; water saturation; and porosity. The AVO curves and gradient-versus-intercept plots are at the picks shown in numbers on the gather display.

SYNTHETIC SEISMIC MODELING WITH ATTENUATION

A synthetic seismic ray-tracer has been created specifically for this project to estimate the effects of the elastic rock properties and attenuation on the seismic amplitude and attributes. The ray-tracer produces P-to-P as well as P-to-S (converted shear) gathers. The algorithm takes into account both P- and S-wave attenuation by means of a Q -filter.

Synthetic Modeling

The results of synthetic seismic modeling with and without taking attenuation into account are displayed in Figures 5.19 and 5.20.

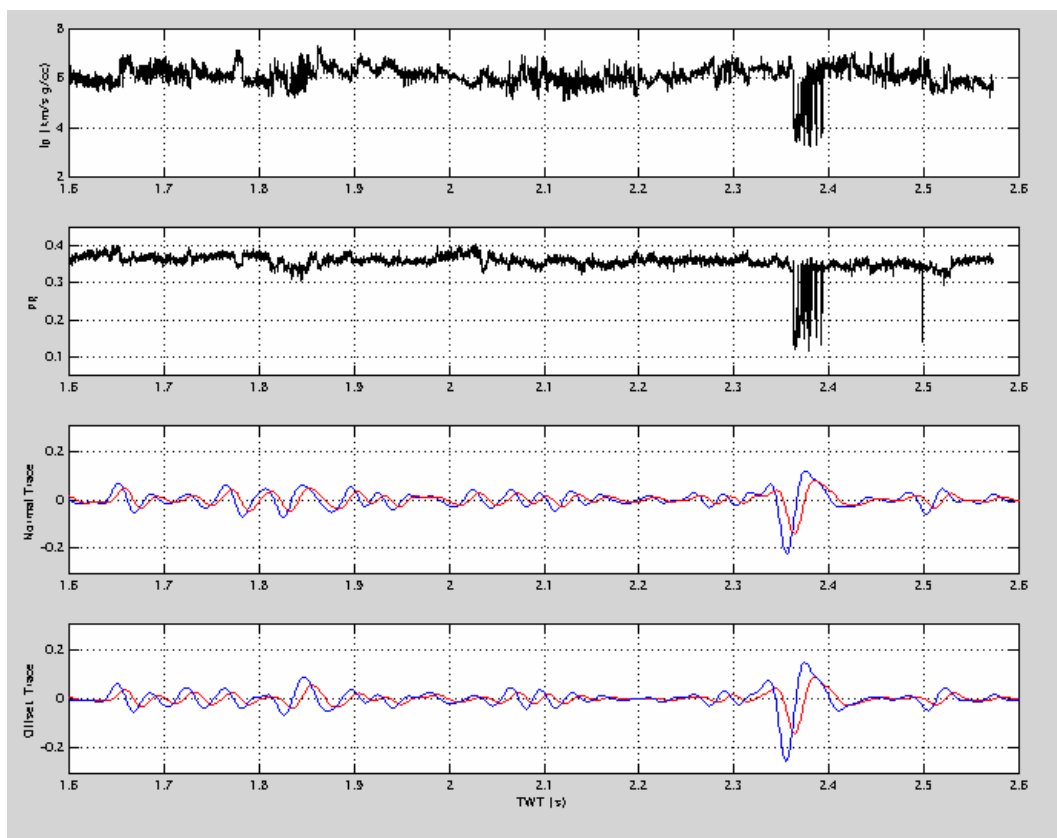


Figure 5.19. Synthetic ray-tracer modeling at 40 Hz. For P-to-P reflection. From top to bottom – impedance; PR; normal-incidence trace; and offset trace versus P-wave TWT. The blue traces in the bottom two frames are calculated without attenuation, while the red traces are calculated with taking the P-wave attenuation into account.

The P-to-P amplitude (Figure 5.19) is noticeably affected by the attenuation for both normal incident and offset traces. This result implies that the P-wave attenuation (Q_p^{-1}) can be extracted from real seismic data.

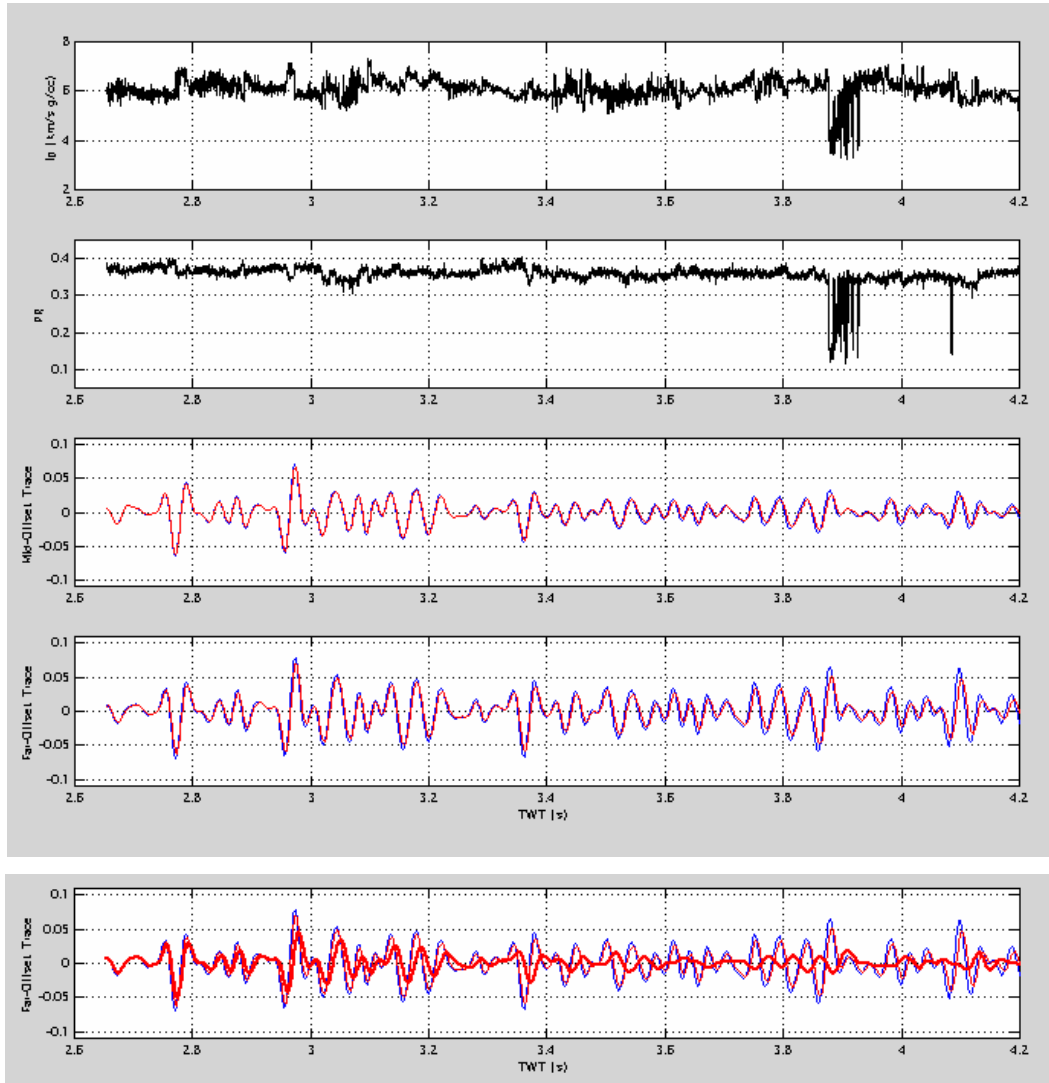


Figure 5.20. Same as Figure 5.8, but for P-to-S reflections. The red traces are calculated with taking the P- and S-wave attenuation into account. The separate frame at the bottom also displays the far-offset trace calculated for the S-wave attenuation ten times as that predicted by the rock physics model (bold red trace).

The converted-wave (P-to-S) traces in Figure 5.20 reflect the fact that the S-wave attenuation is small – the synthetic amplitude computed with attenuation is not very different from that computed without attenuation. To test whether Q_s^{-1} indeed affects the converted-wave amplitude

in this synthetic modeling, we compute a far-offset trace with Q_s^{-1} ten times that predicted by our rock physics modeling (Figure 5.20, separate frame at the bottom). The apparent effect of attenuation on the amplitude is large which means that the S-wave attenuation (Q_s^{-1}) can be extracted from real seismic converted-wave data.

PRE-STACK PP SEISMIC GATHER REVIEW

The PP gathers (pre-stack time migrated) obtained from Seitel Data were reviewed for deep events (e.g., Figures 5.6 and 5.7). The gather data provided covered the area defined by data ranges of INLINE 711 – 1075, 2 and XLINE 2306 – 2482, 1. Note the INLINES have an increment of 2.

An initial inspection of the gathers was conducted to examine the quality of the data. The gathers had been corrected for NMO so therefore the primary events were relatively “flat” across the gather offsets. The offset range was regularized by the migration process to provide an offset range of 375 – 5925, 150 m and giving a maximum fold of 38.

A DIPSCAN process was used to attenuate some of the noise present in the gathers. This is a multi channel process using 3 x 3 gathers that scans the events over a supplied dip range to find the optimum dip that maximizes the stack response after which the data is stacked along the optimum dip.

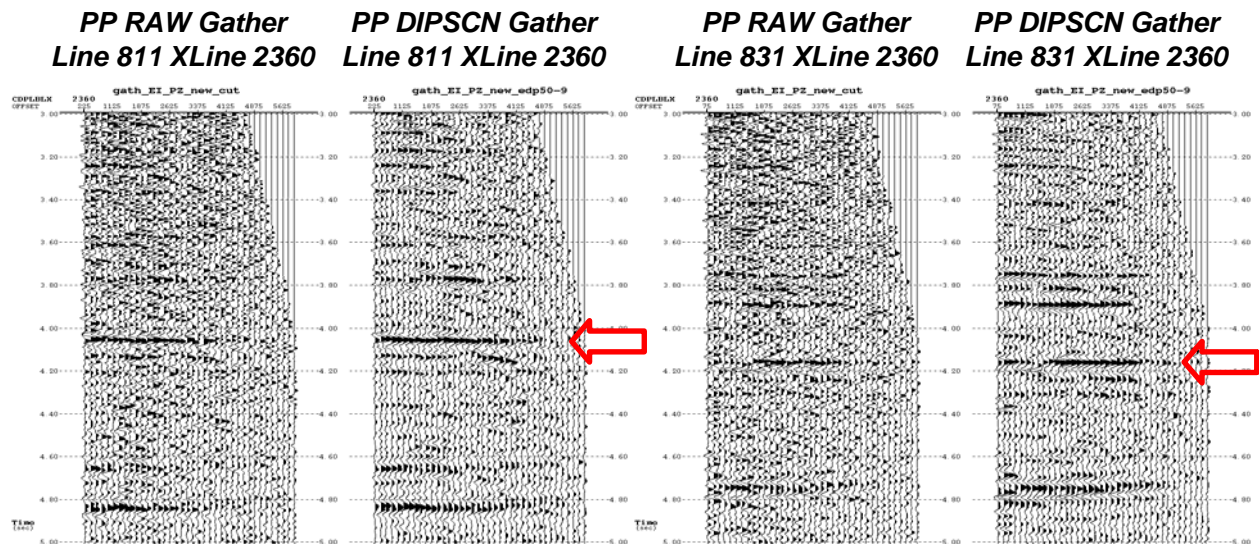


Figure 5.21. RAW and DIPSCAN PP gathers for LINES 811, 831 along XLINE 2360.

The gather displays in Figure 5.21 show the RAW data (left) as supplied and the result of the DIPSCAN process (right). The level of noise attenuation from the DIPSCAN process is clearly seen comparing the right panel to the left panel. This process, therefore, cleans up the gathers to the point where we can visually assess their quality and decide on a path forward.

In assessing the reflectors in Figure 5.21, we first observe that the deep events appear to reduce their signal response after approximately 2/3 of the maximum offset – i.e. after about 4000 m offset. This most likely would pose a problem for elastic attribute analysis techniques. In addition, multiples can clearly be seen in the data, thus implying that multiple-energy removal will be needed before these gathers can be used for elastic attribute analysis.

The high amplitude event marked by the red arrows corresponds to the deep event seen just above 4.2 sec in Figure 5.25. This represents a peak event seen as a gold colored peak on the stack section (Figure 5.22). The gather black peak event and the stack gold peak event align correctly shown.

Note that the polarity and phase of the PP data were not verified in this study. This would be needed using well log data before attempting to validate potential gas sand events from elastic attributes such as AVO or impedance inversion. However, frequency attributes are phase-insensitive, thus it is not required that seismic phase be known prior to performing attenuation estimation.

Therefore, it is apparent from Figure 5.21 that AVO or pre-stack simultaneous inversion would be hard-pressed to extract relevant information from these gathers at this depth. But if the PP AVO data quality is not acceptable at depth, then frequency-based attenuation attributes offer a good alternative to screen for deep gas potential.

TEMPORAL REGISTRATION OF PS TO PP SEISMIC DATA

The registration of PS data to PP data is obligatory when physical combination of attributes is desired. For example, within this project a relationship previously reported between Q_{pp} , Q_p was established to derive Q_s and hence Q_p/Q_s ratio by computation.

We have applied the process developed by Sergey Fomel from BEG. It uses “nails” to provide a starting point prior to performing correlation scanning to fine tune the registration both laterally and temporally.

Initial tests used a small number of “nails” obtained by examining the PP and PS stack volumes. Further to this initial test, we used a larger number of registration points obtained from compatible surfaces interpreted from the PP and PS volumes.

The SW corner of the survey area has some deep structural events located at approximately 3800 ms on PP and 7200 ms on PS stack data as shown in Figure 5.22. These events are the deepest found that were reasonably extensive. The target events can be seen just below the picked events. The surfaces were interpreted using a visualization seed picker snapped to the maximum amplitude and about 8000 points obtained per surface.

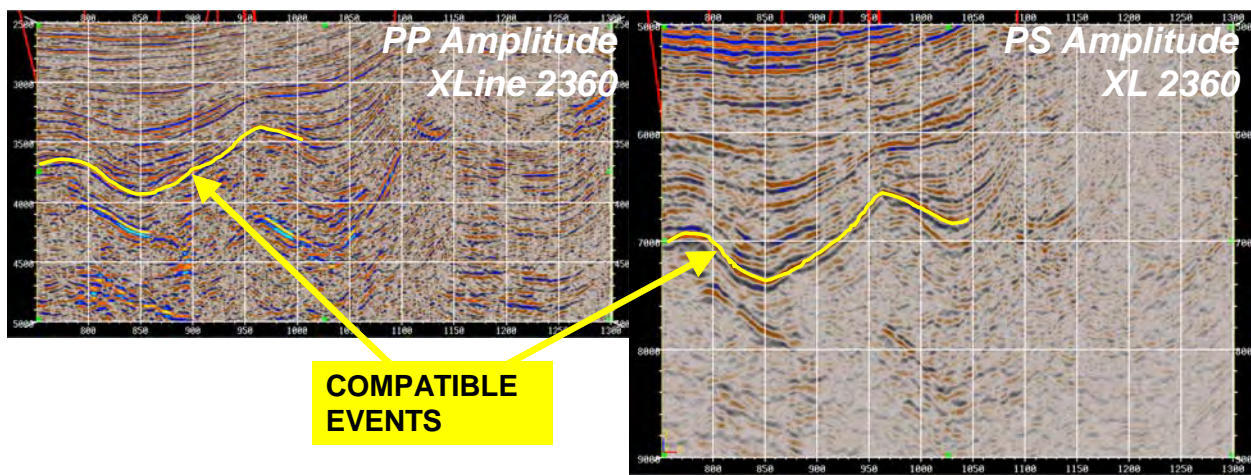


Figure 5.22. PP and PS compatible deep events.

The surface points picked in Figure 5.23 were co-located and only those pairs of times having common locations were used to establish the “nail” reference points.

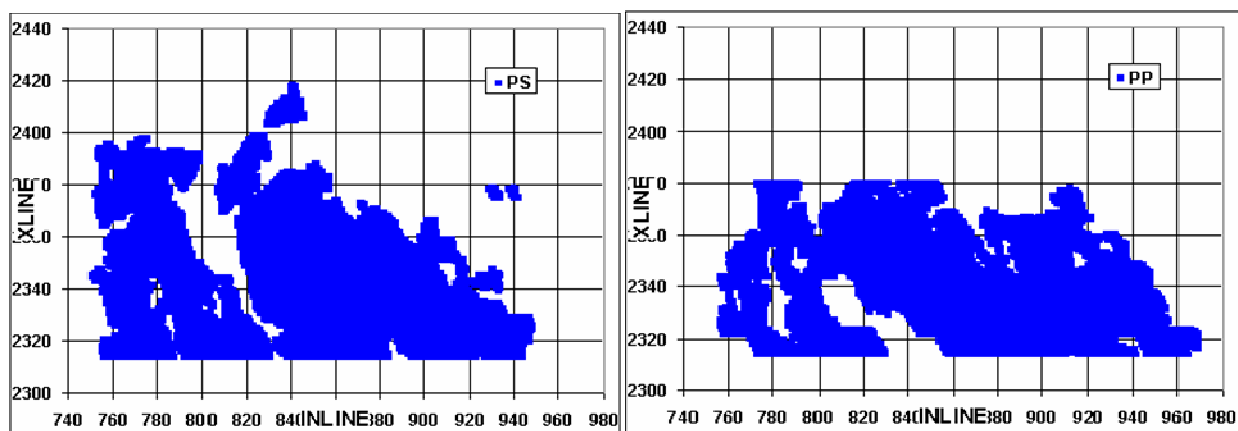


Figure 5.23. PS (left) and PP (right) surface points.

The plot of PS time versus PP time in Figure 5.24 shows a tight relationship with about 50 ms of range exhibited by both PS and PP time over the range of the surfaces. The function describing this trend could be used as a set of “nails” and the correlation run over not much more than +/- 50 ms about this trend. The log trend function shown is just an example of any that can be found. Also, the trend function can be used to extrapolate to deeper times – say to 5 sec PP time - and used as “nails” deeper than the surface times shown.

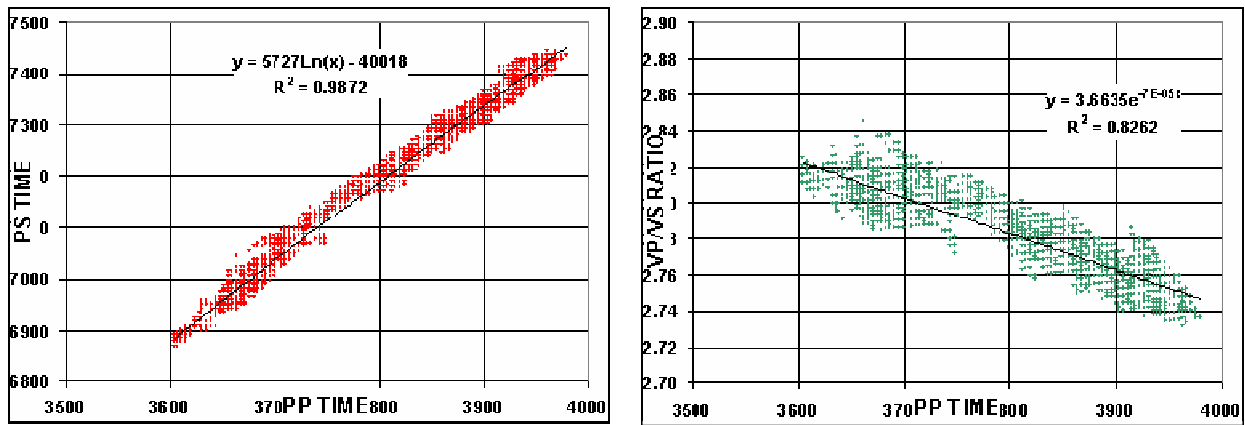


Figure 5.24. PS time vs. PP time (left) and effective Vp/Vs vs. PP time (right).

The effective Vp/Vs ratio was computed from Equation (5.5). Figure 5.24 (left) shows that the time trend slope changes at about 3750 ms PP time, small but noticeable, such that an alternative is two linear trends within this range of times. Deeper extrapolation would be better preserved using the log trend. Instead of using trends, the actual relationship could be used at each CMP location.

Figure 5.24 (right) shows the effective Vp/Vs ratio that is the ratio down to the PP time, and is used as a QC of the method. In future, the ratio could be plotted on the surface and spatially smoothed.

PS TO PP REGISTRATION RESULTS

Sergey Fomel tested his method using data from a subset area in the SW of the project area defined by INLINES 710 – 1110, XLINES 2320 - 2420. The white and yellow target events are

shown by the matching depths of the ellipses in the PP data (Figure 5.25) and the PS data (Figure 5.26). The effective V_p/V_s ratio calculated during the registration is shown in Figure 5.27.

Having demonstrated the feasibility of PP/PS registration, we moved on to Q estimation of both volumes (see next section). That work demonstrated that the PS data was not needed, so no further work in this area was performed during the course of this project.

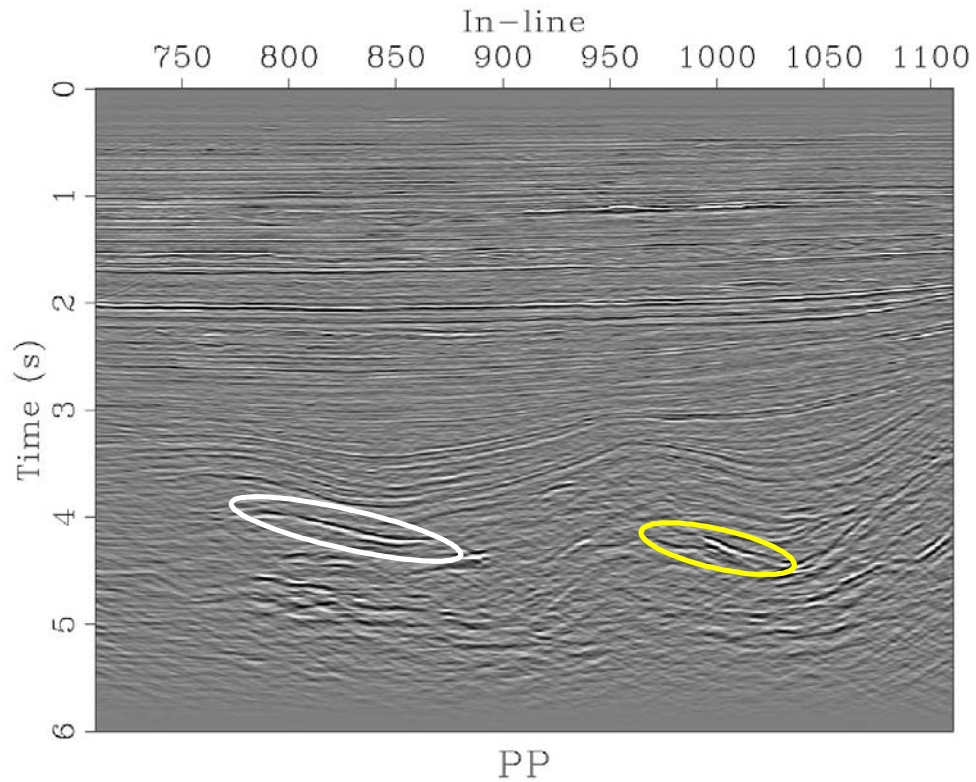


Figure 5.25. PP data input to registration.

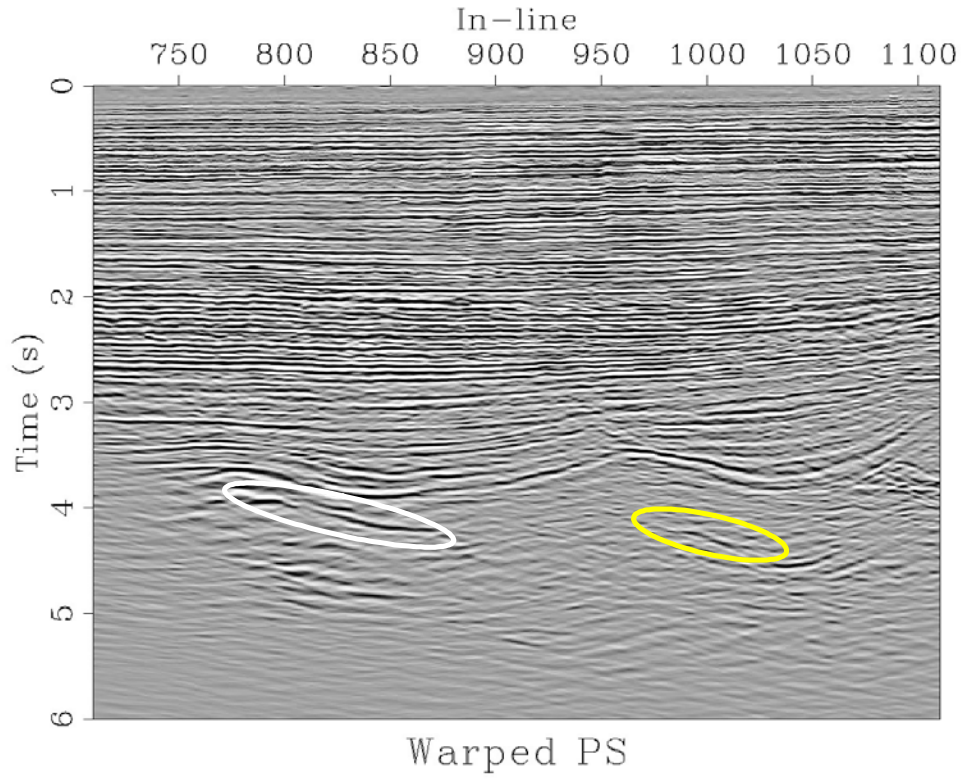


Figure 5.26. Warped PS data output from registration.

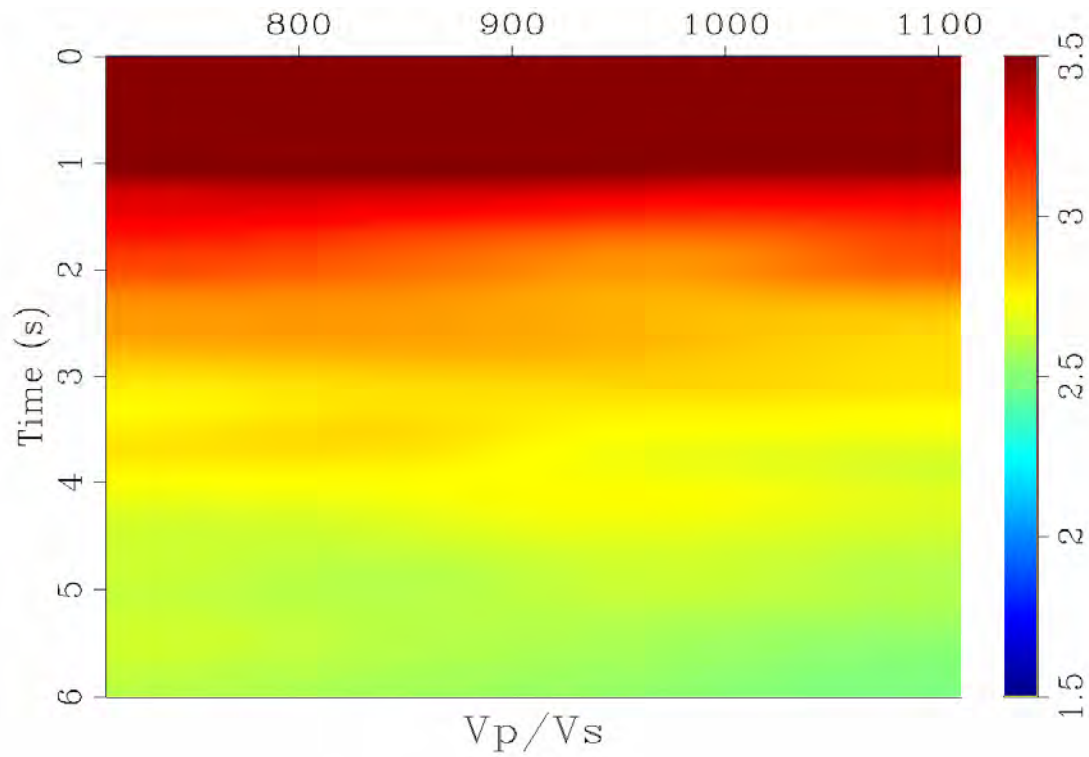


Figure 5.27. Effective V_p/V_s velocity ratio after warping.

SEISMIC INELASTIC ATTRIBUTES RESPONSE

Our research on inelastic attribute algorithms obtained from seismic data has been extensive, and our applications have been applied to a number of data sets world-wide to validate their credibility. A technical description of the inelastic algorithms applied was provided in PART 4 of this report.

This analysis was concentrated in the SW region of the survey area although attributes were computed over the entire region obtained. The SW region contains deeper amplitude events that are primary continuous events and some of these are bright in amplitude.

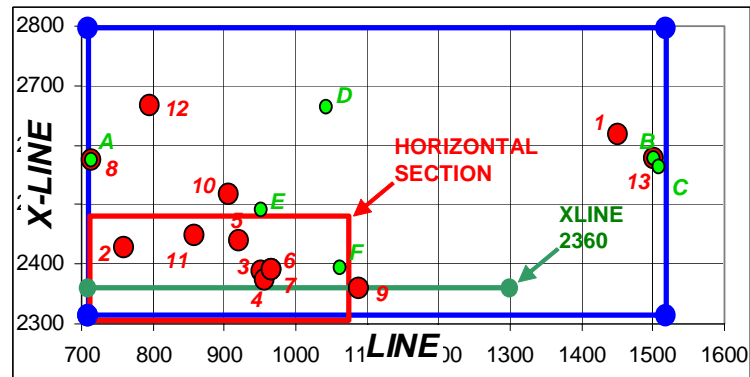


Figure 5.28. Seismic Area Map showing vertical section and area extent of time slice sections.

Various examples of our findings are shown using selected vertical sections (INLINE and XLINE) and TIMESLICE displays. A map showing the position of the vertical section XL 2360 is shown by the green line in Figure 5.28. The PP time slices shown cover the area shown in Figure 5.21 by the red rectangle at time 4240 ms. The PS time slices cover a slightly smaller area.

RESPONSE ON PP DATA VOLUME

Interesting results from a qualitative standpoint are seen on XLINE 2360 between 4000 and 4500 ms (green line - Figure 5.28). Two different fault blocks are evident from the seismic amplitude display and both attributes show attenuation for the events at the top of the fault blocks.

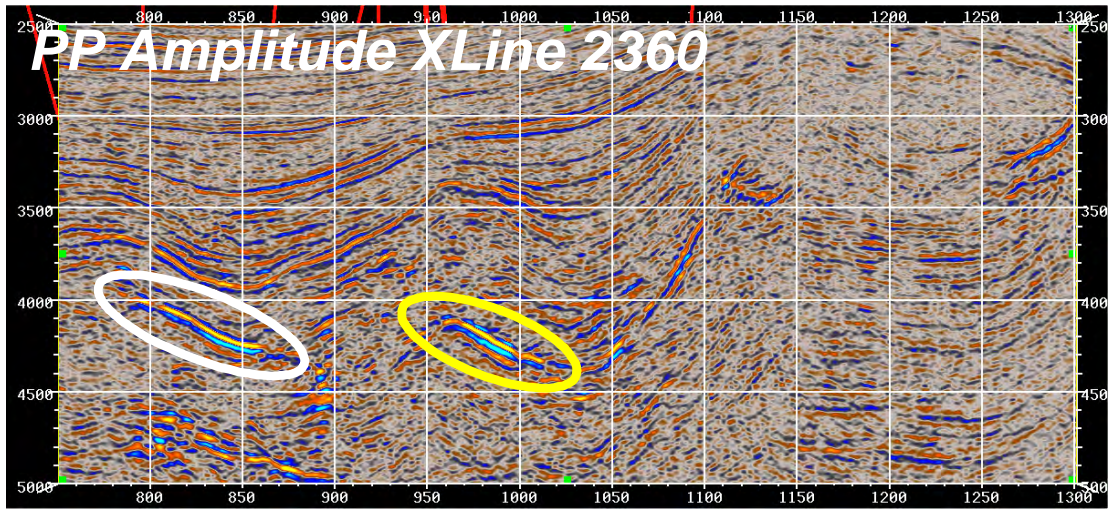


Figure 5.29a. XLINE 2360 PP stack amplitude.

These events maintain their inelastic attribute response laterally away from this XLINE.

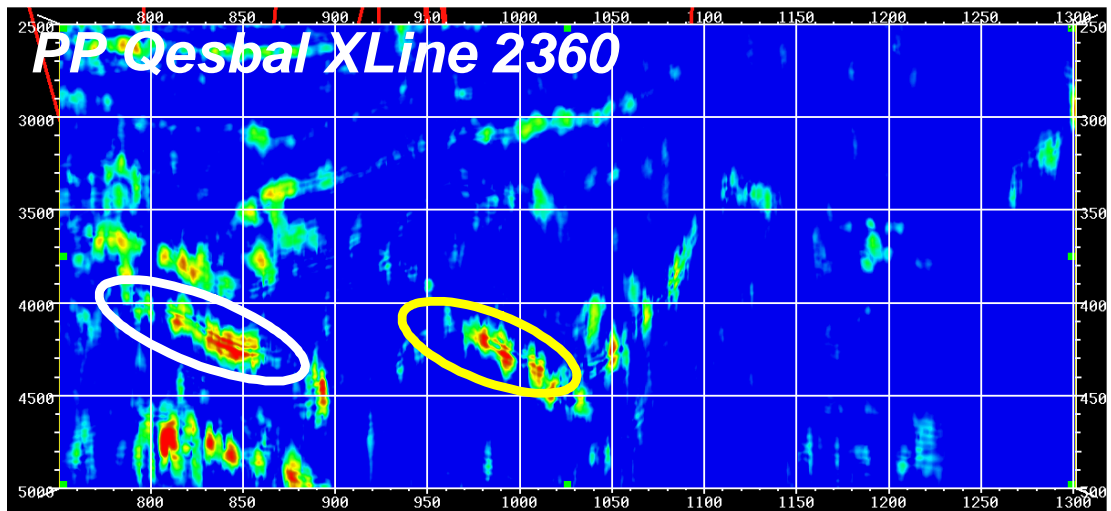


Figure 5.29b. XLINE 2360 PP Frequency Shift Q estimation attribute response.

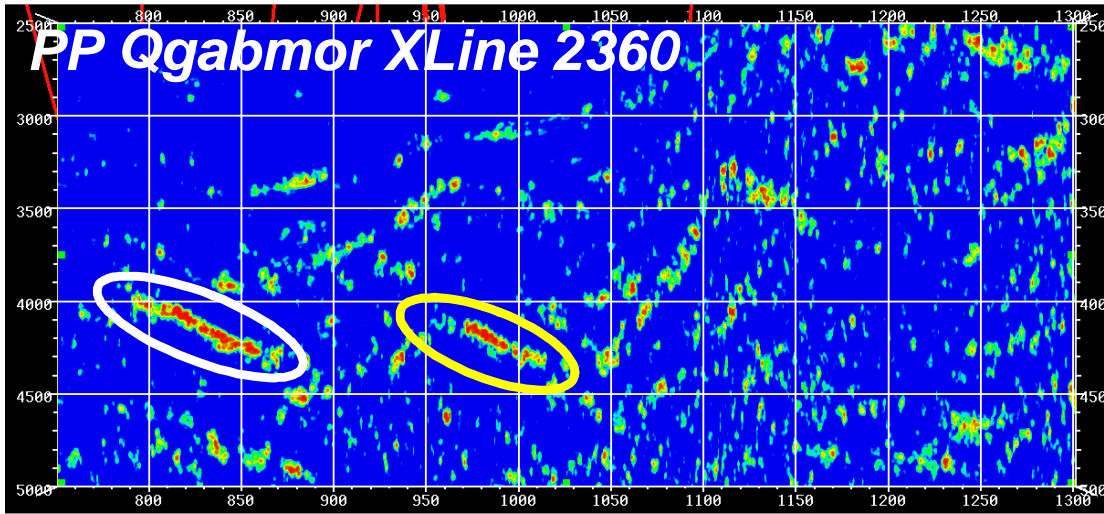


Figure 5.29c. XLINE 2360 PP Log Spectral Ratio Q estimation attribute response.

Figures 5.29b and 5.29c show that the JTFA Log Spectral Ratio Q estimation attribute has higher temporal resolution than the JTFA Frequency Shift Q estimation attribute but increased noise content. The JTFA Frequency Shift Q estimation attribute response indicates other event responses above and below the “white ellipse” event not seen as well on the JTFA Log Spectral Ratio Q estimation response.

This is important since the attributes are responding differently some of the time. The deeper JTFA Frequency Shift Q estimation event below the “white ellipse” corresponds to strong amplitudes in Figure 5.29a not evidenced by the JTFA Log Spectral Ratio Q estimation response.

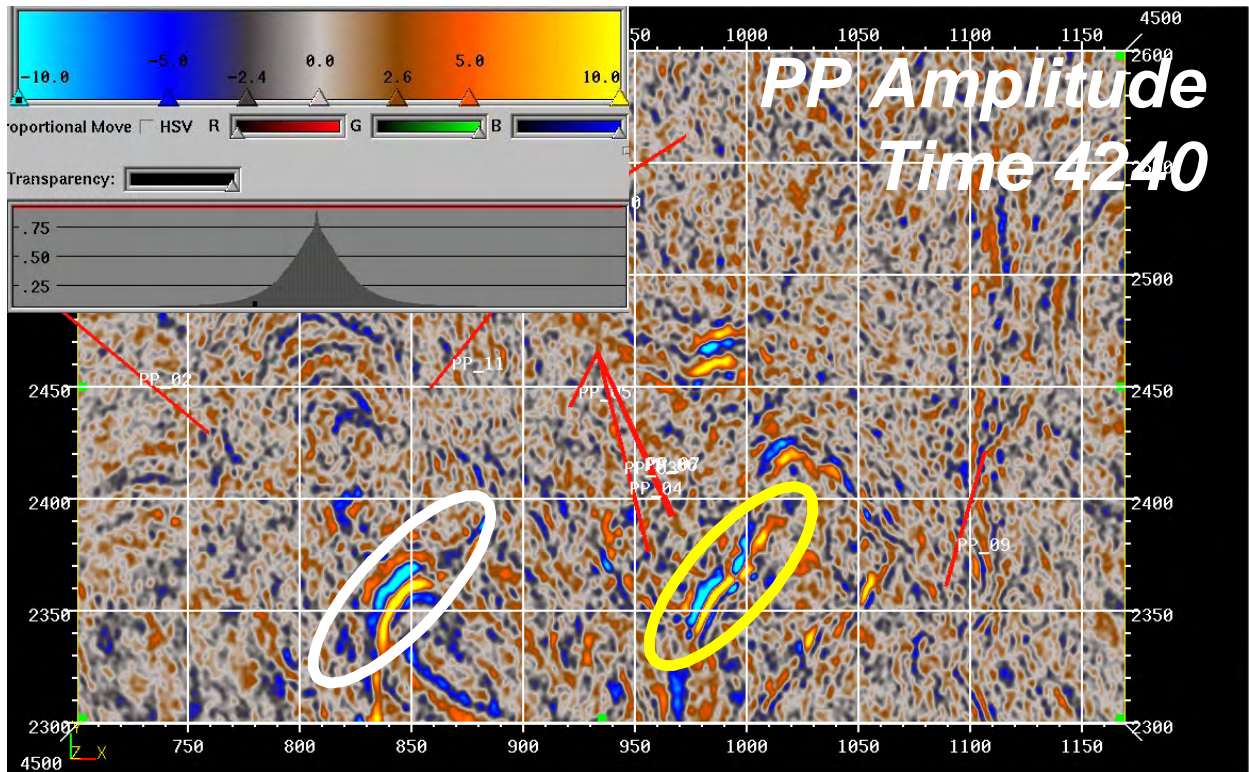


Figure 5.30a. TIME 4240 PP stack amplitude.

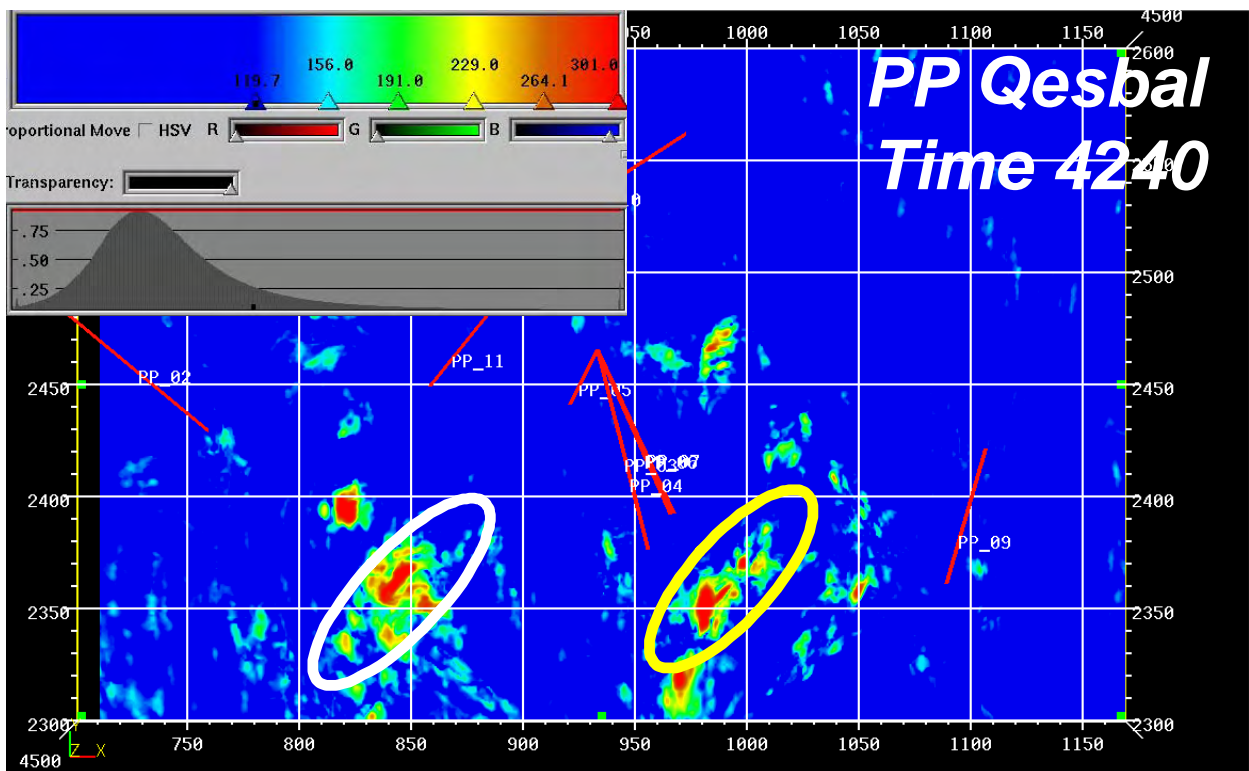


Figure 5.30b. TIME 4240 PP JTFA Frequency Shift Q estimation attribute response.

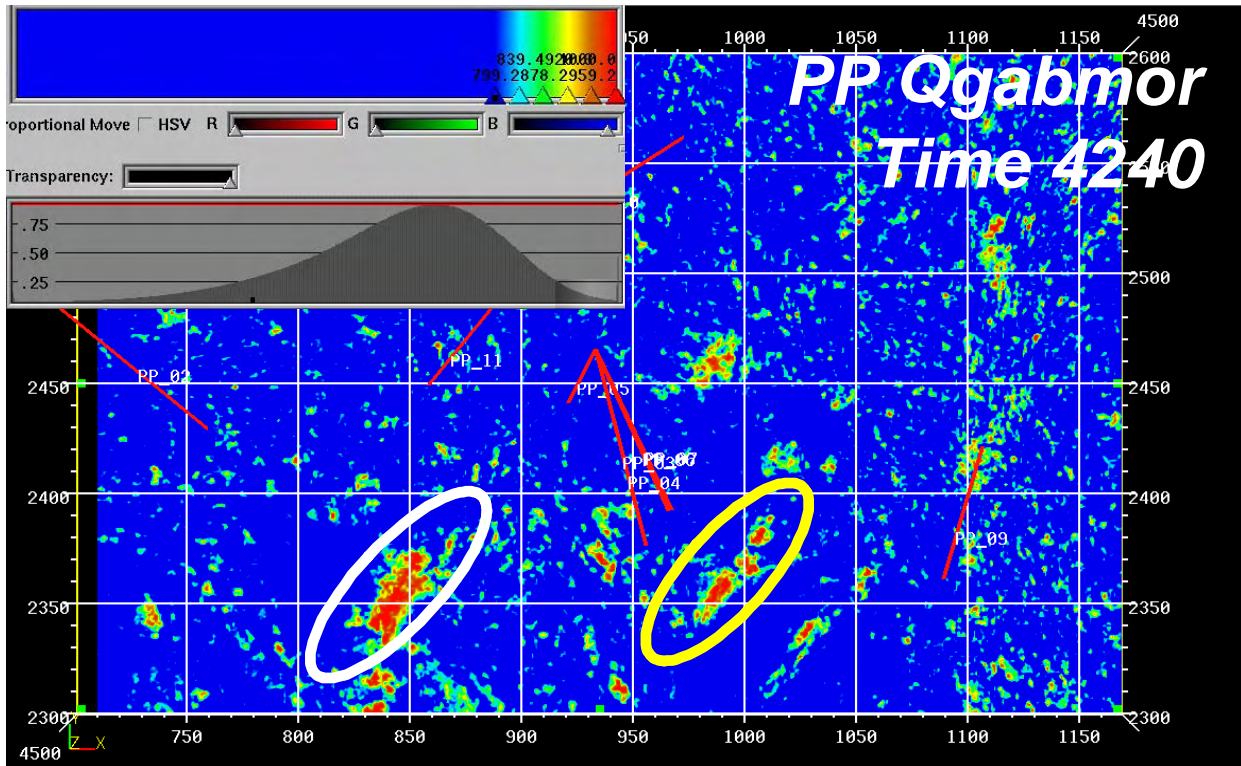


Figure 5.30c. TIME 4240 PP JTFA Log Spectral Ratio Q estimation attribute response.

The white and yellow ellipses in Figures 5.29a – 5.29c are repeated in Figures 5.30a – 5.30b. Again the difference in noise and resolution is exhibited in these time slice displays.

The color bar used for each attribute is shown along with the histogram distribution for the entire attribute volume. The inelastic attribute distribution shape is between Gaussian and Log-normal and in both cases these attributes depict attenuation rather than Q , therefore high values are supposed (at this stage) indicative of gas charge.

Other strong amplitude events do not exhibit the same strength of inelastic attribute response seen for the white and yellow ellipse events. This is further encouragement that the attribute response is anomalous and represents high attenuation.

RESPONSE ON PS DATA VOLUME

Both inelastic attributes were generated from the PS stack data volume. The PS amplitude data in Figure 5.31a shows weaker amplitudes at depth. The PP time range of 4000 – 4500 ms is approximately equivalent to 7500 – 8100 ms PS time.

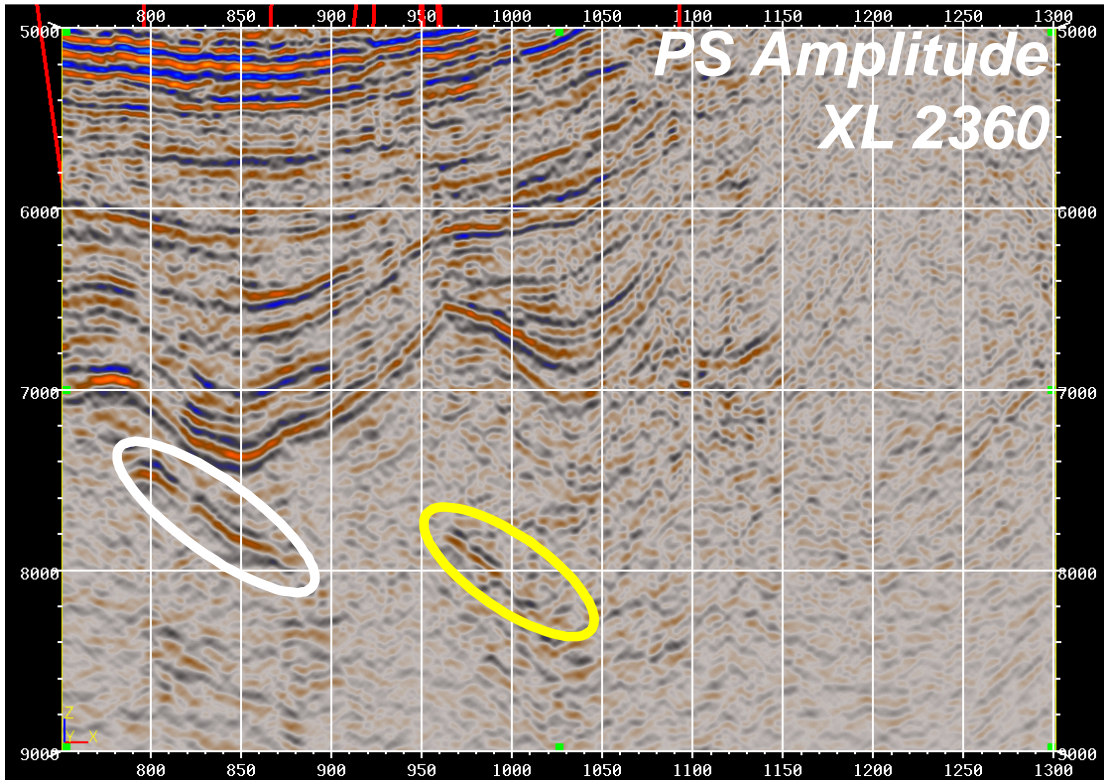


Figure 5.31a. XLINE 2360 PS stack amplitude.

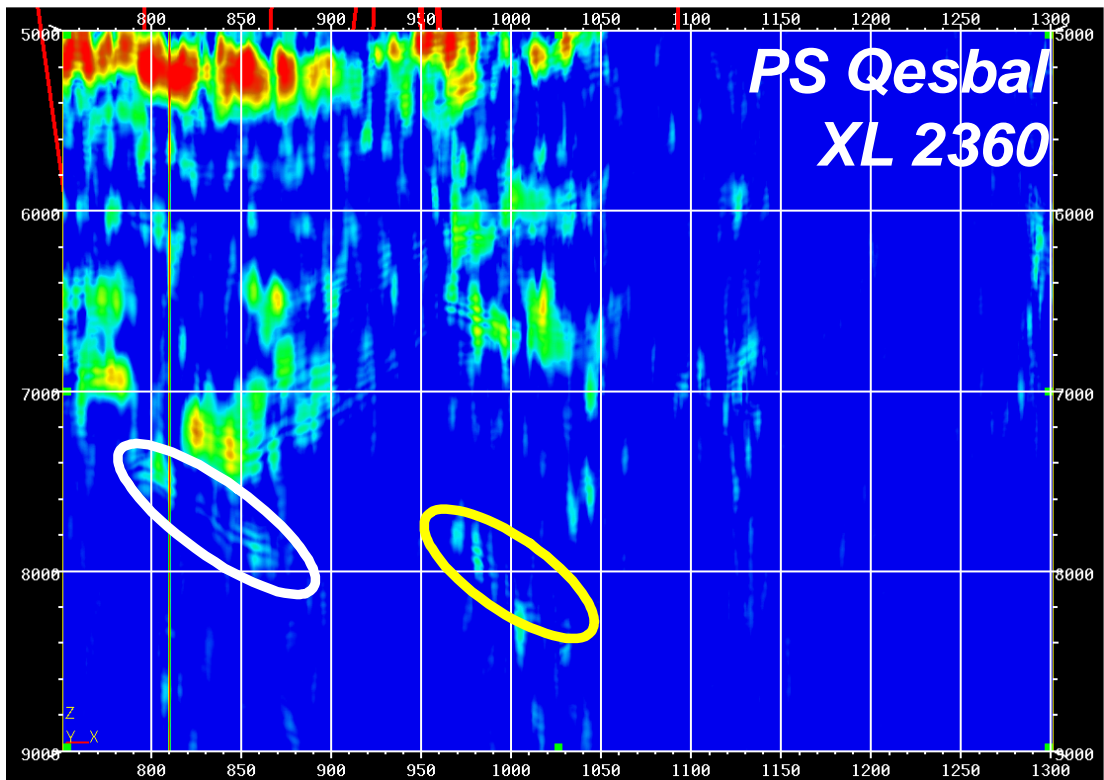


Figure 5.31b. XLINE 2360 PS JTFA Frequency Shift Q estimation attribute response.

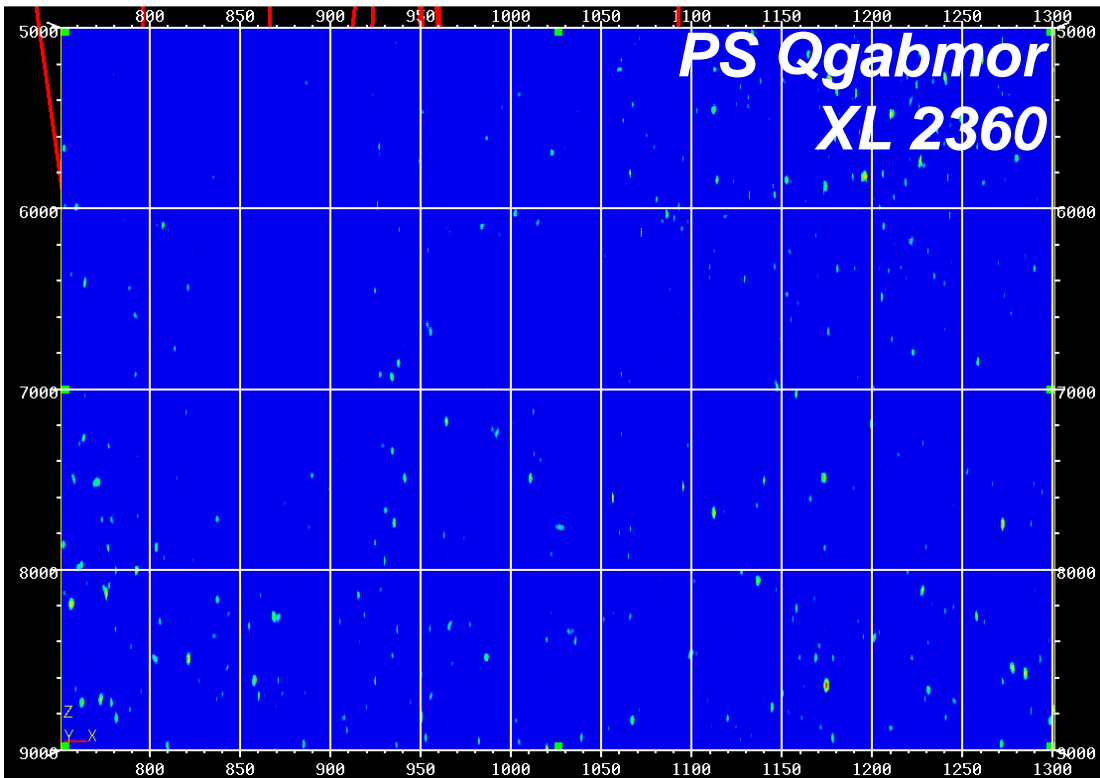


Figure 5.31c. XLINE 2360 PS JTFA Log Spectral Ratio Q estimation attribute response.

The JTFA Frequency Shift Q estimation attribute shows a weak response at the top the white ellipse fault block but no response for the yellow ellipse event. A response is also seen for the syncline event just above the white ellipse event, similar to the response from the PP JTFA Frequency Shift Q estimation attribute.

The JTFA Log Spectral Ratio Q estimation attribute shows no response anywhere in the section displayed, not even in the shallowest events up to 5sec PS time.

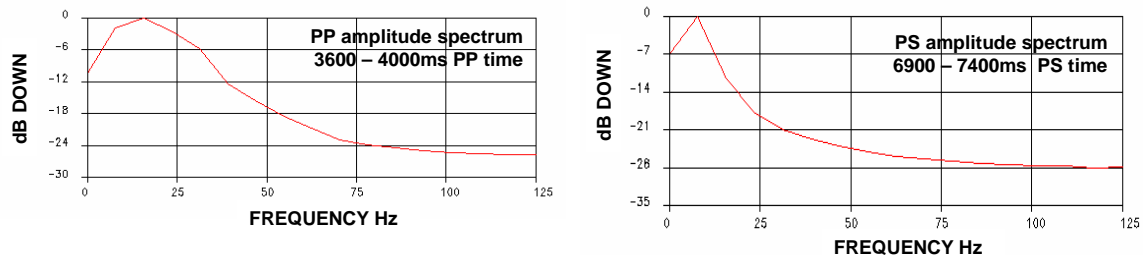


Figure 5.32a. Amplitude Spectra Comparison over similar depth (comparable time) range for PP and PS data.

Amplitude spectra for the PP and PS stack amplitude data run over deep gates along LINE 837 indicate a lower frequency band for the equivalent deep depth range analyzed. The reason for this is not entirely understood.

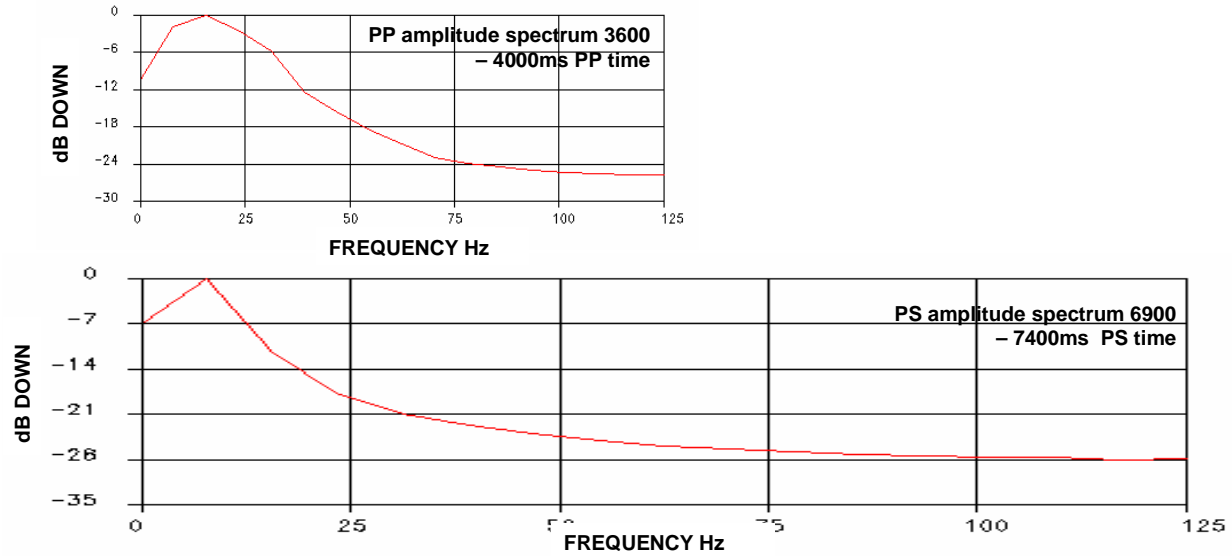


Figure 5.32b. Amplitude Spectra Comparison after simulated PS time registration to PP time.

The PS data has an apparent propagation velocity of approximately half that of the PP data. After PS time registration to PP time, this will increase the frequency band by approximately 2 as simulated in Figure 5.32b. The spectral shape is now more similar to that of the PP data however it is recommended the inelastic attributes are computed using the PS time data.

In this time range, the inelastic PS response is very weak and mostly indistinguishable from the background noise for both the JTFA Frequency Shift and JTFA Log Spectral Ratio Q estimation attributes. From Figure 5.32, a frequency range of the PS data is quite narrow compared to that of the PP data over the same depth range.

Also, the analysis band of 8 – 80 Hz used when generating the inelastic attributes for both the PP and PS data did not include much of the PS energy present and this may have caused the poor PS attribute responses seen at depth.

Following these observations, the PS attenuation attributes were rerun using a bandwidth of 4 – 40 Hz and the comparison with the attributes run using a bandwidth of 8 – 80 Hz are shown in Figures 5.33a, 5.33b.

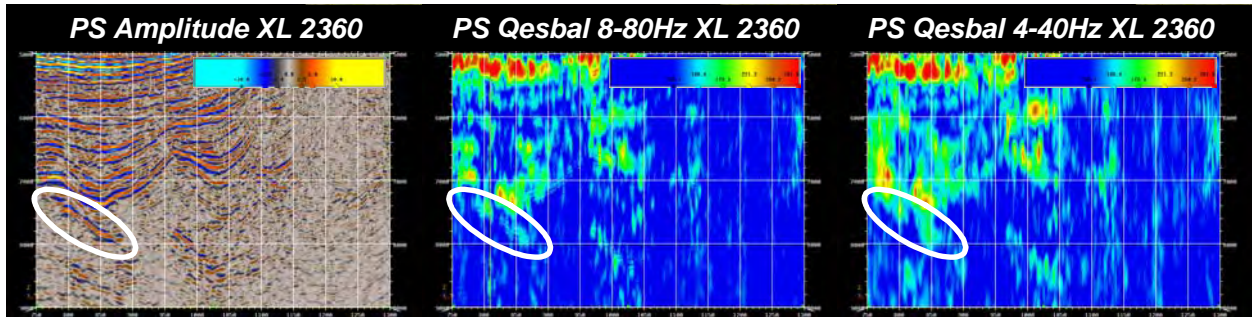


Figure 5.33a. PS XL 2360 amplitude, JTFA Frequency Shift Q estimation attenuation attribute using bandwidths of 8-80 Hz and 4-40 Hz.

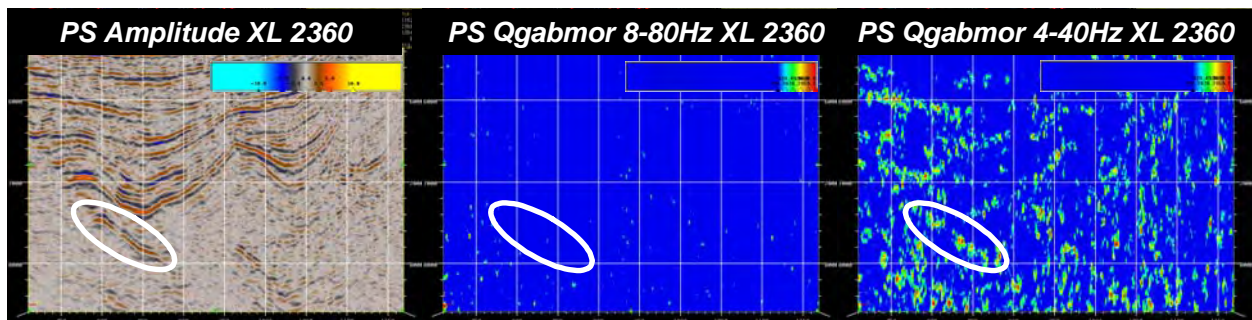


Figure 5.33b. PS XL 2360 amplitude, JTFA Log Spectral Ratio Q estimation attenuation attribute using bandwidths of 8-80 Hz and 4-40 Hz.

While the JTFA Frequency Shift Q estimation attribute shows a similar result (modifying the color bar can make them more similar), the JTFA Log Spectral Ratio Q estimation attribute now reveals a response associated with the left most deep event, however the response overall is quite noisy.

The responses were further examined using time slices at 7600 and 7700 ms PS time, as shown in Figure 5.34. The noisy appearance on the JTFA Log Spectral Ratio Q estimation attenuation attribute seen on the vertical XL2360 section is again seen on the both 7600 and 7700 ms time slices. The JTFA Frequency Shift Q estimation attenuation attribute is less noisy but of lower temporal and lateral resolution.

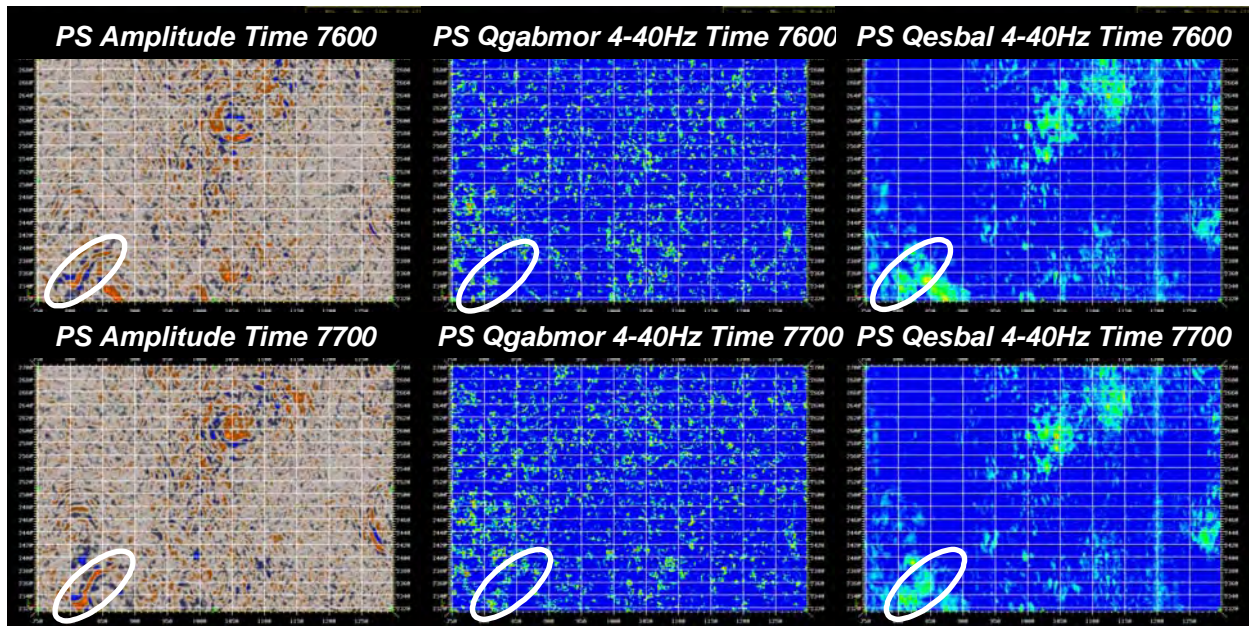


Figure 5.34. Montage of results for Amplitude (as reference) with JTFA Log Spectral Ratio (QGABMOR), and JTFA Frequency Shift (QESBAL) Q estimation attenuation attributes for PS TIMES of 7600 and 7700 ms.

PART 5 SUMMARY

Well Log Data and Rock Physics: The soft-sand model transform shown in Figure 5.12 will serve to (a) discriminate the gas sand from shale and wet sand and (b) estimate its porosity from the impedance inversion volume.

This rock physics model estimates P- and S-wave attenuation from standard well log data. It implies that while the P-wave attenuation is noticeably affected by the presence of hydrocarbons, the S-wave attenuation is not. The model predicts that the ratio of these attenuation values can be used as a hydrocarbon indicator.

A large potential of this model is that it allows for consistent forward modeling of attenuation depending on the properties and conditions in the subsurface to supplement and extend the existing real data. Such rock-physics-based “what-if” forward modeling is a powerful tool of seismic interpretation and has been extensively used with the elastic properties. Our new theoretical development helps extend this approach into the inelastic domain.

Of course, attenuation can be used in exploration and development only if it can be extracted from real seismic data. To test whether such extraction is viable, we create synthetic seismic traces for P-to-P and P-to-S amplitude using our rock physics predictions. In this synthetic

modeling we use a new ray-tracer tool designed specifically for this task. The results prove that the amplitude is indeed affected by attenuation and, therefore, by inference, we conclude that the seismic P- and S-wave attenuation can be measured in the field and eventually used for the purpose of rock diagnostics.

PP Gatherers: The pre-stack seismic gathers had only a basic processing flow applied to them which did not include S/N enhancement or multiple removal. We applied our own proprietary S/N enhancement to the gathers which enhanced them considerably, but multiple removal is beyond the scope of this project and was not done. Therefore, the gathers were of limited use for AVO analysis. However, this limitation has no effect on their applicability for attenuation estimation.

PP-to-PS Data Registration: The preliminary results shown in this report represent the sum total of the work done to date. Additional registration points using a number of different surface pairs would enhance the registration process.

Different surface pairs that are spatially coincident offer an excellent method of estimating the local V_p/V_s ratio, which could be used for example to support a low frequency shear velocity or impedance model directly from data measurements.

Further work was slated to be done but was not necessary given the results of the seismic Q estimation results on PS data.

Seismic Q Estimation on PP and PS Data: The PP amplitude data show indications of potential deep gas charged reservoirs. These data indicate a peak over trough response and if the phase of the response is close to zero-phase, then this would represent harder sand in slower shale background. This is quite possible given the overpressure evidenced by the velocity survey data analyzed previously, and that deep sand could be cemented to some extent.

The phase of the shallow seismic data should be verified using conventional well tie procedures, while the phase of the deep seismic data could be reconciled using deep sand models based on what we might reasonably expect for their elastic properties.

The deep (6900-7400 ms) PS data has a lower bandwidth than the corresponding (3600-4000) PP data. This is mostly due to the slower propagation velocity of the PS compared to the PP data and warping the PS to the PP time will effectively double frequency band making the PS band approach that of the PP data.

The deep (4000-4500ms PP time) events are reasonably well imaged using PP data but the corresponding PS events (7300-7800ms PS time) are only partially imaged. This implies that

the PS data might be able to be used to support the PP structural interpretation in exploration of deep gas targets but it would be difficult to use them alone.

From our theoretical work (Figure 5.35), the PP inelastic response for gas sand is expected to be strong, while the PS inelastic response for gas sand is shown to be basically flat. The PS response is a combination of the P and S reflection travel paths so we expect some intermediate response for PS as shown.

Analysis of these attributes on seismic data indicates they appear to be consistent with theoretical models (Table 5.6). The key in interpreting these attributes is finding strong responses with both algorithms, which does occur at specific reflectors. Areas where this type of response occurs then serves as a basis for high-grading prospective hydrocarbon-bearing reservoirs. The data shows that the most important results for hydrocarbon detection come from conventional PP data, but if PS is also available, it can be used to help differentiate layer from gas- or oil-related effects.

<u>ATTRIBUTE</u>	<u>PP SEISMIC DATA</u>	<u>PS SEISMIC DATA</u>
AMPLITUDE	Strong peak over trough	Medium trough over peak
JTFA Frequency Shift	Strong response	Weak and low resolution response
JTFA Log Spectral Ratio	Strong response	Weak and noisy response

Table 5.6. Summary table of the attribute response for deep seismic data (>4.0 sec PP time).

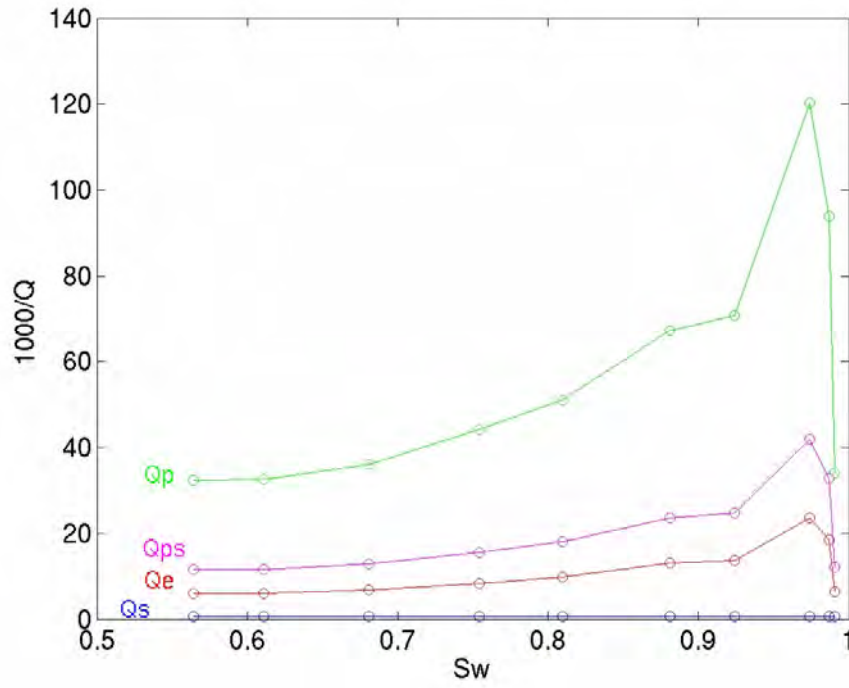


Figure 5.35. Repeat of Fig 1.27 - attenuation vs. saturation - Cadoret measured the curves for Q_e and Q_s .

PROJECT ACCOMPLISHMENTS AND CONCLUSIONS

This project focused on developing new technology to improve deep gas exploration technology using seismic attenuation effects. The project focused on three major goals. These goals were to develop new methods of;

- 1 Computing P-wave and S-wave attenuation from standard well log data such as porosity, V_{clay} and S_w .
- 2 Using the log-derived attenuation for generating P-wave synthetic seismic traces with and without attenuation effects.
- 3 Computing attenuation related attributes from reflection seismic data – both P-wave and mode-converted PS-wave.

These goals were accomplished, and we have shown through testing with different field examples, that attenuation related seismic attributes can be useful in identifying producing deep gas formations.

The main conclusions and key findings from this project are:

- 1 Rock physics methods can be used to compute both Q_p and Q_s from conventional well log data.
- 2 Q_p and Q_s can be computed from PP and PS seismic data, respectively.
- 3 Attenuation can have a substantial impact on seismic response, both post-stack and pre-stack, and cause significant changes in seismic amplitude with offset, especially at the bottom of a gas zone.
- 4 Attenuation in seismic data can be related to gas bearing reservoirs, and can be used as a reconnaissance tool in exploration.

Attenuation should be used in conjunction with other seismic attributes such as elastic attributes and geologic context. However, attenuation alone can be a valuable tool in deep targets because AVO may fail in these environments. Finally, the most important attenuation anomalies come from conventional PP data, but if PS is also available, it can be used to help differentiate layer-based attenuation anomalies from gas- or oil-related effects. These conclusions can be demonstrated by describing the individual accomplishments of each of the main tasks of the project, as given below.

PART 1: ROCK PHYSICS RELATIONS FOR Q_p AND Q_s

P-Wave Attenuation Theory:

In this project, we developed a theory of P-wave attenuation that is theoretically and practically viable and can and should be used for realistic attenuation calculations in reservoir and non-reservoir rock. The strong points of this theory are that it (1) is based on first principles; (2) allows for calculating Q from basic inputs that are readily available from borehole measurements; and (3) produces Q values that are consistent with field measurements. The theory involves a number of assumptions or limitations: (1) the supposition that a wave-induced oscillatory cross-flow of the pore fluid can develop between earth layers that may have very low permeability, such as in shale, and (2) the fact that it does not allow for predicting attenuation as a function of frequency. Instead, it calculates the maximum possible inverse quality factor.

S-Wave Attenuation Theory:

The simple theoretical model offered here relates the P-to-S inverse quality factor ratio to the Poisson's ratio of the background sediment. It relies on a large number of assumptions that are not necessarily honored in real rock. Yet, the attenuation ratio provided by the model is realistic and matches experimental observations. The main result is that in wet rock the P- and S-wave quality factors are approximately the same.

Q_P / Q_{PS} Relationships:

In this project, we developed the connections between the Q_P/Q_S ratio, which has been extensively studied with laboratory and theoretical work, and the ratio Q_P/Q_{PS} , which may be more directly observable in the field using converted mode data. We found that the attenuation-related rules of thumb for saturation are:

- $Q_P/Q_{PS} \sim 1$ for wet sand or shale
- $Q_P/Q_{PS} \ll 1$ for gas sand

The theoretical formulation suggests that it is probably advantageous to interpret attenuation data in the (Q_P, Q_{PS}) domain instead of converting field data to the (Q_P, Q_S) domain. Application of the theory indicates that classical laboratory data indicating that Q_P/Q_S can be an indicator of gas should also apply to observed Q_P/Q_{PS} .

PART 2: LOG-BASED SYNTHETIC SEISMIC MODELING WITH Q

Synthetic Seismic Modeling with Attenuation:

We have shown synthetic traces, both at normal incidence and with offset, in an earth model containing a gas reservoir. We compared traces including effects of realistic attenuation with models assuming a perfectly elastic earth, using Ricker wavelets of 20, 30, 40, and 50 Hz. We find that:

- Lower frequencies lead to lower resolution. In the modeling shown here, striking changes in the reservoir signature occur between 40 Hz and 30 Hz.
- Attenuation leads to velocity dispersion, both in the overburden and in the reservoir. This dispersion tends to delay arrivals in the attenuation model. The very low Q and large dispersion in the gas reservoir also leads to an apparently thicker reservoir (in time) relative to an elastic earth.
- Attenuation in the overburden has a small effect on normal incidence amplitudes at the reservoir top. This attenuation reduces the far offset amplitudes relative to the near offset amplitudes, because the far offset traces travel a longer path.
- The large attenuation in the reservoir leads to greatly reduced base gas amplitudes and greatly reduced gradient.
- The reduction in AVO gradient from attenuation could cause gas to be mistaken for oil, and oil to be mistaken for water.
- Signatures of gas in this exercise are the increased-time thickness of the reservoir interval, lower impedances in the reservoir interval, and large contrasts in base amplitude relative to top amplitude due to attenuation in the reservoir.
- Seismic bandwidth appears to be crucial in identifying the tops as well as the extent of the reservoir, as well as in estimating the uncertainty when matching synthetic and real seismic data.

Tuning and Attenuation:

- Attenuation does not affect the tuning behavior as far as reflections at the top of the attenuating layer are concerned.
- As expected, attenuation does affect the reflection at the bottom of the attenuating layer.
- The latter effect could be fairly strong and affect the summary waveform associated with the attenuating layer.

- The same behavior as shown for the normal-incidence reflections will persist for the P-to-P reflection at an angle and, as a result, it will not affect the AVO curves at the top of the reservoir but will affect those picked at the bottom and, in general, will affect the waveforms associated with angle-stacked reflectivity.
- All the above conclusions hold if there is no attenuation above the main attenuating layer. The situation will change for a stack of attenuating reservoirs.

PART 3: PROPERTIES OF PORE FLUIDS AT HIGH TEMPERATURE AND PRESSURE

We used software from the National Institute of Standards and Testing (NIST) to assess the adiabatic bulk modulus and density of natural gas and brine at pressures up to 200 MPa and temperatures up to 200°C. The results indicate that as pressure increases from the normal range of 20 to 50 MPa to the very high range of 150 to 200 MPa, the bulk modulus of methane may increase tenfold, from about 0.1 to about 1.0 GPa. The latter values are comparable to those for oil. For heavier hydrocarbon gases (ethane, propane, butane, and their mixtures) the modulus will be even higher. This strong increase in the bulk modulus of natural gas may affect the seismic response of deep gas sands and, therefore, needs to be accounted for during the interpretation of deep-gas seismic events as well as in forward modeling.

We show, using real well log data as input into synthetic seismic modeling, that although the character of the AVO response may be not affected by the pressure-related changes in gas properties, the magnitude of this response will be definitely affected. Ultrahigh pressure may affect the properties of natural gas to a degree that translates into seismic signature type in very deep gas targets. The Batzle and Wang equations and NIST model for NaCl brine give similar results for density and compressibility over a wide range of pressure and temperature. For gas density, BW-92 and NIST models give similar results over a wide range of pressure and temperature. However for adiabatic bulk modulus, there are substantial differences between BW-92 and NIST at high pressure and temperature, and the differences depend on the gas specific gravity.

PART 4: LINKING ATTENUATION FROM SEISMIC TO LOGS

Spectral Ratio Analysis Techniques for Q Estimation:

- The effects of finite Q are to decrease amplitude, attenuate higher frequencies faster than lower frequencies, stretch wavelets, and rotate wavelet phase.
- It is difficult to resolve thin Q-layers, but it is easier to detect their presence from their “shadow” – the difference between spectra shallow and deep in the section

- Q-effects can be measured from spectral ratios.
- Accuracy of Q from spectral ratios increases with longer data windows and longer separation between shallow and deep windows, obviously at the expense of resolution
- Spectral ratios can be performed in the time domain from amplitudes and band-pass ratios.
- It is easier to detect relative changes than absolutes.
- An additional practical problem in the field might result from the phenomenon of “wave-front healing.”

Because of wave diffraction plus undershooting from multiple offsets, the loss of high frequencies near a low-Q reservoir might recover with depth. Depending on how windows for spectral ratios are chosen, healing might diminish or mask the Q.

Gabor-Morlet Seismic Q Estimation Algorithms:

Two different methods for Q estimation of seismic data have been presented. These two methods, while differing in their measurement technique for Q and in their response to attenuation, are nevertheless based on the same principle. The technique is Gabor-Morlet Joint Time-Frequency Analysis, and it is used to separate the frequency spectra into discrete, well-behaved bands. The new Q-measurement technique presented here is the comparison of frequency bands within the same time interval by spectrally balancing the frequency bands to approximate the seismic section as it would appear before having undergone attenuation (if dispersion is ignored). The spectrally balanced section can then be compared with the original section to derive an estimate for attenuation.

PART 5: TESTING AND OPTIMIZATION WITH FIELD DATA

Well Log Data and Rock Physics:

The soft-sand model is an appropriate rock physics model to estimate P- and S-wave attenuation from standard well log data. This model was used for this project. It showed that while the P-wave attenuation is noticeably affected by the presence of hydrocarbons, the S-wave attenuation is not. The model predicted that the ratio of these attenuation values can be used as a hydrocarbon indicator. To test whether attenuation could be extracted from seismic data, we created synthetic seismic traces for P-to-P and P-to-S amplitude using our rock physics predictions. In this synthetic modeling we used a new ray-tracer tool designed specifically for this task. The results proved that amplitude is indeed affected by attenuation and, therefore, by inference, we conclude that the seismic P- and S-wave attenuation can be measured in the field and eventually used for the purpose of rock diagnostics.

Seismic Q Estimation on PP and PS Data:

The PP amplitude data show indications of potential deep gas charged reservoirs. These data indicate a peak over trough response which might represent harder sand in slower shale background. This is quite possible given the overpressure evidenced by the velocity survey data analyzed previously, and that deep sand could be cemented to some extent. The deep (6900-7400 ms) PS data has a lower bandwidth than the corresponding (3600- 4000) PP data. This is mostly due to the slower propagation velocity of the PS compared to the PP data. Warping the PS to the PP time will effectively double frequency band making the PS band approach that of the PP data.

The deep (4000-4500ms PP time) events are reasonably well imaged using PP data but the corresponding PS events (7300-7800ms PS time) are only partially imaged. This implies that the PS data might be able to be used to support the PP structural interpretation in exploration of deep gas targets but it would be difficult to use them alone. From our theoretical work, the PP inelastic response for gas sand is expected to be strong, while the PS inelastic response for gas sand is shown to be basically flat. The PS response is a combination of the P and S reflection travel paths so we expect some intermediate response for PS as shown. Analysis of these attributes on seismic data indicates they appear to behave according to theoretical models. The key in interpreting these attributes is finding strong responses with both algorithms, which does occur at specific reflectors. Areas where these types of response occur then serve as a basis for high-grading prospective hydrocarbon-bearing reservoirs.

REFERENCES

- Backus, G.F., 1962, Long-wave elastic anisotropy produced by horizontal layering, *JGR*, 67, 4427-4441.
- Batzle M. and Wang Z., 1992, Seismic properties of pore fluids, *Geophysics*, 57, 1396-1408.
- Brie, A., Pampuri, F., Marsala, A.F., and Meazza, O., 1995, Shear sonic interpretation in gas-bearing sands: SPE 30595, 701-710.
- Burnett, M.D., Castagna, J.P., Méndez-Hernández, E., Rodríguez, G.Z., García, L.F., Vázquez, J.T. M., Avilés, M.T., and Villaseñor, R.V., 2003, Application of spectral decomposition to gas basins in Mexico, *TLE*, 22, 1130-1134.
- Castagna, J.P., Sun, S., and Siegfried, R.W., 2003, Instantaneous spectral analysis: Detection of low-frequency shadows associated with hydrocarbons, *TLE*, 22, 120-127.
- Chatenever, A., and Calhoun, J.C., 1952, Visual examinations of fluid behavior in porous media -- Part 1, *AIME Petroleum Transactions*, 195, 149-195.
- Cadoret, T., 1993, Effet de la Saturation Eau/Gaz sur les Propriétés Acoustiques des Roches, Ph.D. dissertation, University of Paris, VII.
- Dvorkin, J., and Nur, A., 1993, Dynamic Poroelasticity: A Unified Model with the Squirt and the Biot Mechanisms, *Geophysics*, 58, 524-533.
- Dvorkin, J., Mavko, G., and Nur, 1995, Squirt Flow in Fully Saturated Rocks, *Geophysics*, 60, 97-107.
- Dvorkin, J., and Mavko, G., 2006, Modeling Attenuation in Reservoir and Non-reservoir Rock, *The Leading Edge*, 25, 194-196 (Feb. 2006).
- Dvorkin, J., Moos, D., Packwood, J.L., and Nur, A.M., 1999, Identifying patchy saturation from well logs, *Geophysics*, 64, 1756-1759.
- Dvorkin, J., and Nur, A., 1996, Elasticity of High-Porosity Sandstones: Theory for Two North Sea Datasets, *Geophysics*, 61, 1363-1370.
- Dvorkin, J., and Uden, R., 2004, Seismic wave attenuation in a methane hydrate reservoir, *The Leading Edge*, 23, 730-734.
- Ebrom, D., 2004, The low-frequency gas shadow on seismic sections, *TLE*, 23, 772.
- Gabor, D., 1946, Theory of communication, *J. IEEE* 93, 429-457.
- Gal, D., Dvorkin, J., and Nur, A., 1998, A Physical Model for Porosity Reduction in Sandstones, *Geophysics*, 63, 454-459.
- Gassmann, F., 1951, Über die elastizität poroser medien: *Vierteljahrsschrift der Natur. Gessellschaft*, 96, 1-23.
- Guerin, G., and Goldberg, D., 2002, Sonic waveform attenuation in gas-hydrate-bearing sediments from the Mallik 2L-38 research well, Mackenzie Delta, Canada, *JGR*, 107, 1029-1085.
- Hackert, C.L., and Parra, J.O., 2004, Improving Q estimates from seismic reflection data using well-log-based localized spectral correction, *Geophysics*, 69, 1521-1529.
- Hamilton, E.L., 1972, Compressional-wave attenuation in marine sediments, *Geophysics*, 37, 620-646.
- Han, D-H., and Batzle, M., 2000, Velocity, density and modulus of hydrocarbon fluids – data measurement, Extended Abstract, SEG Annual 2000 Meeting.
- Hotelling, H., 1933, Analysis of Complex Statistical Variables with Principal Components, *Journal of Educational Psychology*, 24, 417-420.

- Juhlin, C., 1988, Interpretation of the seismic reflectors in the Gravberg-1 well, in Boden, A., and Eriksson, K., Eds., *Deep drilling in crystalline bedrock*, 1, Springer Verlag, 113–121.
- Juhlin, C., 1990a, Seismic attenuation, shear wave anisotropy, and some aspects of fracturing in the crystalline rock of the Siljan Ring area, central Sweden, Ph.D. Thesis, University of Uppsala.
- Juhlin, C., 1990b, Interpretation of the reflections in the Siljan Ring area based on results from the Gravberg-1 borehole, *Tectonophysics*, 173, 345–360.
- Kennett, B.L.N., 1974, Reflections, Rays, and Reverberations, *Bulletin of the Seismological Society of America*, 64, #6, 1685-1696.
- Kennett, B.L.N., and Kerry, N.J., 1979, Seismic Waves in a Stratified Half Space, *Geophysical Journal of the Royal Astrological Society*, 57, 557-583.
- Klimentos, T., and McCann, C., 1990, Relationships among compressional wave attenuation, porosity, clay content, and permeability in sandstones, *Geophysics*, 55, 998-1014.
- Klimentos, T., 1995, Attenuation of P- and S-waves as a method of distinguishing gas and condensate from oil and water, *Geophysics*, 60, 447-458.
- Knight, R., Dvorkin, J., and Nur, A., 1998, Seismic Signatures of Partial Saturation, *Geophysics*, 63, 132-138.
- Koesoemadinata, A.P, and McMechan, G.A., 2001, Empirical estimation of viscoelastic seismic parameters from petrophysical properties of sandstone, *Geophysics*, 66, 1457-1470.
- Kvamme, L., and Havskov, J., 1989, Q in southern Norway, *Bulletin of Seismological Society of America*, 79, 1575–1588.
- Leary, P., Henyey, T., and Li, Y., 1988, Fracture related reflectors in basement rock from vertical seismic profiling at Cajon Pass, *GRL*, 15, 1057–1060.
- Lilwall, R., 1988, Regional mb:Ms, Lg=Pg amplitude ratios and Lg spectral ratios as criteria for distinguishing between earthquakes and explosions: A theoretical study, *Geophysical Journal*, 93, 137–147.
- Lucet, N., 1989, Vitesse et attenuation des ondes elastiques soniques et ultrasoniques dans les roches sous pression de confinement, Ph.D. thesis, The University of Paris.
- Mavko, G., Chan, C., and Mukerji, T., 1995, Fluid substitution: Estimating changes in V_p without knowing V_s , *Geophysics*, 60, 1750-1755.
- Mavko, G., and Dvorkin, J., 2005, P-wave attenuation in reservoir and non-reservoir rock, Extended Abstract, EAGE 2005.
- Mavko, G., and Jizba, D., 1991, Estimating grain-scale fluid effects on velocity dispersion in rocks, *Geophysics*, 56, 1940-1949.
- Mavko, G., Mukerji, T., and Dvorkin, J., 1998, *Rock Physics Handbook*, Cambridge University Press.
- McDonal, F.J., Angona, F.A., Mills, R.L., Sengbush, R.L., Van Nostrand, R.G., and White, J.E., 1958, Attenuation of shear and compressional waves in Pierre shale, *Geophysics*, 23, 421-439.
- Morlet, J., Arens, G., Fourgeau, E. and Giard, D., 1982, Wave propagation and sampling theory - Part II: Sampling theory and complex waves, *Geophysics*, 47, 222-236.
- Murphy, W.F., 1982, Effects of microstructure and pore fluids on the acoustic properties of granular sedimentary materials, Ph.D. thesis, Stanford University.
- Pratt, R.G., Bauer, K., and Weber, M., 2003, Cross-hole waveform tomography velocity and attenuation images of arctic gas hydrates, Expanded Abstract, SEG International Exposition and Seventy-Third Annual Meeting.

- Pride, S.R., Harris, J.M., Johnson, D.L., Mateeva, A., Nihei, K.T., Nowack, R.L., Rector, J.W., Spetzler, H., Wu, R., Yamamoto, T., Berryman, J.G., and Fehler, M., 2003, Permeability dependence of seismic amplitudes, *TLE*, 22, 518-525.
- Pujol, J.M., Luschen, E, and Hu, Y., 1998, Seismic wave attenuation in metamorphic rocks from VSP data recorded in Germany's continental super-deep borehole, *Geophysics*, 63, 354–365.
- Quan, Y., and Harris, J.M., 1997, Seismic attenuation tomography using the frequency shift method, *geophysics*, 62, 895-905.
- Setzmann, U. and Wagner, W., 1991, A New Equation of State and Tables of Thermodynamic Properties for Methane, *J. Phys. Chem. Ref. Data*, 20, 6, 1061-1151.
- Smith, L. I., 2002, A Tutorial on Principal Components Analysis, http://csnet.otago.ac.nz/cosc453/student_tutorials/principal_components.pdf.
- Sun, X., Tang, X., Cheng, C.H., and Frazer, L.N., 2000, P- and S-wave attenuation logs from monopole sonic data, *Geophysics*, 65, 755-765.
- Toksoz, M.N., and Johnston, D.H., 1981, Seismic wave attenuation, *SEG Geophysics Reprint Series*, 2.
- Winkler, K.W, 1980, The effects of pore fluids and frictional sliding on seismic attenuation, Ph.D. thesis, Stanford University.
- Wood, W.T., Holbrook, W.S., and Hoskins, H., 2000, In situ measurements of P-wave attenuation in the methane hydrate- and gas-bearing sediments of the Blake Ridge, in *proceedings of the ODP, Scientific Results*, Paull, C.K., Matsumoto, R., Wallace, P.J., and Dillon, W.P. (eds.), 164, 265-272.
- Yin, H., 1993, Acoustic velocity and attenuation of rocks: Isotropy, intrinsic anisotropy, and stress-induced anisotropy, Ph.D. thesis, Stanford University.

LIST OF ACRONYMS

AVO: Amplitude versus offset. This refers to the behavior of reflectors with offset in a gather.

BEG: Bureau of Economic Geology, Austin

BW: Batzle & Wang equations specifying bulk modulus and density of pore fluid versus pore pressure and temperature.

DHI: Direct hydrocarbon indicator

GOR: Gas-to-oil ratio

GPa: Giga Pascals

JFTA: Joint time frequency analysis. A technique for measuring the spectra of a number of independent points simultaneously.

NIST: National Institute of Standards and Technology

NMO: Normal move-out. This is a character of seismic gathers. It is the variation in reflection arrival time because of variation in the shotpoint-to-geophone distance, or offset.

OBC: Ocean bottom cable seismic recording configuration

P-wave: Compressional wave

PP: P-wave transmission that is reflected back to the receiver as a P-wave.

PR: Poisson's ratio

PS: P-wave transmission (downgoing wavefront) that has been converted to S-wave on the upgoing wavefront. Technically speaking, this is the "shear wave" data that accompanies the PP volume in multi-component data.

Q: A measure of attenuation. Attenuation (α) is actually equal to $1/Q$.

Qp: Attenuation in P-wave reflections

Qs: Attenuation in S-wave reflections

RMS: Root mean square. A commonly accepted measure of amplitude.

S-wave: Shear wave

Sw: Water saturation well log

TD: Total depth, refers to the length of a well.

TVD: True vertical depth. Refers to the true depth of a well as opposed to the measured depth which is subject to error if the well is not perfectly vertical.

TVDSS: True vertical depth below sea level (sub-sea).

UTM: Universal Transverse Mercator. A geographic projection system.

Vclay: Volume of clay well log

Vp: Compressional velocity well log

Vs: Shear velocity well log

VSP: Vertical seismic profile

APPENDIX 1: PAPERS PRESENTED

A Rock Physics and Attenuation Analysis of a Well from the Gulf of Mexico

Gary. Mavko, Stanford University, Jack Dvorkin, Stanford University and Rock Solid Images, Joel Walls, Rock Solid Images*

(Presented at SEG, 2005)

Abstract

The well selected for the application of our attenuation theory and extraction of attenuation attributes from seismic data is the Texaco well (API 177104132700) in Block 313 of Eugene Island in the Gulf of Mexico (Well 2700). The rock physics diagnostics indicates that the rock can be described by the uncemented (soft-sand) model. This model is used to predict the S-wave velocity that was missing in the original well data. The P- and S-wave inverse quality factors are computed according to our theoretical model. The ratio of these inverse quality factors (P-to-S) is small (on the order of one) in wet rock and large in the gas zone. The seismically-measured attenuation ratio may serve, therefore, as an indicator of hydrocarbons. The synthetic seismic traces computed using the well data and the ray-tracer with attenuation, specifically developed for this project, indicate that attenuation affects the seismic response and, therefore, can be extracted from real seismic data, including the P-to-P and P-to-S reflection amplitude.

Rock Physics Diagnostics – Model for Velocity

The gas saturation in the well was calculated from the resistivity curve while the clay content was estimated by linearly scaling the gamma-ray curve between its minimum and maximum values. It was assumed that the formation water has the bulk modulus 2.85 GPa and density 1.01 g/cc while the gas has the bulk modulus 0.14 GPa and density 0.26 g/cc. The total porosity was calculated from the bulk density by assuming that the density tool samples the virgin formation with gas saturation as calculated from resistivity.

The measured impedance and P-wave velocity are compared to the curves due to the uncemented (soft-sand) model. The proximity of the data and model (Figure 1) indicates that this model is appropriate for the well under examination. This model was then used to predict the S-wave velocity (absent in the measured data) from the P-wave velocity.

The in-situ impedance is plotted versus the total porosity and Poisson's ratio (PR) in Figure 2 where the data are color-coded by gamma-ray and by water saturation. Similar cross-plots are shown in Figure 3 but for wet conditions where the elastic properties and density were calculated using the P-wave-only fluid substitution. The soft-sand model curves for water-saturated rock are superimposed upon the wet-condition data to further emphasize the relevance of this model. The curves are produced for varying porosity and each for fixed clay content. The latter variable changes from one to zero with step 0.2. These model curves fully encompass the well log data.

Attenuation Modeling

Theoretical development of rock physics models for P-wave attenuation are presented in two papers by Dvorkin, et al, 2003. Theory behind the S-wave attenuation computation is presented in Mavko, et al, 2005. We have used these models to compute the attenuation curves on well 2700. The results of P- and S-wave attenuation modeling indicate that the P-wave inverse quality factor (Q_p^{-1}) is only significant in the gas reservoir and small elsewhere (Figure 4 and 5). The inverse S-wave quality factor (Q_s^{-1}) is small everywhere in the interval and close to Q_p^{-1} as calculated in wet rock.

Figure 6 displays the ratio of the P-to-S inverse quality factors (Q_p^{-1}/Q_s^{-1}) plotted versus the P-to-S-wave velocity ratio (V_p/V_s) and color-coded by water saturation (S_w). This cross-plot is for the in-situ conditions.

The low V_p/V_s is typical of gas sand where Q_p^{-1}/Q_s^{-1} is coincidentally large. Therefore, these attributes as well as their hybrids, when extracted from seismic data, may serve as hydrocarbon indicators.

Notice that for the wet low-gamma-ray sand in the bottom part of the well Q_p^{-1}/Q_s^{-1} is small although the V_p/V_s (and PR) contrast between this sand and surrounding shale is negative (but not as strong as in the gas sand). This negative contrast may still produce an AVO anomaly that can be mistakenly attributed to a gas reservoir (Figure 7). Under such circumstances, the attenuation ratio (Q_p^{-1}/Q_s^{-1}) may serve as a unique hydrocarbon indicator.

Raytracer

A synthetic-seismic raytracer has been created specifically for this project to estimate the effects of the elastic rock properties and attenuation on the seismic amplitude and attributes. The raytracer produces P-to-P as well as P-to-S (converted shear) gathers. The algorithm takes into account both P- and S-wave attenuation by means of a Q -filter.

Synthetic Modeling

The results of synthetic seismic modeling with and without taking attenuation into account are displayed in Figure 8 and 9. The P-to-P amplitude (Figure 8) is noticeably affected by the attenuation for both normal incident and offset traces. This result implies that the P-wave attenuation (Q_p^{-1}) can be extracted from real seismic data.

The converted-wave (P-to-S) traces in Figure 9 reflect the fact that the S-wave attenuation is small – the synthetic amplitude computed with attenuation is not very different from that computed without attenuation. To test whether Q_s^{-1} indeed affects the converted-wave amplitude in this synthetic modeling, we compute a far-offset trace with Q_s^{-1} ten times that predicted by our rock physics modeling (Figure 9, separate frame at the bottom). The apparent effect of attenuation on the amplitude is large which means that the S-wave attenuation (Q_s^{-1}) can be extracted from real seismic converted-wave data.

Conclusion

A new rock physics model allows for estimating P- and S-wave attenuation from standard well log data. It implied that while the P-wave attenuation is noticeably affected by the presence of hydrocarbons, the S-wave attenuation is not. The model predicts that the ratio of these attenuation values can be used as a hydrocarbon indicator.

A large potential of this model is that it allows for consistent forward modeling of attenuation depending on the properties and conditions in the subsurface to supplement and extend the existing real data. Such rock-physics-based “what-if” forward modeling is a powerful tool of seismic interpretation and has been extensively used with the elastic properties. Our new theoretical development helps extend this approach into the inelastic domain.

Of course, attenuation can be used in exploration and development only if it can be extracted from real seismic data. To test whether such extraction is viable, we create synthetic seismic traces for P-to-P and P-to-S amplitude using our rock physics predictions. In this synthetic modeling we use a new raytracer tool designed specifically for this task. The results prove that the amplitude is indeed affected by attenuation and, therefore, by inference, we conclude that the seismic P- and S-wave attenuation can be measured in the field and eventually used for the purpose of rock diagnostics.

Future development will include close work with real seismic and well log data to further calibrate and validate the proposed methods of reservoir characterization as well as to chart the areas of their applicability.

Acknowledgements

The work was supported by Rock Solid Images and the US Dept. of Energy (under contract DE-FC26-04NT42243).

References

- Dvorkin, J., G. Mavko, J. Walls, M.T. Taner, N. Derzhi, 2003; Attenuation at Patchy Saturation – A Model, Proceedings of Annual EAGE Convention, Stavanger Norway, June 2-5.
- Dvorkin, J., G. Mavko, and J. Walls, 2003; Seismic wave attenuation at full water saturation, Proceedings SEG Intl. Exposition and 73rd Annual Meeting, Dallas, TX, Oct 26-31.
- G. Mavko, Dvorkin, J., and J. Walls, 2005; A Theoretical Estimate of S-Wave Attenuation in Sediment, Proceedings SEG Intl. Exposition and 75th Annual Meeting, Houston, TX, 6-11 November.

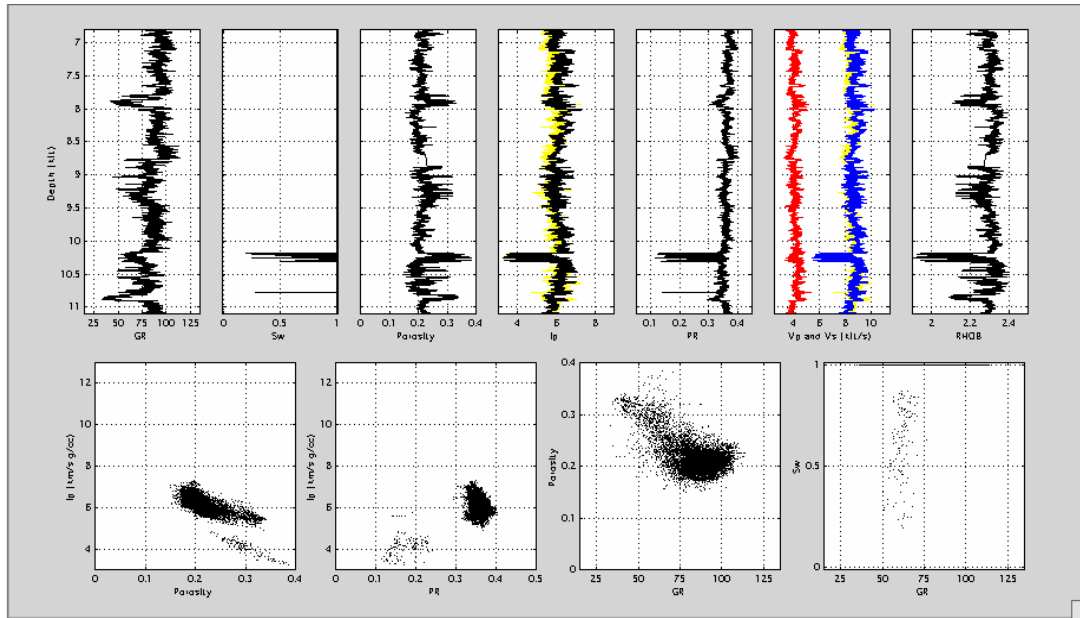


Figure 1. Log data display for Well 2700 under examination. Top, from left to right -- gamma-ray; water saturation; total porosity; P-wave impedance; Poisson's ratio (predicted); P- and S-wave (predicted) velocity; and bulk density. Bottom, form left to right – impedance versus porosity; impedance versus Poisson's ratio; porosity versus gamma-ray; and water saturation versus gamma-ray. The yellow curves superimposed upon the data in the impedance and velocity frames in the top row are calculated from the soft-sand model using the porosity and clay as well as the pore-fluid properties as inputs.

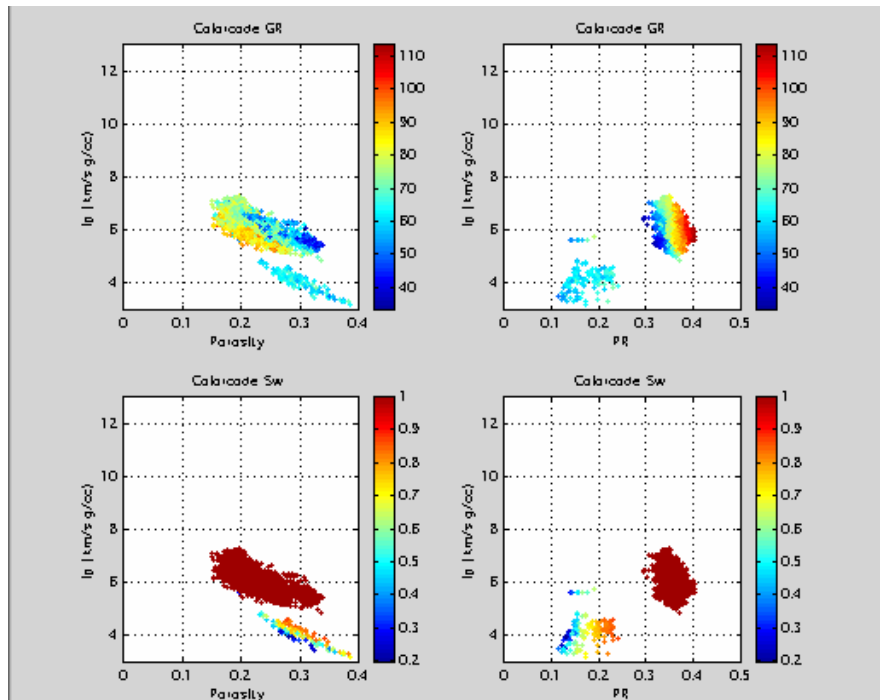


Figure 2. Impedance versus porosity (left) and versus Poisson's ratio (right). The data in the top row are color-coded by GR while that in the bottom row are color-coded by water saturation. In situ data.

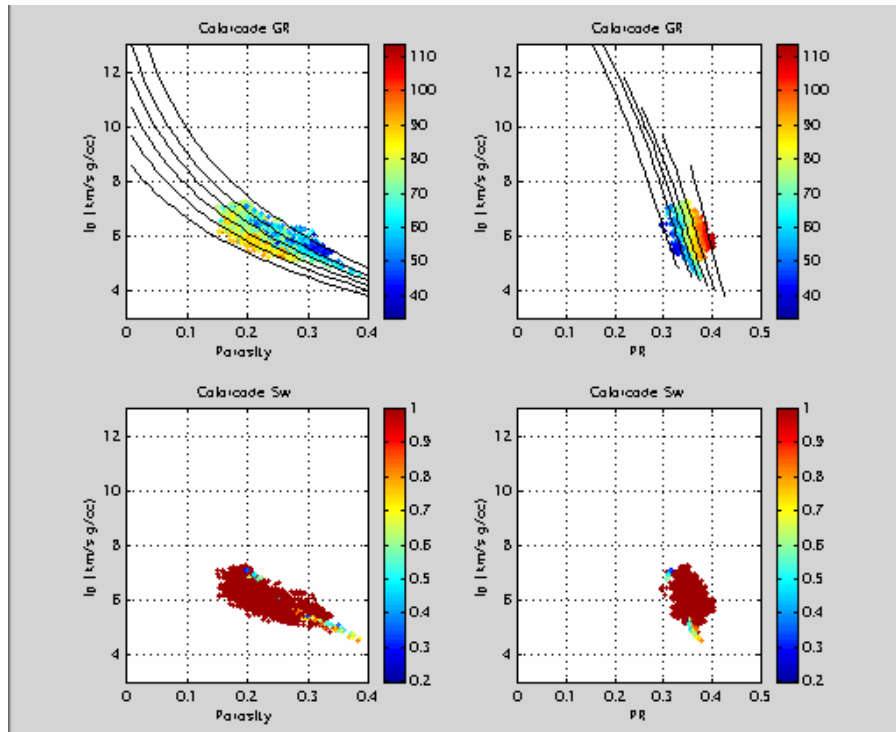


Figure 3. Same as Figure 2 but for wet conditions. The model curves in the top row are from the soft-sand model for clay content varying from one (top curve in the impedance-porosity display and left-most curve in the impedance-PR display) to zero with step 0.2.

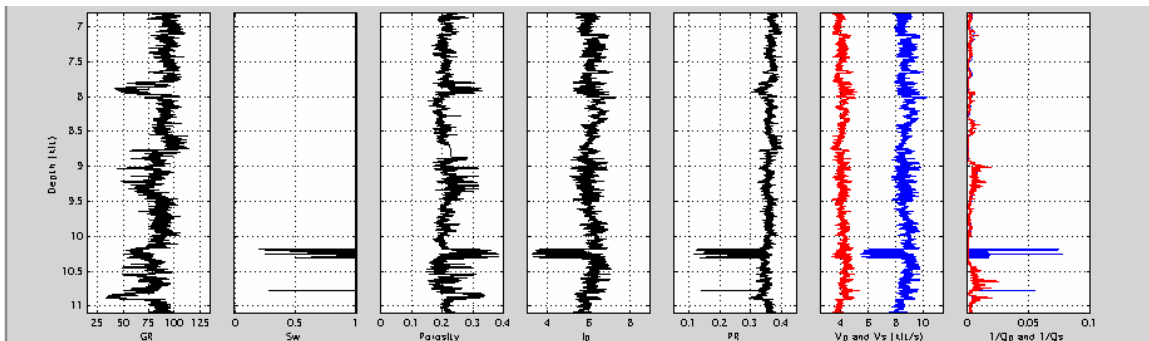


Figure 4. Well log display with the inverse quality factor shown in the last frame (P in blue and S in red).

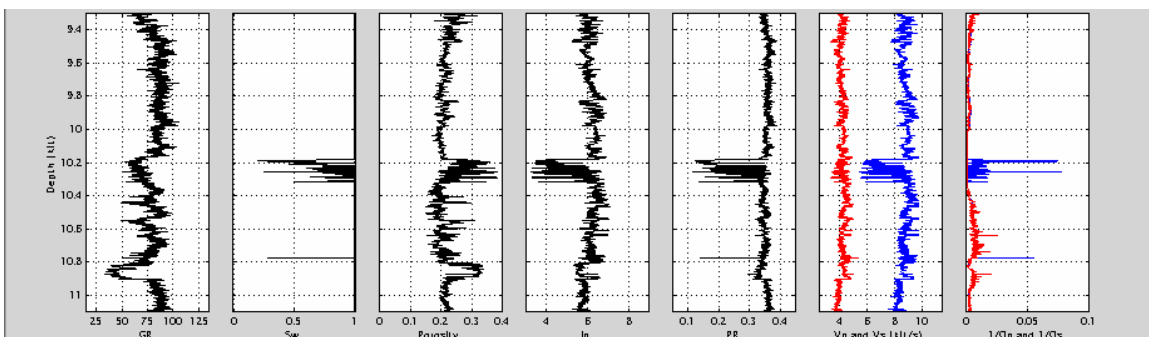


Figure 5. Same as Figure 4, zoomed on the bottom part of the well.

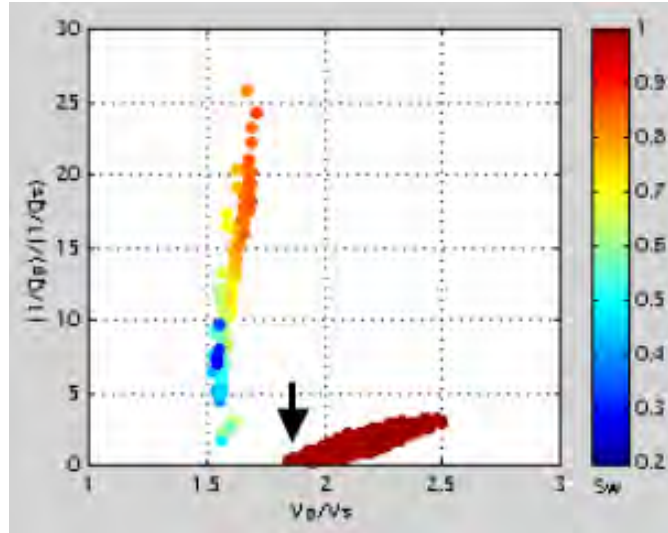


Figure 6. Inverse quality factor ratio versus velocity ratio from Figure 4 color-coded by water saturation. The arrow points to the data for the two wet sand intervals located just above 8 and 11 kft (see GR track in Figure 4).

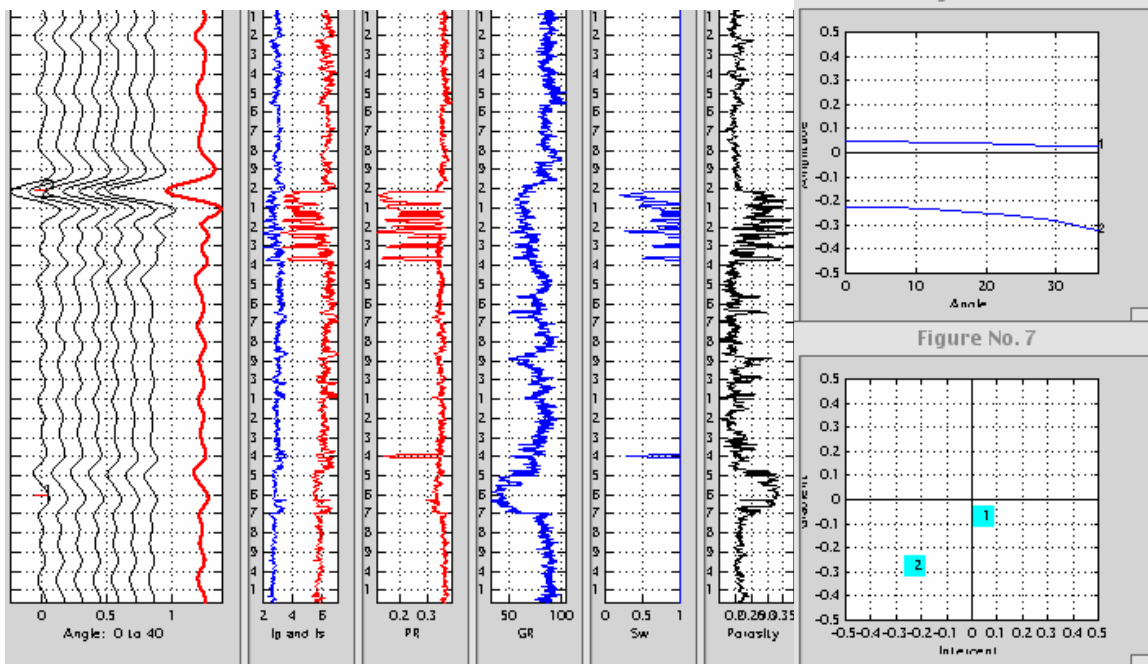


Figure 7. Synthetic seismic traces (40 Hz) in the bottom part of the well showing that the wet sand (pick “1” on the gather) may exhibit a negative gradient although not as strong as gas sand (pick “2” on the gather). From left to right – gather (black) and stack (red); P- and S-wave impedance; Poisson’s ratio; GR; water saturation; and porosity. The AVO curves and gradient-versus-intercept plots are at the picks shown in numbers on the gather display.

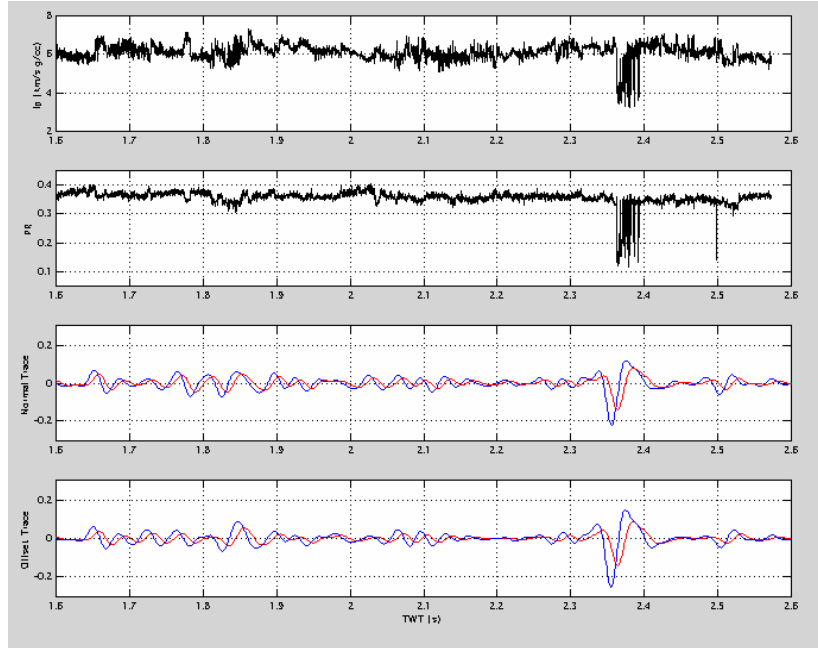


Figure 8. Synthetic raytracer modeling at 40 Hz. P-to-P reflection. From top to bottom – impedance; PR; normal-incidence trace; and offset trace versus P-wave TWT. The blue traces in the bottom two frames are calculated without attenuation while the red traces are calculated with taking the P-wave attenuation into account.

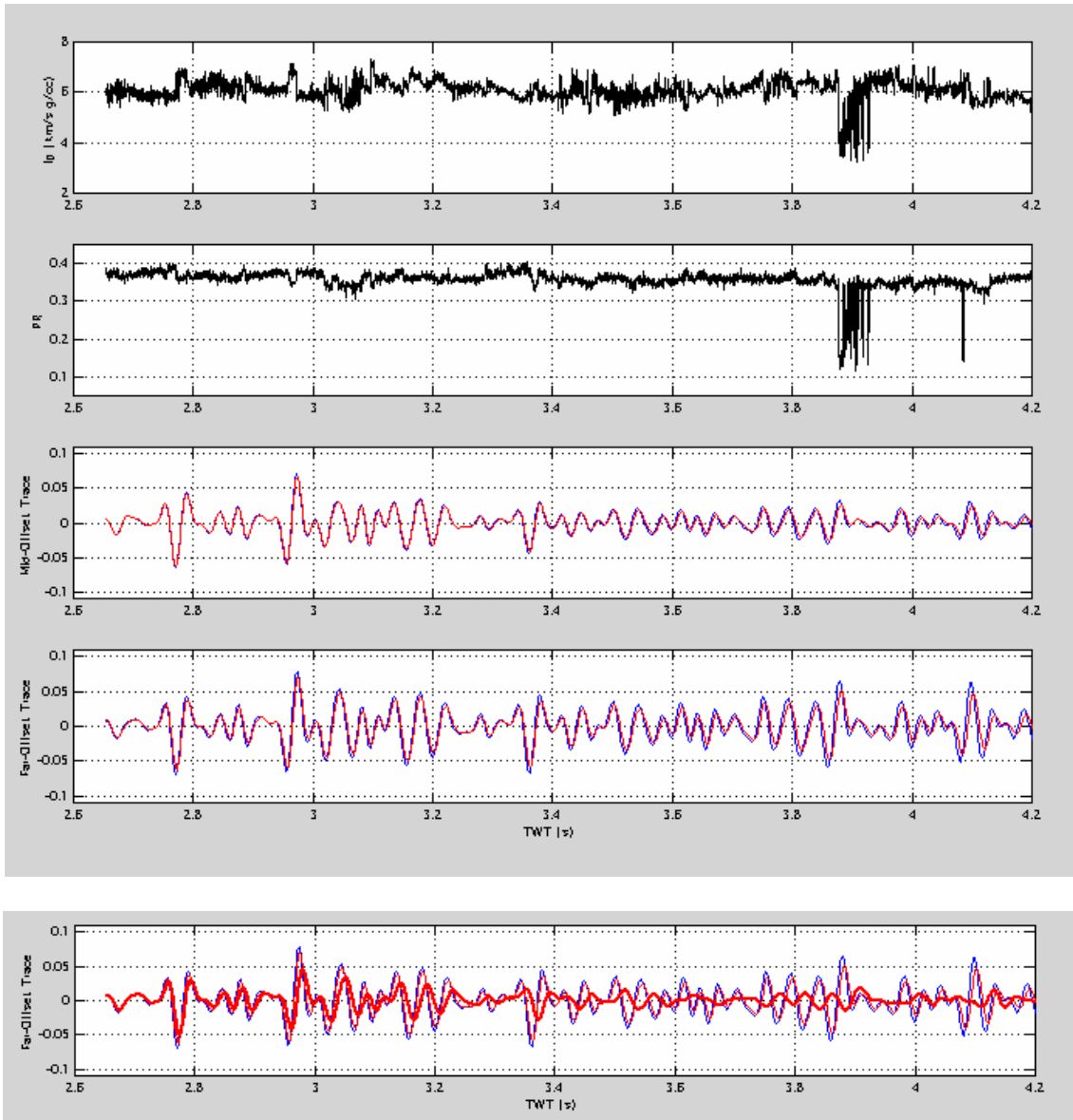


Figure 9. Same as Figure 8 but for P-to-S reflections. The red traces are calculated with taking the P- and S-wave attenuation into account. The separate frame at the bottom also displays the far-offset trace calculated for the S-wave attenuation ten times as that predicted by the rock physics model (bold red trace).

A Theoretical Estimate of S-Wave Attenuation in Sediment

*Gary. Mavko**, *Stanford University, Jack Dvorkin, Stanford University and Rock Solid Images, Joel Walls, Rock Solid Images*

(Presented at SEG, 2005)

ABSTRACT

Some of laboratory and field data (albeit very sparse) indicate that the S-wave attenuation in a sediment sample (a) weakly depends on water saturation and (b) approximately equals the P-wave attenuation at 100% water saturation. These observations are matched by our theoretical model. In this model we assume that (a) the S-wave inverse quality factor is related to the shear-modulus-versus-frequency dispersion by the same viscoelastic relation as the P-wave inverse quality factor (e.g., the standard linear solid) and (b) the shear-modulus-versus-frequency dispersion is linked to the compressional-modulus-versus-frequency dispersion.

To model the latter link, we assume that the reduction in the compressional modulus between the high-frequency and low-frequency limits is due to the introduction of a hypothetical set of aligned defects or flaws (e.g., cracks). Next we assume that the same set of defects is responsible for the reduction in the shear modulus between the high-frequency and low-frequency limits. Finally, by using Hudson's theory for cracked media we link the shear-modulus-versus-frequency dispersion to the compressional-modulus-versus-frequency dispersion and show that the proportionality coefficient between the two is a function of the P-to-S-wave velocity ratio (or Poisson's ratio). This coefficient falls between 0.5 and 3 for Poisson's ratio contained in the 0.25 to 0.35, typical for saturated earth materials.

INTRODUCTION

In order to model the effects of intrinsic attenuation on seismic amplitude and to use these effects to help quantify lithology, porosity, and fluid saturation, it is necessary to measure or compute Q_p and Q_s from well log data. Since direct measurements of Q from sonic logs have been problematic, our approach is to use rock physics methods to estimate Q_p and Q_s from more conventional open-hole well log data. We have previously reported methods to 1) compute Q_p in partially water saturated rock (Dvorkin, et al, 2003), and 2) compute Q_p in fully water saturated rock (Dvorkin, Mavko, Walls, 2003). In this paper, we present a method to compute Q_s from well log data.

S-WAVE ATTENUATION DATA

Laboratory measurements conducted at ultrasonic frequency on small rock plugs as well as in a lower frequency range using the resonant-bar technique on larger samples indicate that the S-wave inverse quality factor (Q_s^{-1}) is weakly dependent on water saturation and is approximately the same as the inverse P-wave quality factor at full saturation ($Q_s^{-1} \approx Q_p^{-1}$).

One example is the resonant-bar data from Murphy (1982) for Massillon sandstone (Figure 1). Lucet (1989) shows that the P-wave attenuation is close to S-wave attenuation in a limestone sample at ultrasonic frequency (Figure 2). However, Q_p^{-1} is larger than Q_s^{-1} at low (resonant-bar) frequency.

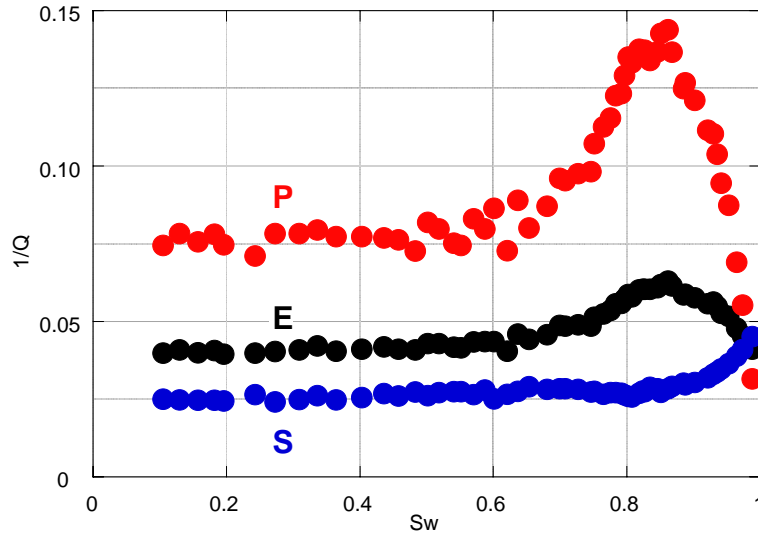


Figure 1. Resonance bar attenuation ($1/Q$) data in Massillon sandstone of 23% porosity (Murphy, 1982). Frequency is between 300 and 600 Hz. The E- and S-wave data (black and blue, respectively) are measured while the P-wave inverse quality factor (red) is calculated from these data according to Winkler (1980).

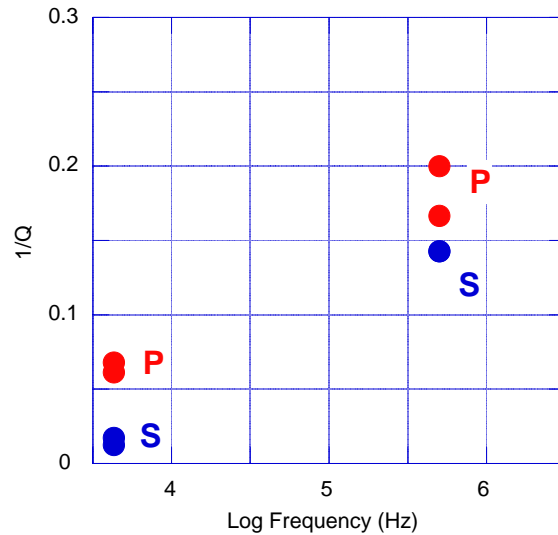


Figure 2. $1/Q$ in a water-saturated limestone sample (Lucet, 1989).

Reliable field data for Q_p^{-1} and Q_s^{-1} is even more sparse than lab data. Useful results are due to Klimentos (1995) who shows from well log data that the S-wave attenuation is approximately the same as the P-wave attenuation in liquid-saturated sandstone while in gas-saturated intervals the P-wave attenuation is much larger than the S-wave attenuation (Figure 3).

Sun et al. (2000) compute the P- and S-wave attenuation from monopole sonic data. The reported Q_p^{-1} and Q_s^{-1} are essentially the same in low-shale-content interval but may be different in the shale.

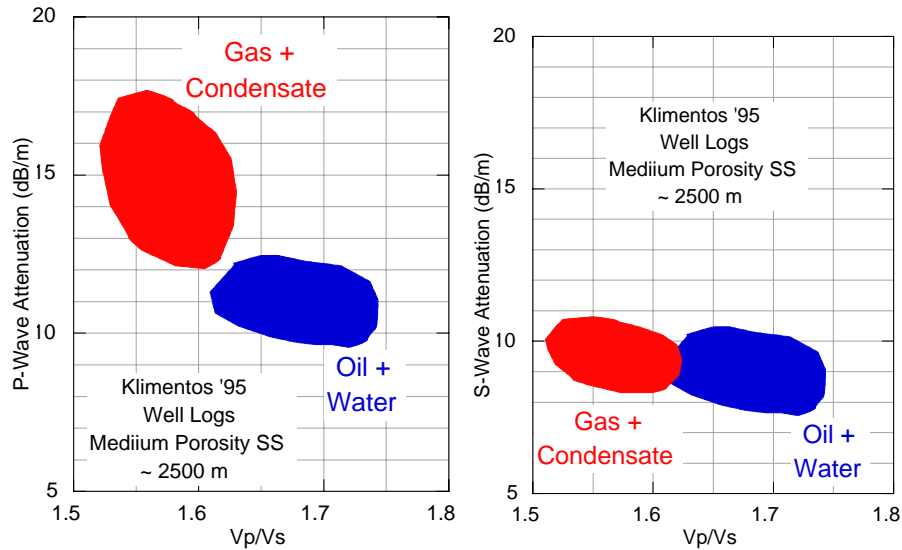


Figure 5. P and S-wave attenuation calculated from full-waveform sonic and dipole log data in medium-porosity sandstone with oil, water, gas, and gas condensate. After Klimentos (1995).

S-WAVE ATTENUATION THEORY

Attenuation and Modulus Dispersion

Our first assumption is that the inverse quality factor is related to the modulus-frequency dispersion by a viscoelastic causality relation, such as, e.g., for the Standard Linear Solid (Mavko et al., 1998):

$$2Q_p^{-1} = \frac{M_\infty - M_0}{\sqrt{M_0 M_\infty}}, \quad 2Q_s^{-1} = \frac{G_\infty - G_0}{\sqrt{G_0 G_\infty}}, \quad (1)$$

where M and G are the compressional and shear moduli, respectively, and the subscripts “ ∞ ” and “0” refer to the high- and low-frequency limits, respectively.

We will also assume that the S-wave attenuation is pore-fluid-independent and proceed with our analysis for fully-water-saturated porous sediment.

Compressional Modulus Dispersion

We will use the Dvorkin and Mavko compressional modulus dispersion theory in wet sediment (Dvorkin and Mavko, 2005; Dvorkin and Uden, 2004). This theory states that the necessary condition for attenuation is elastic heterogeneity in rock. The low-frequency compressional modulus is calculated by theoretically substituting the pore fluid into the spatially averaged rock’s dry-frame modulus while the high-frequency modulus is the spatial average of the heterogeneous saturated-rock modulus. The difference between these two estimates may give rise to noticeable P-wave attenuation if elastic heterogeneity in rock is substantial.

Link between P-wave and S-wave Modulus Dispersion

The physical basis for linking the compressional to shear modulus dispersion is the fact that there is a compressional element in shear deformation. Therefore, if a material

includes viscoelastic elements that are responsible for the frequency-stiffening in the deformation-deformation mode, they will contribute to the stiffening in the pure-shear-deformation mode. Mavko and Jizba (1991) use this principle to estimate the contribution of soft crack-like pores containing liquid to the shear-modulus dispersion at ultrasonic frequency at the pore-scale (the microscopic squirt-flow). They show that the dispersion of the inverse shear modulus is about 4/15 of that in the inverse bulk modulus.

We will use the same principle. Specifically, we will assume that the reduction in the compressional modulus of wet rock between the high-frequency limit and low-frequency limit is due to the introduction of a hypothetical system of aligned defects (cracks) into the material. Next, we will adopt Hudson's theory for cracked media (e.g., Mavko et al., 1998) to quantify these defects. Specifically, the reduction in the compressional modulus in the direction normal to the set of cracks is

$$\begin{aligned} M_\infty - M_0 &= \Delta c_{11}^{\text{Hudson}} \\ &\approx \varepsilon \frac{\lambda^2}{\mu} \frac{4(\lambda + 2\mu)}{3(\lambda + \mu)} \equiv \varepsilon \frac{4}{3} \frac{(M - 2G)^2}{G} \frac{M}{M - G} \end{aligned} \quad (2)$$

where $\Delta c_{11}^{\text{Hudson}}$ is the change in the anisotropic stiffness component; λ and μ are Lamé's constants of the background medium ($\mu \equiv G$); and ε is the crack density -- $\varepsilon = 3\phi/(4\pi\alpha)$ -- where ϕ is the porosity and α the aspect ratio. Assuming that $M = \sqrt{M_0 M_\infty}$ we find from Equations (1) and (2) that

$$\begin{aligned} 2Q_p^{-1} &= \frac{M_\infty - M_0}{\sqrt{M_0 M_\infty}} \\ &= \varepsilon \frac{4}{3} \frac{(M - 2G)^2}{G(M - G)} = \varepsilon \frac{4}{3} \frac{(M/G - 2)^2}{(M/G - 1)}. \end{aligned} \quad (3)$$

The corresponding change in the shear modulus for the same set of aligned defects is given by the stiffness component c_{44} . The change in this component ($\Delta c_{44}^{\text{Hudson}}$) due to the presence of cracks is

$$\begin{aligned} G_\infty - G_0 &= \Delta c_{44}^{\text{Hudson}} \\ &\approx \varepsilon \mu \frac{16(\lambda + 2\mu)}{3(3\lambda + 4\mu)} \equiv \varepsilon G \frac{16}{3} \frac{M}{3M - 2G}. \end{aligned} \quad (4)$$

Assume next that $G = \sqrt{G_0 G_\infty}$. Then Equations (1) and (4) yield

$$\begin{aligned} 2Q_s^{-1} &= \frac{G_\infty - G_0}{\sqrt{G_0 G_\infty}} = \varepsilon \frac{16}{3} \frac{M}{3M - 2G} \\ &= \varepsilon \frac{16}{3} \frac{M/G}{3M/G - 2}. \end{aligned} \quad (5)$$

By combining Equations (3) and (5) we find

$$\frac{Q_p^{-1}}{Q_s^{-1}} = \frac{1}{4} \frac{(M/G-2)^2(3M/G-2)}{(M/G-1)(M/G)}, \quad (6)$$

where

$$\frac{M}{G} = \frac{2-2\nu}{1-2\nu} = \frac{V_p^2}{V_s^2}, \quad (7)$$

and ν is Poisson's ratio.

In another variant of the same approach we may assume that the same set of defects is now randomly oriented in the material and thus does not introduce anisotropy. In this case the reduction in the isotropic shear modulus $\Delta\mu^{\text{Hudson}}$ is

$$\begin{aligned} G_\infty - G_0 &= \Delta\mu^{\text{Hudson}} \\ &\approx \varepsilon \frac{2}{15} \mu \left[\frac{16(\lambda+2\mu)}{3\lambda+4\mu} + \frac{8(\lambda+2\mu)}{3(\lambda+\mu)} \right]. \end{aligned} \quad (8)$$

In this case we find

$$\begin{aligned} 2Q_s^{-1} &= \frac{G_\infty - G_0}{\sqrt{G_0 G_\infty}} \\ &= \varepsilon \frac{16}{15} \left[\frac{2M/G}{3M/G-2} + \frac{M/G}{3(M/G-1)} \right] \end{aligned} \quad (9)$$

and, as a result,

$$\frac{Q_p^{-1}}{Q_s^{-1}} = \frac{5}{4} \frac{(M/G-2)^2}{(M/G-1)} \left[\frac{2M/G}{3M/G-2} + \frac{M/G}{3(M/G-1)} \right]. \quad (10)$$

Equations (6) and (10) present two versions for calculating Q_s^{-1} from Q_p^{-1} . It is important to remember that *in these calculations the wet-rock Q_p^{-1} has to be used*, i.e., in a hydrocarbon-saturated interval the original fluid has to be substituted for water and Q_p^{-1} calculated afterwards.

Finally, in the third variant of this approach we assume that the reduction in the compressional modulus is due to a set of randomly oriented isotropic defects and the same set of defects is responsible for the reduction in the shear modulus.

$$\frac{Q_p^{-1}}{Q_s^{-1}} = \frac{4}{3} \frac{1}{\lambda/\mu+2} + \frac{5}{12} \frac{(3\lambda/\mu+4)(3\lambda/\mu+2)^2}{(\lambda/\mu+2)(9\lambda/\mu+10)} \quad (11)$$

$$= \frac{1}{M/G} \left[\frac{4}{3} + \frac{5}{4} \frac{(M/G-2/3)(M/G-4/3)^2}{M/G-8/9} \right].$$

The Q_p^{-1}/Q_s^{-1} as given by Equations (6), (10), and (11) is plotted versus ν in Figure 7. The three curves due to the three equations used differ from each other. However, most importantly, they all predict Q_p^{-1}/Q_s^{-1} between 1 and 3 in the Poisson's ratio range between 0.30 and 0.35 which is typical for wet sediment. This predicted range of Q_p^{-1}/Q_s^{-1} matches the experimental observations.

CONCLUSION

A simple theoretical model offered here relates the P-to-S inverse quality factor ratio to the Poisson's ratio of the background sediment. It relies on a large number of assumptions that are not necessarily honored in real rock. Yet, the attenuation ratio provided by the model is realistic and matches experimental observations. The main result is that in wet rock the P- and S-wave quality factors are approximately the same.

The theory essentially assumes that the waves propagate normal to the bedding or, more precisely, normal to the hypothetical defects responsible for the modulus dispersion. In more rigorous treatment of the problem, the direction of wave propagation needs to be taken into account or, at least its effects on the errors evaluated.

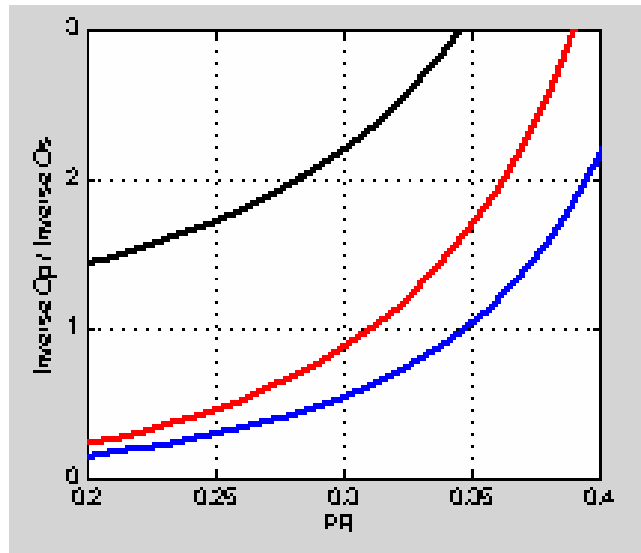


Figure 6. P-to-S inverse quality factor ratio versus Poisson's ratio. Blue curve (bottom) is from Equation (6), red curve (middle) is from Equation (10), and black curve (top) is from Equation (11).

ACKNOWLEDGEMENTS

The work was supported by Rock Solid Images, the US Dept. of Energy (under contract DE-FC26-04NT42243), and Stanford Rock Physics Laboratory.

REFERENCES

- Dvorkin, J., G. Mavko, J. Walls, M.T. Taner, N. Derzhi, 2003; Attenuation at Patchy Saturation – A Model, Proceedings of Annual EAGE Convention, Stavanger Norway, June 2-5.
- Dvorkin, J., and Uden, R., 2004, Seismic wave attenuation in a methane hydrate reservoir, *The Leading Edge*, 23, 730-734.
- Dvorkin, J., G. Mavko, and J. Walls, 2003; Seismic wave attenuation at full water saturation, Proceedings SEG Intl. Exposition and 73rd Annual Meeting, Dallas, TX, Oct 26-31.
- Klimentos, T., 1995, Attenuation of P- and S-waves as a method of distinguishing gas and condensate from oil and water, *Geophysics*, 60, 447-458.
- Lucet, N., 1989, Vitesse et atténuation des ondes élastiques soniques et ultrasoniques dans les roches sous pression de confinement, Ph.D. thesis, The University of Paris.
- Mavko, G., and Dvorkin, J., 2005, P-wave attenuation in reservoir and non-reservoir rock, Extended Abstract, EAGE 2005, Madrid.
- Mavko, G., and Jizba, D., 1991, Estimating grain-scale fluid effects on velocity dispersion in rocks, *Geophysics*, 56, 1940-1949.
- Mavko, G., Mukerji, T., and Dvorkin, J., 1998, *Rock Physics Handbook*, Cambridge University press.
- Murphy, W.F., 1982, Effects of microstructure and pore fluids on the acoustic properties of granular sedimentary materials, Ph.D. thesis, Stanford University.
- Sun, X., Tang, X., Cheng, C.H., and Frazer, L.N., 2000, P- and S-wave attenuation logs from monopole sonic data, *Geophysics*, 65, 755-765.
- Winkler, K.W, 1980, The effects of pore fluids and frictional sliding on seismic attenuation, Ph.D. thesis, Stanford University

Effects of pore fluid properties at high pressure and temperature on seismic response

*Joel Walls**, *Rock Solid Images and Jack Dvorkin*, *Rock Solid Images and Stanford University*

(Presented at SEG, 2005)

Summary

We use software from the National Institute of Standards and Testing (NIST) to assess the adiabatic bulk modulus and density of natural gas and brine at pressures up to 200 MPa and temperatures up to 200°C. The calculations are based on equations of state which are calibrated and verified by many experimental measurements. The results indicate that as pressure increases from the normal range of 20 to 50 MPa to the very high range of 150 to 200 MPa, the bulk modulus of methane may increase tenfold, from about 0.1 to about 1.0 GPa. The latter values are comparable to those for oil. For heavier hydrocarbon gases (ethane, propane, butane, and their mixtures) the modulus will be even higher.

This strong increase in the bulk modulus of natural gas may affect the seismic response of deep gas sands and, therefore, needs to be accounted for during the interpretation of deep-gas seismic events as well as in forward modeling. We show, using real well log data as input into synthetic seismic modeling, that although the character of the AVO response may be not affected by the pressure-related changes in gas properties, the magnitude of this response will be definitely affected.

Introduction

Commonly used fluid substitution equations by Gassmann (1951) indicate that the elastic properties of rocks, especially relatively soft sediments, can be strongly affected by the compressibility of the pore fluid. This difference in seismic properties is due to the strong difference between the bulk modulus of gas, oil, and water.

Because of the strong influence of the pore fluid properties on the seismic response, the industry needs to have reliable ways of estimating the bulk modulus and density of pore fluid, especially natural gas, versus pore pressure and temperature. Batzle and Wang (1992), in their classical Geophysics publication, provided equations that relate the bulk modulus and density of gas, oil, and water to gas gravity, oil gravity, gas-to-oil ratio, brine salinity, and, most important, pressure and temperature. These equations (BW) are widely used in the industry. Experiments on measuring the needed fluid properties continue (e.g., Han and Batzle, 2000). However, the pressure range of applicability of the BW equations as well as recent experiments does not extend beyond 50 MPa.

The normal pore pressure in the subsurface (in MPa) is approximately ten times the vertical depth in km. This means that 50 MPa occurs at approximately 5 km TVD. In overpressured formations, the pressure may be higher even at shallower depths. Also, tremendous amounts of domestic natural gas (55 Tcf offshore, according to MMS, and 135 Tcf onshore, according to USGS) may be available at depths below 15,000 ft (about

5 km TVD) and as deep as 25,000 ft (about 7.5 km). This promising domestic gas potential calls for improvements in the interpretation of very deep seismic events and, as part of this technical task, valid estimates for the bulk modulus and density of the pore fluid, especially gas, in deep reservoirs at very high pressure.

Comparison to Batzle-Wang (1992)

NIST provides two software packages, REFPROP7 for calculating the needed properties of natural gases, and NACL for calculating the properties of brine. Both packages provide adiabatic as well as isothermal properties, the former relevant to geophysics and the latter to petroleum engineering. The packages are based on equations of state calibrated by an extensive experimental database (e.g., Setzmann and Wagner, 1991).

Examples of calculations of the density and adiabatic bulk modulus for pure methane versus pressure at temperature 50, 125, and 200°C are shown in Figure 1. In the same figure we present curves calculated for the same conditions according to the Batzle and Wang (BW) equations. Although the BW equations have not been validated above 50 MPa, we use them in the entire range of pressure under examination.

The NIST and BW density curves for pure methane are essentially the same below 50 MPa and only slightly deviate from each other in the range between 50 and 200 MPa. The bulk modulus from NIST and BW are similar below 50 MPa and get progressively farther apart as pressure increases to 200 MPa. The maximum difference at the extreme conditions of 200°C and 200 MPa is about 25%. This means that the BW equations for the density of methane can be used with confidence at very high pressures, but the bulk modulus values at 100 MPa and above will be substantially underestimated.

Effect on Elastic Properties of Sand

In order to understand how the properties of methane at high pressure and temperature affect the elastic properties of sand, we select two high-porosity sand samples from the North Sea. One sample comes from the Troll field. It is friable and has 34% porosity and the room-dry P- and S-wave velocity 2.224 and 1.394 km/s, respectively. The other sample comes from the Oseberg field. It is slightly cemented fast sand of 30% porosity and the dry-room velocity 3.330 km/s for P- and 2.073 km/s for S-waves.

Gassmann's fluid substitution was used to calculate the impedance and Poisson's ratio (PR) of these two samples as the air in the pores was replaced by methane in the range of temperature and pressure considered in the previous section. During this exercise, the only variables were the density and bulk modulus of methane versus temperature and pressure.

The results shown in Figure 2 indicate that the impedance in both samples will be affected, although not strongly, by the changes in methane's properties due to temperature and pressure. The effect on PR is more pronounced, especially, in the softer Troll sample. In this sample, the increase in PR is from about 0.2 to about 0.3 as the pore

pressure varies between zero and 200 MPa. This change may eventually translate into the AVO type of a deep soft sand. The difference in the impedance curves between BW-92 and NIST results is small, as shown in Figure 2. However, Poisson's ratio is more sensitive to the differences, especially at certain combinations of pressure and temperature.

Effect on AVO

We use full-offset synthetic seismic modeling to evaluate how gas property change with pressure may affect the AVO signatures of gas sand. For this purpose we select a well with gas sand at the bottom (Figure 3). First we calculate synthetic seismic traces for the conditions existing in the well. Next we theoretically substitute the original gas in the pay at not-very-high pressure by gas at ultrahigh pressure, according to gas property calculations shown in Figure 1. This fluid substitution affects both the impedance and PR of the gas sand in the well. These elastic property changes affect the AVO response of the sand extracted from the synthetic gather. While for the real in-situ conditions the AVO response at the top of the sand is of Class 3, the response for the sand with gas at ultrahigh pressure is much weaker and merges towards weak Class 2.

Properties of Brine

We have computed the properties of NaCl brine versus temperature (from 25 to 250°C) and pressure (fixed at 100 MPa). The difference between the NIST model and BW-92 is minimal both for the density and bulk modulus.

Heavier Hydrocarbon Gases

To explore the effects of high pressure and temperature on gases other than methane, we also computed bulk modulus and density for pure ethane, propane, and butane. As shown in Figure 4, these computations show that for methane (specific gravity 0.56), BW-92 modulus is about 26% lower than NIST at 125 MPa and 200 C. For propane (specific gravity 1.52), BW-92 modulus is about 56% higher than NIST at 125 MPa and 200C. For butane (specific gravity 2.01) the differences are even larger.

Conclusions

Ultrahigh pressure may affect the properties of natural gas to a degree that translates into seismic signature type in very deep gas targets.

The Batzle and Wang equations and NIST model for NaCl brine give similar results for density and compressibility over a wide range of pressure and temperature. For gas density, BW-92 and NIST models give similar results over a wide range of pressure and temperature. However for adiabatic bulk modulus, there are substantial differences between BW-92 and NIST at high pressure and temperature, and the differences depend on the gas specific gravity.

Acknowledgement

This work was supported by Rock Solid Images and the US Dept. of Energy (under contract DE-FC26-04NT42243). We thank Eric Lemmon, Mark McLinden, and Marcia Huber of NIST for their help and advice.

References

Batzle M. and Wang Z., 1992, Seismic properties of pore fluids, *Geophysics*, 57, 1396-1408.

Gassmann, F., 1951, *Über die elastizität poroser medien: Vierteljahrsschrift der Natur. Gessellschaft*, 96, 1-23.

Han, D-H., and Batzle, M., 2000, Velocity, density and modulus of hydrocarbon fluids – data measurement, *Extended Abstract, SEG Annual 2000 Meeting*.

Setzmann, U. and Wagner, W., 1991, A New Equation of State and Tables of Thermodynamic Properties for Methane, *J. Phys. Chem. Ref. Data*, 20, 6, 1061-1151.

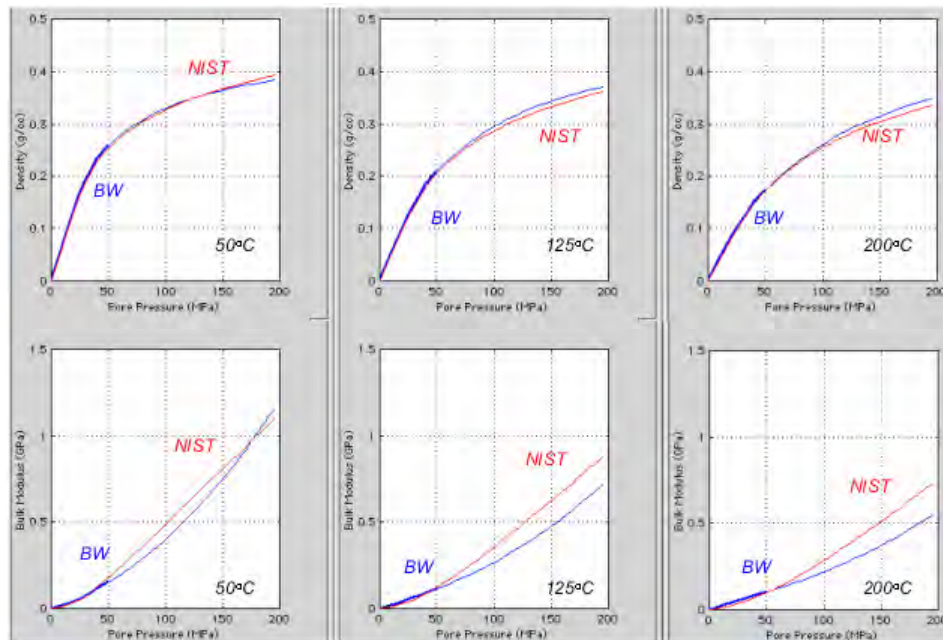


Figure 1. The density (top) and bulk modulus (bottom) of methane versus pressure and at varying temperature. The red curves are according to NIST while the blue curves are according to BW. The bold parts of the BW curves are for pressure below 50 MPa in which range the BW equations have been validated.

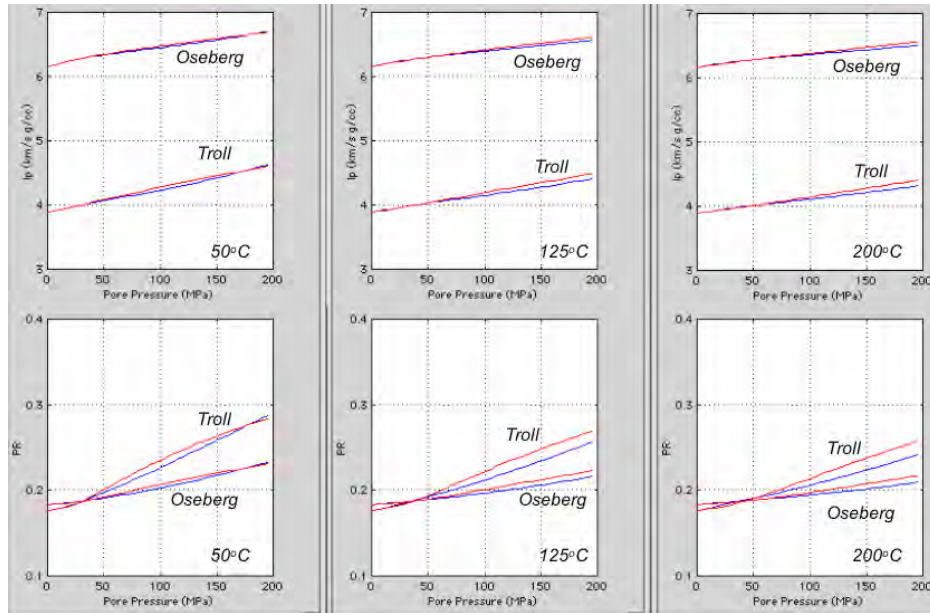


Figure 2. The impedance (top) and Poisson’s ratio (bottom) for the Troll and Oseberg samples versus pressure and at varying temperature. In these calculations the only variables were the density and bulk modulus of methane as displayed in Figure 2. The red curves are according to NIST while the blue curves are according to BW.

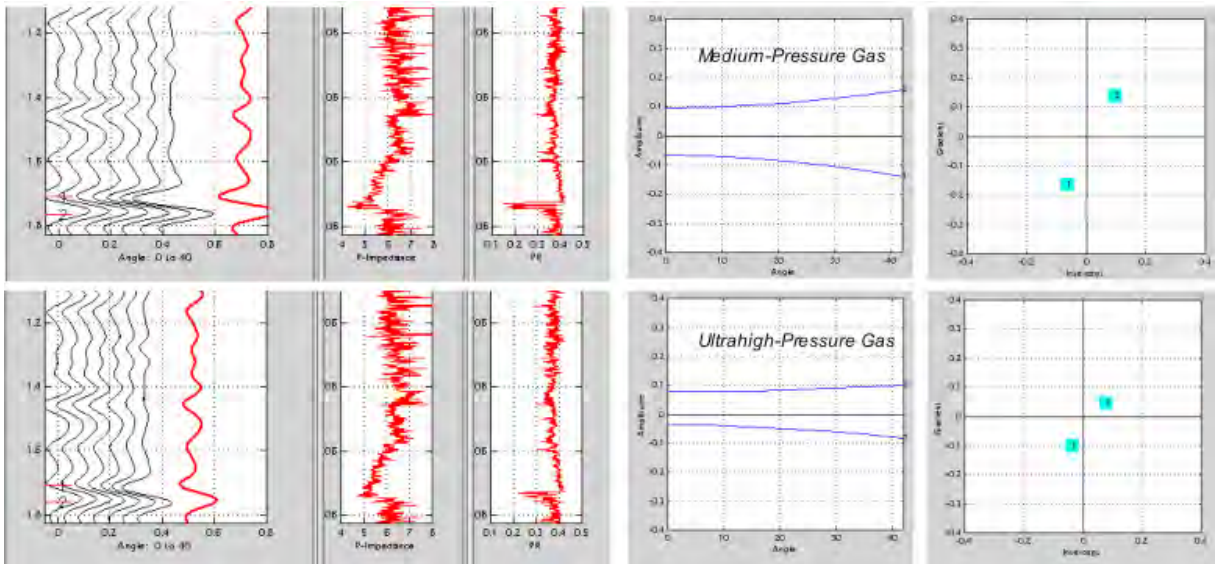


Figure 3. Synthetic seismic for a well with gas sand for the in-situ (top) and ultrahigh pressure (bottom) conditions. From left to right: gather (black) and stack (red); impedance and PR in the well; AVO curves extracted from the gather at the top of the sand (lower) and bottom of the sand (upper); gradient versus intercept for these AVO curves. The numbers in the large blue circles correspond to those at the AVO curves and at the gather.

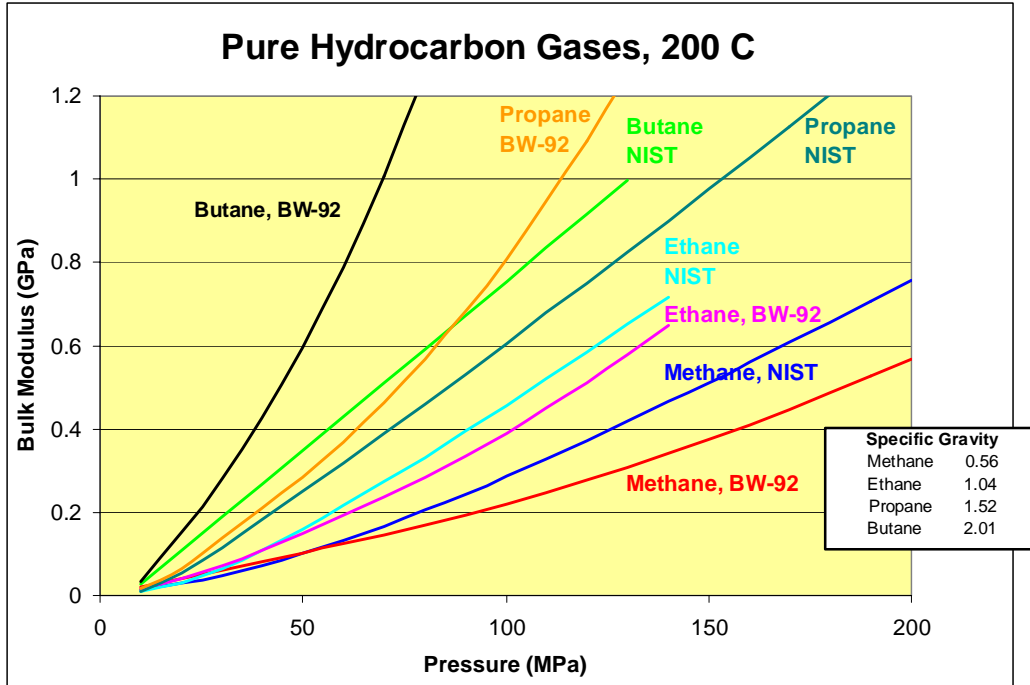


Figure 4: Effect of pressure on adiabatic bulk modulus of methane, ethane, propane and butane as computed by Batzle-Wang, 1992 and NIST model (200 C)

Q Estimation using Gabor-Morlet Joint Time-Frequency Analysis Techniques

Scott Singleton^{1}, M. Turhan Taner¹, Sven Treitel²*

¹Rock Solid Images, ²TriDekon, Inc.

(Presented at SEG, 2006)

Summary

Two new methods of Q estimation are presented for the first time. Both are based on Gabor-Morlet spectral decomposition. They differ substantially from traditional Q estimation methods which rely on the comparison of spectral characteristics of a shallow time window (approximating a seismic wave prior to encountering attenuation) with those of a deeper time window (after the wave has been attenuated). Instead, the fundamental principle in both new methods is a technique with which the spectral characteristics of each time interval are determined. We consider two data volumes. The first is the original data, while the second is the original data after it has compensated for attenuation effects by use of Gabor-Morlet spectral balancing. Both methods assume dispersion can be ignored, which of course is not strictly true because the Kramers-Krönig relations are then not satisfied. However, to a first approximation they give reasonable results.

Introduction

Research and development of algorithms to measure and compensate for the effects of attenuation in seismic data have been ongoing efforts for several decades. Taner and Treitel (RSI internal report, 2006) have tabulated 17 established as well as unproven Q estimation methods, and one established Q compensation approach. Most of these methods are described in the published literature.

About $\frac{2}{3}$ of the Q estimation algorithms and the single Q compensation algorithm listed in Taner & Treitel (loc.cit.) were coded and tested. Many of these methods suggested the presence of intrinsic absorption in the seismic data, but their effectiveness and stability varied considerably, depending on the quality and processing history of the seismic data and on the rock properties. For instance, the AVO class of the rocks had a large influence on the probability of success. Most methods were able to image Class III bright spots but far fewer could image Class II or Class IIP (phase reversal) anomalies, most of which do not have distinct stacked amplitude signatures.

Two promising algorithms warranted further work following initial tests. Both methods make use of a Gabor-Morlet spectral decomposition technique known as Joint Time-Frequency Analysis (JTFA). The difference between the two algorithms lies in the particular Q measurement technique used following JTFA.

Method

Gabor-Morlet JTFA: The Gabor-Morlet transform and Joint Time-Frequency Analysis are now well-known and widely-used methods to analyze non-stationary data such as seismic records.

Gabor (1946) developed his Joint Time Frequency Analysis method (JTFA) by using an exponentially-tapered complex cosine wavelet with central frequencies linearly spaced on the frequency axis. Morlet, et. al. (1982) rejuvenated JTFA by again using Gabor wavelets, but now with the central frequencies equally spaced in octaves on the frequency axis. It can be shown that such spacing produces a constant wavelet shape (Morlet, et. al., 1982).

In the time domain, a so-called complex ‘‘Gabor’’ wavelet $g(t)$ with shape factor b and angular frequency ω is:

$$g(t) = \exp(-bt^2)\exp(i\omega t) \quad (1)$$

Its Fourier amplitude spectrum is a tabulated definite integral, and can be written as:

$$G(\omega) = \int_{-\infty}^{\infty} g(t)\exp(-i\omega t)dt = \sqrt{\frac{\pi}{b}} \exp\{-(\omega - \omega_c)^2 / 4b\} \quad (2)$$

where ω_c is the centroid frequency at which $G(\omega)$ is maximum.

We prefer Gabor-Morlet wavelets because they produce a stable (non-ringing), smooth spectrum consisting of a summation of a finite set of spectral sub-bands with minimal overlap. In turn, this means that the individual, sub-band wavelets are properly coupled without intervening voids.

Spectral Balancing: Most Q estimation methods rely on the comparison of a shallow time interval with a deeper time interval that has been attenuated as a result of intrinsic absorption. On noise-free synthetics with stationary wavelets these methods usually work well. However, on seismic data they can be problematic because the wavelets tend to be non-stationary.

Our Q estimation method attempts to overcome this pitfall. Its key component is that the original attenuated data is compared to the same time interval from which the intrinsic absorption effects have first been estimated, then removed.

‘‘ Q compensation’’ is the process that corrects both the amplitude and phase spectra of seismic data for the effects of attenuation. The Kramers-Krönig relations are satisfied when this type of correction is made. Spectral balancing, on the other hand, corrects only the amplitude spectrum for the effects of propagation through an inelastic medium. The phase spectrum is *not* corrected for dispersion that, theoretically, must always accompany intrinsic absorption. Our assumption is that dispersion can often be ignored, and, thus, the spectrally balanced section adequately represents data without Q effects.

JTFA Frequency Shift Method of Q Estimation: Attenuation can be viewed as the action of a low-pass pass filter: it suppresses higher frequencies proportionally more than

lower frequencies. Thus if we can measure the overall frequency shift in the data, we can estimate relative and/or approximate Q .

In this method, our goal is to estimate anomalously absorptive zones in the data. Thus, our central task is to eliminate extrinsic attenuation (scattering) effects, while at the same time preserving anomalously attenuating zones that have undergone intrinsic absorption. This is achieved by trend removal where we assume the trend represents an attenuation profile that progressively increases with time and is caused by scattering effects.

To do this, we first spectrally balance the data. Then the original data is subtracted from the spectrally balanced data. The difference will show anomalous zones as well as trend differences between the original and spectrally balanced data. Finally, we compute the mean frequency of this residual data:

$$\tilde{f} = \sum_i f \cdot |G_i(f)| / \sum_i |G_i(f)| \quad (3)$$

where $|G_i(f)|$ are the sub-band amplitude spectra.

An areal trend line is fit through the residual data by means of a low pass filter applied to the mean frequency curves (3). This is done over a large number of traces. Anomalous zones are then assumed to be given by the residuals between the mean frequency curves (3) and the areal trend.

JTFA Log Spectral Ratio Method of Q Estimation: This method is similar to the Frequency Shift method, except that the natural log of the JTFA spectrum is taken and solved directly for $1/Q$. Consider the expression:

$$A(f, t) = A(f, 0) \exp(-\pi ft / Q) \quad (5)$$

where f is the circular frequency in Hz, $A(f, t)$ is the Joint Time Frequency (JTF) spectrum of the observed attenuated trace, $A(f, 0)$ is the JTF spectrum of the *spectrally balanced* trace, and $\exp(-\pi ft / Q)$ is the (non-dispersive) attenuation operator describing our basic Q model:

$$A_t(f) = A_0(f) \exp(-\pi ft / Q) \quad (6)$$

Taking natural logs of both sides of (5):

$$\text{Ln}\{A(f, t)\} - \text{Ln}\{A(f, 0)\} = -\pi ft / Q \quad (7)$$

from which we obtain the desired value of $1/Q$:

$$1/Q = [\text{Ln}\{A(f, 0)\} - \text{Ln}\{A(f, t)\}] / \pi ft \quad (8)$$

Because this method follows directly from the basic description of an inelastic medium, it can be expected to give a measure of total, or “apparent”, attenuation.

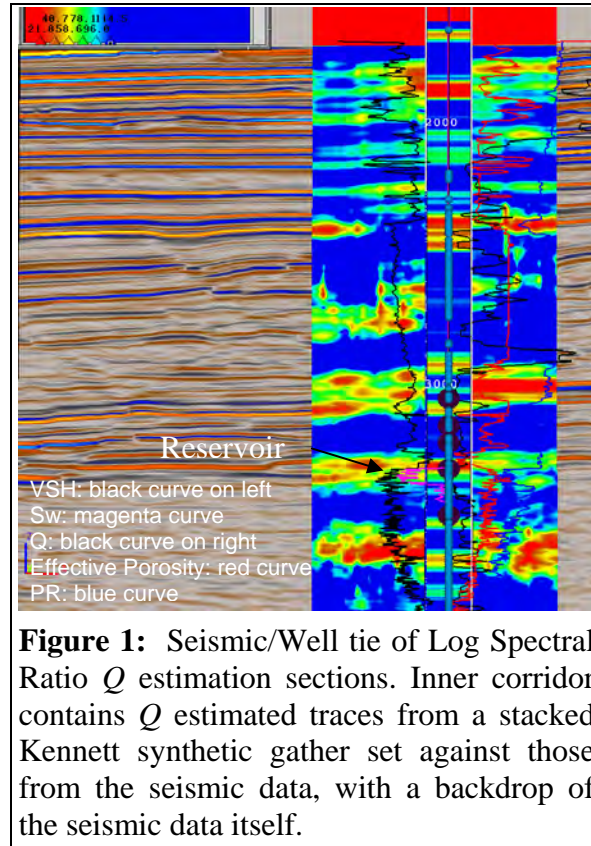
Results

To date, 8 data sets have been tested with these two Q estimation algorithms. Three of the data sets failed to detect attenuation in the intervals in which well control indicated probable intrinsic absorption. However, all three were of marginal quality. It is possible that inappropriate processing algorithms may have been used in an attempt to improve the data quality. This could have ended up removing or significantly altering the attenuation profile of the data. Thus, lesson #1 to be learned is to be very selective of data sets on which Q estimation is to be attempted.

Of the 5 remaining data sets, 3 will be presented verbally (all show different AVO class behavior) but due to space limitations only one will be shown in the present abstract. This data set has an AVO Class II response on the gathers, and so the reservoir top is represented by a trough. However, this trough is only of moderate amplitude on stacked sections (Figures 1 and 2).

Calibration of each data set is achieved by tying VSP corridor stacks and synthetics to the seismic data, and then applying the Q estimation algorithms to these tied data. Full-offset, wave equation synthetics were used (Kennett, 1974; Kennett and Kerry, 1979). These synthetics can be computed in the presence or absence of both multiples and intrinsic attenuation. If attenuation is to be modeled, a Q log must be available. Our Q log is one generated with the Dvorkin Heterogeneous Method (Dvorkin and Uden, 2004; Dvorkin and Mavko, 2006).

The tie achieved between the synthetic and seismic Q estimated sections is good, especially in the lower portion which contains the reservoir zone (Figures 1 and 2). In some places there appear to be two or more closely spaced attenuation zones on the synthetics, yet only a single broad zone appears on the seismic data. This is probably due to higher resolution of the synthetic in the noise-free case.

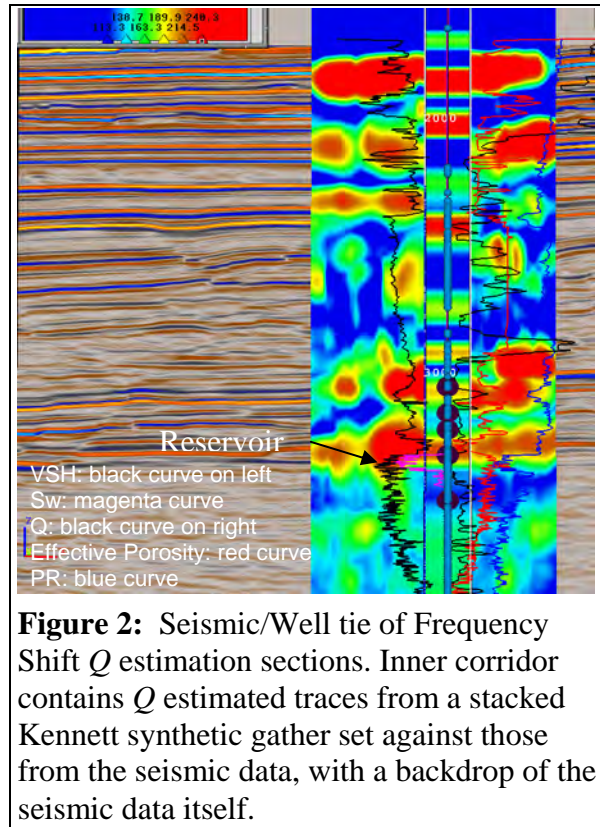


Lateral variation of seismic attributes along a mapped horizon is important because this tells us the distribution of calibrated, and thus known, rock properties. In our initial tests, lateral variations of the inelastic Q measurements were calibrated using AVO (elastic) attributes such as intercept and gradient, as well as the principal components of intercept and gradient (Figures 3 and 4). Principal component 2 (PC2, the distance away from the mudrock line) is a very good indicator of AVO anomalies. When PC2 is combined with either PC1 or the gradient itself, the AVO class can be determined in addition to its magnitude. (For details on Principal Component Analysis, see Hotelling, 1933, or Smith, 2002)

In this data example, the well appears to be on the edge of a gradient anomaly which extends off to the upper left (Figure 3). The PC2 attribute reveals that this anomaly is milder than first thought, and that more pronounced anomalies exist further away and down-dip from the well (Figure 4).

The Q estimation responses differ considerably (Figures 5 and 6), which is to be expected from the theoretical development given earlier. The Log Spectral Ratio method is usually a good measure of total, or “apparent”, attenuation (defined as the harmonic average of intrinsic attenuation, or absorption, and extrinsic attenuation, or scattering). However, the Frequency Shift method seems to respond more to intrinsic absorption. This method is sensitive to amplitudes and will typically produce anomalies if high amplitudes are

present. On the other hand, in an AVO Class IIP environment where no stack amplitudes are present, this method will show no response.



Thus, both methods must be used in conjunction (except in AVO Class IIP environments where special care must be exercised). For instance, comparison of Figures 5 and 6 shows that both methods produce anomalies that overlap in part, including the region surrounding the well location showing the gradient anomaly. Those areas with overlaps are thus good candidates for further investigation with other analytical reservoir characterization tools.

Conclusions

Two different methods for Q estimation of seismic data have been presented. These two methods, while differing in their measurement technique for Q and in their response to attenuation, are nevertheless based on the same principle. The technique is Gabor-Morlet Joint Time-Frequency Analysis, and it is used to separate the frequency spectra into discrete, well-behaved bands.

The new Q -measurement technique presented here is the comparison of frequency bands within the *same time interval* by spectrally balancing the frequency bands to approximate the seismic section as it would appear before having undergone attenuation (if dispersion is ignored). The spectrally balanced section can then be compared with the original section to derive an estimate for attenuation

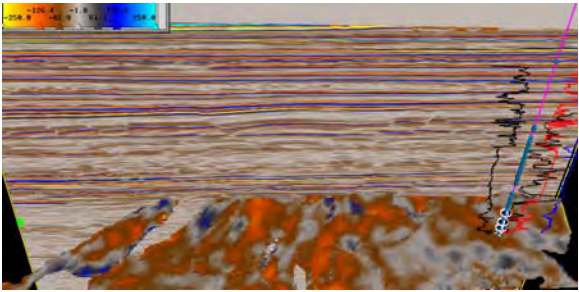


Figure 3: Horizon at top of reservoir zone (trough on seismic data). Gradient amplitude is shown drap on surface. High negatives indicate potential AVO anomalies. Well logs are same as on Figures 1 & 2. Seismic data is in background

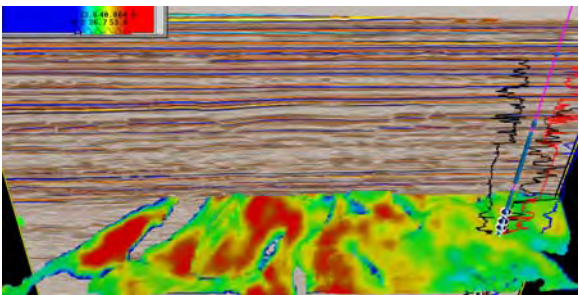


Figure 4: Horizon at top of reservoir zone (trough on seismic data). Principle Component 2 amplitude is shown drap on surface. Values indicate distance from mudrock line, positive is an AVO anomaly at top of reservoir. Well logs are same as on Figures 1 & 2. Seismic data is in background.

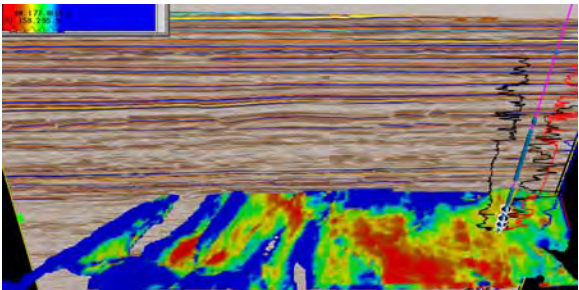


Figure 5: Horizon at top of reservoir zone (trough on seismic data). Log Spectral Ratio Q Estimation amplitude is shown drap on surface. Low values (in red) indicate attenuation (Q) anomalies. Well logs are same as on Figures 1 & 2. Seismic data is in background.

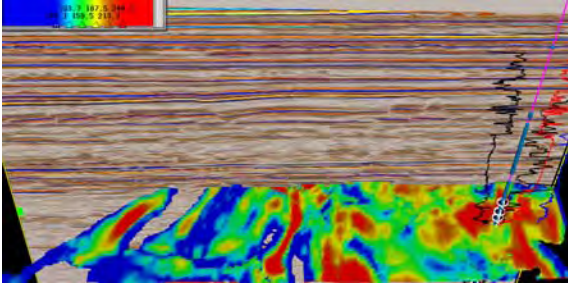


Figure 6: Horizon at top of reservoir zone (trough on seismic data). Frequency Shift Q Estimation amplitude is shown draped on surface. High values (in red) indicate attenuation ($1/Q$) anomalies. Well logs are same as on Figures 1 & 2. Seismic data is in background.

References

Dvorkin, J., and Uden, R., 2004, Seismic Wave Attenuation in a Methane Hydrate Reservoir, *The Leading Edge*, 23, 730-732 (August 2004).

Dvorkin, J., and Mavko, G., 2006, Modeling Attenuation in Reservoir and Non-reservoir Rock, *The Leading Edge*, 25, 194-196 (Feb. 2006).

Gabor, D., 1946, Theory of communication, *J. IEEE* 93, 429-457.

Hotelling, H., 1933, Analysis of Complex Statistical Variables with Principal Components, *Journal of Educational Psychology*, 24, 417-420.

Kennett, B.L.N., 1974, Reflections, Rays, and Reverberations, *Bulletin of the Seismological Society of America*, 64, #6, 1685-1696.

Kennett, B.L.N., and Kerry, N.J., 1979, Seismic Waves in a Stratified Half Space, *Geophysical Journal of the Royal Astrological Society*, 57, 557-583.

Morlet, J., Arens, G., Fourgeau, E. and Giard, D., 1982, Wave propagation and sampling theory - Part II: Sampling theory and complex waves, *Geophysics*, 47, 222-236.

Smith, L. I., 2002, A Tutorial on Principal Components Analysis, http://csnet.otago.ac.nz/cosc453/student_tutorials/principal_components.pdf.

Acknowledgements

We wish to thank Statoil for allowing us to use their data and to present it in this abstract. This work was done as part of the Rock Solid Images Lithology and Fluid Prediction Consortium and US Dept. of Energy contract DE-FC26-04NT42243.

APPENDIX 2:
Deep Gas Exploration using P and S Wave Seismic Attenuation
(Article Submitted to Gas Tips)

Project # DE-FC26-04NT42243

Contributors

Dr. Joel Walls*

Dr. M. T. Taner*

Richard Uden*

Scott Singleton*

Naum Derzhi*

Dr. Gary Mavko**

Dr. Jack Dvorkin**

*Principal Contractor:

Rock Solid Images

2600 S. Gessner Suite 650

Houston, TX, 77036

**Subcontractor:

Petrophysical Consulting Inc.

730 Glenmere Way

Emerald Hills, CA, 94062

Introduction

Deeply buried gas reservoirs along the Gulf of Mexico shelf are an important future energy resource for the US. One of the greatest problems encountered by operators in this area is identifying commercially viable targets for drilling. This is largely because most common 3D seismic methods for direct hydrocarbon indication (DHI), such as amplitude versus offset (AVO) are not reliable at great depths. Many wells have been drilled on deep AVO anomalies, only to find non-commercial quantities of gas (the so called “fizz-water” problem). Other problems in detecting deep sweet spots result from inadequate offset in the seismic data acquisition and high fluid pressures, which tend to make gas look more like water in a seismic data volume.

In 2004, Rock Solid Images undertook a DOE funded project to demonstrate novel and robust techniques for reducing hydrocarbon indicator risk in deep gas sands by exploiting an additional set of completely independent indicators – the rock inelastic properties. Inelastic rock properties are often expressed as a “quality factor” or simply “Q”. These inelastic properties of P-wave and S-wave energy (Q_p and Q_s) from multi-component seismic provide a crucial added dimension that can be used to discriminate pore fluids and lithology.

The objective of this project was to develop and test a new methodology for computing P-wave and S-wave attenuation from standard well log data, using the well log-derived attenuation for generating P-wave synthetic seismic traces with and without attenuation effects, and then extracting seismic attenuation attributes from multi-component P-wave and S-wave seismic data and relating these to the presence of oil or natural gas.

These goals were achieved, resulting in a new algorithm to compute both Q_p and Q_s from conventional well log data, an algorithm to create full offset, full waveform synthetics incorporating the effects of attenuation, and two algorithms to compute attenuation from seismic data. The primary findings from this project were that P- and S-wave attenuation in seismic data:

- 1 can be related to gas-bearing reservoirs
- 2 can be used as a reconnaissance tool in exploration
- 3 can have a substantial impact on seismic response, both post-stack and pre-stack, and cause significant changes in seismic amplitude with offset, especially at the bottom of a gas zone
- 4 should be used in conjunction with other seismic attributes such as elastic attributes and geologic context in order to reduce risk in the search for direct hydrocarbon indicators
- 5 can be a valuable tool in deep targets because AVO may fail in these environments.

The Field Experiment

Multi-component, Ocean Bottom Cable (OBC) seismic data were obtained from Seitel Data Inc. (Seitel) located in the Eugene Island area of the Gulf of Mexico. The OBC system deployed 4 receiver components - 3 orthogonal geophones plus 1 hydrophone. This data was processed to PP (P-wave down, P-wave up) and PS (P-wave down, S-wave up) stack volume reflection amplitudes by Seitel over the total area shown in Figure 1 (left).

Data for this project was acquired over the southern area (approximately 20 x 10 km) shown in Figure 1 (right) covering partly or fully Eugene Island blocks EI306 - 310, EI313 - 317 and EI328 - 332.

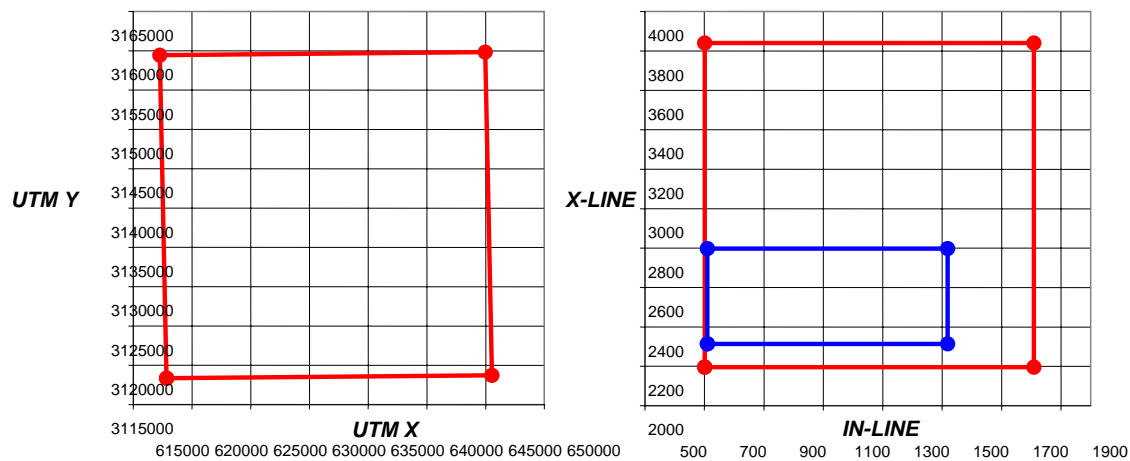


Figure 1: the total survey area - left panel in UTM coordinate space; the total survey area (red) and project area (blue) in seismic IN-LINE and X-LINE coordinate space.

Amplitude and Attenuation from the PP Data

Interesting results from a qualitative standpoint are seen on XLINE 2360 between 4000 and 4500 ms (Figure 2). Two different fault blocks are evident from the seismic amplitude display and both attributes show attenuation for the events at the top of the fault blocks. These events maintain their inelastic attribute response laterally away from this XLINE.

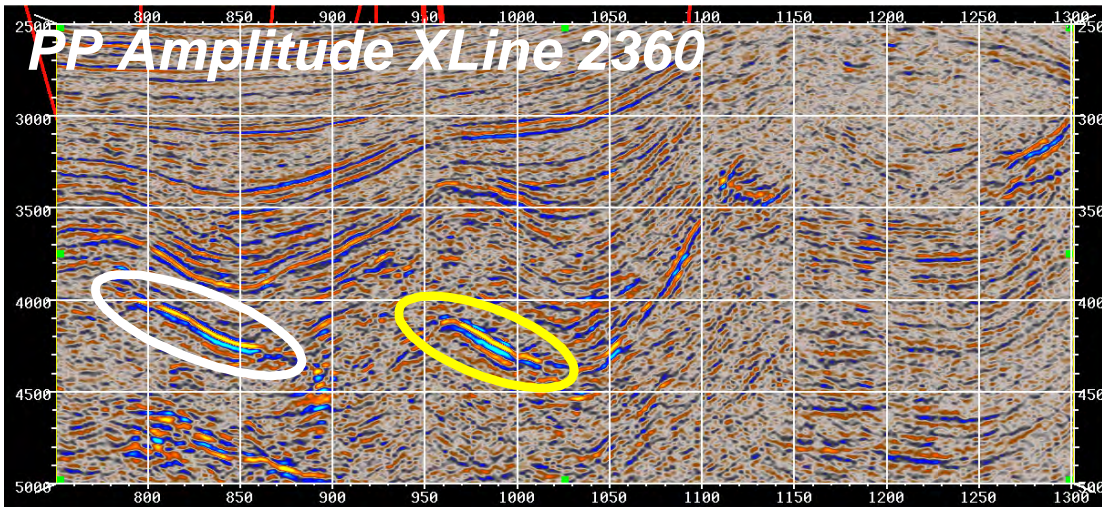


Figure 2a: XLINE 2360 PP stack amplitude

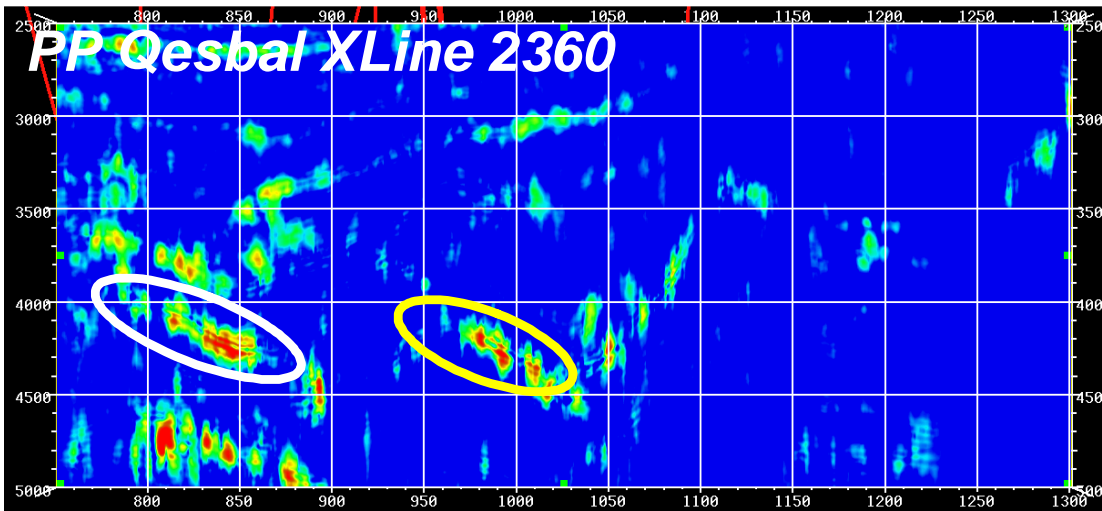


Figure 2b: XLINE 2360 PP Frequency Shift Q attribute response

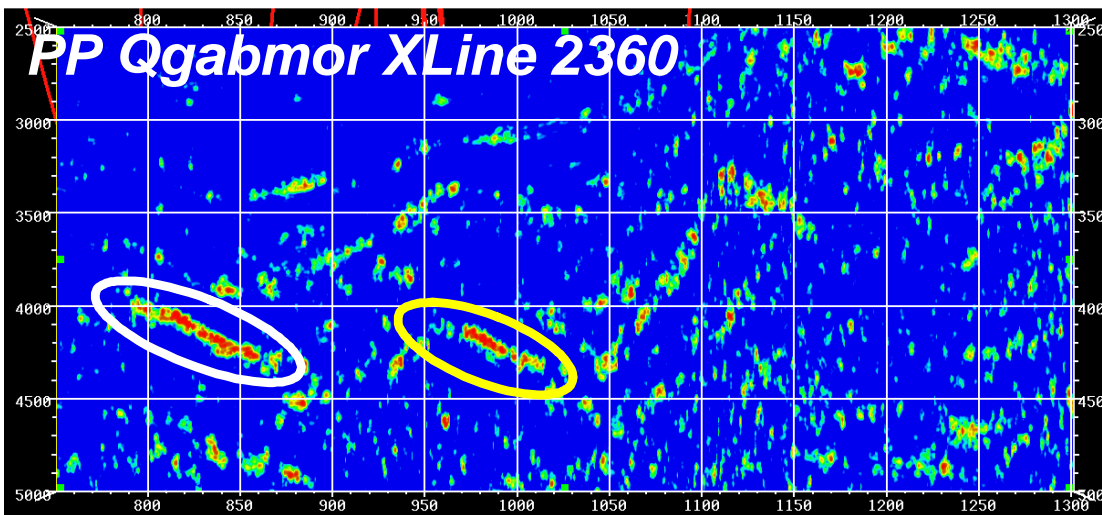


Figure 2c: XLINE 2360 PP Log Spectral Ratio Q attribute response

Figures 2b and 2c show that the Log Spectral Ratio Q estimation attribute has higher temporal resolution than the Frequency Shift Q estimation attribute but increased noise content. The Frequency Shift Q attribute indicates other event responses above and below the white circled event that are not seen as well on the Log Spectral Ratio Q attribute response.

This is important since the attributes are responding differently some of the time. The deeper Frequency Shift Q estimation event below the circled event corresponds to strong amplitudes in Figure 2a not evidenced by the Log Spectral Ratio Q estimation response.

Amplitude and Attenuation from the PS Data

Both inelastic attributes were generated from the PS stack data volume. The PS amplitude data in Figure 3a shows weaker amplitudes at depth. The PP time range of 4000 – 4500 ms is approximately equivalent to 7500 – 8100 ms PS time.

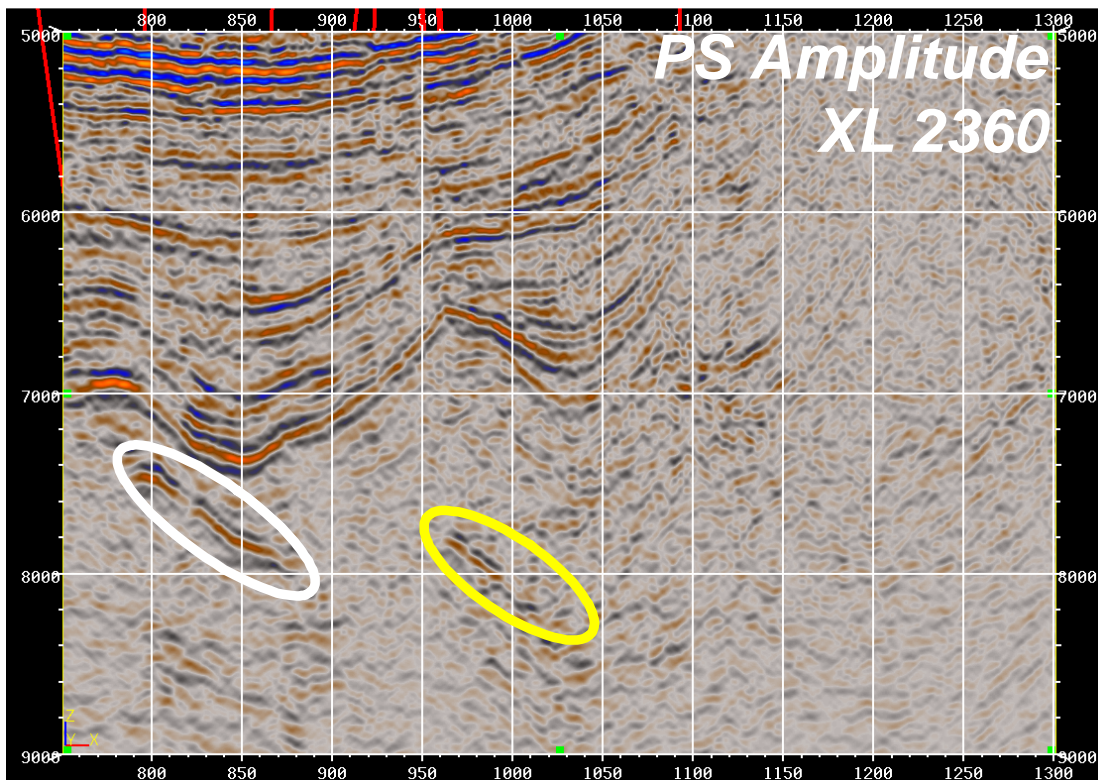


Figure 3a: XLINE 2360 PS stack amplitude

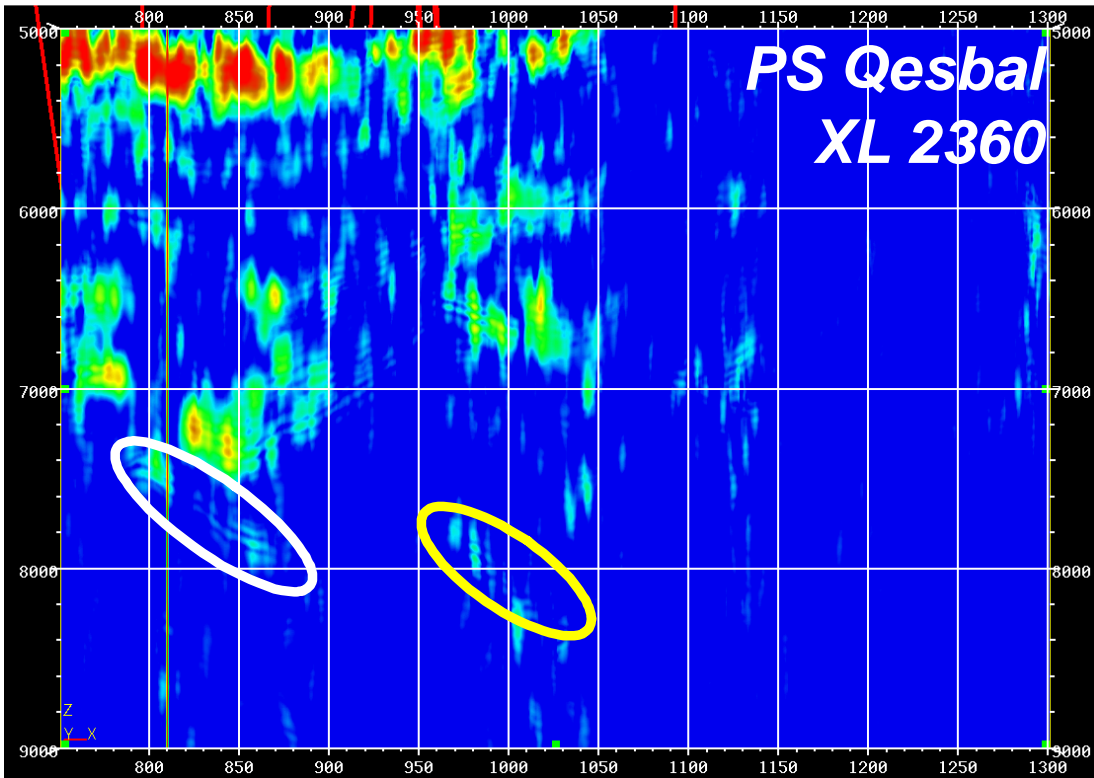


Figure 3b: XLINE 2360 PS Frequency Shift Q estimation attribute response

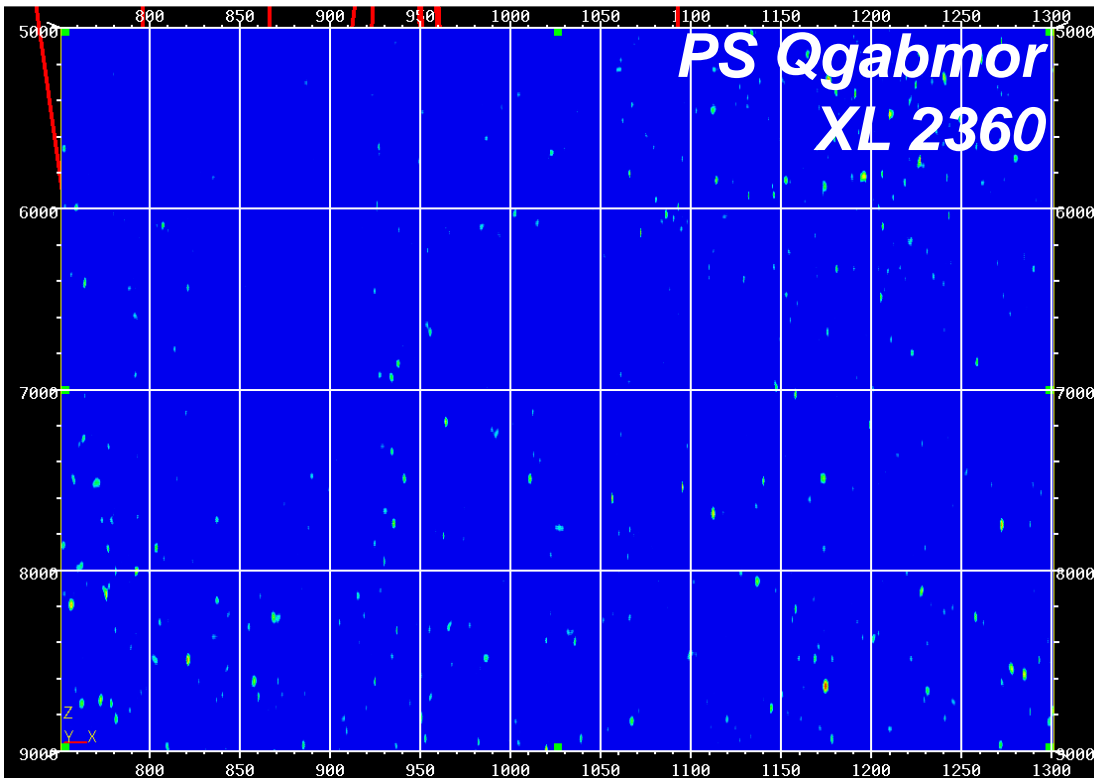


Figure 3c: XLINE 2360 PS Log Spectral Ratio Q estimation attribute response

The Frequency Shift Q estimation attribute shows a weak response at the top the white ellipse fault block but no response for the yellow ellipse event. A response is also seen for the syncline event just above the white ellipse event, similar to the response from the PP Frequency Shift Q estimation attribute. The Log Spectral Ratio Q estimation attribute shows no response anywhere in the section displayed, not even in the shallowest events up to 5sec PS time.

Discussion

Seismic Q Estimation on PP and PS Data: The PP amplitude data show indications of potential deep gas charged reservoirs. These data indicate a peak over trough response and if the phase of the response is close to zero-phase, then this would represent harder sand in slower shale background. This is quite possible given the overpressure evidenced by the velocity survey data analyzed previously, and considering that deep sand could be cemented to some extent.

The deep (6900-7400 ms) PS data has a lower bandwidth than the corresponding (3600-4000) PP data. This is mostly due to the slower propagation velocity of the PS compared to the PP data and warping the PS to the PP time will effectively double frequency band making the PS band approach that of the PP data.

The deep (4000-4500ms PP time) events are reasonably well imaged using PP data but the corresponding PS events (7300-7800ms PS time) are only partially imaged. This implies that the PS data might be able to be used to support the PP structural interpretation in exploration of deep gas targets but it would be difficult to use them alone.

From our theoretical work, the PP inelastic response for gas sand is expected to be strong, while the PS inelastic response for gas sand is shown to be basically flat. The PS response is a combination of the P and S reflection travel paths so we expect some intermediate response for PS as shown.

Analysis of these attributes on seismic data indicates that they do behave according to the theoretical models. The key in interpreting these attributes is finding strong responses with both algorithms, and this does occur at specific reflectors. Such reflectors can be viewed as high-graded prospects for hydrocarbon exploration.

Summary and Conclusions



In 2004, Rock Solid Images undertook a project to demonstrate novel and robust techniques for reducing hydrocarbon indicator risk in deep gas sands by exploiting an additional set of completely independent indicators – the rock inelastic properties. These inelastic properties of P-wave and S-wave energy from multi-component seismic provide a crucial tool that can be used to discriminate pore fluids and lithology.

The primary conclusions from this work are:

- 1 Rock physics methods can be used to compute both Q_p and Q_s from conventional well log data.
- 2 Q_p can be computed from PP and PS seismic data.
- 3 Attenuation can have a substantial impact on seismic response, both post-stack and pre-stack, and can cause significant changes in seismic amplitude with offset, especially at the bottom of a gas zone.
- 4 Attenuation in seismic data can be related to gas-bearing reservoirs, and can be used as a reconnaissance tool in exploration.
- 5 Attenuation should be used in conjunction with other seismic attributes such as elastic attributes and geologic context. However, attenuation can be a valuable tool in deep targets where AVO is less reliable.


The methods and tools developed in this project are now being used commercially by Rock Solid Images to help U.S.-based oil and gas exploration and production companies find and produce new gas resources in the U.S. Gulf of Mexico, onshore Texas, and Rocky Mountain region. In addition, Rock Solid Images has been granted a US patent (#7088639) based on an earlier DOE funded project on P-wave attenuation. The patent describes a comprehensive method for using seismic attenuation in hydrocarbon reservoir characterization.

APPENDIX 3:
FINAL PRESENTATION TO NETL/DOE
MORGANTOWN, PA
SEPTEMBER 5, 2006
(POWERPOINT)

  **DOE-NETL**

**September 6, 2006
Morgantown, WV**

**Novel Use of P-wave and S-wave
Seismic Attenuation for Deep
Natural Gas Exploration and
Development**

 **ROCK SOLID
images**

© 1998-2004 Rock Solid Images, all rights reserved

Industry Needs and Current Technology

Finding significant new gas resources in the Gulf of Mexico requires new geophysical methods that A) work at greater depths, and B) reduce uncertainty in direct hydrocarbon indication (DHI) from seismic data

Most current DHI methods depend on estimates of no more than two or three fundamental *elastic* seismic properties (P-velocity, S-velocity, and density, or combinations of them) while there can be many more lithologic and fluid unknowns. Our project was designed to demonstrate novel and robust techniques for reducing hydrocarbon indicator risk, by exploiting an additional set of completely independent indicators – the rock *inelastic* properties (attenuation, dispersion, Q).

Project Objectives

This project has focused on developing new technology to allow seismic data to be analyzed for attenuation effects to target deep gas exploration. The project focused on three major goals:

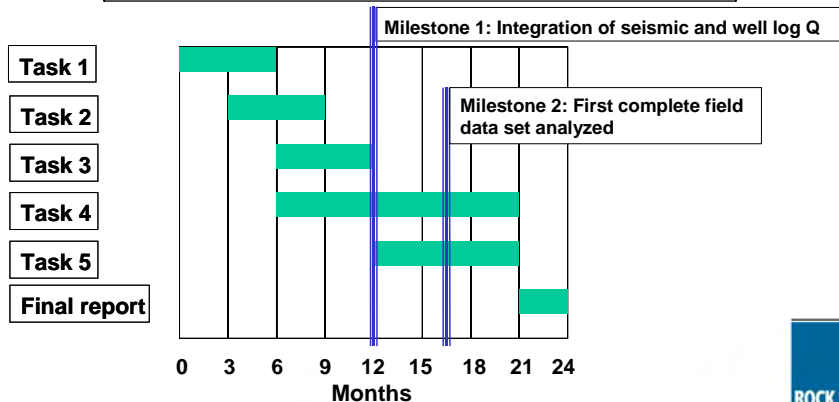
- Develop methods to compute P-wave and mode converted data attenuation from standard well log data such as porosity, V_{clay} and S_w .
- Develop methods to use the log-derived attenuation for generating P-wave and mode converted synthetic seismic traces with and without attenuation effects.
- Develop new methods to compute attenuation related attributes from reflection seismic data – both P-wave and OBC data.

These goals were accomplished, and we have shown through testing with different field examples, that attenuation related seismic attributes can be useful in identifying producing deep gas formations.

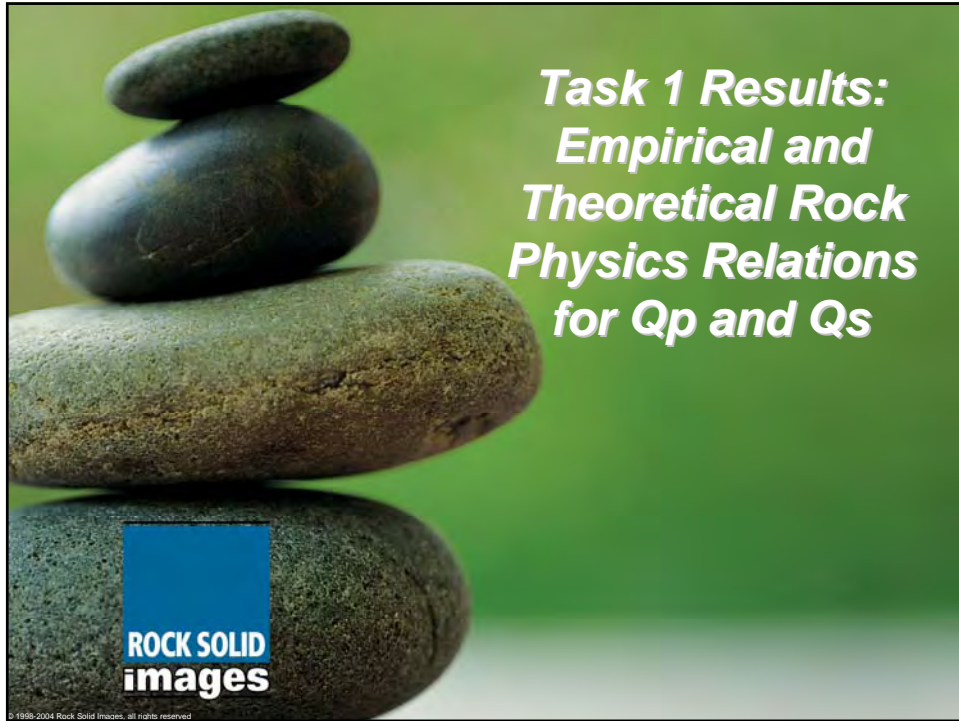
ROCK SOLID
images

Tasks, Timing

Task and Description
Task 1: Empirical and Theoretical Rock Physics Relations for Q_p and Q_s
Task 2: Log-based Synthetic Seismic Modeling with Q
Task 3: Properties of Pore Fluids at High Temperature and Pressure
Task 4: Linking Attenuation from Seismic To Logs (Milestone 1)
Task 5: Testing and Optimization with Field Data (Milestone 2)



ROCK SOLID
images



Qp Fundamentals Theory – Task 1

If the deformational response of a physical material to a load not only depends on the magnitude of this load but also on the rate of change of the load, the material is called viscoelastic.

In a viscoelastic medium, the modulus-frequency dispersion and inverse quality factor are linked by the causality Kramers-Kronig relations (Mavko et al., 1998):

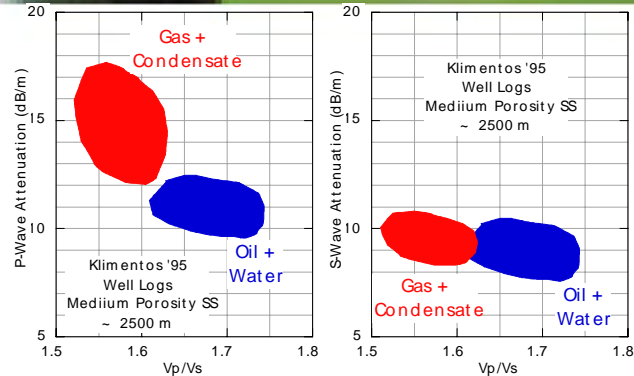
$$Q^{-1}(\omega) = \frac{|\omega|}{\pi M_R(\omega)} \int_{-\infty}^{\infty} \frac{M_R(\alpha) - M_R(0)}{\alpha} \frac{d\alpha}{\alpha - \omega},$$

$$M_R(\omega) - M_R(0) = \frac{-\omega}{\pi} \int_{-\infty}^{\infty} \frac{Q(\alpha) M_R(\alpha)}{|\alpha|} \frac{d\alpha}{\alpha - \omega},$$

where ω is the angular frequency and $M_R(\omega)$ is the real part of the complex modulus .



Qs Attenuation in Sediments – Task 1



Reliable field data for Q_p & Q_s is even more sparse than lab data.

Useful results are due to Klimentos (1995) who shows from well log data that the S-wave attenuation is approximately the same as the P-wave attenuation in liquid-saturated sandstone while in gas-saturated intervals the P-wave attenuation is much larger than the S-wave attenuation

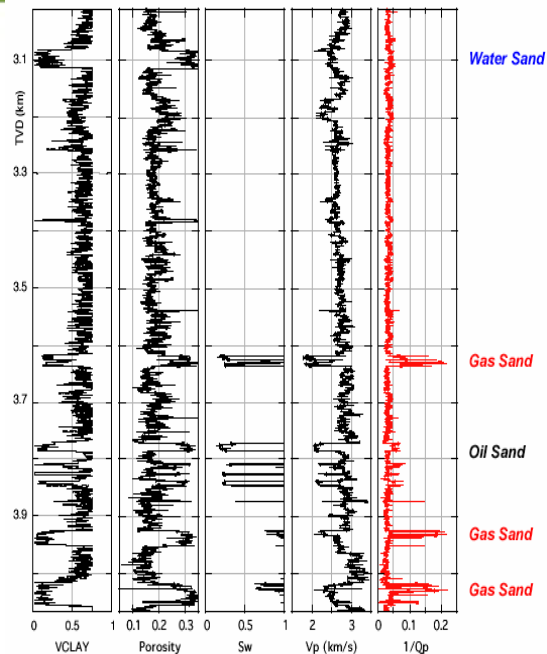
ROCK SOLID
images

Qp Fundamentals Example – Task 1

Well log data from a deep water (>3000 ft) gas well in central GOM was used as input to the Q computation module.

The input log curves and the output $1/Q_p$ curve (in red).

The results show that gas filled sands have considerably higher attenuation than surrounding wet silts and shale, suggesting that Q_p could be a possible direct hydrocarbon indicator.



Qs from Qp: Three Methods – Task 1

Qs is computed from Qp utilizing the link between compressional and shear modulus dispersion.

We assume that the reduction in the compressional modulus of wet rock between the high-frequency limit and low-frequency limit is due to the introduction of a hypothetical system of aligned defects (cracks) into the material (uses Hudson's cracked media theory).

$$\frac{Q_p^{-1}}{Q_s^{-1}} = \frac{1}{4} \frac{(M/G-2)^2(3M/G-2)}{(M/G-1)(M/G)}$$

A second variation is to assume that the crack alignment is random (no anisotropy).

$$\frac{Q_p^{-1}}{Q_s^{-1}} = \frac{5}{4} \frac{(M/G-2)^2}{(M/G-1)} \left[\frac{2M/G}{(3M/G-2)} + \frac{M/G}{3(M/G-1)} \right]$$

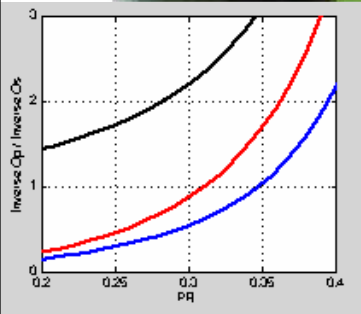
Remember that in these calculations the wet-rock has to be used, i.e., in a hydrocarbon-saturated interval the original fluid has to be substituted for water and calculated afterwards.

A third variation assumes that a set of randomly oriented isotropic defects is responsible for reductions in both compressional and shear modulus.

$$\begin{aligned} \frac{Q_p^{-1}}{Q_s^{-1}} &= \frac{4}{3} \frac{1}{\lambda/\mu+2} + \frac{5}{12} \frac{(3\lambda/\mu+4)(3\lambda/\mu+2)^2}{(\lambda/\mu+2)(9\lambda/\mu+10)} \\ &= \frac{1}{M/G} \left[\frac{4}{3} + \frac{5}{4} \frac{(M/G-2/3)(M/G-4/3)^2}{M/G-8/9} \right] \end{aligned}$$

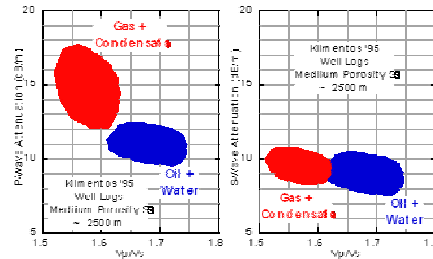
ROCK SOLID
images

Task 1 Summary



Three independent methods predict Qp/Qs between 1 and 3 for a Poisson's ratio range between 0.30 and 0.35 which is typical for wet sediment.

Predicted range from Method 2 (red) agrees with experimental observations.



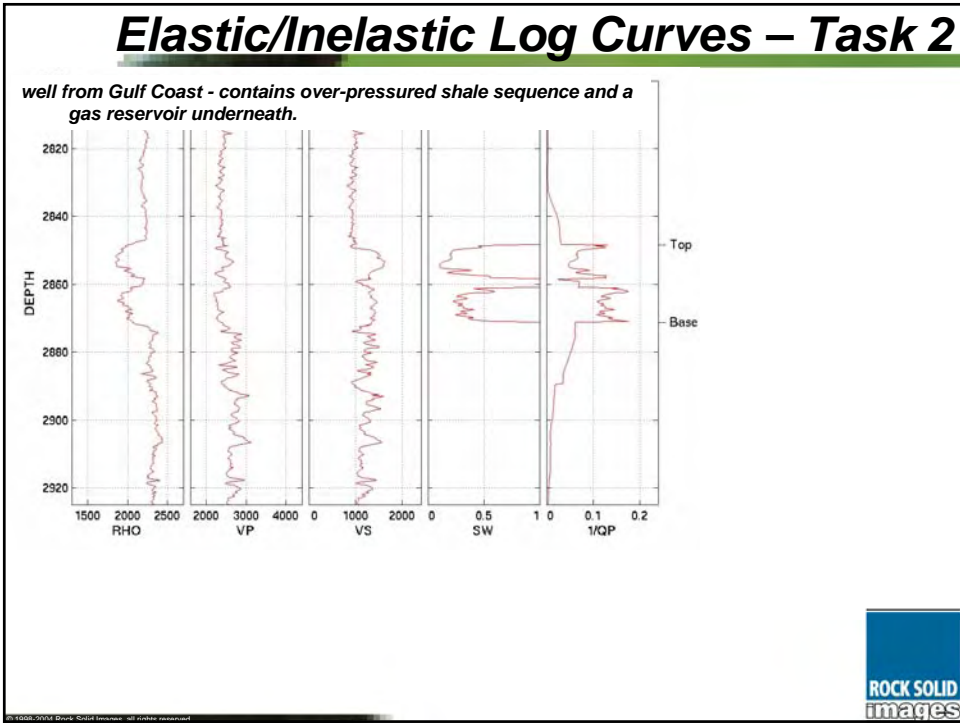
The simple theoretical model offered here relates the P-to-S inverse quality factor ratio to the Poisson's ratio of the background sediment. The attenuation ratio provided by the model is realistic and matches experimental observations. The main result is that in wet rock the P- and S-wave quality factors are approximately the same.

ROCK SOLID
images

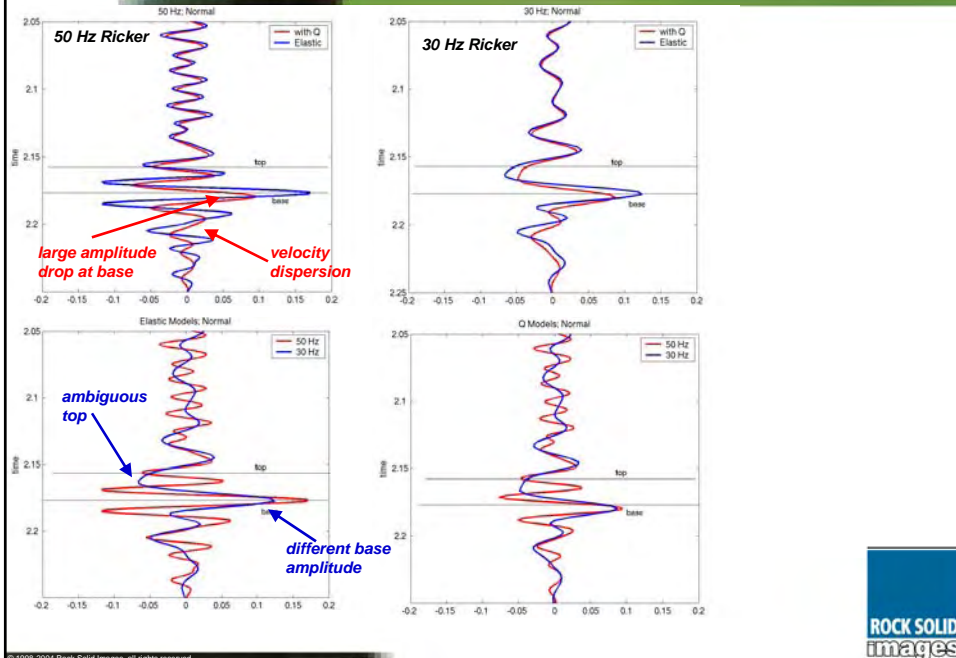
Task 2 Results: Log-based Synthetic Seismic Modeling with Q

ROCK SOLID images

© 1998-2004 Rock Solid Images, all rights reserved

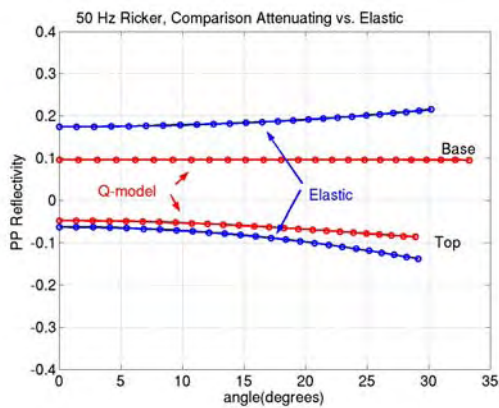


Normal Incidence Synthetics – Task 2



ROCK SOLID
images

AVO Responses – Task 2



Attenuation in the reservoir has a small impact on the top-gas amplitude, although the modestly attenuating overburden does reduce the top-gas reflection.

One effect that is evident from the top reflections is that the AVO gradient is reduced by the attenuating overburden, because the far-offset signals travel a longer path than the near offset signals, and therefore suffer greater losses.

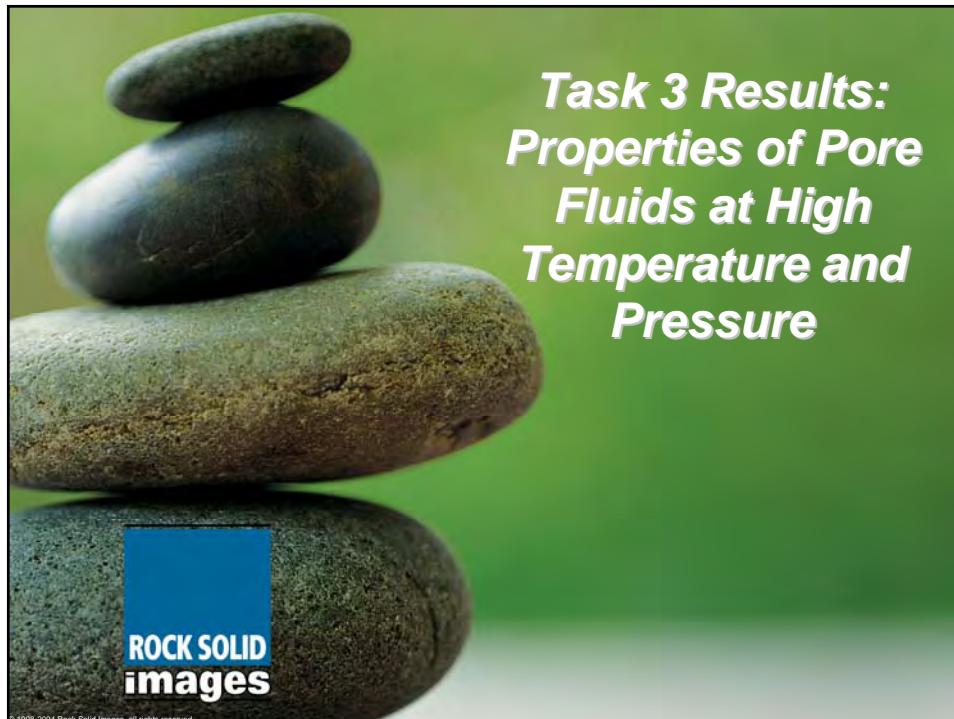
The base gas reflections in the attenuating model have amplitudes only about half of what we see in the elastic model. This is partly due to the overburden, but mostly due to large attenuation occurring in the gas reservoir itself.

ROCK SOLID
images

Task 2 Summary

1. *Lower frequencies lead to lower resolution.*
2. *Attenuation leads to velocity dispersion, both in the overburden and in the reservoir. This dispersion tends to delay arrivals in the attenuation model. The very low Q and large dispersion in the gas reservoir also leads to an apparently thicker reservoir (in time) relative to an elastic earth.*
3. *Attenuation in the overburden has a small effect on normal incidence amplitudes at the reservoir top. Although, attenuation in the overburden reduces the far offset amplitudes relative to the near offset amplitudes, because the far offset traces travel a longer path.*
4. *The large attenuation in the reservoir leads to greatly reduced base gas amplitudes and greatly reduced gradient.*
5. *The reduction in AVO gradient from attenuation could cause gas to be mistaken for oil, and oil to be mistaken for water.*
6. *Signatures of gas in this exercise are the increased-time thickness of the reservoir interval, lower impedances in the reservoir interval, and large contrasts in base amplitude relative to top amplitude due to attenuation in the reservoir.*
7. *Seismic bandwidth appears to be crucial in identifying the tops and the extent of the reservoir, as well as in estimating the uncertainty when matching synthetic and real seismic data.*

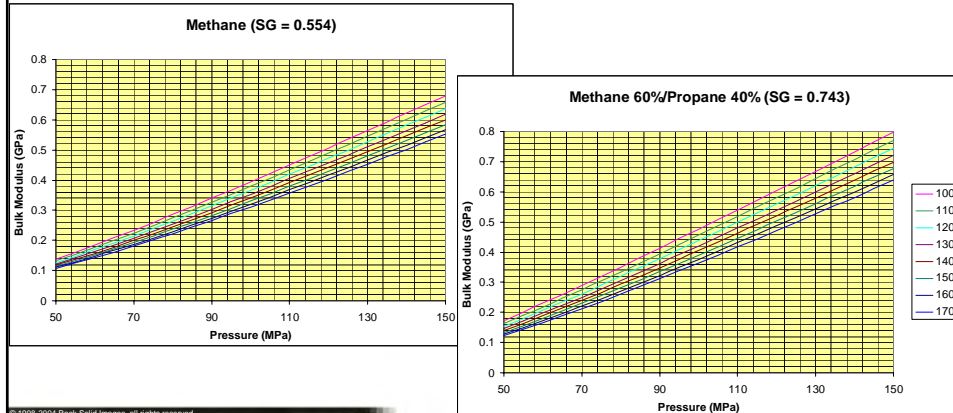
ROCK SOLID
images



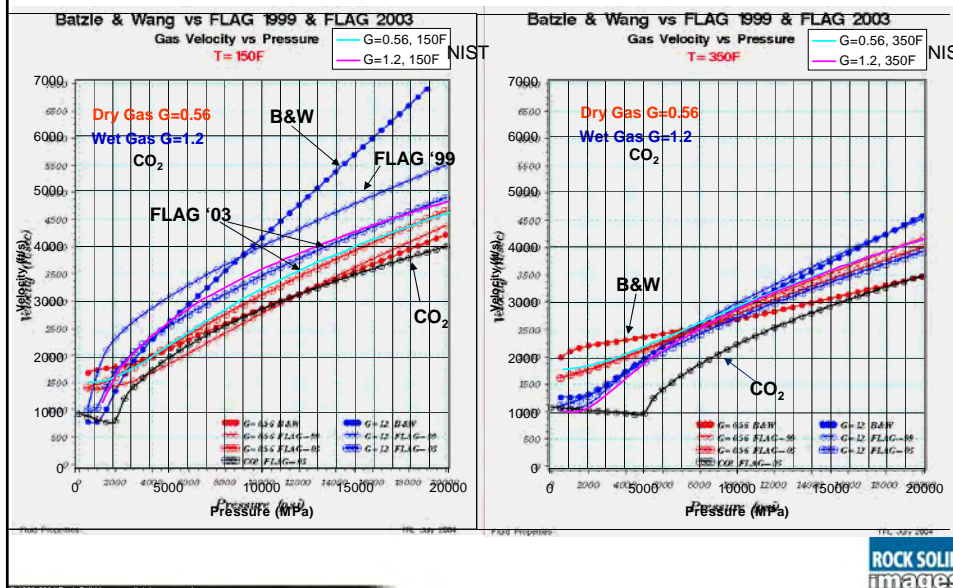
Properties of Pore Fluids HPHT – Task 3

We used the NIST published algorithms to compute the high temperature and pressure bulk modulus of methane gas and two mixtures of methane and propane.

The purpose of this work is to provide accurate pore fluid properties for rock physics calculations. Older methods such as Batzle-Wang, 1992 can give adiabatic bulk modulus values that are in error by as much as 25%. We provided tables and plots for the gas properties over a range of pressure from 50 mPa to 150 mPa and at temperatures ranging from 100 C to 170 C.



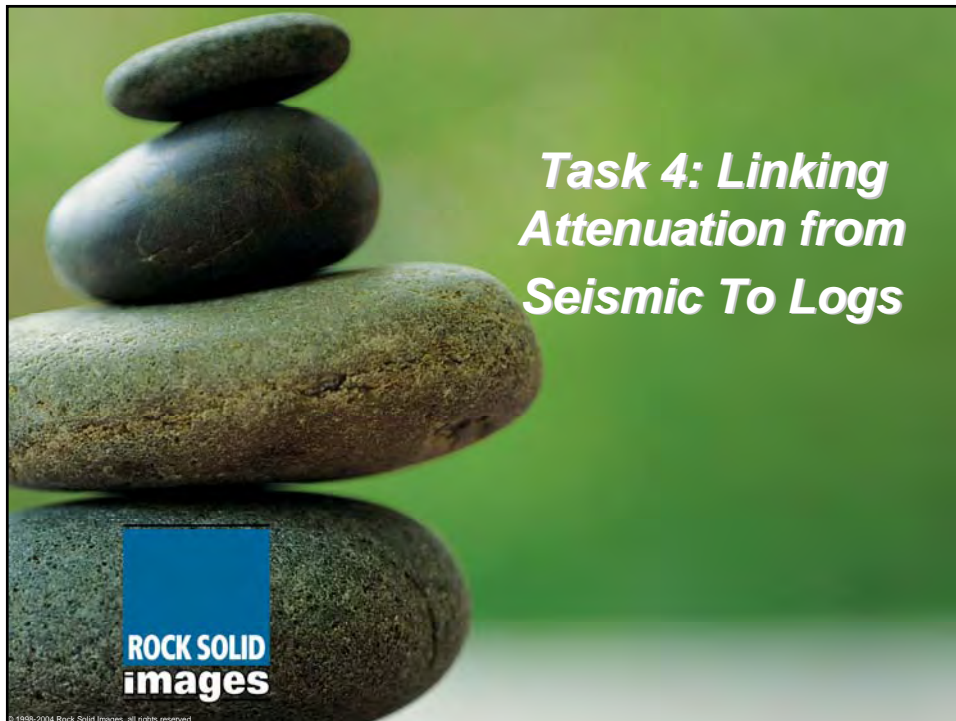
Gas Velocities Batzle & Wang vs FLAG '99 & FLAG '03



Task 3 Summary

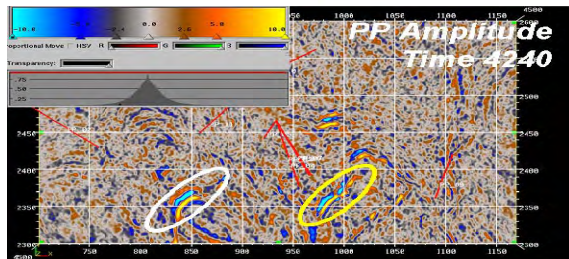
- Gas modulus and density can be predicted for deep, high pressure reservoirs using NIST algorithms
- NIST results agree very well with results of Han and Batzle (UofH and CSM Fluid Props Consortium)

ROCK SOLID
images



INPUT DATA

Log Spectral Ratio - GOM



We use the log expression:

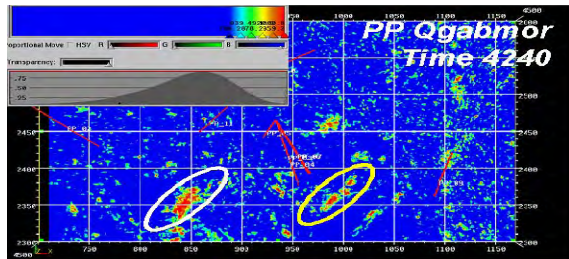
$$1/Q = [Ln\{A(f,0)\} - Ln\{A(f,t)\}] / \pi ft$$

to calculate frequency attenuation in a seismic section.

Because this method solves the attenuation equation in its pure form, it measures "total" attenuation, which includes intrinsic (layer) attenuation and extrinsic (scattering) attenuation.

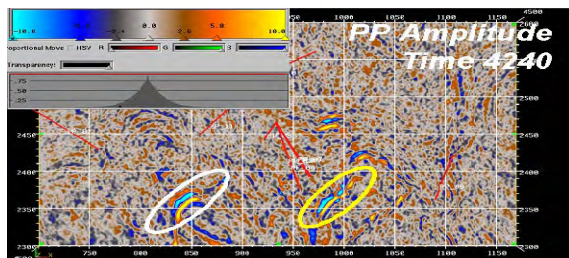
The reservoir sands are enclosed by the magenta ellipse, as are zones of attenuation (blue). Other sources of intrinsic or extrinsic attenuation can also be seen in the section.

LOG SPECTRAL RATIO

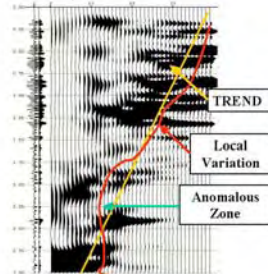


BACKGROUND Q

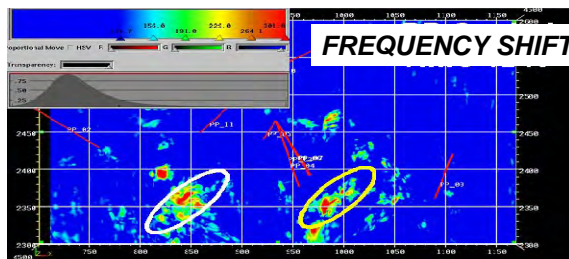
Frequency Shift - GOM



This method makes an attempt to remove extrinsic (scattering) attenuation by calculating and removing the low frequency "trend". This low frequency trend is assumed to be the result of a progressively increasing amount of scattering in the seismic section.



Anomalous zones of frequency loss are then highlighted. This assumption works in many depositional settings, but not all.



Closing the Loop

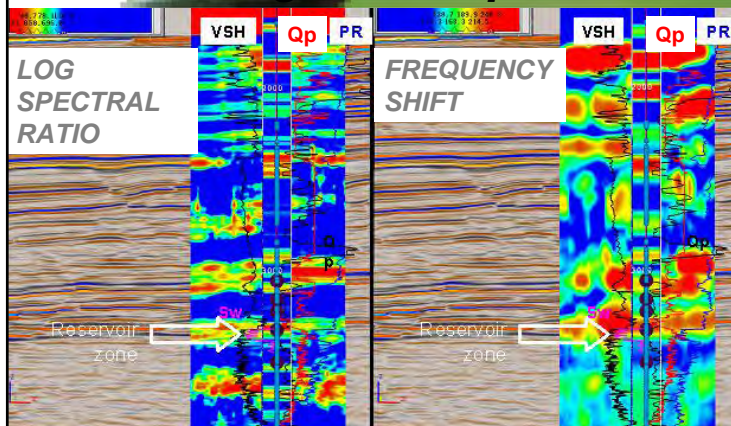
This term describes the process of benchmarking the seismic Q estimation methods using known Q models

The workflow generates 1-D earth models with known Q assigned to various layers using rock physics transforms of standard well log data

- then generates normal incidence synthetics, simulating recorded reflection seismic traces in the attenuating earth
- and applies Q-estimation algorithms to the traces to extract an apparent profile of Q
- and finally compares the estimated Q with the initial model Q, as a means to objectively evaluate the performance of our tools.

ROCK SOLID
images

Closing the Loop – Offshore Norway

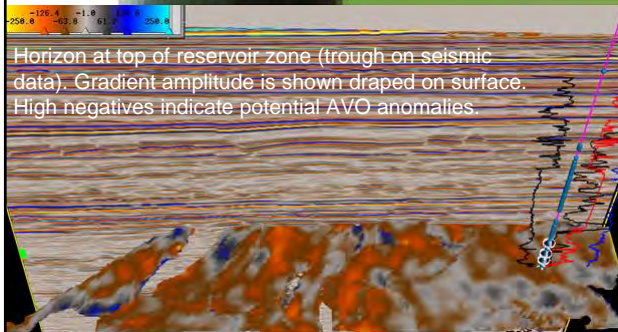


Seismic/Well tie of Log Spectral Ratio and Frequency Shift Q estimation sections.

Inner corridor contains Q estimated traces from a stacked Wave Equation synthetic gather set against those from the seismic data, with a backdrop of the seismic data itself.

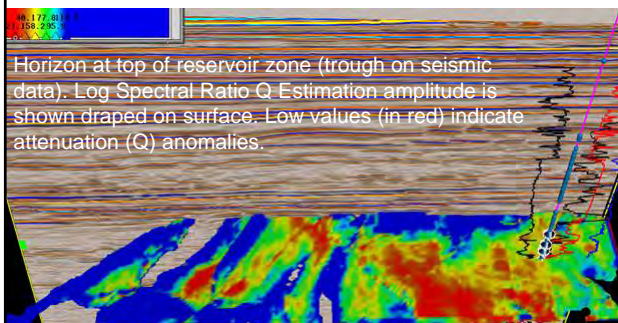
ROCK SOLID
images

Elastic & Inelastic – Offshore Norway



Anomalies on elastic gradient attributes are compared to inelastic attributes at top of reservoir zone.

The elastic and inelastic responses are significantly different. The elastic attributes are responding to tuning as the reservoir thins to the left. The inelastic attributes are not affected by tuning.



The result is a misleading impression of fluid content from the elastic attributes. However, both sets of attributes agree at the well location. They are both weak because the reservoir is low saturation and low quality.

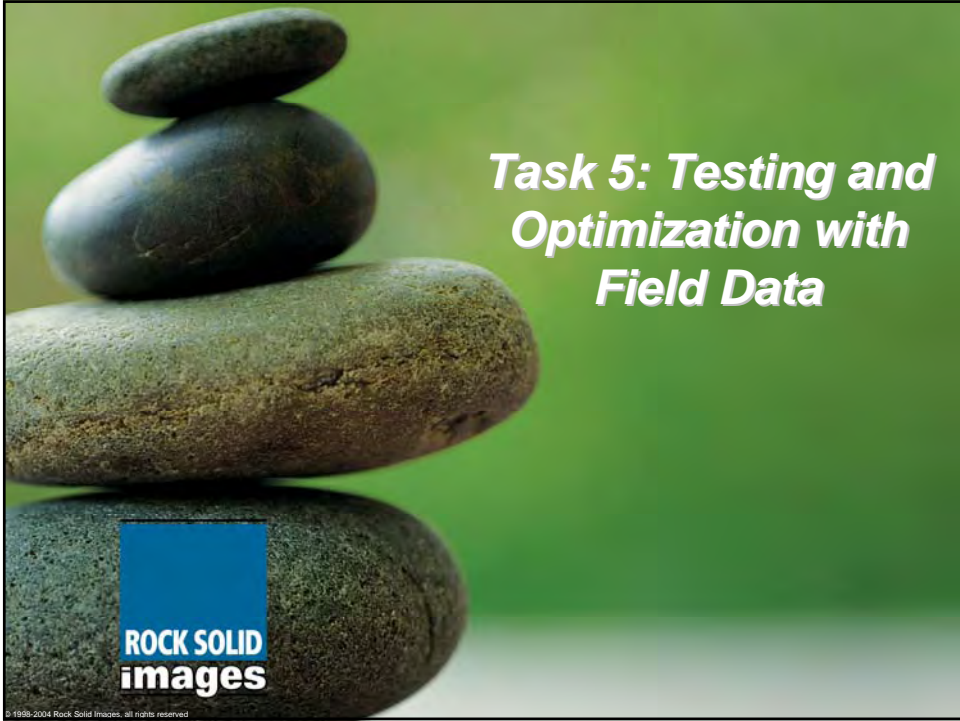
ROCK SOLID
images

Task 4 Summary

1. The link between Q from well data and field seismic data has been established.
2. The effects of low Q are to decrease amplitude, attenuate higher frequencies faster than lower frequencies, stretch wavelets, and rotate wavelet phase.
3. Two methods for computing attenuation from seismic data have been developed; Log Spectral Ratio and Frequency Shift. Both are based on the same Gabor-Morlet Joint Time-Frequency Analysis used to separate the frequency spectra into discrete, well-behaved bands.
4. The new Q-measurement techniques presented here use comparison of frequency bands *within the same time interval* by spectrally balancing the frequency bands to approximate the seismic section as it would appear before having undergone attenuation (*if dispersion is ignored*). The spectrally balanced section can then be compared with the original section to derive an estimate for attenuation.
5. Because the two methods measure different aspects of the attenuation profile, and make different assumptions, they must be used together to avoid potential erroneous interpretations.
6. These attenuation measurements are important to deep gas reservoir assessment because elastic attributes are subject to considerable error due to low gather quality in deep sections.

ROCK SOLID
images

© 2009-2010 Rock Solid Images. All rights reserved.



Task 5: Testing and Optimization with Field Data

**ROCK SOLID
images**

© 1998-2004 Rock Solid Images, all rights reserved

Eugene Island Field Testing

Ocean Bottom Cable (OBC) seismic data were obtained from Seitel Data Inc (Seitel) located in the Eugene Island area of the Gulf of Mexico.

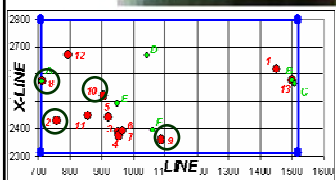
The OBC system deployed 4 receiver components, 3 orthogonal geophones plus 1 hydrophone.

This data was processed to PP and PS stack volume reflection amplitudes by Seitel.

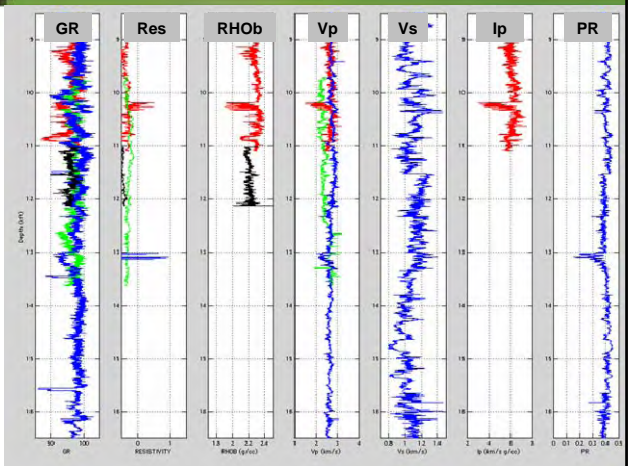
Bottom hole locations of the 13 youngest wells greater than 10000 ft TD within the seismic data area shown in red. Green wells are the velocity survey wells.

© 1998-2004 Rock Solid Images, all rights reserved

Well Log Data



Wells 2, 8, 9 & 10 contain incomplete log suites, but all contributed to the derivation of the soft sand model

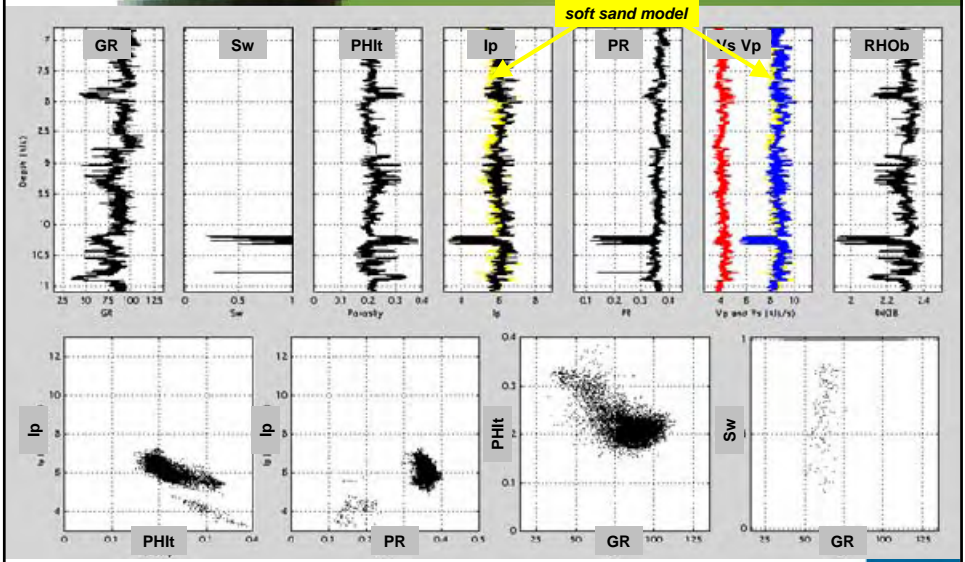


Log data display for the four wells under examination.

- blue for well # 2
- red for well # 8
- green for well # 9
- black for well # 10.



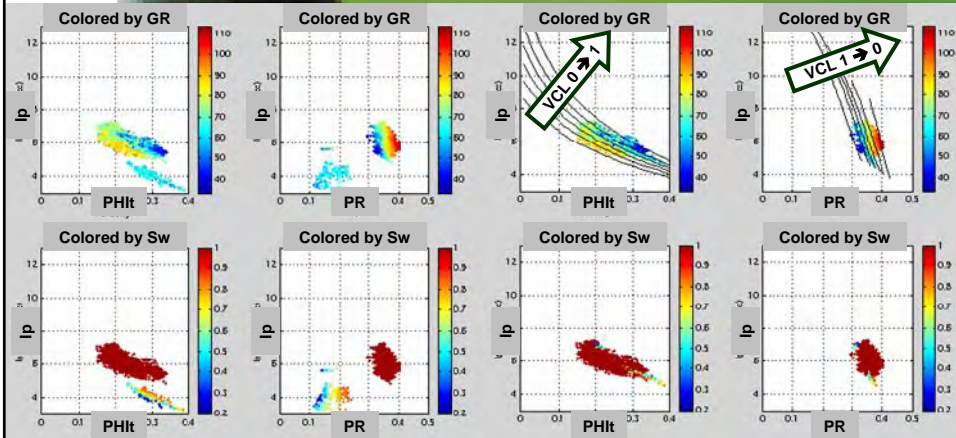
Well # 8 Soft Sand Model



Log data display for well # 8. The yellow curves superimposed upon the data in the impedance and velocity frames were calculated from the soft-sand model using the porosity and clay as well as the pore-fluid properties as inputs.



Well # 8 Soft Sand Model

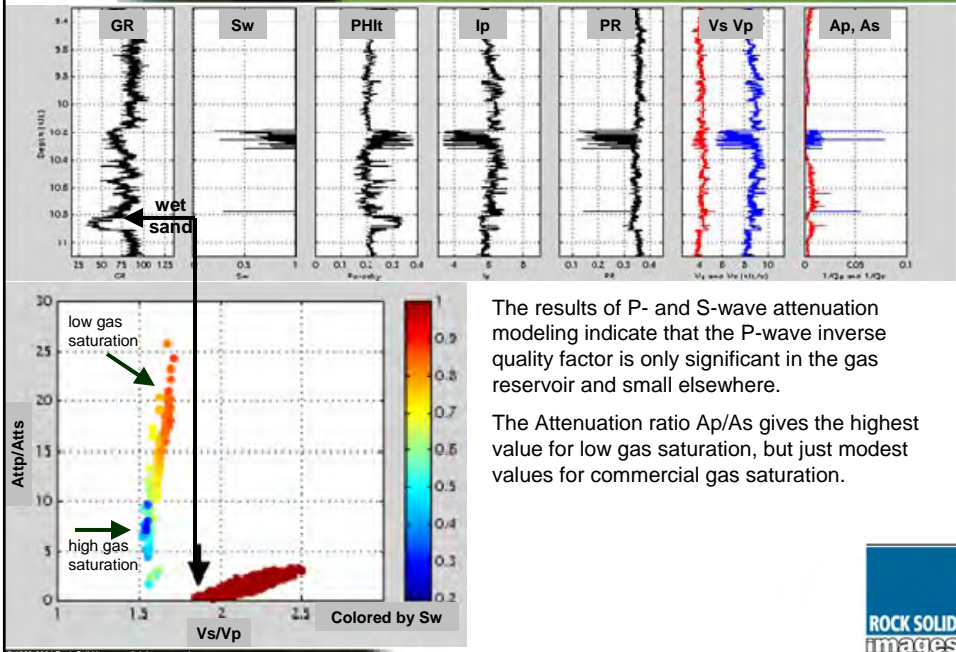


Well # 8 – in-situ conditions

Well # 8 – wet conditions – the data fits very well inside the soft sand model bounds.

ROCK SOLID
images

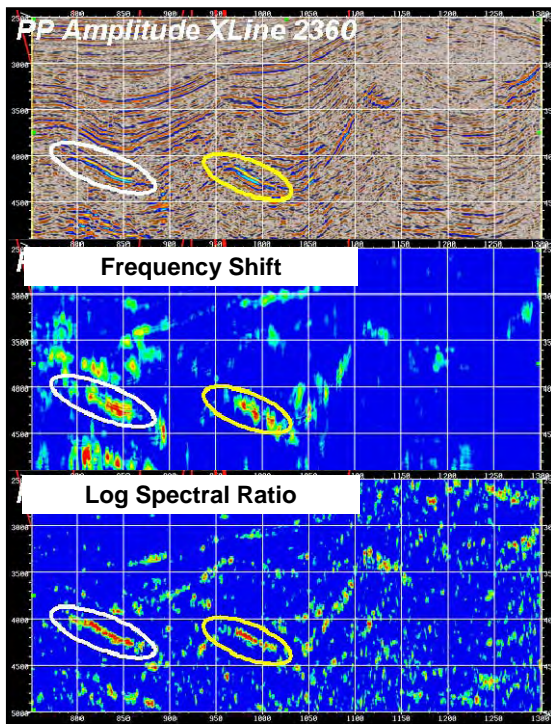
Attenuation Modeling



The results of P- and S-wave attenuation modeling indicate that the P-wave inverse quality factor is only significant in the gas reservoir and small elsewhere.

The Attenuation ratio A_p/A_s gives the highest value for low gas saturation, but just modest values for commercial gas saturation.

ROCK SOLID
images



PP Attenuation

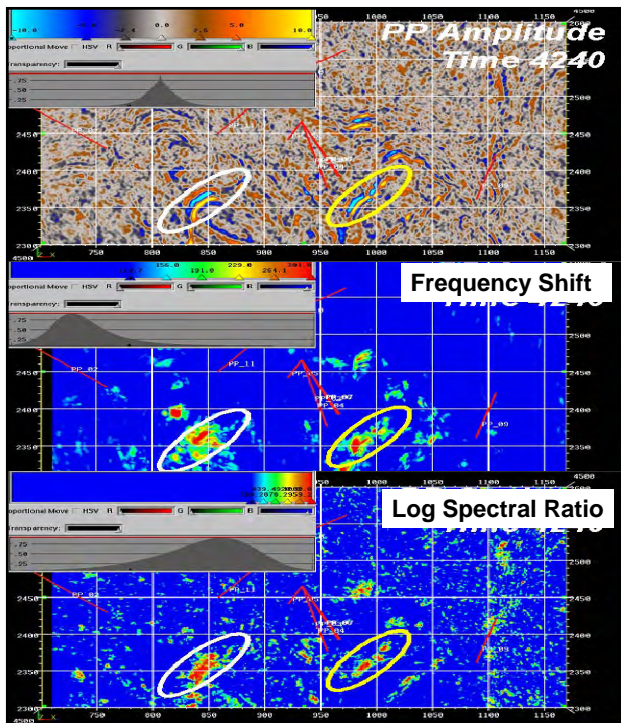
Qualitative results are seen on XLINE 2360 between 4000 and 4500 ms on XL 2360 and the neighboring area.

Two different fault blocks are evident from the seismic amplitude display and both Q attributes show attenuation for the events at the updip ends of the fault blocks.

The Log Spectral Ratio attribute has higher temporal resolution than the Frequency Shift attribute but increased noise content. The Frequency Shift attribute response shows other event responses above and below the "white ellipse" event not seen as well on the Log Spectral Ratio response.

This is important since the attributes are responding differently due to their inherent assumptions. Because of this, positive intrinsic (layer) attenuation anomalies can only result from the agreement of both methods.

ROCK SOLID
images

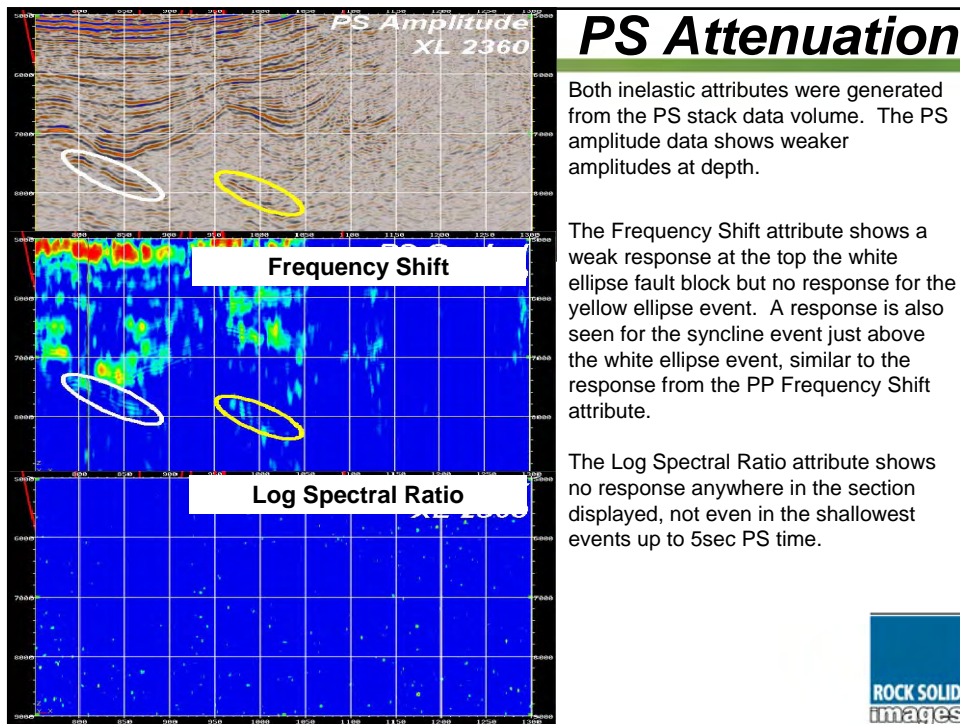


PP Atten

Horizontal sections indicating spatially continuity of Q attribute responses in each fault block.

Other strong amplitude events do not exhibit the same strength of inelastic attribute response seen for the white and yellow ellipse events. This is further encouragement that the attribute response is anomalous and represents high intrinsic (layer) attenuation.

ROCK SOLID
images



PS Attenuation

Both inelastic attributes were generated from the PS stack data volume. The PS amplitude data shows weaker amplitudes at depth.

The Frequency Shift attribute shows a weak response at the top the white ellipse fault block but no response for the yellow ellipse event. A response is also seen for the syncline event just above the white ellipse event, similar to the response from the PP Frequency Shift attribute.

The Log Spectral Ratio attribute shows no response anywhere in the section displayed, not even in the shallowest events up to 5sec PS time.

ROCK SOLID
images

Task 5 Summary

1. The PP amplitude data show indications of potential deep gas charged reservoirs. These data indicate a peak over trough response and if the phase of the response is close to zero-phase, then this would represent harder sand in slower shale background. This is possible given the overpressure evidenced by the velocity survey data analyzed previously, and that deep sand could be cemented to some extent.
2. The deep (6900-7400 ms) PS data has a lower bandwidth than the corresponding (3600-4000) PP data. The reasons for this were discussed earlier and thought mostly due to the slower propagation velocity of the PS compared to the PP data and warping the PS to the PP time will effectively double frequency band making the PS band approach that of the PP data.
3. The deep (4000-4500ms PP time) events are reasonably well imaged using PP data and the corresponding PS events (7300-7800ms PS time) are partially imaged. This implies that the PS data can be used to support the PP structural interpretation in exploration of deep gas targets.
4. Rock physics predicts the Qp response for gas sand is expected to be strong, while the Qs response for gas sand should be weak, as shown in this field data. This provides strong evidence for gas in the deep zones.

ROCK SOLID
images

Current and Future Applications

- **Current**
 - Gas hydrates exploration in Nankai Trough (JOGMEC)
 - Tight gas sand overpressure detection in Green River Basin (Devon)
 - Oil exploration in Norwegian Sea (Norsk Hydro)
- **Future**
 - Gas exploration in Saudi Arabia
 - Deep gas exploration in Gulf of Mexico (multiple E&P companies)
 - Gas hydrates exploration in Gulf of Mexico (DOE)

ROCK SOLID
images

Significance of Project Results to Industry

- Q_p and Q_s can now be computed from standard well log curves.
- Q_p and Q_s can also be computed from PP and PS seismic data
- Q_p is a useful DHI attribute for gas
- Q_s helps eliminate false positives caused by scattering losses
- Q is especially important for deep targets where traditional AVO may fail

ROCK SOLID
images

Contributors

- Joel Walls, PI
- M.T. Taner
- Richard Uden
- Scott Singleton
- Naum Derzhi
- Jack Dvorkin, consultant
- Gary Mavko, consultant
- Sven Trietel, consultant

